Comportement thermo-hydro-mécanique et microstructure de l'argilite du Callovo-Oxfordien

Hamza Menaceur

THESE

Pour obtenir le grade de

Docteur de l'Université Paris-Est

Discipline : Géotechnique

Présentée par

Hamza MENACEUR

Soutenue à Champs-sur-Marne le 10 décembre 2014

Intitulée

Comportement thermo-hydro-mécanique et microstructure de l'argilite du Callovo-Oxfordien

Laboratoire NAVIER – CERMES

JURY

Pr. Albert GIRAUD	Rapporteur	Institut National Polytechnique de Lorraine
Pr. Jian-Fu SHAO	Rapporteur	Ecole Polytechnique – Université de Lille
Pr. Christian DAVID	Examinateur	Université Cergy Pontoise
Dr. Jean TALANDIER	Examinateur	Agence nationale pour la gestion des déchets radioactifs
Dr. Anh Minh TANG	Examinateur	Ecole des Ponts ParisTech
Pr. Pierre DELAGE	Directeur de thèse	Ecole des Ponts ParisTech

THESE

Pour obtenir le grade de

Docteur de l'Université Paris-Est

Discipline : Géotechnique

Présentée par

Hamza MENACEUR

Soutenue à Champs-sur-Marne le 10 décembre 2014

Intitulée

Comportement thermo-hydro-mécanique et microstructure de l'argilite du Callovo-Oxfordien

Laboratoire NAVIER – CERMES

à mes parents

à Aïcha

à mes sœurs et mes frères

à l'Algérie

Remerciements

Ce travail a été réalisé au sein du laboratoire Navier-CERMES de l'Ecole des Ponts ParisTech dans le cadre du projet GL Géomécanique de l'ANDRA. Je souhaite vivement remercier les personnes qui ont contribué à accomplir avec succès l'ensemble de mes tâches.

Je remercie très chaleureusement mon directeur de thèse Pr. Pierre DELAGE pour m'avoir accordé une grande disponibilité, ses encouragements et sa confiance. Son expérience, sa rigueur scientifique, sa pédagogie ont constitué un soutient indispensable à la réalisation de cette étude.

Je remercie sincèrement mon encadrant Anh-Minh TANG qui m'a apporté un soutien considérable. Je le remercie pour ses idées brillantes et les échanges fructueux qu'on a eus.

J'adresse tous mes remerciements à Pr. Christian DAVID qui a présidé le jury de thèse, à Pr. Jian-Fu SHAO et Pr. Albert GIRAUD qui m'ont fait l'honneur d'accepter d'être rapporteurs de ma thèse, ainsi que Jean TALANDIER, d'avoir accepté de faire partie de mon jury.

Je remercie chaleureusement Monsieur Siavash GHABEZLOO, chercheur à l'Ecole des Ponts ParisTech pour ses conseils enrichissants tout au long de cette thèse.

La partie expérimentale de ce travail n'aurait pas été possible sans l'aide constante d'une équipe technique performante. Je remercie particulièrement Hocine DELMI qui m'a apporté une aide sans égale pour la réalisation de mes essais. Je remercie également Emmanuel DE LAURE, Marine LEMAIRE, Baptiste CHABOT, et Xavier BOULAY pour leur aide et conseils.

Je remercie également l'ensemble des chercheurs de l'équipe CERMES pour leur générosité scientifique et les connaissances qu'ils ont pu me transmettre lors de nos multiples discussions et échanges quotidiens.

Je remercie tous mes amis du CERMES et ailleurs pour leur encouragement, leur soutien et tout les moments très agréables que j'ai eus avec eux.

Hamza

Résumé

Le développement de l'énergie nucléaire durant les dernières années nécessite de trouver des solutions pour le stockage et le confinement des déchets radioactifs. Une solution envisagée est l'enfouissement dans les formations argileuses peu perméables comme les argilites. Dans cette perspective, l'Andra a mis l'accent sur l'étude du comportement à court et à long terme de l'argilite du Callovo-Oxfordien (COx), considérée comme une roche hôte potentielle en France. Dans le cadre de ce projet, une étude expérimentale microscopique et macroscopique sur le comportement thermo-hydro-mécanique de l'argilite du COx a été réalisée.

Dans un premier temps, une investigation microstructurale des propriétés de rétention d'eau a été réalisée. L'étude de la courbe de rétention d'eau déterminée par la technique de contrôle de succion par phase vapeur et incluant les changements de volume et de degré de saturation en fonction de la succion le long des chemins de séchage et humidification a été complétée par une étude microstructurale basées sur des mesures porosimétriques par intrusion de mercure sur éprouvettes lyophilisées. On observe que les concepts régissant l'hydratation des smectites peuvent être utilisés pour une meilleure compréhension des effets de changement de teneur en eau sur la microstructure de l'argilite.

Le comportement en compression-gonflement avec un aspect microstructural a été étudié par la réalisation d'un programme d'essai oedométriques haute pression et l'utilisation conjointe de la porosimétrie au mercure et le microscope électronique à balayage. Les résultats obtenus ont montré que le potentiel du gonflement était lié à la densité de fissuration engendrée lors de la compression.

Le comportement thermo-mécanique de l'argilite du COx saturée a été étudié à partir d'essais de cisaillement et de chauffage en condition drainée réalisés à l'aide d'une cellule triaxiale cylindre creux à faible chemin de drainage. Les essais de cisaillement à 25°C montrent des résistances au cisaillement plus faible pour des éprouvettes de plus forte porosité. Les essais triaxiaux à 80°C montrent un comportement plus ductile, une résistance au cisaillement moins importante et pas d'effet significatif sur les paramètres élastiques de l'argilite. L'analyse des résultats des essais de chauffage drainée confirme un comportement plastique contractant, similaire aux argiles normalement consolidées, pour l'argilite du COx.

La possibilité de réactivation d'un plan de cisaillement lors d'un essai de chauffage non drainé d'un échantillon de l'argilite du COx est mise en évidence. Les résultats obtenus montrent que la pressurisation thermique du fluide interstitiel peut, du fait du relâchement de contrainte induit, réactiver une fissure de cisaillement existante.

Les propriétés d'auto-colmatage de l'argilite du Callovo-Oxfordien, dans une gamme de température de 25-80°C, ont été étudiées par la réalisation d'essais de perméabilité sur un échantillon endommagé par un chargement déviatorique. Les résultats montrent que la présence des plans de cisaillement n'affecte pas la perméabilité, ce qui confirme la bonne capacité d'auto-colmatage de l'argilite du COx.

Mots clés

Argilite · roche · microstructure · propriétés de rétention d'eau · gonflement · résistance au cisaillement · auto-colmatage · cellule triaxiale cylindre creux · comportement thermique.

Abstract

The development of nuclear energy in recent years requires safe solutions for the storage of radioactive waste. A solution proposed for high activity radioactive waste is the storage in deep low permeability geological formations such as claystones. In this perspective, Andra, the French agency for the management of radioactive wastes, supported investigations on the short and long term behaviour of the Callovo-Oxfordian (COx) claystone, considered as a potential host rock in France. In this framework, a microscopic and macroscopic experimental study on the thermo-hydro-mechanical behaviour of COx claystone was carried out.

In this work, a microstructure investigation of the water retention properties of the COx claystone was performed. The water retention properties were determined by controlling suction through the vapour phase, with also the monitoring of volume changes and changes in degree of saturation as a function of suction along the drying and wetting paths. The study was completed by a microstructure investigation based on the use of mercury intrusion porosimetry on freeze-dried specimens. It was observed that the concepts governing the hydration of smectites appeared useful to better understand the effects of changes in water content and suction on the microstructure of COx claystone.

In a second step, the compression-swelling behaviour of the COx claystone was related to microstructure features by performing high pressure oedometer compression tests and by running mercury intrusion porosimetry tests and scanning electron microscope observations on specimens submitted to compression and stress release. The results obtained showed that the potential of swelling was linked to the density of cracks generated during compression.

The thermo-mechanical behaviour of fully saturated COx claystone specimens was investigated from shear and drained heating tests using a hollow cylinder triaxial device specially developed for low permeability materials. The shear tests at 25°C evidenced lower shear strength on specimens with higher porosity. The preliminary results obtained at 80°C evidenced a more ductile response, with slightly smaller shear strength and little changes of the elastic parameters at elevated temperature. Drained isotropic heating tests confirmed the contracting volumetric plastic behaviour of the COx argillite, similar to normally consolidated clays.

The effect of thermal pressurisation of the pore water on a specimen with a pre-existing shear plan was investigated. The results showed that undrained heating under shear stress decreased the effective stress, bringing back the sheared specimen to failure.

The self-sealing properties of COx claystone at 25 and 80°C were investigated by conducting steady state permeability tests on sheared specimens at various stages. The results showed that the overall permeability of the sheared specimen at 25 and 80°C was comparable to that before shearing, confirming the good self-sealing properties of COx claystone.

Keywords

Claystone · shale · microstructure · water retention properties · swelling · shear strength · self-sealing · hollow cylinder triaxial cell · thermal response.

Publications

1. P DELAGE, **H MENACEUR**, AM TANG, J TALANDIER (2014). Suction effects in deep Callovo-Oxfordian claystone. *Géotechnique Letters* 3(2) : 84-88.

2. **H MENACEUR**, P DELAGE, AM TANG, N CONIL (2014). On the Thermo-Hydro-Mechanical behaviour of a sheared Callovo-Oxfordian claystone sample with respect to the EDZ behaviour. Submitted in International Journal of Rock Mechanics and Rock Engineering.

3. **H MENACEUR**, P DELAGE, AM TANG, NCONIL (2014). On the thermo-mechanical behaviour of Callovo-Oxfordian claystone. Submitted in International Journal of Rock Mechanics and Rock Engineering.

4. **H MENACEUR**, P DELAGE, AM TANG, J TALANDIER (2014). A microstructure investigation of the compression-swelling behaviour of shales: the case of the Callovo-Oxfordian claystone. Submitted in Engineering Geology.

5. **H MENACEUR**, P DELAGE, AM TANG, N CONIL (2014). Auto-colmatage d'un plan de cisaillement dans l'argilite du Callovo-Oxfordien. Conférence JNGG 2014.

6. M Wan, P DELAGE, **H MENACEUR**, AM TANG, J TALANDIER (2014). Propriétés de rétention d'eau de l'argilite du Callovo-Oxfordien. Conférence JNGG 2014.

7. M Wan, **H MENACEUR**, P DELAGE, AM TANG, B GATMIRI (2012). Propriétés de rétention d'eau de l'argilite du Callovo-Oxfordien. 2eme Colloque international des Sols Non Saturés et Environnement (Unsat Alger 2012), Alger 5-6 Novembre 2012.

8. **H MENACEUR**, P DELAGE, AM TANG (2013). The self sealing properties of the Callovo-Oxfordian claystone. Poster presented in 24th ALERT Workshop, Aussois.

9. P DELAGE, M Mohajerani, **H MENACEUR**, N CONIL (2013). Coupling between damage and swelling in the callovo-oxfordian claystone. ALERT Workshop, Aussois.

10. **H MENACEUR**, P DELAGE, AM TANG, J TALANDIER (2014). Permeability measurements on unsheared and sheared specimens of the Callovo-Oxfordian claystone at ambient and elevated temperature. Poster presented in Workshop Low Permeability Materials, Cergy.

Sommaire

Introduction générale

1. Contexte général: stockage dans les couches géologiques profondes

Le stockage des déchets radioactifs dans les formations géologiques profondes, peu perméables et tectoniquement stables, comme les argilites est considéré comme une solution satisfaisante de sécurité pour la population et l'environnement en France comme dans de nombreux pays étrangers. Ces formations hôtes sont principalement des couches argileuses (France, Belgique, Suisse), des mines de sel (USA, Allemagne) et des sous-sols granitiques (Japon, Canada).

La classification des déchets radioactifs s'effectue selon deux critères : (i) la période de radioactivité contenue dans le déchet, (ii) le type de rayonnement et le niveau de radioactivité. Ces déchets sont classés en trois groupes :

- Déchets A : déchets de faible et moyenne activité à vie courte qui constituent 85 % du volume total des déchets mais moins de 1% de la radioactivité ;
- Déchets B : déchets de moyenne activité à vie longue qui représentent environ 4% du volume total des déchets et moins de 8% de la radioactivité. ils sont essentiellement produits lors du retraitement du combustible, de la maintenance courante et des opérations d'entretien des usines de retraitement ou du parc électronucléaire (Su et al. 2005) ;
- Déchets C : déchets de haute activité à vie longue (HAVL) qui constituent environ 2% du volume total mais 92% de la radioactivité. Ce sont des déchets de vitrifiés issus du retraitement des combustibles usés. Ces déchets sont exothermiques.

Pour les déchets de type A, la solution de stockage consiste à les entreposer dans des centres de stockage en surface. En revanche, cette option n'est pas adaptée pour les déchets de type B et C car ils sont actifs pendant plusieurs dizaines de milliers d'années voire millions d'années. La solution envisagée pour ces deux types de déchets est l'enfouissement et le confinement dans les couches géologiques profondes.

Dans le cas de la France, l'argilite du Callovo-Oxfordien (COx) a été sélectionnée comme barrière géologique potentielle pour le stockage des déchets radioactifs (Figure 1) par l'Andra, l'Agence nationale pour la gestion des déchets radioactifs. L'Andra a développé un

laboratoire de recherche souterrain dans la formation du COx à 490 m de profondeur près du village de Bure (Est de la France) pour effectuer des investigations in situ destinées à étudier les divers aspects de stockage des déchets radioactifs, y compris le comportement thermo-hydro-mécanique de la roche hôte dans le champ proche.

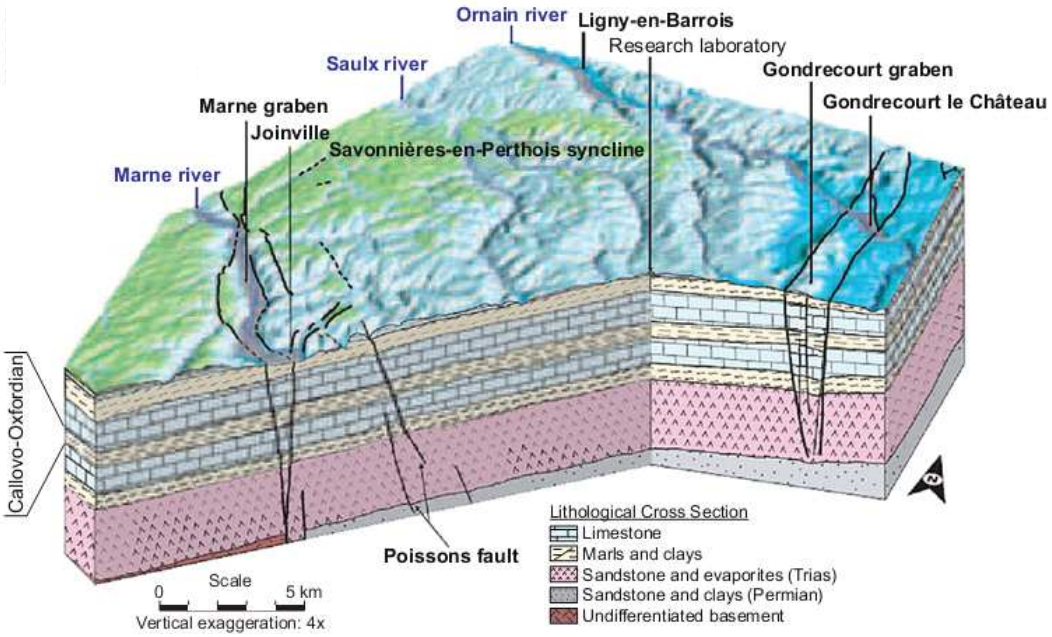

Figure 1. Diagramme des formations géologiques de Meuse/Haute-Marne (d'après Andra 2005).

Le concept de stockage prévoit une réversibilité sur une certaine période afin de laisser aux générations futures une liberté de décision quant au choix de gestion, et en particulier la possibilité d'un retrait des colis stockés ou des aménagements possibles du processus de stockage. De plus, l'ouverture permet de réaliser un certain nombre d'observations et de mesures sur le site. Cependant, pendant toute la durée d'exploitation, la formation géologique est assez profondément perturbée par un ensemble des sollicitations thermo-hydro-mécanique couplées (Tsang et al. 2005).

Tout d'abord, l'excavation des galeries souterraines engendre une perturbation majeure dans la formation et conduit à la création d'une zone endommagée mécaniquement, désignée par *Excavation Damaged Zone* (*EDZ*). Cette étape peut conduire une dégradation des propriétés hydromécaniques, notamment la perméabilité (paramètre important pour les critères de sûreté) à cause de la formation des fractures en cisaillement et l'ouverture de joints en traction. Ensuite, la ventilation des galeries avec de l'air à humidité variable peut également participer à cette dégradation. L'augmentation de température due à la nature exothermique des déchets est également un aspect important à étudier. Une température maximale de 90°C

à la paroi des colis est prise en compte dans le concept français. Cette température élevée modifie à long terme la température ambiante autour des galeries et elle affecte également la distribution des pressions d'eau. Après la fermeture du stockage, une resaturation progressive commence par infiltration d'eau provenant de la roche.

Cette brève présentation du contexte de stockage montre la nécessite d'apporter des réponses satisfaisantes à cette problématique du comportement thermo-hydro-mécanique de l'argilite du COx. Dans ce contexte, de nombreux travaux de recherche ont été réalisés dans les dernières décennies afin de d'étudier le comportement des matériaux argileux pendant les différentes étapes de la vie d'un site de stockage.

2. L'argilite du Callovo-Oxfordien

2.1. Lithologie

D'un point de vue géologique, l'argilite du Callovo-Oxfordien est une roche sédimentaire déposée depuis 155 millions d'années (la limite Jurassique moyen-supérieur) entre deux couches de plusieurs centaines de mètres d'épaisseur, de Dogger calcaire et Oxfordien calcaire (Figure 2). Cette couche de 130 m d'épaisseur, comprise entre -420 et -550m a l'aplomb du laboratoire souterrain, correspond à l'Unité C2. Celle-ci est caractérisée par deux ensembles lithologiques majeurs subdivisés en quatre lithofacies, notés C2a, C2b, C2c et C2d (Figure 2) :

- Les unités supérieures composées des lithofacies C2c et C2d. Elles sont décrites comme des faciès d'alternance d'argilite et d'argilite silto-calcaire. Ces unités se caractérisent par un enrichissement rapide de la phase silteuse (20 à 60%) et carbonatée (de 25 à 80% au sommet de la formation, Andra 2012) ;
- Les unités inférieures composées des lithofacies C2a et C2b. Elles représentent ¾ de l'épaisseur de la formation. Elles sont associées à la zone la plus argileuse et la plus homogène du Callovo-Oxfordien avec des teneurs en argiles pouvant atteindre localement 50 %. Elles se subdivisent en 4 sous unités dont l'unité Cb2, unité la plus argileuse du Callovo-Oxfordien où se situe le laboratoire souterrain. Ces séquences sédimentaires sont l'expression des variations du niveau marin ayant affecté le Bassin Parisien au Callovo-Oxfordien.

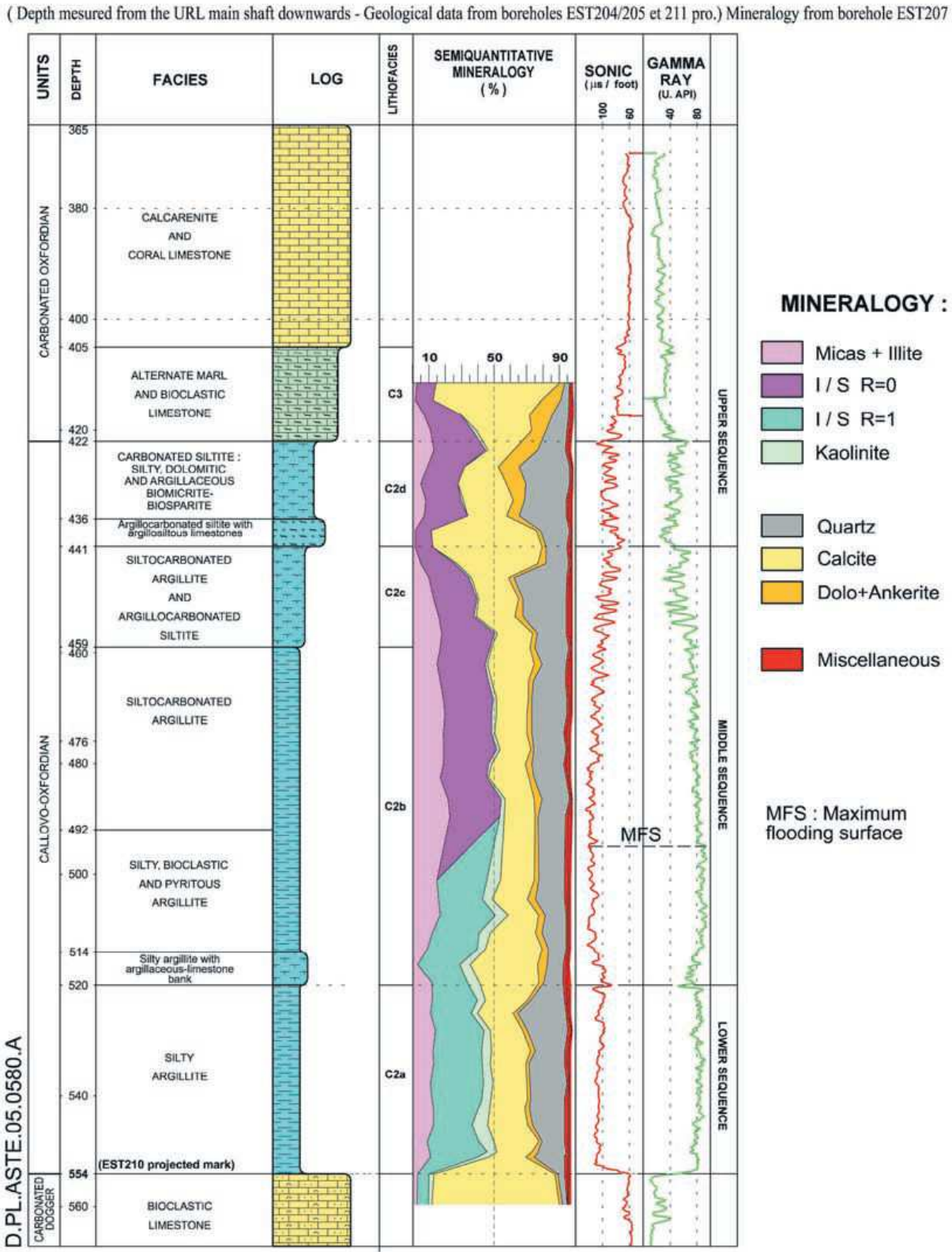

Figure 2. Lithologie et minéralogie des argilites du Callovo-Oxfordien à l'aplomb du laboratoire souterrain de recherche de Bure (Meuse/Haute-Marne).

2.2. Minéralogie

La diffraction des rayons X (DRX) a été utilisée pour caractériser la composition minéralogique de l'argilite du Callovo-Oxfordien. En plus de la diffraction des rayons X, l'estimation semi-quantitative des différentes phases existantes a été combinée avec la composition chimique de l'ensemble de la roche et la capacité d'échange de cations (CEC). La présence de certains minéraux a été également confirmée par les observations faites au microscope électronique à balayage (MEB).

L'argilite du Callovo-Oxfordien est principalement composée de trois groupes de minéraux : minéraux argileux, calcite et quartz. Les proportions des minéraux changent au long de la profondeur (Figure 2). Au niveau du laboratoire souterrain de Bure (490 m), la composition minéralogique moyenne de l'argilite est la suivante (Gaucher et al. 2004): 45-50% de minéraux argileux, 28% de carbonate et 23% de quartz. L'argilite contient également 4% d'autres minéraux dits «lourds», essentiellement de la pyrite (0,5-1%) et la sidérite (0,5-3%).

Les minéraux argileux sont majoritairement constitués d'interstratifiés illite/smectite divisés en deux types : (i) les interstratifiés illite/smectite type-R1 dans la partie supérieure de la formation (voir Figure 2), contenant 20-40% de smectites. (ii) les interstratifiés illite/smectite type-R0 dans la partie inférieure de la formation, constitués par 50-70% de smectites. La transition de R1 à R0 s'effectue progressivement à une profondeur d'environ 490m, correspondant au niveau du laboratoire souterrain avec des teneurs en argiles pouvant atteindre les 50%.

2.3. Microstructure

L'étude de la microstructure est nécessaire pour mieux comprendre la distribution spatiale et la géométrie des minéraux composants. Elle nécessite une zone d'investigation suffisamment grande afin de fournir une meilleure représentation du matériau étudié. La microstructure des roches sédimentaires riches en minéraux argileux est peu étudiée dans la bibliographie. Ce manque de données est essentiellement lié à la limitation et la résolution de différentes méthodes expérimentales utilisées et qui sont souvent complémentaires. Dans le cas de l'argilite du Callovo-Oxfordien, la microstructure a été étudiée à différente échelles depuis les mesures en forage et en laboratoire jusqu'aux analyses et descriptions plus ponctuelles des minéraux (Yven et al. 2007). La Figure 3 présente le modèle conceptuel proposé pour l'argilite du COx par Yven et al. (2007). Ce modèle repose sur l'utilisation de

différentes techniques expérimentales (notamment microscope électronique à balayage, autoradiographie, porosimètrie au mercure, pétrole, hélium et l'adsorption d'azote). Le modèle montre comment les inclusions de calcite et de quartz sont noyées dans la matrice argileuse (représentant 45-50% de la composition minéralogique à 490 m de profondeur) avec une porosité interconnectée. On peut également observer que les minéraux gonflants, essentiellement les interstratifiés illite / smectite, sont, d'après ce modèle, censés se trouver dans certaines plaquettes avec une distinction claire entre les plaquettes gonflantes et non gonflantes, une hypothèse qui n'est pas discutée dans le détail de l'article.

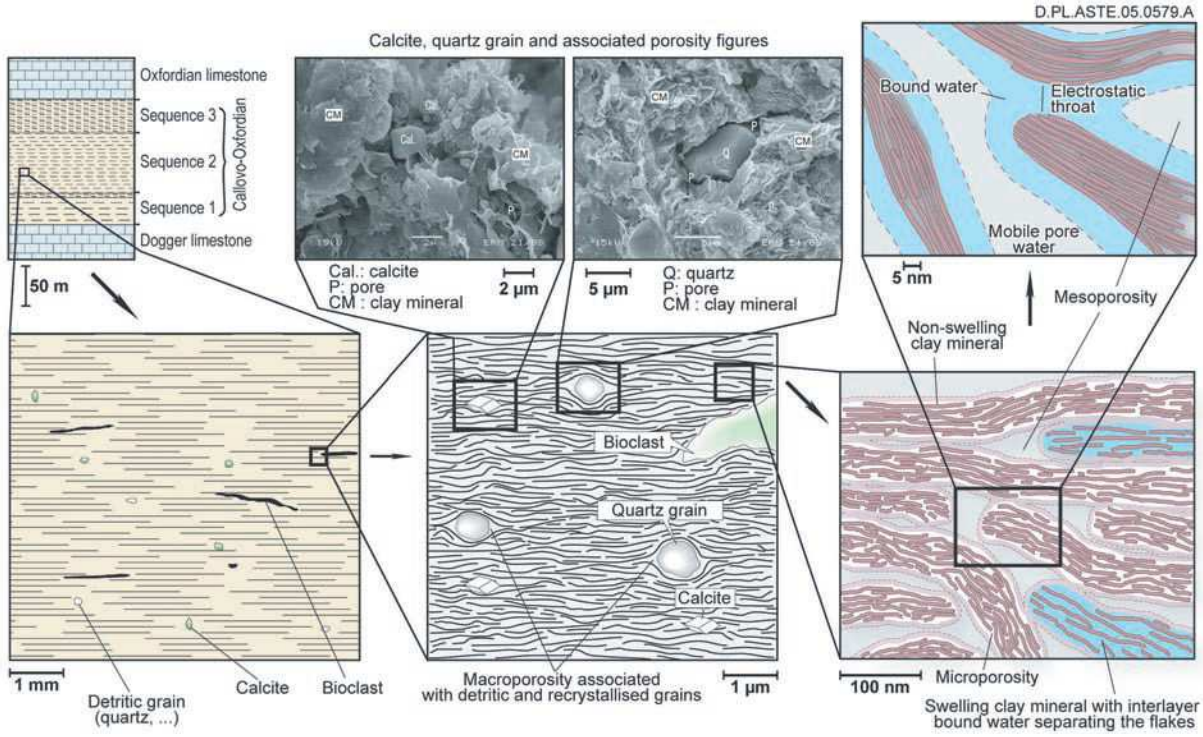

Figure 3. Schéma illustrant la microstructure de l'argilite du Callovo-Oxfordien (Yven et al. 2007).

La Figure 3 permet également de définir deux familles distinctes de porosité d'après Yven et al. (2007):

- Une porosité à l'interface entre la matrice argileuse et les autres minéraux est caractérisée par des pores micrométriques (entre la matrice argileuse et les inclusions de quartz) et par des pores sous-micrométriques (entre la matrice argileuse et les inclusions de calcite). Cette macroporosité représente approximativement 20 à 40% de la porosité total connectée dans les zones riche en carbonates ;

- Une porosité interne de la matrice argileuse est caractérisée par des tailles de pores infra-micrométrique et nanométriques. Cette porosité forme environ 60 à 80% de la porosité totale connectée. Une faible microporosité est également présente (environ 2%) et qui forme la porosité intra-plaquettes.

Un autre exemple de texture est présenté dans la Figure 4 par une cartographie de la porosité (Sammartino et al. 2002) pour un échantillon de l'argilite du COx provenant de lithofacies C2c. La Figure4a montre une image générée par autoradiographie où l'intensité des niveaux de gris de chaque pixel est proportionnelle à leur porosité absolue. La présence de deux zones distinctes a été clairement identifiée dans cette figure : (i) les zones riches en minéraux argileux (CLA), (ii) les zones riches en carbonates (CCA). Un modèle de répartition de la porosité par autoradiographie est proposé dans la Figure 4b. On peut observer que la porosité est répartie en trois zones : zones bleues (porosités inferieures à 13%), zones vertes (porosités comprises entre 13 et 20%) et zones rouges (porosités comprises entre 20 et 30%).

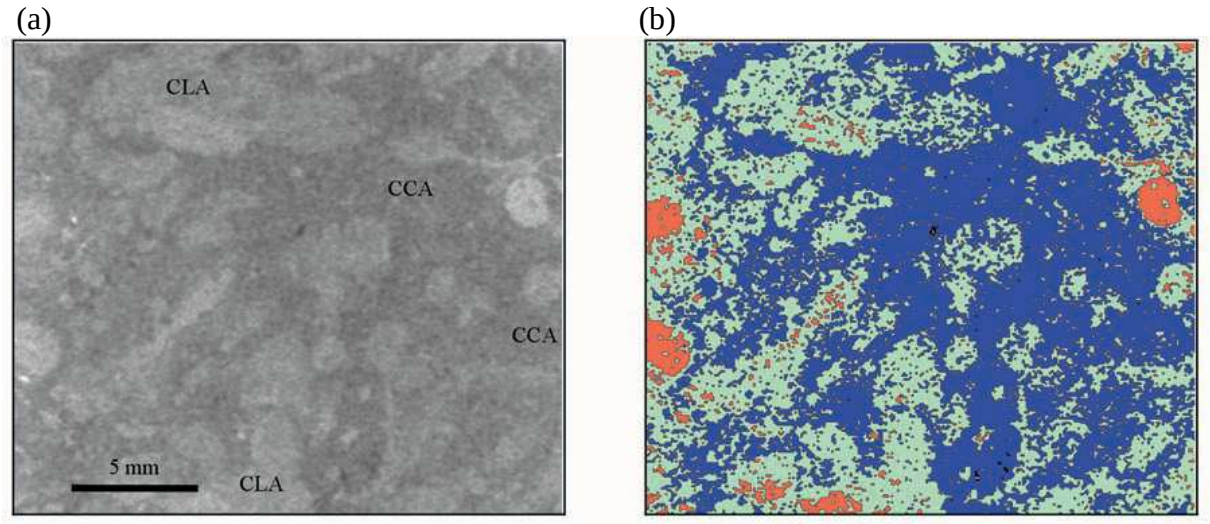

Figure 4. Cartographie de la porosité par autoradiographie d'après Sammartino et al. (2002).

Une zone à faible porosité a été localisée par autoradiographie (Figure 5a) qui correspond à la zone bleue de la Figure 4b (zone CCA). Elle souligne l'existence d'une charge détritique relativement importante (des minéraux de calcite et quartz) dans la matrice argileuse. La distribution spatiale de ces minéraux permet de déterminer un réseau de porosité, soit à l'interface entre la matrice argileuse et les autres minéraux ou à l'intérieur de la matrice argileuse elle-même. A ce niveau d'observation, cette zone semble inclure aucun ou très peu de porosité intra-plaquettes.

Une autre zone plus poreuse est présentée dans la Figure 5b. Elle correspond aux zones vertes dans la Figure 4b (zone CLA). La matrice argileuse est représentée par une couleur violette. Contrairement à la zone moins poreuse (Figure 5a), les minéraux détritiques ne constituent pas un squelette connecté dont l'organisation aurait un impact significatif sur la porosité.

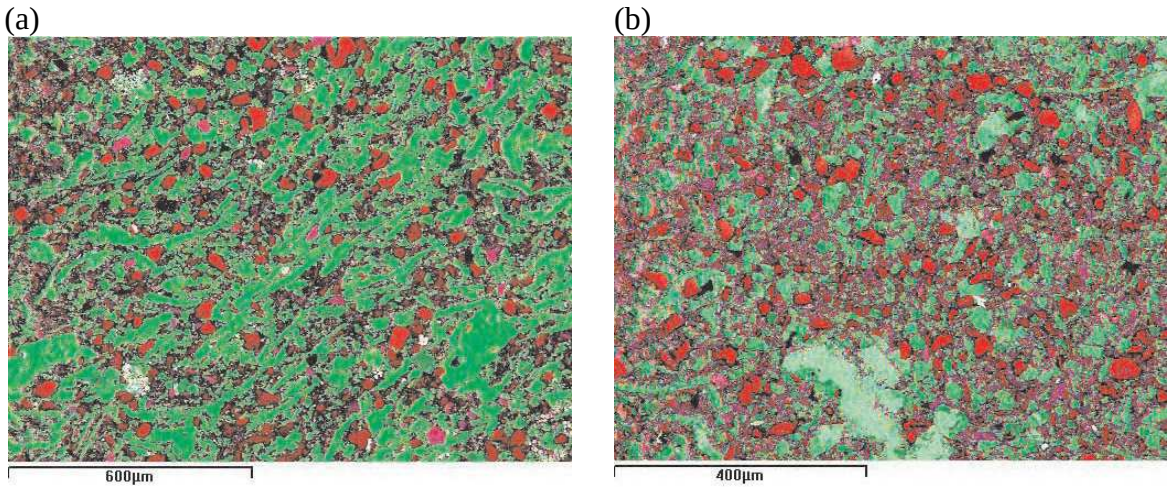

Figure 5. (a) : Zone CCA : zone riche en minéraux détritiques, (b) : Zone CLA : zone riche en matrice argileuse.

3. Les éléments principaux de cette thèse

Le travail de thèse présenté dans ce mémoire a été réalisé dans le cadre du programme scientifique du Groupement de Laboratoires Géomécanique de l'Andra. Il vise à étudier le comportement thermo-hydro-mécanique de l'argilite du COx par des approches expérimentales microscopique et macroscopique. Les échantillons d'argilite testés ont été sollicités suivant différents chemin de chargement hydrique, mécanique et thermique à l'aide de différents dispositifs expérimentaux. Les études expérimentales ont porté principalement sur (i) l'effet des chemins de séchage et humidification sur la microstructure à l'aide de l'utilisation de la porosimétrie au mercure, (ii) l'étude du couplage compression-gonflement avec un aspect microstructural par l'utilisation conjointe de la porosimétrie au mercure et le microscope électronique à balayage, (iii) l'effet de la température sur le comportement déviatorique et les changements de volumes en conditions drainées isotropes, et (iv) l'effet d'un endommagement engendré par un cisaillement sur la perméabilité à une température ambiante (25°C) et une température plus élevée (80°C), avec la possibilité de réactivation des plans de cisaillement par le phénomène de pressurisation thermique dans un échantillon endommagé.

Ce mémoire se présente sous la forme de quatre chapitres qui tenteront de répondre aux questions exposées ci-dessous :

- Le premier chapitre présente une étude microstructurale des propriétés de rétention d'eau de l'argilite du COx sous la forme d'une publication. L'étude complète de la courbe de rétention d'eau déterminée par la technique de contrôle de succion par phase vapeur et incluant les changements de volume et de degré de saturation en fonction de la succion le long des chemins de séchage et humidification a été complétée par une étude microstructurale basées sur des mesures porosimétriques par intrusion de mercure.
- Dans le deuxième chapitre, on présente tout d'abord un programme expérimental destiné à comprendre les effets de la succion sur un échantillon de l'argilite du COx sous la forme d'un article accepté dans la revue « *Géotechnique Letters* ». Une étude du couplage compression-gonflement avec un aspect microstructural est ensuite présentée sous la forme d'une publication soumise à la revue « *Engineering Geology* ». Ce chapitre est complété par la présentation de la détermination d'une loi phénoménologique permettant de définir les déformations physico-chimiques liées au gonflement durant la phase de déchargement conduite sur des échantillons préalablement comprimés à différents niveaux de contraintes.
- Le troisième chapitre présente une étude expérimentale du comportement thermo-mécanique de l'argilite du COx saturée à l'aide de la cellule triaxiale à cylindre creux à faible chemin de drainage (Monfared et al. 2011a). On présente tout d'abord une synthèse des résultats publiés sur le comportement déviatorique ainsi que sur l'effet de la température sur la réponse volumique de l'argilite du COx. Les aspects thermo-mécaniques étudiés concernent : (i) la réponse en cisaillement drainé sous différents états de contraintes et températures et (ii) la réponse en chauffage drainé. Des mesures de perméabilités ont été également réalisées pour voir un effet éventuel de la température sur la perméabilité de cette l'argilite. Les résultats obtenus dans cette étude sont présentés sous la forme d'un article écrit en anglais et soumis dans la revue « *International Journal of Rock Mechanics and Mining Science* ».
- Le quatrième chapitre est consacré à l'étude des propriétés d'auto-colmatage de l'argilite du COx par la réalisation des essais de perméabilité radiale avant et après cisaillement. La réponse d'un essai de chauffage en condition non drainée d'un échantillon préalablement porté à la rupture suivant un chemin de contrainte

moyenne totale constante, comparable à celui suivi lors de l'excavation d'une galerie, est également étudiée. Ce chapitre correspond à un article soumis dans la revue « *Rock Mechanics and Rock Engineering* ».

Chapitre 1 : Propriétés de rétention d'eau de l'argilite du Callovo-Oxfordien

Introduction

Lors de l'excavation des galeries dans le contexte de stockage des déchets radioactifs à haute activité dans les couches géologiques profondes, l'argilite du Callovo-Oxfordien (COx) dans le champ proche autour des galeries sera soumise à la fois à une désaturation induite par les effets de la ventilation puis à une resaturation de l'eau provenant de la roche saturée une fois les galeries fermées. Pour mieux comprendre ce phénomène, une bonne compréhension des propriétés de rétention d'eau de l'argilite du Cox est nécessaire.

Ces propriétés ont été étudiées par Pham et al. (2007) qui ont mis en évidence les effets d'hystérésis ainsi que les changements de la vitesse des ultrasons et la contrainte induite par des cycles d'hydratation sur des échantillons de l'argilite du COx soumis à différentes humidités relatives contrôlées. Plus récemment, une étude détaillée des propriétés de rétention d'eau de l'argilite du COx a été réalisée par Wan, Delage et al. (2013) afin de fournir une description complète des changements de volume, teneur en eau et degré de saturation le long des chemins de séchage et humidification. Cette étude a également montrée le retrait et le gonflement de l'argilite pendant les cycles de succion avec un effet d'hystérésis.

Ce chapitre présente une étude microstructurale des propriétés de rétention d'eau de l'argilite du COx suite à l'étude de Wan et al. 2013. La compréhension des mécanismes de séchage et humidification (retrait et gonflement) est examinée par la réalisation d'essais de porosimètrie au mercure sur des échantillons lyophilisés à l'état initial et à différentes succions imposées. On observe que les concepts régissant l'hydratation des smectites peuvent être utilisés pour une meilleure compréhension des effets de changement de teneur en eau sur l'argilite.

Cette étude microstructurale est l'objet d'un article destiné à une revue internationale. Le manuscrit de cet article est présenté dans ce chapitre.

A microstructure investigation of the water retention properties of shales: the case of the Callovo-Oxfordian claystone

Hamza MENACEUR[1], Pierre DELAGE[1], Jean Talandier[2]

[1] *Ecole des Ponts ParisTech, Navier/CERMES, France*

[2] *Andra, Chatenay-Malabry, France*

Abstract

The Callovo-Oxfordian (COx) claystone is considered in France as a possible host rock for the disposal of high level long lived radioactive waste at great depth. During the operational phase, the walls of the galleries and of the disposal cells will be successively subjected to desaturation induced by ventilation followed by resaturation once the galleries are closed. To better understand this phenomenon, a sound understanding of the water retention properties of the COx claystone is necessary. Following a previous study by the same group, this paper presents an investigation of microstructure changes of COx claystone under suction changes. Microstructure was investigated based on the use of the mercury intrusion porosimetry on freeze-dried specimens submitted to various suctions. Along the drying path, the initial microstructure, characterised by a well classified unimodal pore population around a mean diameter value of 32 nm, changes with the same shape of the PSD curve slightly moved towards smaller diameters (27-28 nm) at suctions of 150 and 331 MPa, respectively. The infra-porosity too small to be intruded by mercury (diameter smaller than 5.5 nm) reduces from 4% to 3%. Oven-drying reduces the mean diameter to 20 nm and the infra-porosity to 1%. Wetting up to 9 MPa suction leads to saturation with no significant change of the PSD curve, whereas wetting at zero suction gives rise to the appearance of a large pore population resulting from the development of cracks with width of several micrometers, together with an enlargement of the initial pore population above the mean diameter. The concepts describing the step hydration of smectites by the successive placement of 1, 2, 3 and 4 layers of water molecules with respect to the suction applied appeared useful to better understand the water retention properties of the COx claystone.

1. Introduction

The French Radioactive Waste Management Agency (Andra) is currently considering the Callovo-Oxfordian claystone (COx), an indurated clay rock 155 million years old (limit upper-middle Jurassic), as a potential host rock for radioactive waste disposal at great depth. An Underground Research Laboratory (URL) has been excavated at a depth of 490 m by Andra in the 150 m thick layer of the COx claystone close to the village of Bure in the North-east of France in order to carry out in-situ experiments and to assess the reliability of the host rock as a geological barrier for radioactive waste confinement (Lebon and Mouroux 1999). Due to the excavation and ventilation of the galleries, the close field around the galleries and the disposal cells is prone to desaturation, that will be followed by progressive resaturation by the pore water from the host rock at the end of the operating stage once the galleries are closed. Better knowledge of the water retention properties of the COx claystone is hence necessary.

Particular attention has been paid in recent years to investigate the significant water sensitivity of claystones. By carrying out Environmental Scanning Electron Microscope (ESEM) observations on COx claystones samples submitted to cyclic changes in relative humidity, Montes-Hernandez et al. (2004) observed the water sensitivity of the clay fraction, with significant successive openings and closures of cracks. Valès (2008), Bornert et al. (2010) and Wang et al. (2014) also evidenced the appearance of cracks resulting from hydration under zero stress conditions by using Digital Image Correlation (DIC) at microscopic scale. The water retention properties of the COx claystone have been investigated by Pham et al. (2007) who evidenced some hysteresis effects together with the changes in ultrasonic velocity and in strain induced by hydration cycles on COx samples at various controlled relative humidities. Boulin et al. (2008) determined the water retention curve of the COx claystone from its pore size distribution (determined by mercury intrusion porosimetry) and found reasonable agreement with the main wetting path of the water retention curve.

This paper is following a former one from the same group by Wan et al. (2013) who have provided a complete description of the changes in water content, volume and degree of saturation of the COx claystone along drying and wetting paths, also evidencing the swelling shrinkage behaviour of the claystone under controlled suction and hysteresis effects. In this paper, a better understanding of the water retention properties of the COx claystone is looked for thanks to a study of the microstructure changes due to changes in suction along various

paths of the water retention curve. Microstructure investigation is carried out by using mercury intrusion porosimetry.

2. Material and methods

2.1. The COx claystone

The COx claystone is a sedimentary rock deposited 155 millions years ago on top of a layer of Dogger limestone that was afterwards covered by an Oxfordian limestone layer. The thickness of the COx layer is about 150 m. The COx claystone is composed of a clay matrix containing some detritic grains of quartz and calcite. The mineralogical composition of the COx claystone varies with depth, particularly in terms of clay fraction and carbonate content. At the depth of the Bure URL (490 m), the average mineralogical composition of COx claystone is as follows (Gaucher et al. 2004): 45-50% clay fraction (mainly interstratified minerals of illite–smectite), 20% carbonate, 22% quartz and 9% other minerals (feldspars, pyrite, dolomite, siderite and phosphate minerals). The total connected porosity varies in the COX layer between 14% in carbonated levels and 19.5% in the more argillaceous levels (Yven et al. 2007).

The specimens were drilled from a 80 mm diameter and 300 mm long core (EST44584) perpendicular to bedding that was extracted at the level the URL (490 m). The initial characteristics of the specimens are presented in Table 1. The water content was determined by measuring the initial and final weights of a rock piece before and after drying in the oven at 105 °C for 48 hours. The porosity and degree of saturation were calculated from carefully measuring the sample volume by using hydrostatic weighing. The initial total suction was determined by using a dew point potentiometer (WP4, Decagon). As seen in the Table, the specimens EST44584 are not fully saturated at initial state with a degree of saturation around 77.6 % corresponding to a suction of 34 MPa for a porosity of 17.0 %. The dry density and specific gravity values are 2.16 and 2.6 Mg/m^3, respectively. Partial saturation resulted from the combined actions of coring, transport, storage and specimen preparation.

Table 1. Initial characteristics of the tested specimens.

Specimen	EST44584
Depth (m)	490
Water content (%)	6.1
Dry density (Mg/m^3)	2.16
Specific gravity (Mg/m^3)	2.6
Void ratio	0.205
Porosity (%)	17.0
Degree of saturation (%)	77.6
Suction (MPa)	34

2.2. Experimental techniques

The core was confined within a plastic tube immediately after having been drilled from the borehole until the preparation of samples for laboratory experiments. In spite of this precaution, macroscopic cracks were observed after opening the core. The bedding plane of the COx specimens makes it quite difficult to trim samples without breaking them. All tests were run on specimens of 38 mm in diameter and between 8-10 mm in height. To do so, the cylinder core was firstly sliced by using a diamond wire saw at low speed in dry condition in order to preserve the integrity of the sample, to obtain a cylinder sample of 80 mm in thickness. The cylinder was then placed in a special metal confining mould and cored to the desired diameter (38 mm) by using a diamond barrel in dry condition. Finally, seven small specimens of 8-10 mm in thickness were obtained from the cylinder of 38 mm diameter by using the diamond wire saw.

The determination of the water retention properties of the COx claystone was carried out by controlling suction through the vapour phase. This technique consists in placing the specimens into desiccators containing saturated saline solutions. The saturated saline solutions used and the corresponding suctions and relative humidity at 20 °C are shown in Table 2 (Delage et al. 1998). The highest suction (331 MPa) was imposed with a saturated saline solution of KOH. A smaller value of 150 MPa was imposed by using $MgCl_2$. Zero and 9 MPa of suction were imposed by using pure water and KNO_3 respectively. Specimens were left in the desiccators until reaching mass stabilization (checked by periodic precision weighing). Once equilibrated, a suction measurement was made by using the WP4 dew point potentiometer to confirm the achievement of the desired value of suction. Afterwards, the specimens were immediately waxed using slush wax (at lowest possible temperature before

solidification, see Wan et al. 2013 for more detail). Careful weighing was carried out prior and after waxing, giving a good determination of the wax weight and volume. The specimen volume was obtained by subtracting the wax volume from that of the waxed specimen. The wax technique was also used to obtain the specimen volume at initial state (34 MPa of suction, degree of saturation of 77.6%). Finally, the specimens were cut into small pieces to measure their water content by oven drying. The void ratio and degree of saturation were determined by measuring the volume by means of hydrostatic weighing.

Table 2. Solutions used with corresponding relative humidity and suctions at 20°C (after Delage et al. 1998).

Solution	Relative humidity (%)	Suction (MPa)
KOH	9	331
$MgCl_2$	33	150
KNO_3	93.7	9
Pure water	100	0

2.3. Microstructure investigation

Microstructure investigation was carried out by using mercury intrusion porosimetry (MIP). MIP tests were conducted on various specimens at different suctions along the drying or wetting paths followed. To preserve the microstructure, dehydration was made by freeze-drying small pieces of claystone (1–3 g in weight) that were previously quickly frozen by immersion in slush nitrogen. Slush nitrogen was obtained by applying vacuum on liquid nitrogen, bringing down its temperature from – 196°C (boiling temperature) to – 210°C (freezing temperature). Fast immersion in slush nitrogen is preferable because no boiling occurs around the specimen, resulting in faster freezing of water with no volume change (see Tovey and Wong 1973, Gillott 1973, Delage and Pellerin 1984 and Delage et al. 2006 for more details). MIP tests were carried out in a Micromeritics-AutoPore IV 9500 porosimeter from a low initial pressure of 3.4 kPa up to 227.5 MPa, corresponding to entrance pore diameters of 363.6 µm and 5.5 nm respectively.

The intruded mercury porosity (n_{Hg}) was defined as the ratio of mercury intrusion volume V_{Hg} to specimen total volume V:

$$n_{Hg} = \frac{V_{Hg}}{V} \tag{1}$$

The pore entrance diameter (D) was determined from the intrusion pressure P_{Hg} by assuming a cylindrical pore shape according to the Laplace-Young equation:

$$D = \frac{4\sigma \cos\theta}{P_{Hg}} \tag{2}$$

where σ is the mercury-solid interfacial tension and θ is the mercury-solid contact angle (σ =0.484 N/m and θ =141.3° according to Diamond 1970).

2.4. Test program

A first series of samples were submitted to drying-wetting path (A1 to B2, see Table 3) from the initial water content (equal to 6.12 % with a 34 suction and a degree of saturation of 77.6%). Two specimens were simultaneously dried under suctions of 150 and 331 MPa along the drying path, to check repeatability. Specimens A1 and B1 were used to define the specimen characteritics and to investigate their microstructure at 150 and 331 MPa respectively. Once dried at 331 MPa, specimens A2 and B2 were afterwards wetted at 9 MPa and zero suctions, so as to determine the main wetting path. Along the wetting path, both specimens were periodically taken out from the dessiccator for weighing so as to determine their water content. Their suction was also measured by means of the WP4 dew-point tensiometer.

Table 3. Drying-wetting paths.

Specimen	Initial state	150 MPa	331 MPa	9 MPa	0 MPa
A1	★ →	★			
A2	★ →	★ →	★ →	★ →	★
B1	★ →		★		
B2	★ →		★ →		★

A second series of tests corresponds to a wetting-drying path (Table 4). Starting from the initial water content (6.12 %), three other specimens (C, D1 and D2) were firstly wetted under decreasing suctions (9 MPa for specimen C and zero suction for specimens D1, D2). Specimen D2 was then used to determine the main drying path up to suctions of 150 MPa and 331 MPa.

Table 4. Wetting-draying paths.

Specimen	Initial state	9 MPa	0 MPa	150 MPa	331 MPa
C	★ →	★			
D1	★ →		★		
D2	★ →		★ →	★ →	★

3. Experimental results

3.1. Transient phases

The changes in water content with respect to time from the initial state (w = 6.12%) along the drying and wetting paths are shown in Figure 1. In a standard manner, the higher the suction, the larger the decrease in water content along drying paths. Higher water contents are achieved at smaller suctions along wetting paths. Good correspondence between the two specimens simultaneously used (except at 9 MPa suction) shows good repeatability. The data show that water content equilibration is reached after 25 days at the highest imposed suction (331 MPa) and after 18 days at 150 MPa. Specimen C wetted at 9 MPa suction came close to equilibrium after only 8 days compared to 18 and 25 days necessary to reach suctions of 150 and 331 MPa, respectively. At zero suction, equilibrium does not seem to be fully reached after 40 days with final water contents of 10.6% for D1 and 10.4% for D2.

Figure 2 presents the wetting phases of specimens A2 and B2 from 331 MPa to 9 MPa and zero suction respectively, together with the drying phase of specimen D2 from zero to 331 MPa. As commented previously, these phases allowed determine the main wetting and drying paths. Subsequent wetting appeared to be significantly faster than the previous drying phases with curves starting with sub-vertical slopes. Specimen A2 came close to equilibrium (suction of 9 MPa) after only 10 days. Figure 2 also shows that the jump observed on specimen A2 from 1.6% to 5.6% in water content corresponding to suction decrease from 331 to 22 MPa exhibits a 70% increase in total water content during only 2 days. Specimen

B2 reaches a water content of 11.2% at 0 MPa. Starting from a wet state at zero suction (w = 10.4%), specimen D2 reaches water contents of 2.32% at 150 MPa and 1.26% at 331 MPa.

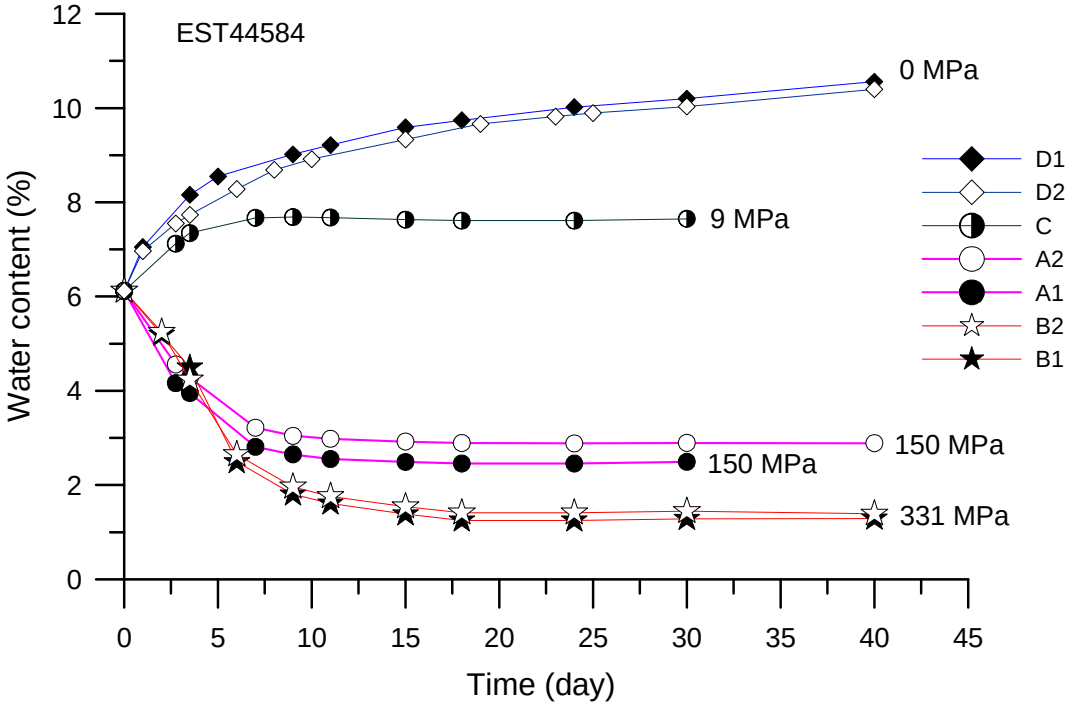

Figure 1. Water content versus time from the initial state to various suctions.

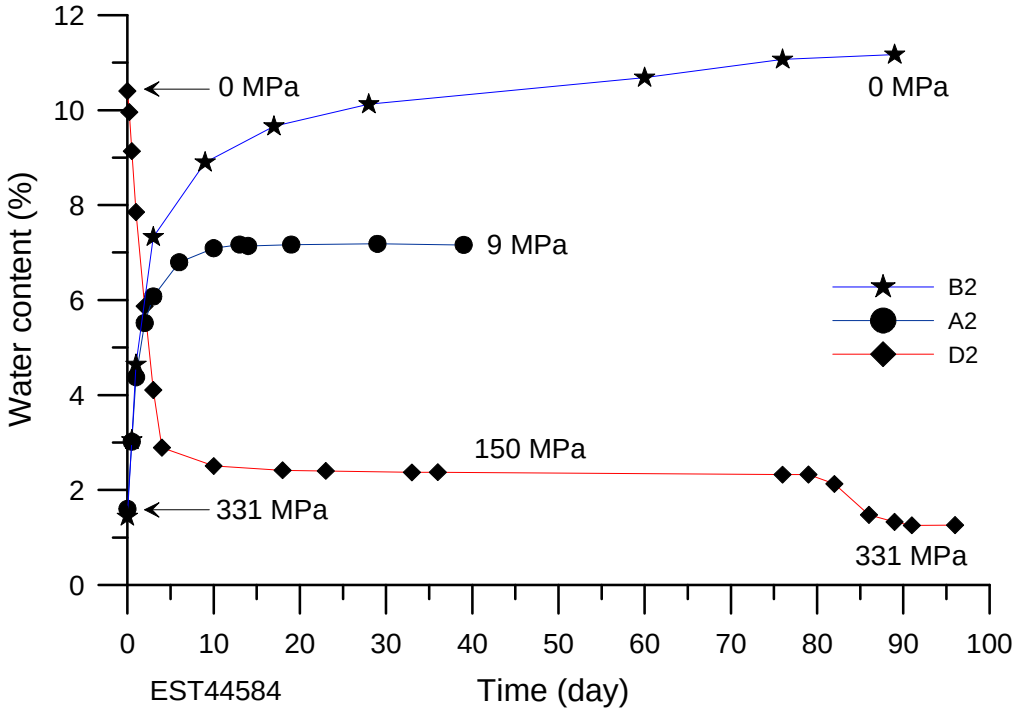

Figure 2. Water content versus time for the subsequent drying/wetting to various suctions.

3.2. Water retention curve

The water retention curve expressed in terms of changes in water content versus suction is presented in Figure 3. The points at zero suction are arbitrarily plotted at a suction of 0.01 MPa. As described in section 2.3, starting from the initial state (w = 6.12%, suction 34 MPa), two points were obtained along the drying path at controlled suctions of 150 and 331 MPa and two other points along the wetting path at suction of 9 and 0 MPa. Data along the main wetting and drying paths were also obtained by suction measurements and water content determination along the wetting path from 331 to 0 MPa for specimen B2 and along the drying path from zero suction to 331 MPa for specimen D2. Good correspondence is observed along the main wetting path between the data of specimens B2 and A2 that was wetted between 331 and 9 MPa, providing some confidence in the quality of the data.

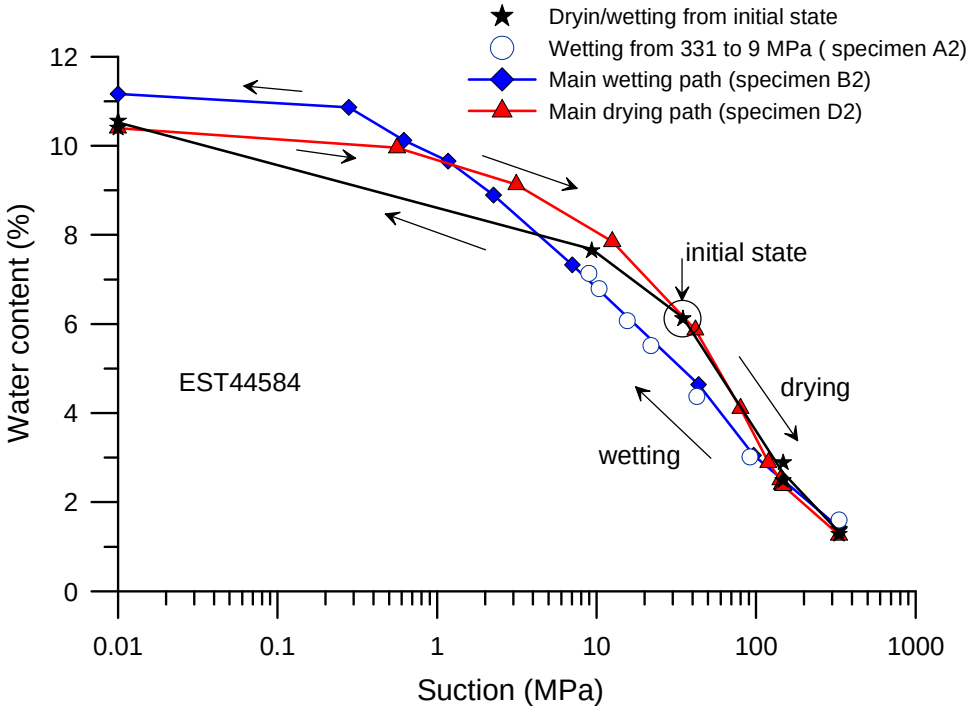

Figure 3. Water retention curve of COx claystone.

Examination of the main drying and wetting paths shows that the water retention properties of the COx claystone are characterized, commonly, by a hysteresis effect. The data also show that the initial state resulting from desaturation from the in-situ saturated state is located, commonly, on the main drying path. The wetting path starting from the initial state shows that the point at 9 MPa of suction (specimen C) is located below the main drying path, which is typical of scanning curves (there is unfortunately no other point between 9 MPa and

zero suction along this path). A particularity observed here is that the main wetting path from the dry state at 331 MPa suction is defining at zero suction higher water content (11.2%) than that (10.4%) obtained from wetting the specimen at initial water content. This does not correspond to standard water retention properties in unsaturated soils and will be commented later.

3.3. Volume changes

As previously described in section 2.2, the parameters determined at each suction equilibration were the water content, the volume, the porosity and the degree of saturation. Results are presented in terms of changes in degree of saturation versus suction in Figure 4a, in degree of saturation versus water content in Figure 4b and in volumetric changes versus suction in Figure 4c. The data taken from similar tests by Pham et al. (2007) and by Wan et al. (2013) are also plotted, with good agreement between the data.

As already commented in detail by Wan et al. (2013), the specimen following the wetting path from the initial state comes close to saturation at 9 MPa (S_r = 96%, w = 7.65 %, Figure 4b). At suction smaller than 9 MPa, the significant increase observed in water content (Figure 4b) occurs in saturated condition. Along the drying path from initial state, a linear relationship is observed between the degree of saturation and the water content with an average decrease of 13% in degree of saturation for a decrease of 1% in water content. The main wetting curve obtained once the specimen has been dried to the highest suction (331 MPa) is located below the curves of drying-wetting from initial state (Figure 4a), confirming the hysteresis observed by Wan et al. (2013).

The changes in volumetric strain with respect to suction (Figure 4c) show that the drying from the initial state to 331 MPa of suction results in a shrinkage of 2.0% while wetting to zero suction induces a swelling strain of 6.1%. Figure 4c also shows that reducing suction along the wetting path from initial state occurs with little swelling (0.3%) from 34 to 9 MPa and significant swelling below 9 MPa (6.1% at zero suction). As commented above, this significant swelling occurred within a saturated specimen. The specimen previously dried up to 331 MPa before wetting to zero suction (main wetting path) is not brought back to the same point as that of the specimen submitted to a wetting path from initial state, with some irreversible swelling strain (1.6%) and higher volume at zero suction. However, the main wetting path seems to be close to the drying curve from initial state at higher suction

(> 40 MPa) showing some reversibility in the volume change behaviour under stress free conditions at highest suctions.

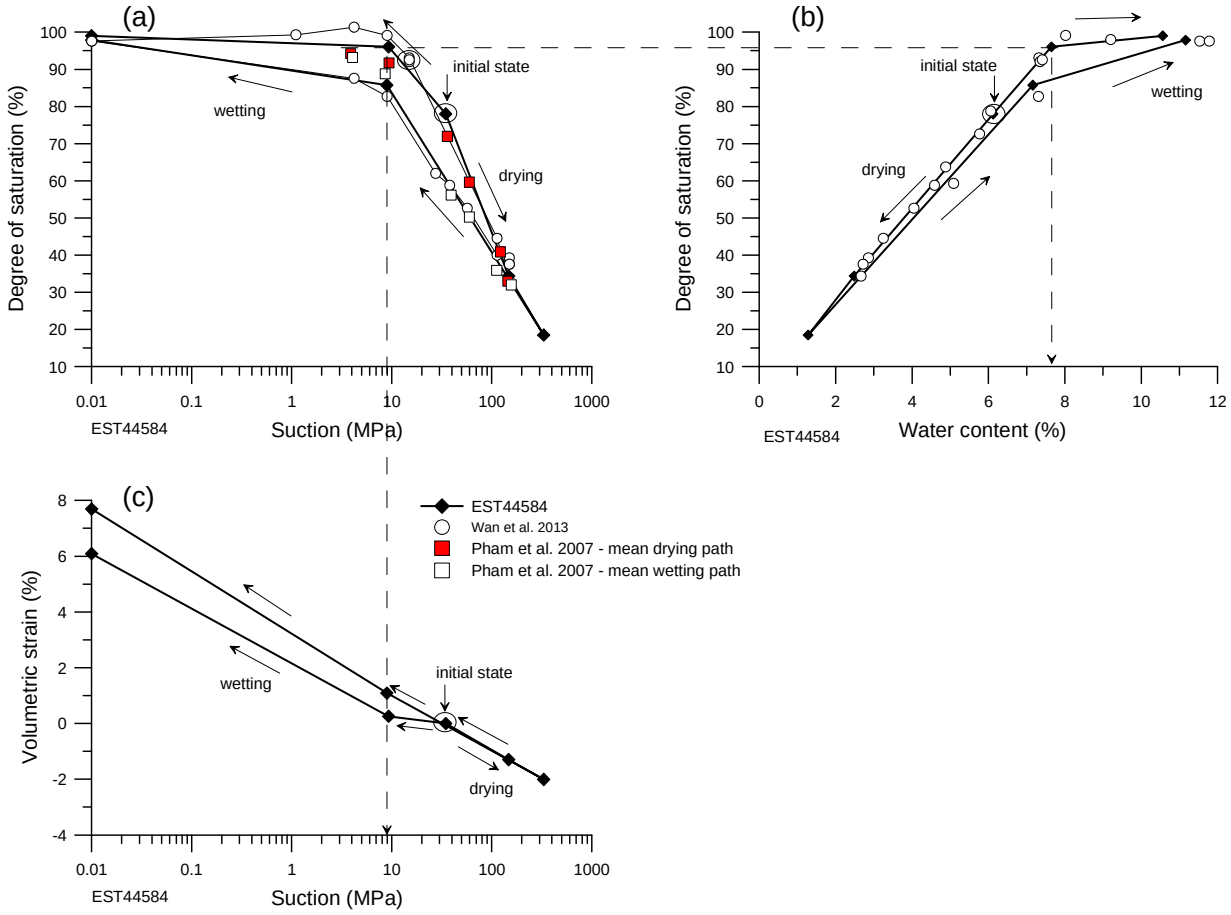

Figure 4. Water retention curve and volumetric behaviour obtained by the suction controlled method.

3.4. Mercury intrusion porosimetry

The results of the MIP test obtained at initial state (S_r = 77.6%, porosity n = 17.0%) are presented in Figure 5a in cumulative plot and Figure 5b in a density function plot. The total porosity n of the specimen is also plotted in the cumulative curve, showing that the mercury intruded porosity n_{Hg} is smaller than the total one, with an infra-porosity n -n_{Hg} of 4%. Pores smaller than the lower limit of 5.5 nm (corresponding to the maximum mercury pressure of 227.5 MPa) cannot be intruded. The non negligible infra-porosity found here confirms previous findings by Yven et al. (2007) and Boulin et al. (2008) who estimated the porosity not intruded by mercury at 25% of the total porosity, in accordance with the 23.5% value with diameter smaller than 5.5 nm found here. The density function of Figure 5b

exhibits at initial state a typical monomodal curve with quite a well defined pore population identified by an inflection point at 32 nm. Note that Sammartino et al. (2003), Yven et al. (2007) and Boulin et al. (2008) who performed their MIP analysis on air dried specimens obtained smaller average diameter of around 20 nm. As shown by these authors, this pore population is related to the average entrance pore diameter within the clay matrix.

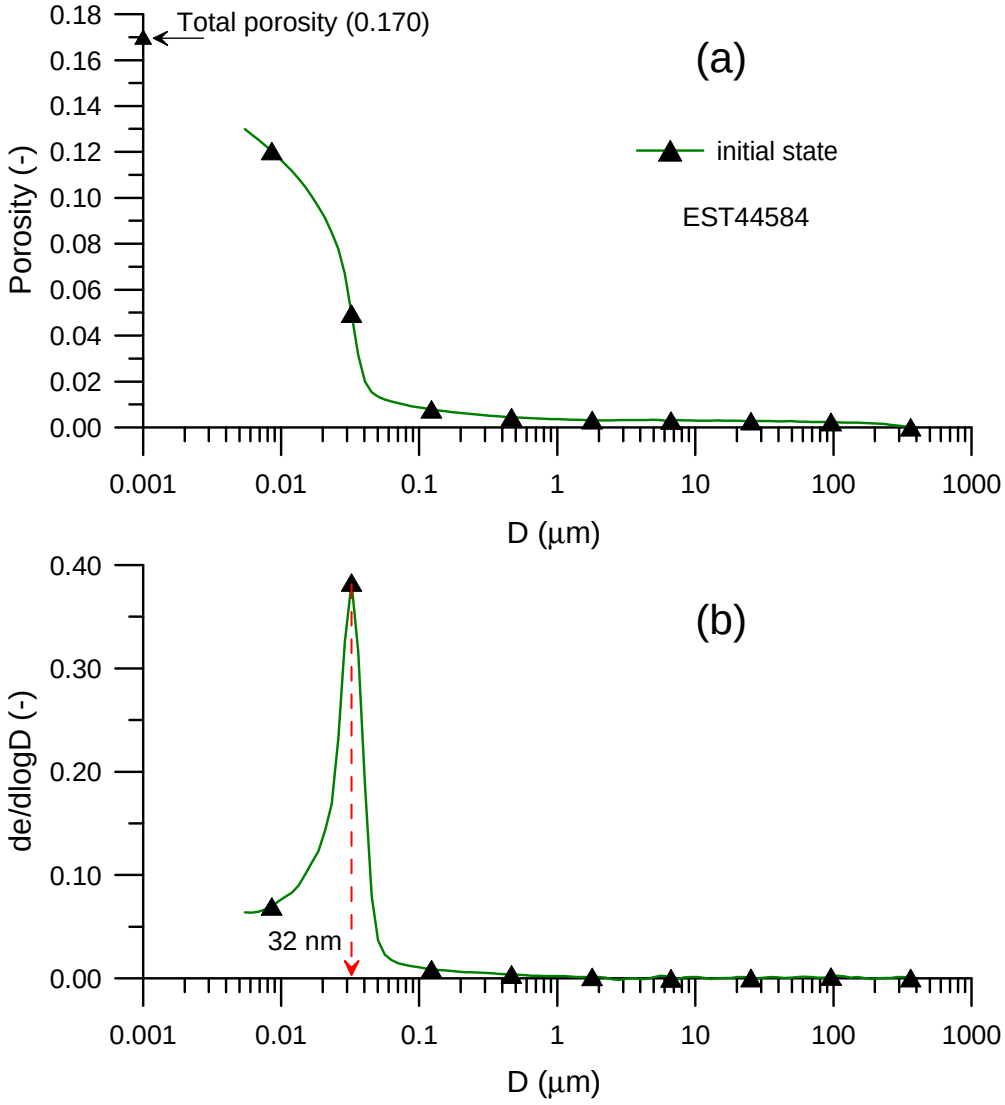

Figure 5. Pore size distribution curves of specimen EST44584 at initial state.

Figure 6 presents the pore size distribution curves of specimens A1 and B2 dried at 150 and 331 MPa respectively from the initial state, together with the PSD data of the specimen at initial state of Figure 5 and that of a specimen oven-dried at 105°C during 48h. MIP data are presented in terms of cumulative curves (Figure 6a and Figure 7a, where an enlargement of the PSD curves between 0.001 and 0.1 µm is presented) and density function

(Figure 6b and Figure 7b, enlarged in the same zone). In Figure 6a, all curves are plotted starting from the same point at the maximum pore diameter. The total porosities obtained from volume measurements are also given. The intruded mercury porosities n_{Hg} of the specimens dried up to 150 (A1) and 331 MPa (B1) are equal to 12.8 and 12.2%, respectively, compared to total porosities of 15.9 and 15.2%, respectively, showing that the infra-porosities not intruded by mercury (D < 5.5 nm) are again lower than the total ones. The infra-porosities are smaller than that at initial state (n - n_{Hg} = 3.0% for both specimens dried up to 150 and 331 MPa, compared to 4% at initial state). Conversely, the mercury intruded porosity of the oven-dried specimen (12%) appears to be quite close to the total one (13%) giving an infra-porosity n - n_{Hg} = 1% significantly smaller than at suctions of 150 and 331 MPa (3%, see Table 5).

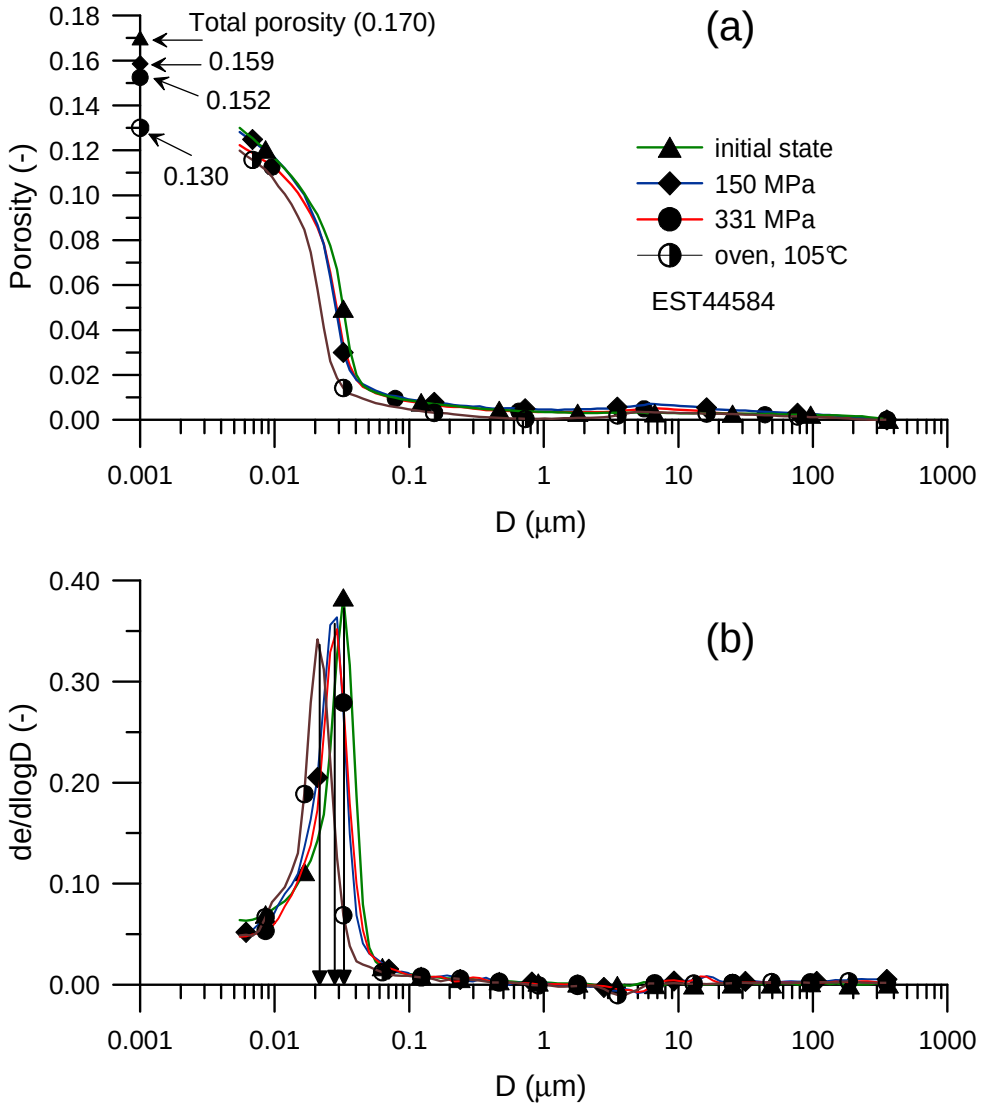

Figure 6. Pore size distribution curves of specimen EST44584 at initial state, 150 MPa and 331 MPa.

Table 5. Porosity values obtained.

Specimen	Suction (MPa)	Intruded porosity n_{Hg} (%)	Total porosity total volume measurement n (%)	Total porosity hydrostatic weighing n	Infra porosity $n - n_{Hg}$
Initial state	34	13.0	17.0	17.0	4.0
D1	0	15.6	21.7	21.6	6.1
B2	0	16.6	22.8	22.9	6.2
C	9	13.1	17.2	17.2	4.1
A2	9	13.0	17.9	17.7	4.9
A1	150	12.8	15.8	15.8	3.0
B1	331	12.2	15.2	15.3	3.0
D2	331	12.4	14.8	14.8	2.4

In the enlargement of cumulative curves at small pores of Figure 7a, the degree of saturation of each specimen is also reported, based on the hypothesis that water is contained in smaller pores due to the nature of both physico-chemical clay water interactions and capillary effects. The arrows indicate the maximum diameter of the pores saturated by water. One can observe that the main pore population is almost saturated (up to a diameter of 33 nm) at initial state (suction 34 MPa, S_r = 77.6%, mean radius 32 nm) whereas this population becomes full of air at 150 MPa suction and S_r = 34.4% with reduction of the mean radius at 28 nm and with the largest saturated pore having a diameter of 13 nm. At 331 MPa, (S_r = 18.5%), the largest saturated pore has a diameter of around 4.9 nm with however no significant change in the mean radius value that slightly decreases to 27 nm. In other words, the desaturation of pores between 13 and 4.9 nm does not significantly affect the microstructure at the level of both the mean pore population and of the infra-porosity that remains constant (3%). Conversely, the effect of oven-drying is much stronger than drying at 150 and 331 MPa suctions, with a reduction of the mean pore diameter to 21 nm and, more importantly, a significant reduction of the infra-porosity to 1%. There is obviously a gap between the highest applied suction (331 MPa) and the total removal of water from the microstructure by oven-drying. Note that the 21 nm mean pore diameter obtained on the oven-dried specimen is comparable to the values obtained by Sammartino et al. (2003) and Boulin et al. (2008) on oven-dried specimens (respectively dried at 105 and 70°C), confirming that drying provided an under-estimated value of the mean pore diameter of the COx claystone.

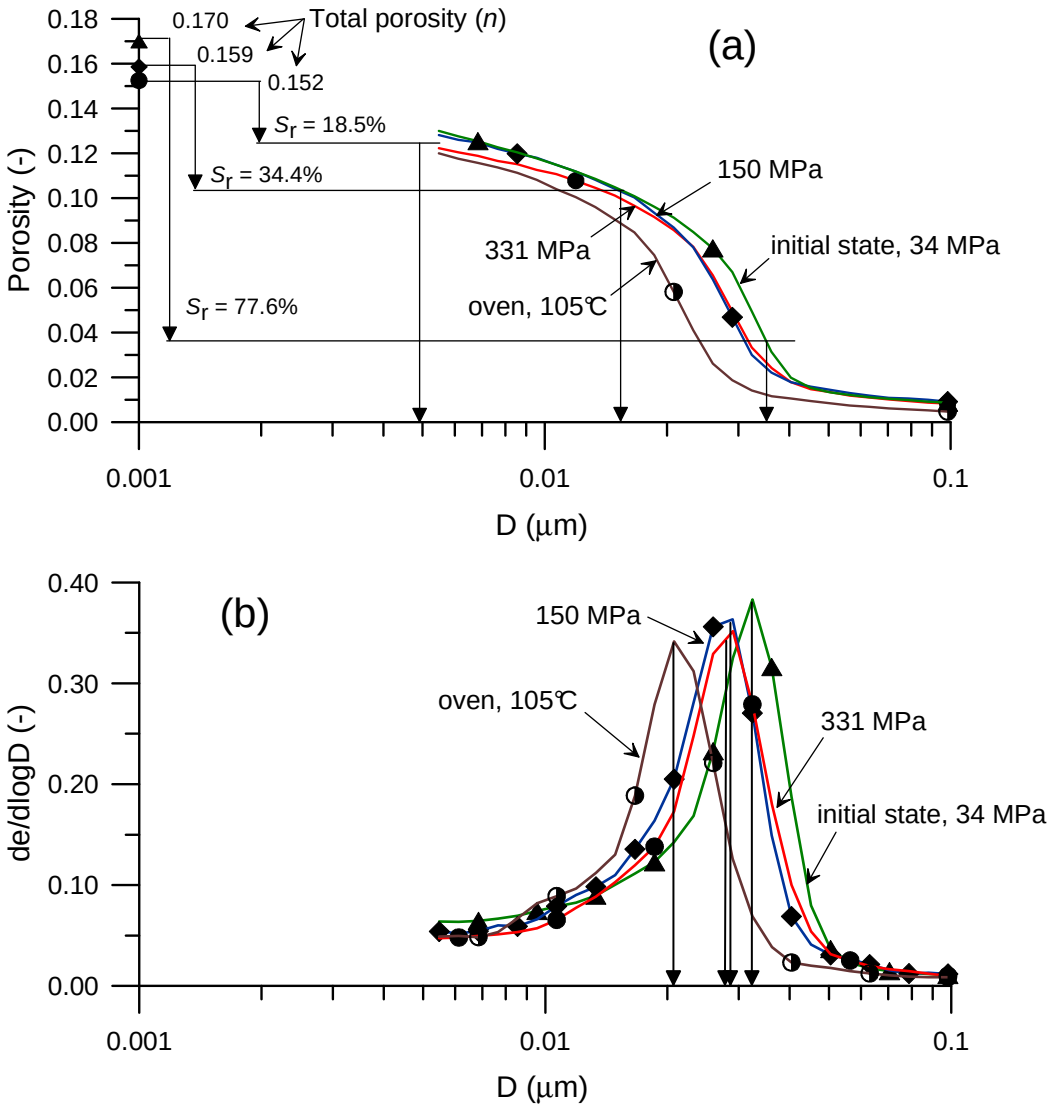

Figure 7. Enlargement of cumulative PSD curves at small pores at initial state, 150 MPa and 331 MPa.

In Figure 8, the pore size distribution curves of the two specimens wetted from initial state at low suctions (9 MPa and zero) and higher degree of saturation (S_r =96% and 99% for s = 9 and 0 MPa, respectively) are presented together with the data at initial state (S_r = 78%, s = 34 MPa). Also plotted in the Figure are the total porosities of the specimens. The PSD cumulative and density function curves at 9 MPa suction (S_r = 96%) are quite similar to that at initial state (Figure 8a) with an only slight increase in total porosity at 9 MPa (0.2%), showing that the infra-porosity is also similar in both cases. This is compatible with the negligible volume change observed in the volume change/suction curve of Figure 4c when passing from initial state (s = 34 MPa) to a suction of 9 MPa. The specimen saturation from S_r = 78% to 96% hence occurs by complete filling of the mean pore population with very little microstructure changes both in the porosity intruded and not intruded by mercury.

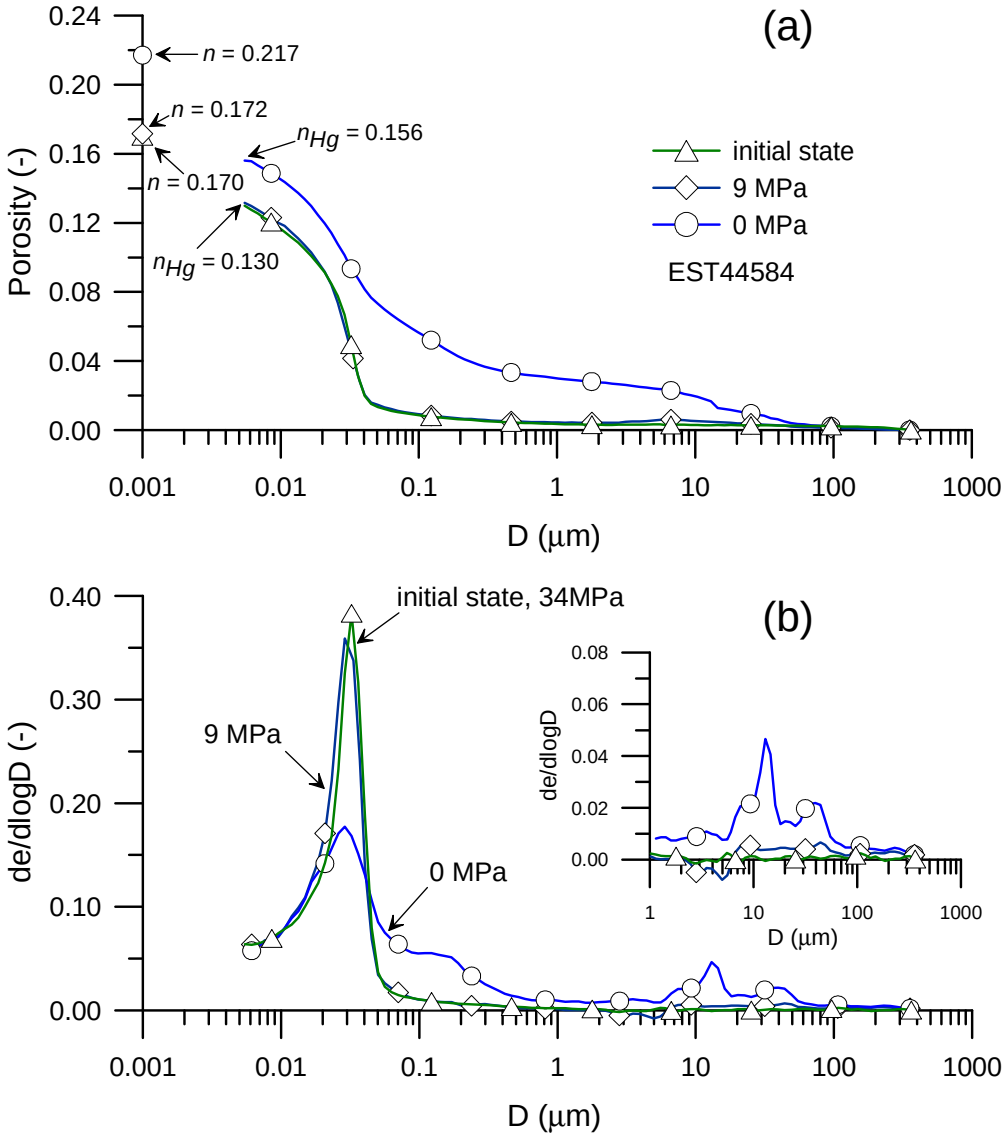

Figure 8. Pore size distribution curves of specimen EST44584 at initial state, 9 MPa and 0 MPa.

Figure 9 presents the PSD curves of the two specimens at 9 MPa obtained from initial state and after drying at 331 MPa, compared to the initial state. Observation of the volume changes with respect to suction in Figure 4c indicates a larger volume for the sample wetted from a suction of 331 MPa. Inspection of the PSD curves of Figure 9 shows that both curves at 9 MPa are similar with however a slight difference observed in the cumulative curve at pores larger than 6 µm.

The reduction in suction from 9 MPa to 0 MPa occurs at quasi-saturated state (see Figure 4a) with a significant 6.1% swelling giving a final water content of 10.5% and degree of saturation of 99% (see Figure 4c). Indeed, significant changes are also observed at the microstructure level, as shown by the change in shape of the PSD curve of specimen D1 at zero suction that becomes bimodal. Changes affect three levels of porosity:

i) The infra porosity n - n_{Hg} that increases from 4% at 9 MPa to 6.1% at zero suction with an intruded porosity of 15.6% and a total one of 21.7%;

ii) The large porosity with appearance of a new pore population corresponding to a proportion of 10.5% of the total porosity in the range of diameters between 7 and 100 µm with a mean diameter around 12 µm;

iii) An enlargement of the previous pore population that moves from a narrow range between 12 and 50 nm (see density function curve in Figure 8b) to a wider range between 12 and 500 nm with a new plateau between 60 and 200 nm. Note however that no change is observed in the density function curves between 5 and 20 nm.

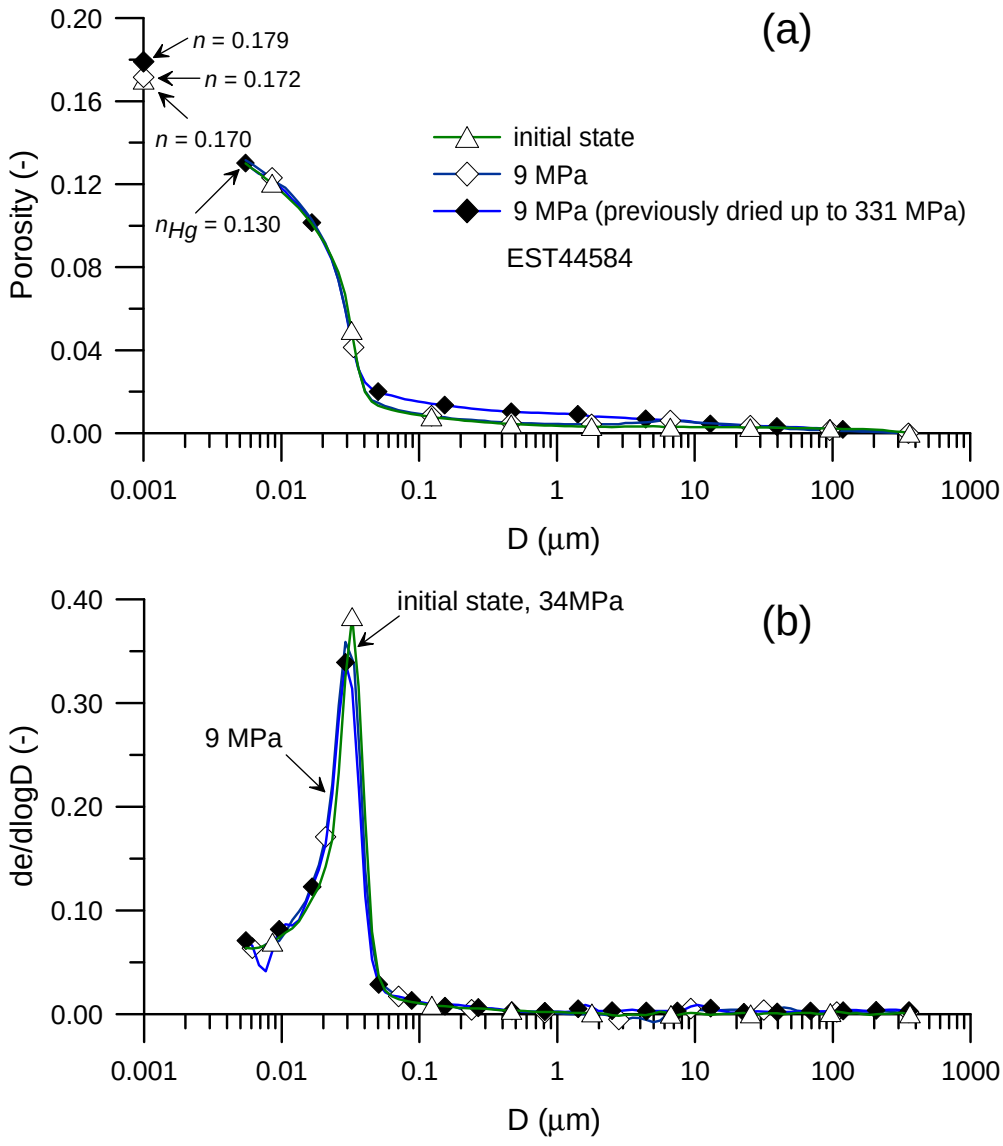

Figure 9. Pore size distribution curves of specimen EST44584 at initial state, 9 MPa (from initial state) and 9 MPa (from dry state at 331 MPa).

Figure 10 shows the pore size distribution curves at zero suction for the two specimens D1 and B2 wetted from initial state (34 MPa suction) and after having been submitted to a suction cycle up to 331 MPa and back to zero along the main wetting path, respectively. The mercury intruded porosity n_{Hg} of D1 and B2 specimens is equal to 15.6 and 16.6%, respectively, corresponding to total porosity of 21.7 and 22.8%, respectively. The porosity not intruded by mercury does not change significantly, with $n - n_{Hg}$ equal to 6.1% for the specimen directly wetted to zero suction (D1) and 6.2% for the specimen wetted to zero suction after drying at 331 MPa. The two PSD curves are similar, but the superimposition of the cumulative curves in the small pores area (Figure 10b) indicates that the slight change in total porosity is mainly due to changes at the level of pores larger than 2 µm.

In Figure 11, the PSD curves of the driest specimens at 331 MPa suction obtained either from the initial state (34 MPa, B1) and from the wet state (zero suction, D2) after following the main wetting path are presented together and compared to the initial state. The curves at 331 MPa are comparable and slightly differ from the curve at intact state (slight decrease in mean pore radius and decrease in infra-porosity, as commented previously). The similarity between the curves at 331 MPa indicates that the drying of specimen D2 previously submitted to wetting at zero suction leads to complete erasing of the modifications due to hydration and swelling described above (Figure 10):

i) The infra-porosity of the previously wetted specimen came back from 6% to 2.4% compared to 3% for that dried from initial state;

ii) The large pores population between 7 and 100 µm completely disappeared;

iii) The mean pore population became again well classified as indicated by the peak of the density function curve with pores diameters brought back between 10 and 60 nm.

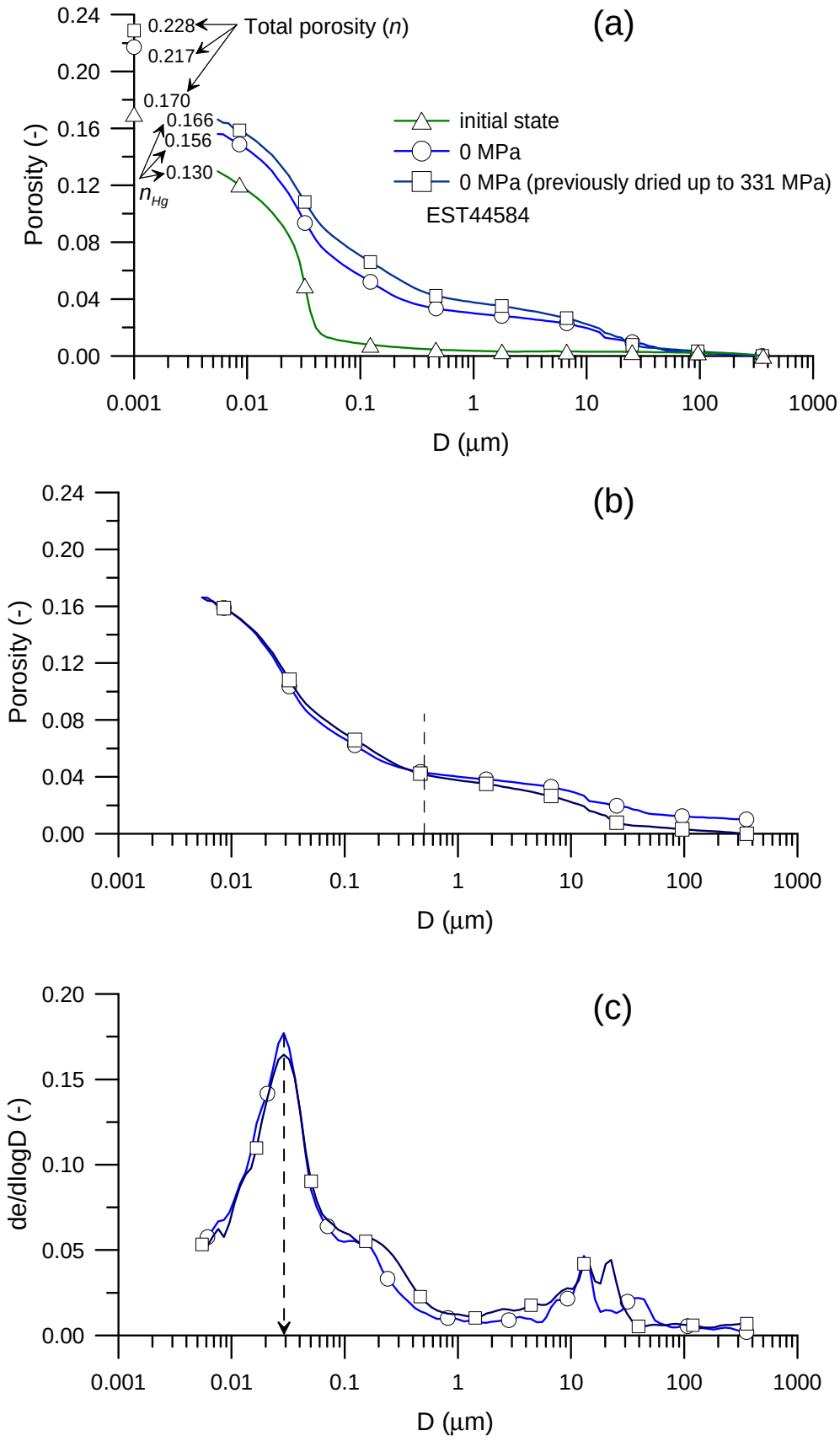

Figure 10. Pore size distribution curves of specimen EST44584 at 0 MPa.

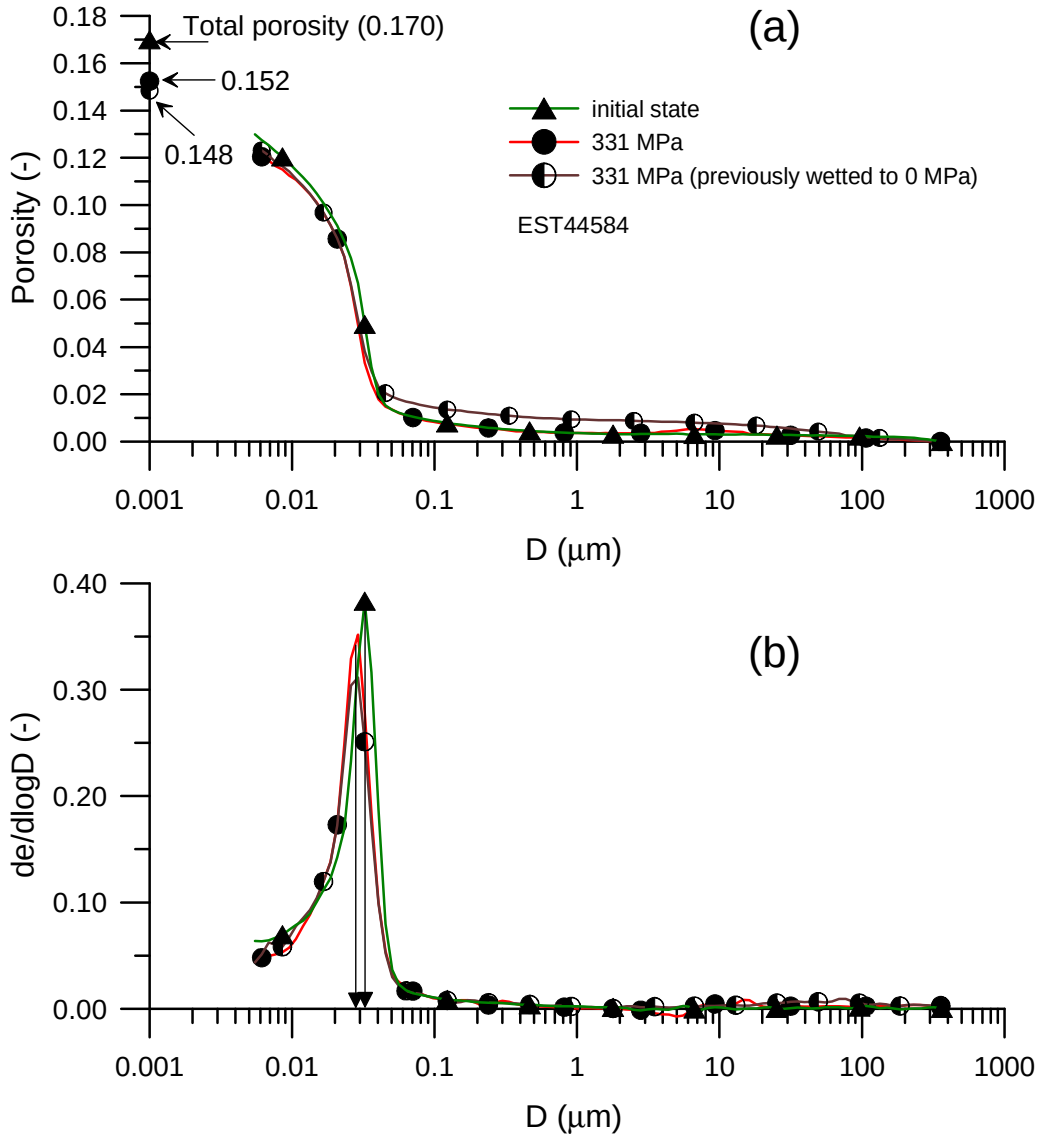

Figure 11. Pore size distribution curves of the sample EST44584 at 331 MPa.

4. Discussion

4.1. Initial state

To interpret the microstructure changes with respect to suction changes along various paths of the water retention curve observed here through MIP investigations, it was found useful to consider the conceptual model of the COx claystone microstructure presented in Figure 12 and proposed by Yven et al. (2007) from data obtained by using various techniques including scanning electron microscope, autoradiography, mercury intrusion porosimetry, oil, helium and nitrogen adsorption. The model schematically shows how individual calcite or

quartz detritic grains are embedded into a clay matrix with interconnected porosity that represents 45 – 50% of total constituents at the depth of 490 m considered here.

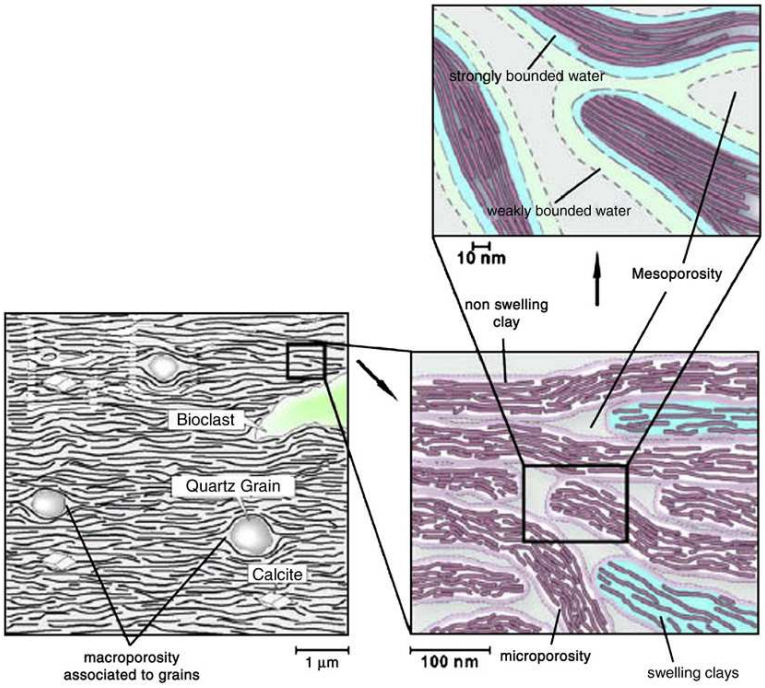

Figure 12. Conceptual model of COx clay microstructure (after Yven et al. 2007).

The interpretation of the well defined single pore population defined by an average value of 32 nm observed in the PSD curve of Figure 5 can be made by assimilating the clay matrix to an assembly of bricks made up of platelets of comparable thickness, as can be seen in the scheme of Figure 12. The mean pore radius hence provides an estimate of the average platelet thickness. With an interlayer spacing of 0.96 nm (9.6 Å) typical of the mineralogical structure of (dry) smectites and illites and with an average platelet thickness of 32 nm, an average number of around 32 layers by platelets can be roughly estimated, in accordance with data provided by Mitchell and Soga (2005). Note that in the model of Figure 12, the interstratified illite-smectite swelling minerals are supposed to be located only in some platelets, with clear distinction between swelling and non swelling platelets, a hypothesis not discussed in the paper that probably needs further confirmation.

4.2. The hydration of smectites

Given the significant effects of the changes in water content (or suction) on the changes in volume (swelling-shrinkage) and in microstructure of the COx claystone and given the importance of the smectite fraction of the clay matrix in this regard, it was found interesting to consider in more detail some mechanisms that govern the hydration of smectites.

Interlayer spacing larger than 9.6 Å should be considered in the case of hydrated smectites within the interstratified illite-smectite layers of the clay matrix, given that smectite hydration is known to result from step increases of the interlayer spacing with increased water content (or decrease in applied suction). Indeed, one, two or three layers of water molecules adsorbed along the smectite phase correspond to interlayer spacing of 12.6, 15.6 and 18.6 Å respectively (Mooney et al. 1952, Méring and Glaeser 1954, Norrish 1954), giving a thickness of 3 Å for one layer of water molecules. Another interesting result obtained by various authors (including Ben Rhaïem et al. 1987, Bérend et al. 1995, Cases et al. 1997, Sayiouri et al. 2004 and Ferrage et al. 2005) by using X ray diffraction techniques is that the number of layers adsorbed along the smectite faces depends on the relative humidity imposed during hydration. As an example, Sayiouri et al. (2004) observed in a MX 80 Wyoming compacted montmorillonite that one layer of water molecules was adsorbed at suctions larger than 50 MPa, two layers between 50 and 7 MPa and three layers below 7 MPa, with a fourth layers adsorbed at low suctions smaller than 0.1 MPa. Similarly, Ferrage et al. (2005) worked on purified SWy-1 montmorillonites saturated with various cations and observed, on a Na montmorillonite, that one layer was adsorbed at relative humidity (RH) smaller than 60% (suction of 70 MPa) with the transition between one and two layers occurring between 60 and 80% RH (suctions of 70 and 30 MPa, respectively). On a Ca montmorillonite, the two layers hydration occurred at smaller RH value of 40% (suction of 126 MPa). It seems that a 95% RH (suction of 7 MPa) can be considered as the upper limit of the two water layers in clays, as shown by Laird et al. (1995) who observed a transition from 2 to 3 layers starting from 95 % RH for both 5 reference smectites.

As a rough estimation, for a natural claystone containing some smectite minerals, one can hence consider that one layer of water molecules could be adsorbed at suctions above five or more tens of MPa, with a second layer at around one or two tens of MPa. These order of magnitudes of suction might be useful in the analysis of the microstructure changes

observed here given the values of suction considered in the determination of the water retention curves (0, 9, 150 and 331 MPa).

4.3. Drying phase

Observation of the PSD curves of Figure 6, in which the curve at initial state is compared to that at 150, 330 MPa suction and to that of the oven-dried specimen, shows that drying is characterized by a reduction of the mean diameter of the single well defined pore population from 32 nm (intact) to 28 (150 MPa), 27 (331 MPa) and 21 nm (oven-dried). Based on the brick model, this corresponds to a reduction in thickness of the bricks, i.e. of the platelets. This reduction can only be due to change in the interlayer spacing of smectite, given that illite minerals are not sensitive to change in water content and keep an interlayer spacing of 9.6 Å. Based on the suction values given above, it can be reasonably considered that all specimens at suction higher than 150 MPa have only one layer of adsorbed water molecules along the smectite minerals within the clay platelets. At initial state and a suction of 34 MPa, the data of Sayiouri et al. (2004) would indicate the possibility of having two layers adsorbed, in reasonable compatibility with the data of Ferrage et al. (2005). The reduction of the average diameter from 32 to 28 nm can then be linked to the transition from two to one adsorbed layer of water molecules.

Oven drying resulted in having no more water layer adsorbed (Ferrage et al. 2005) and the rough estimation of the average number of clay layer in one platelet of interstratified illite-smectite could then be done by using the mean diameter of 21 nm of the oven-dried specimen, providing a number of 21-22 clay layers with an interlayer spacing of 9.6 Å. Then the introduction of one water layer would result in the placement of an average number of 23 layers of 3 Å thick layers of water molecules, resulting in an increase in the platelet thickness of 7 nm, from 21 to 28 nm. This rough calculation seems to indicate that the interstratified minerals would be only made up of smectite with little illite fraction, which is probably not realistic. Note however that this hypothesis would provide an estimation of the average theoretical platelet thickness increased of 7 nm with two adsorbed water layers, giving a value of 35 nm not so far from that measured (32 nm). This seems to demonstrate that the rough analysis based on the step hydration process evidenced in pure and compacted smectites could be of some interest to analyse the drying and shrinkage behaviour of the COx claystone.

Another important point is the significant reduction of the infra-porosity to 1% after oven drying, compared to 3% at 150 and 331 MPa, and 4% at 34 MPa. This reduction can also be related to the shrinkage of platelets that also reduce the porosity of diameter smaller than 5.5 nm. Indeed, the existence of porosity too small to be detected by MIP is well known in compacted smectites (see for instance Delage et al. 2006) whereas full intrusion has been observed in kaolinites and illites (Ahmed et al. 1974, Sridharan et al. 1974) or in natural fine-grained soils containing illite (Delage and Lefebvre 1984). An interpretation could be that once dried, the interstratified platelets only have clay layers of thickness of 9.6 Å and behave in terms of pore configuration like illites. In other words, the bricks are shrunk enough with very small internal porosity after the expulsion of the last layer of water molecules.

4.4. Wetting phase

Very little change was observed between the sample at initial state (34 MPa) and that at 9 MPa both in average mean pore diameter and infra-porosity. This is reasonably compatible with the suction values given by Sayiouri et al. (2004) that indicate that the two water layers could be stable under this suction range with the third water layer only adsorbed at suction smaller than 7 MPa.

Wang (2012) investigated the nonlinearity of swelling in the COx claystone by the combined use of high resolution imaging by ESEM and Digital Image Correlation. They showed that the swelling strain was not significant and evolved linearly between 75 and 95% RH (39 and 7 MPa suction respectively), whereas it became significant between 95 and 99.8% of relative humidity. This is in agreement with the results obtained here when passing from initial state (s = 34 MPa) to a suction of 9 MPa. The constant values obtained both in the porosity intruded and not intruded by mercury can be explained by the stability of the water layers in the clay platelets in this suction range.

The significant swelling due to wetting at zero suction was analysed through three mechanisms in section 3.4. The mechanism i) that concerns the infra porosity can be related to the adsorption of a third or even a fourth layer of water molecules within the infra-porosity that increased from 4% (initial state at 34 MPa) to 6.1% at zero suction. Based on the hydration model used above, adding a new water layer would result in an increase of 7 nm in the platelet thickness, giving an average value of 39 nm. Adding a fourth water layer would lead to an average thickness of 46 nm. These increases in thickness are compatible with mechanism ii) with an enlargement of the diameter of the mean pore population towards

larger value. It does not however explain the appearance of pores as large as 200 or 300 nm that can be linked to a higher degree of disorder, as observed in compacted bentonites (Sayiouri et al. 2004) in which the suction reduction below 0.1 MPa (appearance of the fourth layer) also involved a reduction in thickness of the platelets due to layer exfoliation together with an increase in the number of platelets. Further investigation is necessary here in the case of the COx claystone to better understand this phenomenon.

The appearance of the large pore population with diameters between 7 and 100 µm is related to the creation of cracks that can be observed visually and that have also been observed by Wang et al. 2014 by using Digital Image Correlation at microscopic level. These cracks, that are saturated as observed in Figure 4a, were suspected in the analysis of the water retention properties of the COx claystone provided by Wan et al. (2013). Observation of Figure 10b indicates that a sample previously dried at 331 MPa and brought to zero suction exhibits more large pores in the 20 – 30 µm range, as a consequence of higher damage due to the suction cycle that in turn results in slightly larger swelling with a porosity at zero suction of 22.8% compared to 21.7% when directly wetted from initial state.

Finally, it is interesting to observe that all the pores of any kind (mechanisms i. in the infra-porosity, ii. in inter-platelets pores and iii. with cracks in the clay matrix) that developed during hydration and swelling are completely erased under high suction (331 MPa), as shown in Figure 11 in which no difference is observed between the specimen dried from initial state and that previously swollen. It is likely that the inter-crystalline water exchanges with the three or four water layers along the smectites minerals are reversible mechanisms, but at least the cracks observed after swelling that have been closed by high suction will reopen under further rehydration.

5. Conclusion

The use of mercury intrusion porosimetry on freeze-dried specimens appeared to be quite fruitful to provide better understanding of the changes in microstructure that occur along the wetting and drying paths of the water retention curve of the COx claystone. Interestingly, the concepts developed to describe the hydration mechanisms of smectites and their dependency to suction changes appear to be applicable to the hydration of the interstratified illite-smectite minerals that are responsible of the change in water content and the swelling-shrinkage behaviour of the COx claystone.

The initial state, that is located on the drying path of the water retention curve, is characterized by a suction of 34 MPa that corresponds to the adsorption of two layers of water molecules along the smectite faces. Releasing suction to 9 MPa results in the saturation of the claystone but it does not significantly affects the COx microstructure with no swelling and change in the pore size distribution curve, in accordance with the stability of the two layers of water molecules in this suction range. Conversely, passing from 9 MPa to zero suction allows the placement of a third, or even a fourth layer of water molecules that results in significant changes in the inter-platelets porosity. Simultaneously, a network of saturated cracks appears and the global swelling observed at zero suction comes from the combined action of the changes in the inter-platelet porosity and the generation of cracks.

Drying the specimen at 150 and 331 MPa suctions results in a reduction from 32 to 28-27 nm of the mean diameter of the pore size distribution curve that keeps the same shape. Simultaneously, the infra-porosity not intruded by mercury with diameter smaller than 5.5 nm reduces from 4% to 3%. Both features are in agreement with the placement of one layer of water molecules in this suction range, which explain the small differences in microstructure observed at these two suctions. Conversely, oven-drying at 105°C results in a further decrease to 21 nm in the mean diameter of the inter-platelet porosity that is coupled with a reduction of the infra-porosity to 1%. These features are compatible with the state of smectite minerals at dry state, with no water layer adsorbed and an interlayer space of 9.6 Å.

The validity of the concepts of hydration of smectites indeed provides deeper insight in the understanding of changes in water contents and swelling-shrinkage behaviour of the COx claystone. They confirm, as was observed when comparing the water retention behaviour of powder and compacted smectites, that microstructure effects are mainly governed by physico-chemical interactions, with little effects of the initial fabric and structure of the claystone. In other words, the intensity of these interactions are strong enough to surpass the inter-particle bonding of the initial state, even in the case of the strong inter-particle bonds within the clay matrix of the claystone. It seems probable that these conclusions might also help to better understand the self sealing behaviour of the claystones that contain a significant proportion of smectites, like the Callovo-Oxfordian claystone of the Opalinus clay. More generally, these findings should help with any problem linked to swelling in shales, like in petroleum industry (stability of boreholes in shales) or tunnelling (interaction between shames and the support).

Acknowledgements

The authors are indebted to Andra, the French agency of radioactive waste disposal, who financially supported this research through the PhD thesis of the first author and provided the specimens of Callovo-oxfordian claystone.

References

[1] Ahmed S, Lovell CW, Diamonds S (1974). Pore sizes and strength of compacted clay. ASCE J. Geotech. Engng 100, No. 4, 407–425

[2] ANDRA (2005). Synthesis argile: evaluation of the feasibility of a geological repository in argillaceous formation. http://www.andra.fr/international/ download/andra-international-en/document/editions/266va.pdf

[3] Aversa S, Evangelista A, Leroueil S, Picarelli L (1993). Some aspects of the mechanical behaviour of structured soils and soft rocks. In: Anagnostopoulos, editor. Geotechnical engineering of hard soils–soft rocks. Rotterdam: Balkema

[4] Bérend I, Cases JM, François M, Uriot JP, Michot LJ, Masion A, Thomas F (1995). Mechanism of adsorption and desorption of water vapour by homoionic montmorillonites: 2. The Li+, Na+, K+, Rb+ and Cs+ exchanged forms. Clays and Clay Minerals, 43, 324−336.

[5] Ben Rhaiem H, Pons CH, Tessier D (1985) Factors affecting the microstructure of smectites: role of cations and history of applied stresses, In: Schultz et al. (eds) Proc Int Clay Conf, Denver, The Clay Mineralogical Soc, pp 292–297

[6] Bornert M, Vales F, Gharbi H, Nguyen Minh D (2010). Multiscale full-field strain measurements for micromechanical investigations of the hydromechanical behaviour of clayey rocks Strain 46(1): 33–46

[7] Boulin PF, Angulo-Jaramillo R, Daian JF, Talandier J, Berne P (2008). Pore gas connectivity analysis in Callovo–Oxfordian argillite. Applied Clay Science 42: (1–2) 276–283

[8] Carter TG, Castro SO, Carvalho JL, Hattersley D, Wood K, Barone FS, et al (2010). Tunnelling issues with Chilean tertiary volcaniclastic rocks. Mir conference; Problemi di stabilit a nelle opere geotecniche. Capitolo 11, Torino

[9] Cases JM, Bérend I, François M, Uriot JP, Michot LJ, Thomas F (1997). Mechanism of

adsorption and desorption of water vapour by homoionic montmorillonite: 3. The Mg2+, Ca2+, Sr2+ and Ba2+ exchanged forms. Clays and Clay Minerals, 45, 8−22.

[10] Delage P, Pellerin FM (1984). Influence de la lyophilisation sur la structure d'une argile sensible du Quebec. Clay Minerals 19(2): 151–160

[11] Delage P, Lefebvre G (1984). Study of the structure of a sensitive Champlain clay and of its evolution during consolidation. Canadian Geotechnical Journal 21 (1): 21–35

[12] Delage P, Marcial D, Cui YJ, Ruiz X (2006). Ageing effects in a compacted bentonite: a microstructure approach. Géotechnique 56 (5): 291–304

[13] Delage P, Le TT, Tang AM, Cui YJ, Li XL (2007). Suction effects in deep Boom clay block samples. Géotechnique 57 (1): 239–244

[14] Delage P. 2010. A microstructure approach of the sensitivity and compressibility of some Eastern Canada sensitive clays. *Géotechnique* 60 (5), 353-368

[15] Delage P, Menaceur H, Tang AM, Talandier J (2014). Suction effects in deep Callovo-Oxfordian claystone specimen. Géotechnique Letters 3(2), 84-88

[16] Diamond, S. (1970). Pore size distribution in clays. Clays Clay Miner. 18, 7–23

[17] Ferrage E, Lanson B, Sakharov BA, Drits VA (2005). Investigation of smectite hydration properties by modeling experimental X-ray diffraction patterns: Part I. Montmorillonite hydration properties. Am. Mineral. 90, 1358–1374

[18] Gaucher G, Robelin C, Matray JM, Négrel G, Gros Y, Heitz JF, Vinsot A, Rebours H, Cassagnabère, Bouchet A (2004). ANDRA underground research laboratory: interpretation of the mineralogical and geochemical data acquired in the Callovian-Oxfordian formation by investigative drilling. Physics and Chemistry of the Earth 29: 55-77

[19] Gillott JE (1973). Methods of sample preparation for microstructural analysis of soil. Proc. 4th Int. Working Meeting on Soil Micromorphology, ed GK Rutherford, Kingston, 143–164

[20] Lebon P, Mouroux B (1999). Knowledge of the three French underground laboratory sites. Engineering Geology 52: 251–256

[21] Méring J, Glaeser R (1954). Sur le rôle de la valence des cations échangeables dans la montmorillonite. Bulletin de la Société Francaise de Minéralogie et Cristallographie, 77, 519−530

[22] Mitchell JK, Soga K (2005). Fundamentals of soil behaviour. John Wiley New-York

[23] Mooney RW, Keenan AC, Wood LA (1952). Adsorption of water vapor by montmorillonite. II. Effect of exchangeable ions and lattice swelling as measured from X-ray diffraction. J. Am. Chem. Soc. 74: 1371–1374

[24] Norrish K (1954). The swelling of montmorillonite. Discussions of the Faraday society, 18, 120−133

[25] Pham QT, Vales F, Malinsky L, Nguyen Minh D, Gharbi H (2007). Effects of desaturation-resaturation on mudstone. Physics and Chemistry of the Earth 32: 646–655

[26] Saiyouri N, Tessier D, Hicher PY (2004). Experimental study of swelling in unsaturated compacted clays. Clay Minerals 39:469–479

[27] Sammartino S, Bouchet A, Prêt D, Parneix JC, Tevissen E (2003). Spatial distribution of porosity and minerals in clay rocks from the Callovo–Oxfordian formation (Meuse/Haute-Marne, Eastern France)—implications on ionics species diffusion and rock sorption capability. Applied Clay Science 23 (1–4): 157–166

[28] Sridharan A, Altschaeffl AG, Diamond S (1971). Pore size distribution studies. J. Soil Mech. Found. Div. ASCE 97, No. 5, 771–787

[29] Tovey NK, Wong KY (1973). The preparation of soils and other geological materials for the scanning electron microscope. Proceedings of the International Symposium on Soil Structure, Gothenburg, Sweden, 176-183

[30] Valès F, Nguyen Minh D, Gharbi H, Rejeb A (2004). Experimental study of the influence of the degree of saturation on physical and mechanical properties in Tournemire shale (France) Applied Clay Science 26:197–207

[31] Wan M, Delage P, Tang AM, Talandier J (2013). Water retention properties of the Callovo-Oxfordian claystone. International Journal of Rock Mechanics and Mining Sciences 64: 96–104

[32] Wang LL (2012). Micromechanical experimental investigation and modelling of strain and damage of argillites under combined hydric and mechanical loads. PhD thesis, Ecole Polytechnique, France

[33] Wang LL, Bornert M, Héripré E, Yang DS, Chanchole S (2014). Irreversible deformation and damage in argillaceous rocks induced by wetting/drying. Journal of Applied Geophysics 107: 108-118

[34] Wileveau Y, Cornet FH, Desroches J, Blumling P (2007) Complete in situ stress determination in an argillite sedimentary formation. Phys Chem Earth A/B/C;

32(8–14):866–78

[35] Yven B, Sammartino S, Geroud Y, Homand F, Villieras F (2007). Mineralogy texture and porosity of Callovo-Oxfordian claystones of the Meuse/Haute-Marne region (eastern Paris Basin), Mémoires de la Société géologique de France, ISSN 0249-7549, 178: 73-90

Chapitre 2 : Comportement en compression - gonflement du l'argilite du Callovo-Oxfordien

Introduction

Le comportement au gonflement de l'argilite du Callovo-Oxfordien (COx) et ses propriétés d'auto-colmatage sont liés, étant donné que l'auto-colmatage est généré par la mobilisation des smectites dans les fissures. Cela a été démontré dans une fissure de traction artificielle entre deux demi-cylindres de l'argilite du COx par Davy et al. (2007). La relation entre le gonflement et l'endommagement a été également mise en évidence par Carter et al. (2010) qui ont observé que le gonflement était fortement mobilisé dans les zones de cisaillement à partir des essais au laboratoire et des observations in-situ.

Dans le travail de Mohajerani et al. (2011), une série d'essais oedométriques haute pression (jusqu'à 113 MPa) a été réalisée sur des échantillons de l'argilite du COx. Les résultats ont montré que la compression à plus grande contrainte entraîne un gonflement plus important, du fait d'un plus grand endommagement dû à la compression sous une plus forte contrainte. De fait, les argilites sont très sensibles aux changements de contrainte et de teneur en eau, qui peuvent causer de l'endommagement, comme démontré également par Valès (2008), Bornert et al. (2010) et Wang et al. (2014) qui ont mis en évidence l'apparition de fissures pendant l'hydratation en condition libre en utilisant la corrélation d'images numériques (DIC) à l'échelle microscopique.

Dans ce contexte, on présente dans ce chapitre une étude microstructurale du couplage compression-gonflement de l'argilite du COx. Dans un premier temps, un échantillon a été resaturé sous gonflement empêché (endommagement minimisé) et ensuite désaturé par un déchargement instantané à teneur en eau constante. Une autre série d'essais oedométrique haute pression a été réalisée pour confirmer les observations de Mohajerani et al. (2011) avec une investigation microstructurale détaillée par l'utilisation de la porosimétrie au de mercure et le microscope électronique à balayage. Finalement, on présente une loi phénoménologique permettant de définir les déformations élastiques et physico-chimiques liées au gonflement pendant la phase de déchargement.

P. DELAGE, H. MENACEUR, AM. TANG and J.TALANDIER. (2014). *Géotechnique Letters* 3(2) : 84-88

Suction effects in deep Callovo-Oxfordian claystone

Pierre DELAGE[1], Hamza MENACEUR[1], Anh-Minh TANG[1], Jean Talandier[2]

[1] *Ecole des Ponts ParisTech, Navier/CERMES, France*

[2] *ANDRA, Chatenay-Malabry, France*

Abstract

An experimental program aimed at investigating suction effects in a specimen of Callovo-Oxfordian claystone extracted at great depth (479 m) was carried out. A specimen that was saturated in an oedometer with limited swelling exhibited significant swelling and desaturation upon quick unloading at constant water content. The microstructure after unloading was compared to the initial one based on mercury intrusion porosimetry measurements. Since the pore size distribution curves before and after loading appeared to be comparable in the range of pore sizes covered by mercury intrusion (entrance diameter between 363.6 μm and 5.5 nm), it was concluded, based on microstructure considerations, that swelling occurred in pores with diameter smaller than 5.5 nm, from a water transfer within the clay matrix from inter-platelets to intra-platelets pores. This mechanism might occur when excavating galleries in areas of the Excavation damaged zone that support instantaneous unloading sequences, as a first desaturation process prior to subsequent evaporation due to the ventilation of galleries.

Keywords

Clays · Fabric/structure of soils · Partial saturation · Radioactive waste disposal · Rocks/rock mechanics · Suction.

1. Introduction

It is well known that saturated clay specimens carefully extracted at standard geotechnical depths (various tens of meters) exhibit suction (Skempton and Sowa 1963, Bishop et al. 1975, Doran et al. 2000, Delage et al. 2007). In the case of the "perfect sampling" of an isotropic elastic sample and provided the sample remain fully saturated once extracted, this suction is supposed to be equal to the mean effective stress the specimen was submitted to prior to extraction (Bishop et al. 1975). A necessary condition for the sample to remain saturated is that its air entry value should not exceed the mean effective in-situ stress. In the case of the Boom clay, suction effects have been investigated by Delage et al. (2007) who found that specimens extracted at a depth of 225 m in the Underground Research Laboratory (URL) of Mol (Belgium) exhibited a suction value between 2 and 3 MPa, close to the mean in-situ effective stress (2.12 MPa). This work also confirmed that swelling clays to be tested in the triaxial apparatus should not be put in contact in water without previously being submitted to a mean effective stress as close as possible to that existing in-situ to avoid swelling and damage that would degrade the mechanical response and reduce the volumetric yield stress.

Compared to clays, claystones have been consolidated and strengthened by very long diagenesis periods during much longer geologic history, resulting in significantly lower porosity, strong diagenesis bonds and higher mechanical resistance. Following the previous investigation in the Boom clay, suction effects were investigated in the Callovo-Oxfordian (COx) claystone by testing specimens extracted at a depth of 479 m in the Bure URL in Eastern France. Investigation of the effects of desaturation in claystones (Pham et al. 2007, Jougnot et al. 2010 and Wan et al. 2013) is of some interest due to the consequences of the ventilation of the galleries along the gallery walls.

2. Materials and methods

The Callovo-Oxfordian claystone is a marine sediment from the Jurassic period deposited 160 millions years ago between the Callovian and the Oxfordian ages in the western area of the Parisian basin (Gens 2011). It has been since that time submitted to various tectonic effects including some hrizontal stresses resulting from the Alpine orogenese. The stress state measured in the 490 m deep Bure URL is as follows (Wileveau et al. 2007):

- σ_v = 12.7 MPa
- σ_h = 12.4 MPa
- σ_H = 12.7 – 14.8 MPa
- u = 4.9 MPa

The vertical stress σ_v is close to the minor horizontal stress σ_h and smaller than the major horizontal stress σ_H. For this reason and some others (Mohajerani et al. 2011), usual concepts of preconsolidation valid in clays do not apply to the COx claystone. Based in the above values, the equivalent effective Terzaghi mean stress $p'=\frac{1}{3}(\sigma'_v+2\sigma'_h)$ is between 7.7 and 8.4 MPa (with $\sigma'_i = \sigma_i - u$).

Table 1 provides a comparison between the geotechnical properties of the Boom clay (at a depth of 225 m) and that of the COx clay (at a depth of 479 m with maximal clay fraction of 48-50%, Gaucher et al. 2004). The differences in water content (w), Young's modulus and unconfined shear strength illustrate the significant difference between a stiff clay (Boom clay) and a claystone (COx).

Table 1. Geotechnical characteristics of the Boom clay and COx claystone

	Boom clay	Callovo-Oxfordian claystone
Geology[1]	Oligocene (Rupelian)	Jurassic (Callovo-Oxfordian)
Age[1]	30 millions years	160 millions years
Depth	225 m	479 m
Water content[1] w (%)	20-30	< 6.5
Porosity n (%)	35-40[1]	14-19[2]
Clay fraction (%)	40-70[1]	48-50[3]
Young's modulus[1] (GPa)	0.2-0.4	3.6-8.5
Initial specimen suction	2.8 MPa[4, 5]	34 MPa[6]

[1] After Gens, 2011
[2] After Yven et al. 2007
[3] After Gaucher et al. 2004
[4] After Delage et al. 2007
[5] Measured by the filter paper method
[6] Measured by the Decagon dew-point tensiometer

The COx claystone is characterised by a clay matrix (clay fraction close to 50% at a 490 m depth) composed of interstratified illite-smectite minerals (Gaucher et al. 2004) with also significant proportions of grains of calcite (20%) and quartz (22%). Further understanding about the microstructure, mineralogy and porosity of the COx claystone was gained by Yven et al. (2007) by using different methods (including scanning electron microscope, autoradiography, mercury intrusion porosimetry, oil, helium and nitrogen

adsorption), resulting in the conceptual model presented in Figure 1. The model shows how individual calcite or quartz grains are contained into a clay matrix with interconnected porosity.

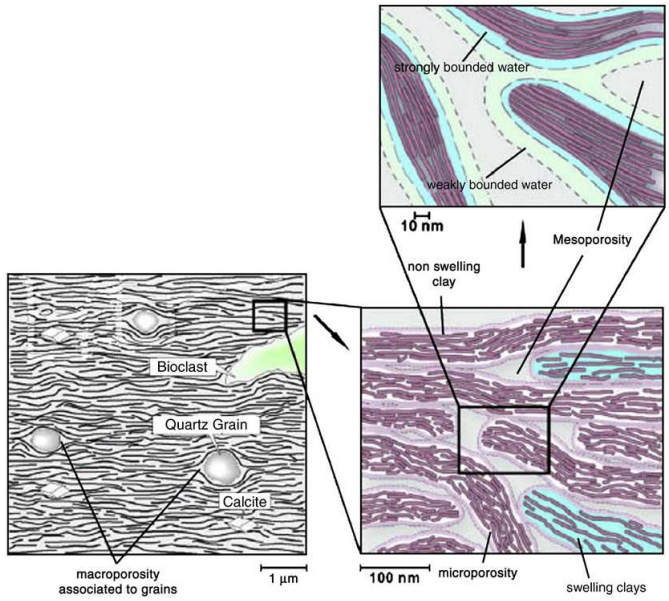

Figure 1. Conceptual model of the COx clay microstructure (Yven et al. 2007)

Figure 2 provides a typical pore size distribution curve of the COx claystone obtained by mercury intrusion porosimetry (MIP) on a freeze-dried specimen, showing a well defined single pore population (with an average diameter of 32 nm in agreement with Yven et al. 2007 and Boulin et al. 2008) that is typical of the clay matrix. The intruded porosity represents 75% of the total porosity (n = 17.4% and also represented in the graph). This data is in good agreement with that of Yven et al. (2007) who estimated the porosity of small dimension (3 - 10 nm) to 33.5 % of the total porosity in accordance with the 34% of porosity smaller than 10 nm found here.

The remaining porosity is located within the clay matrix in smaller pores that cannot be investigated by MIP (Yven et al. 2007). This is a well known feature in clay materials containing smectites, due to very thin intra-platelets (or intra-crystalline) porosity (see Delage et al. 2006 in compacted smectites). The interpretation of the single pore population observed in Figure 2 can be made by assimilating the clay matrix to an assembly of bricks made up of platelets, as can be seen in Figure 1. The mean pore radius hence provides an estimate of the average platelets thickness. With an elemental clay thickness of 1 nm typical

of smectites and illites and an average platelet thickness of 30 nm, an average number of 30 layers by platelets can be roughly estimated, in accordance with data provided by Mitchell and Soga (2005).

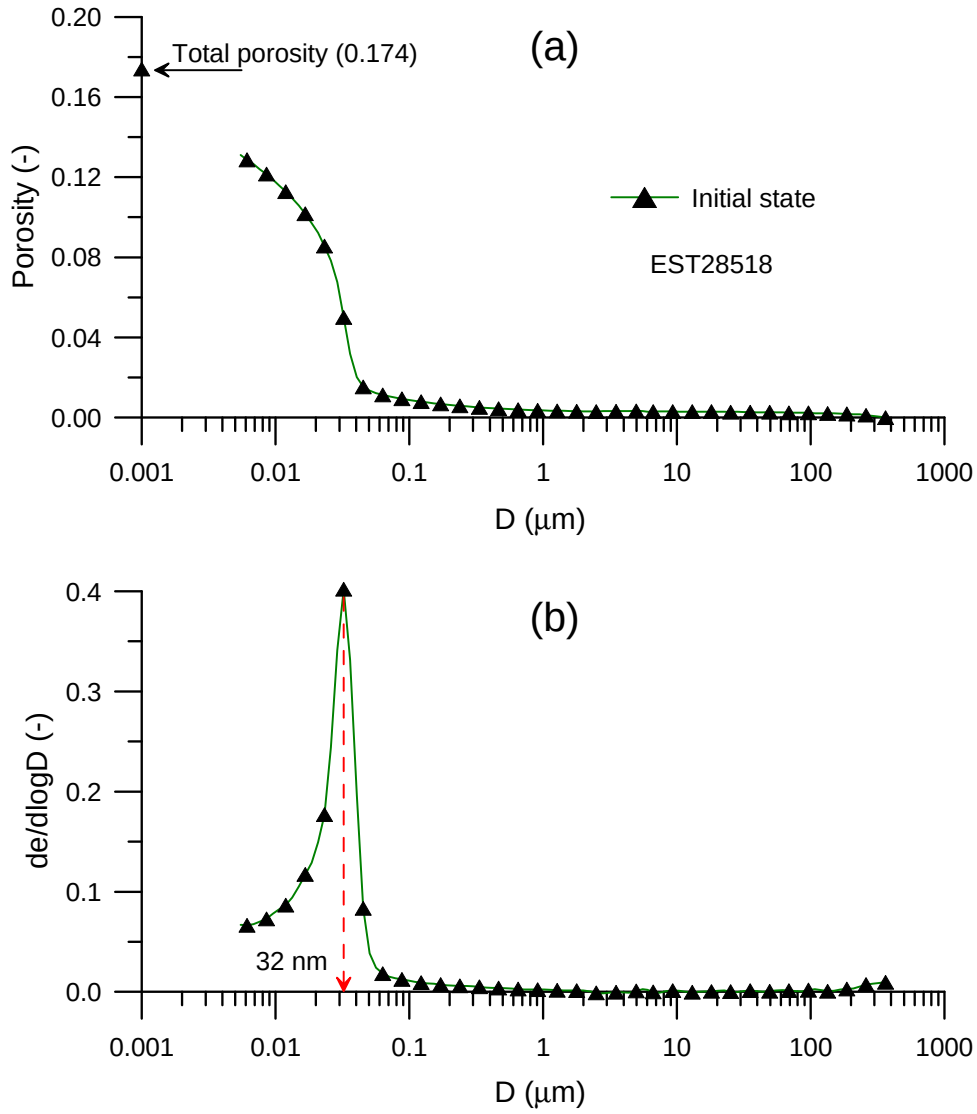

Figure 2. Pore size distribution curves of the sample at initial state.

Tests were carried out in a room at controlled temperature and relative humidity (20°C and 80% respectively). Following Mohajerani et al. (2011), the saturation of the sample was conducted on a high stress double lever arm oedometer (Marcial et al. 2002) by carefully limiting volume changes during water infiltration. To do so, the vertical displacement gauge was manually followed and the specimen was progressively loaded to compensate any swelling with a limit fixed at 2 µm. The detail of the procedure is illustrated

in Figure 3 that shows that the maximum stress applied to neutralize the swelling was equal to 3.48 MPa for a sample with an initial degree of saturation (S_r) of 77% and a suction of 34 MPa (WP4 measurement). The relatively high displacement of 16 µm observed at the end of first day is due to imperfect control during night time. To investigate suction effects on such a specimen resaturated with limited volume change, the specimen was afterwards quickly unloaded at constant water content. To do so, the porous stones were first desaturated by air flushing.

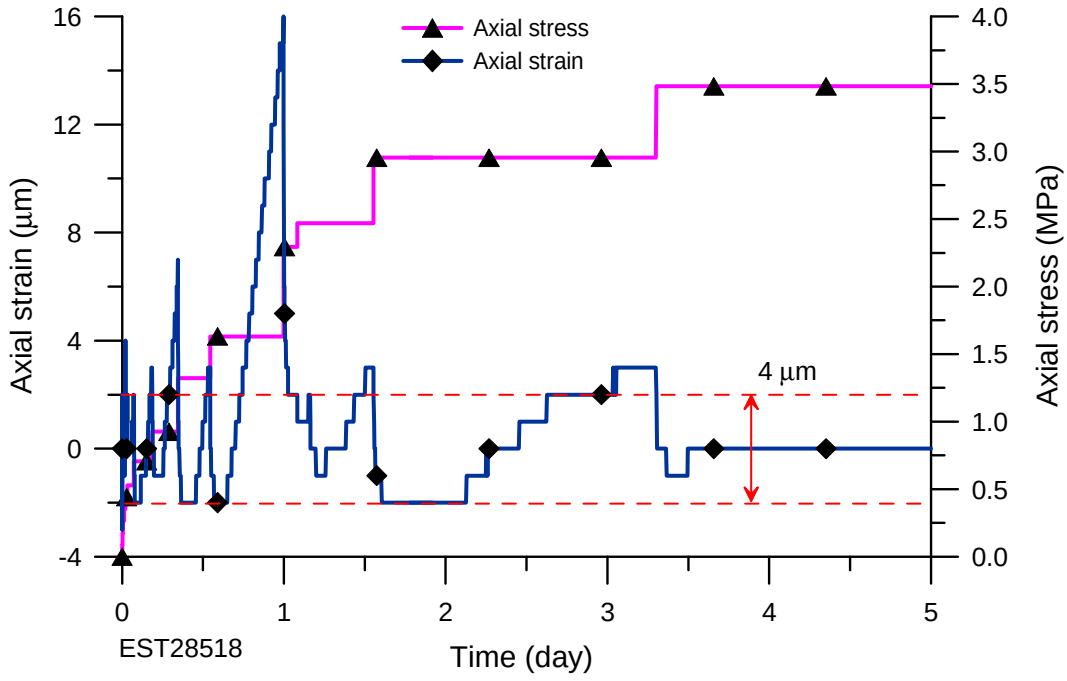

Figure 3. Resaturation with limited swelling

Pore-size distribution measurements (Mercury Porosimeter micromeritics-AutoPore IV 9500**)** were conducted on freeze-dried specimens to investigate microstructure changes. Specimens were previously frozen at - 210°C by using slush nitrogen (obtained by previously putting liquid nitrogen under vacuum, Delage et al. 2006). The range of pores investigated was between 363.6 µm (minimum pressure of 3.4 kPa) to 5.5 nm (maximum pressure of 227.5 MPa).

3. Results

The stress-strain path corresponding to the instantaneous constant water unloading phase from the 3.48 MPa vertical stress is represented in Figure 4. Unloading was performed stepwise at intermediate stresses of 0.8 MPa (in the semi-log graph, complete unloading is arbitrarily represented at a stress of 0.1 kPa). The unloading process lasted 5 minutes and exhibited an increase in porosity from 17.4 to 18% calculated from the swelling observed in Figure 4. The sample was afterwards extracted from the oedometer cell allowing for (slight) radial and axial expansion as shown in Table 2. Careful calliper measurements carried out 15 minutes after unloading sample provided a porosity value of 20.9 %. Obviously, significant axial swelling occurred at constant water content once the sample was extracted from the ring. Note that hydrostatic weighing provided a porosity value of 21.2 % quite close to that obtained by calliper measurements, also represented in Figure 4. The specimen was afterwards isolated from evaporation by wrapping in a plastic film and rapidly frozen to keep constant water content.

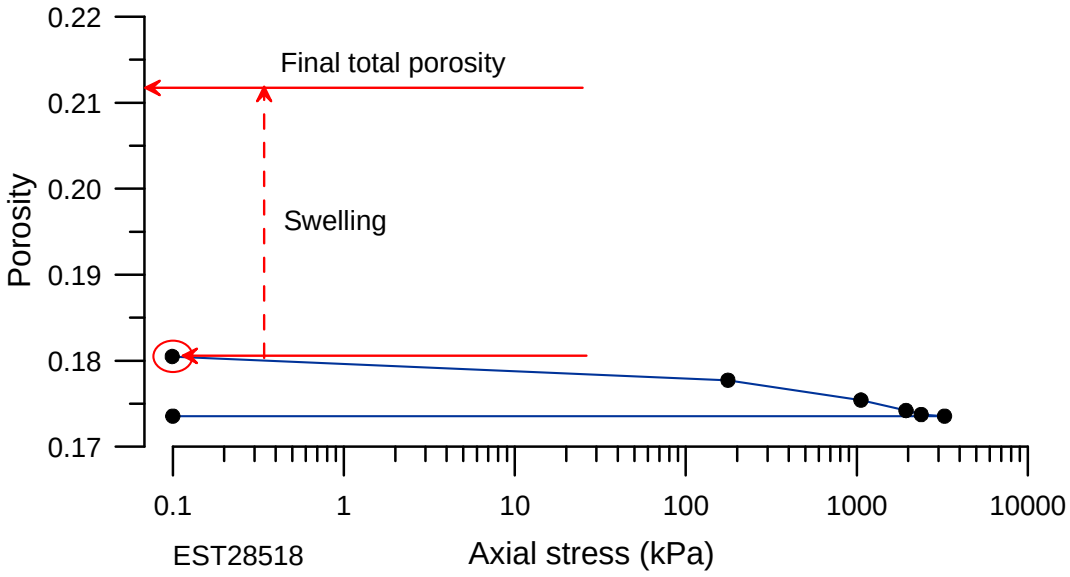

Figure 4. Unloading phase at constant water content

One can observe that, in spite of having a constant water content (w = 8.4%), the swelling observed (final porosity n = 21.2% compared to 17.4%) resulted in a simultaneous desaturation of the specimen with a final value of the degree of saturation S_r = 81% corresponding to a 21 MPa suction (WP4 measurement). This means that the air-entry value

of the sample has been exceeded. Indeed, this value, estimated between 7 and 9 MPa according to gas penetration tests (De La Vaissière and Talandier 2012) is significantly smaller than the final value of 21 MPa.

Table 2. Characteristics of the tested sample.

Sample	State	*h (mm)*	*d (mm)*	*m (g)*	*w* (%)	*e*	*n* (%)	S_r (%)	*s* (MPa)
EST28518	Before test (initial state)	8.86	37.92	23.75	6.3	0.21	17.4	77	34
EST28518	After test (final state)	9.19	38.06	24.48	8.4	0.27	21.2	81	21

The pore size distribution (PSD) curve of the swollen sample is presented in Figure 5. Also reported in the graph is the total porosity (21.2%). Surprisingly, the shape of the PSD of the swollen unsaturated specimen at constant water content is quite comparable to the initial one presented in Figure 2. It exhibits a single pore population with a mean radius of 32 nm, comparable to that of the intact sample (although slightly less well classified as indicated by the density function curve). No large pore population representing possible cracks due to hydraulic damage and swelling (Yang et al. 2012, Wan et al. 2013) is observed. Also, visual examination of the sample didn't evidence any visible cracks with thickness larger than the maximum diameter identified by mercury intrusion (363.6 µm).

Global specimen expansion at constant water content is then only possible within the intra-platelet infra-porosity (too small to be intruded by mercury) with a transfer of water from the larger inter-platelets pores (average 32 nm) to the smaller intra-platelet pores that results in crystalline swelling. Here, swelling occurs within the inter-stratified illite smectite clay platelets.

As any clay material, the pore water of the COx clay includes both capillary and hydration water (e.g. Revil and Li 2013). By only considering capillary effects, the suction exerted when desaturating 32 nm diameter pores is given by the Young-Laplace equation:

$$p = \frac{2\sigma \cos\theta}{r} \tag{1}$$

in which σ is the water/air interfacial tension equal to 72.8×10^{-3} N/m and θ the solid-liquid contact angle with $\cos\theta = 1$ for water. A pressure value of 9.1 MPa is obtained, slightly higher than the air-entry value of the COx claystone, confirming the predominance of capillary effects in the clay water interaction in these pores schematically represented in

Figure 1. Comparing this value with the final suction of 21 MPa finally measured in the sample indicates that inter-platelets pores have been desaturated. The high suction value is hence mainly due to strong clay-water interaction occurring inside the platelets, confirming the intra-crystalline nature of the swelling.

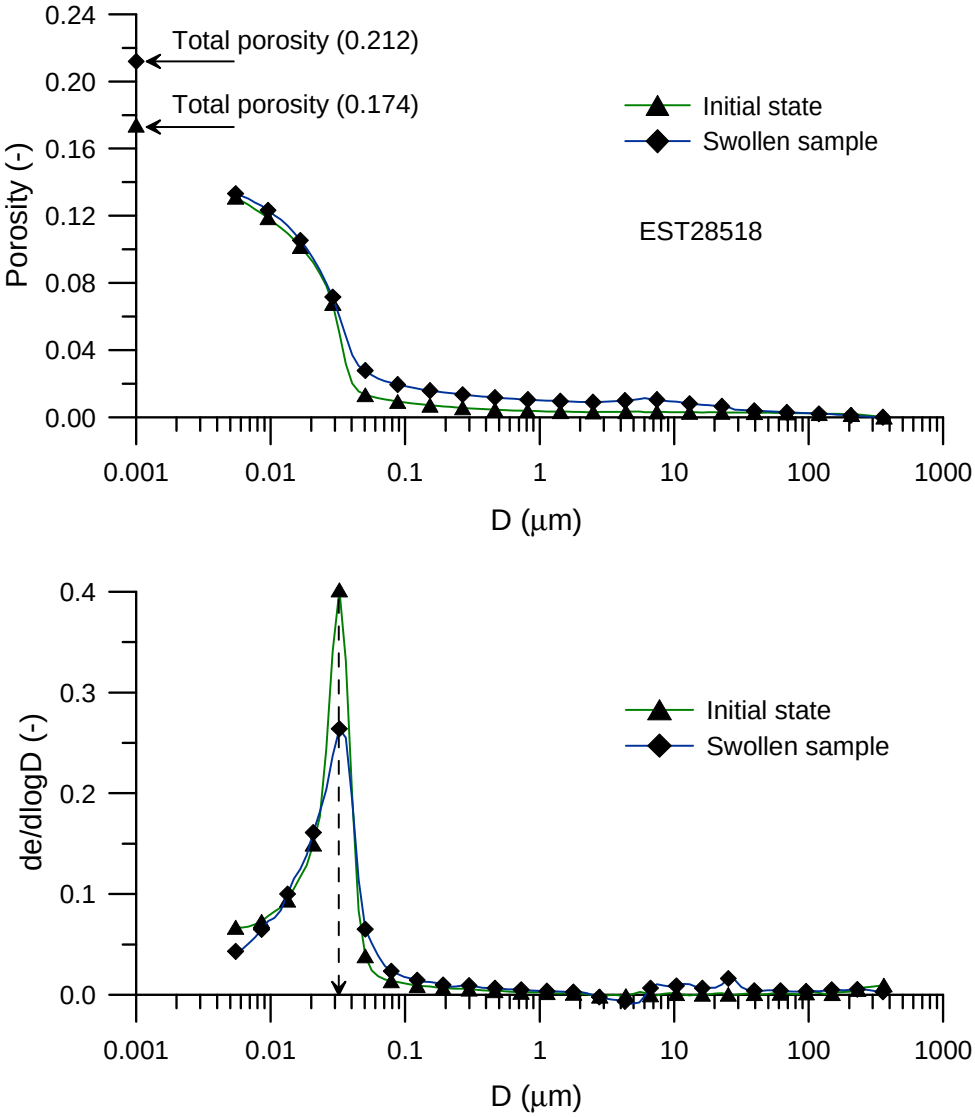

Figure 5. Pore size distribution curves, swollen sample and initial state.

A question about the rate of water transmission between the large inter-platelets pores and the thin intra-platelets ones arises given the very low permeability and slow water transfer suspected. This internal water transfer, comparable in nature to long term internal transfers observed in compacted bentonite at constant water content (Delage et al. 2006) has been completed in around 30 minutes after unloading. Actually, the slowing effects due to

the low permeability (around 10^{-20} m^2 in the COx claystone) are compensated by the small distance that water molecules have to travel from the inter-platelets pore to the intra-platelets ones.

4. Conclusion

Suction effects were investigated in a specimen of the Callovo-Oxfordian claystone extracted at great depth (479 m) in the underground research laboratory of ANDRA in Bure (France). The specimen was first saturated with limited volume change by progressively increasing vertical stress up to 3.48 MPa. The specimen was afterwards quickly unloaded at constant water content, exhibiting significant swelling and desaturation, 30 minutes after extraction from the oedometer ring with a suction significantly larger than the air entry value. The pore size distribution of the swollen sample was comparable to that of the initial one with no appearance of large pores, indicating that swelling was due to a water transfer within the clay matrix from inter-platelets pores to intra-platelet pores, in a pore range that is too small to be detected by mercury intrusion. This phenomenon may occur during gallery excavation in areas of the excavation damaged zone submitted to instantaneous stress release, as a first stage of desaturation, prior to the subsequent evaporation due to the ventilation of the galleries.

Acknowledgments

The authors are grateful to ANDRA (French Agency for Radioactive Waste Management) for funding this research. The ideas expressed here are from the authors and do not engage ANDRA.

References

Bishop A.W., Kumapley N.K. and El Ruwayih A. 1974; The influence of pore water tension on the strength of a clay. *Proc. Royal Soc. London* vol. 1286, 511-554.

Boulin P.F., Angulo-Jaramillo R., Daian J.F., Talandier J., Berne P. 2008; Pore gas connectivity analysis in Callovo–Oxfordian argillite. Applied Clay Science; 42: (1–2) 276–283.

Delage P., Marcial D., Cui Y.J., Ruiz X. 2006; Ageing effects in a compacted bentonite: a microstructure approach. Géotechnique; 56(5): 291–304.

Delage P., Le T.T., Tang A.M., Cui Y.J., Li X.L. 2007; Suction effects in deep Boom clay block samples. Géotechnique; 57(1): 239–244.

De La Vaissière R., Talandier J. 2012; Gas injection tests in the Meuse/Haute Marne underground research laboratory. Proceedings of the Transfert 2012 Conference, Ecole Centrale de Lille Eds, 360–368.

Doran, I.G, Sivakumar, V, Graham, J. and Johnson, A. 2000; Estimation of in-situ stresses using anisotropic elasticity and suction measurements. Géotechnique 50, No. 2, 189-196.

Gaucher E., Robelin C., Matray J.M., Négrel G., Gros Y., Heitz J.F., Vinsot A., Rebours H., Cassagnabère A., Bouchet A. 2007; ANDRA underground research laboratory : interpretation of the mineralogical and geochemical data acquired in the Callovian-Oxfordian formation by investigative drilling. Physics and Chemistry of the Earth; 29: 55–77.

Gens A. 2011; On the hydromechanical behaviour of argillaceous hard soils-weak rocks. In: Proc. 15th European conference on Soil Mechanics & Geotechnical Engineering, Athens.

Jougnot D., A. Revil, N. Lu, and A. Wayllace. 2010. Transport properties of the Calloxo-Oxfordian clay-rock under partially saturated conditions, Water Resources Research, 46, W08514, doi:10.1029/2009WR008552.

Marcial D., Delage P., Cui Y.J. 2002; On the high stress compression of bentonites. Canadian Geotechnical Journal; 39(4): 812-820.

Mitchell J.K., Soga K. 2005; Fundamentals of soil behaviour. John Wiley, New-York.

Mohajerani M., Delage P., Monfared M., Sulem J., Tang A.M., Gatmiri B. 2011; Oedometric compression and swelling behavior of the Callovo-Oxfordian argillite. International Journal of Rock Mechanics and Mining Sciences; 48(4): 606–615.

Pham Q.T., Vales F., Malinsky L., Nguyen Minh D., Gharbi H. 2007; Effects of desaturation-resaturation on mudstone. Physics and Chemistry of the Earth; 32: 646–655.

Revil A. and N. Lu, Unified water sorption and desorption isotherms for clayey porous materials, Water Resources Research, 49(9), 5685-5699.

Skempton, A. W. 1961; Horizontal stresses in an overconsolidated Eocene clay. Proceedings of the 5th International Conference on Soils Mechanic and Foundation Engineering, Paris, pp. 351-357.

Skempton, A. W. and Sowa, V. A. 1963; The behaviour of saturated clays during sampling and testing. *Géotechnique* 13, No. 4, 269-290.

Wan M., Delage P., Tang A.M., Talandier J. 2013; Water retention properties of the Callovo-Oxfordian claystone. International Journal of Rock Mechanics and Mining Sciences; 64: 96–104.

Wileveau Y., Cornet F.H., Desroches J., Blumling P. 2007; Complete in situ stress determination in an argillite sedimentary formation. Physics and Chemistry of the Earth; 32(8–14): 866–878.

Yang D., Chanchole S., Valli P., Chen L. 2012; Study of the Anisotropic Properties of Argillite Under Moisture and Mechanical Loads. Rock Mechanics and Rock Engineering; 46(2): 247–257.

Yven B., Sammartino S., Géroud Y., Homand F., Villiéras F. 2007; Mineralogy, texture and porosity of Callovo-Oxfordian claystones of the Meuse/Haute-Marne region (eastern Paris Basin). Mémoires de la Société géologique de France; 178: 73–90.

A microstructure investigation of the compression-swelling behaviour of shales: the case of the Callovo-Oxfordian claystone

Hamza MENACEUR[1], Pierre DELAGE[1], Anh-Minh TANG[1], Jean Talandier[2]

[1] *Ecole des Ponts ParisTech, Navier/CERMES, France*

[2] *ANDRA, Chatenay-Malabry, France*

Abstract

To further examine a conceptual model proposed by Mohajerani et al. (2011) on the compression-swelling behaviour of claystones, a microstructure study based on the combined use of mercury intrusion porosimetry and scanning electron microscopy was carried out on freeze-dried specimens of the Callovo-Oxfordian claystone submitted to various compression/swelling paths. Specimens were compressed in the oedometer to stress of 56 and 113 MPa prior to be unloaded in two conditions: i) at constant water content and ii) by allowing water infiltration, as in standard swelling tests. Careful examination and interpretation of the specimen released at constant water content (that also swelled due to internal water transfer) allowed interpret compression as the combined action of pore collapse (resulting in local cracks) at the level of inter-platelets pores within the clay matrix of the claystone, and the compression of the platelets themselves by expulsion of some water molecules adsorbed along the smectite sheets in the interstratified illite-smectite minerals where they are located. Swelling after water infiltration resulted in pore changes at two levels: through the creation of large cracks of several tens of micrometers, and to some disorder at the level of the inter-platelets porosity that became less well organised with a larger pore range compared to the initial state.

1. Introduction

The Callovo-Oxfordian (COx) claystone is considered as a potential host rock for high activity radioactive waste disposal at great depth in France because of its low permeability, adequate self-sealing potential and high retention capacity (e.g. ANDRA 2005, Escoffier at al. 2005, Davy et al. 2007, Zhang and Rothfuchs 2008). ANDRA, the French Radioactive Waste Management Agency, has developed an Underground Research Laboratory (URL) close to the village of Bure in the North-east of France in order to carry out in-situ experiments and investigations on radioactive waste disposal at great depth (Lebon and Mouroux 1999). The URL is composed of galleries excavated at a two levels (depths of 445 and 490 m) in the 150 m thick layer of the COx claystone, an indurated clay rock 155 billion years old (limit upper-middle Jurassic). The subhorizontal layer of the COx claystone (1 – 1.5° tilting) is located in between two several hundred meters thick layers of Dogger (bottom) and Oxfordian (top) limestones. The in-situ stress state at the level of the Bure URL at 490 m has been investigated in detail by Wileveau et al. (2007). The total stress values obtained are as follows: vertical stress σ_v = 12.7 MPa, minor horizontal total stress σ_h = 12.4 MPa and major horizontal total stress σ_H = 16.2 MPa, indicating a nearly isotropic stress state, with a pore pressure of 4.9 MPa.

In recent years, the coupled hydro-mechanical behaviour of claystones has been investigated in the context of radioactive waste disposal. Particular attention has been paid to the properties of both the COx claystone and the Opalinus clay from the Mont-Terri URL run by the Swiss agency for radioactive waste disposal (NAGRA). The significant water-sensitivity of claystones has been evidenced (e.g. Valès et al. 2004) together with the paramount importance of i) the smectites minerals contained in the clay matrix and ii) the resulting swelling and self-sealing properties that are crucial in terms of confinement efficiency, particularly through the excavated damaged zone (EDZ, Tsang et al. 2005) in the close field around galleries and repository cells (Davy et al. 2007, Monfared et al. 2012, Zhang 2013). The water-tightness of the EDZ is crucial, particularly in the case of the French concept of high level radioactive waste disposal in which waste canisters are to be placed in repository cells in direct contact with the COx claystone, with no engineered barrier in between the canisters and the claystone.

The swelling behaviour of the COx claystone is directly linked to its self-sealing properties, given that self-sealing is generated by the mobilization of smectites minerals in

confined cracks. This was clearly shown in an artificial tensile crack by Davy et al. (2007) who measured a 3 MPa swelling pressure between to half-cylinders obtained by previously submitting a triaxial specimen to a Brasilian tensile test. The relation between swelling and damage has also been evidenced by Carter et al. (2010) from tunnelling in swelling ground. From field observations and laboratory tests, Carter et al. (2010) observed that swelling was highly enhanced in sheared zones and they showed that either natural mechanical disturbance (fault, shear band) or man induced disturbance (excavating-trimming) could break down the bonds that, in normal rock mass, confine the swelling clays from freely expanding. Aversa et al. (1993), in their study on the mechanical behaviour of Italian tectonised shales, performed oedometric tests and observed that samples compressed under higher stresses had greater swelling index, a feature that they related to the presence of discontinuities. The swelling properties due to discontinuities were also investigated in the extreme case of crushed COx argillite by Tang et al. (2011). Based on oedometer tests, these authors obtained swelling pressures between 1 to 5 MPa, comparable to the data of Davy et al. (2007)..

In this context, Mohajerani et al. (2011) performed a series of high stress (up to 113 MPa) oedometer compression tests on specimens of the COx claystone and showed that compression at larger stress resulted in more damage and in stronger swelling capability. Indeed, claystones are quite sensitive to changes in stress and water content that may result in damage. This has been demonstrated by Valès (2008), Bornert et al. (2010) and Wang et al. (2014) by using Digital Image Correlation (DIC) at microscopic scale to evidence the appearance of cracks resulting from hydration under zero stress conditions. The occurrence of swelling and hydric damage was also indirectly demonstrated by Wan et al. (2013) in a detailed investigation of the water retention properties of the COx claystone.

In their interpretation of enhanced damage and swelling during compression, Mohajerani et al. (2011) proposed a conceptual model coupling compression, induced damage and enhanced swelling, based on conclusions drawn on the changes in microstructure occurring in structured fine grained soils during compression by Delage and Lefebvre (1984). The model proposed was that of a fragile porous matrix defined by a given pore size distribution (PSD) curve that was compressed by the progressive and orderly collapse of the pores, from the largest to the smallest. In other words, a given level of stress collapsed pores of a given size, allowing then to link the slope of the pore size distribution curve to the compressibility index in structured soils (see Delage 2010 and Delage 2014 for more details). This model, extended to compacted soils (Delage 2009) was applied by

Mohajerani et al. (2011) to the COx claystone that was considered as a rigid porous matrix defined by a clearly unimodal PSD curve defined by inter-particle pores within the clay matrix (Yven et al. 2007). Like Delage and Lefebvre (1984), Mohajerani et al. (2011) also considered that collapsed pores resulted in locally remoulded zones made up of cracks, illustrating local mechanical damage prone to afterwards exhibit enhanced swelling.

In this paper, an attempt to check Mohajerani et al. (2011)'s findings by a detailed microstructure investigation based on the combined use of mercury intrusion porosimetry (MIP) and scanning electron microscopy (SEM) on properly dehydrated specimen (freeze-drying with quick freezing of small specimens) is made, following the methodology initially proposed by Delage and Lefebvre (1984). Microstructure investigation was conducted on COx specimens at initial state and submitted to various compression stresses prior to be released either at constant water content (instantaneous stress release) or after swelling.

2. Material and methods

2.1. The COx claystone

The COx claystone is an indurated clay with a mineralogical composition that varies with depth. The total connected porosity varies between 14% in carbonated (stronger) levels and 19.5% in more argillaceous (weaker) levels (Yven et al. 2007). At the URL depth (490 m), the COx contains 45–50% clay minerals that constitute a matrix in which other detritic components (20–30% carbonates and 20–30% quartz and feldspar) are embedded (Gaucher et al. 2004). In this study, tests were performed on specimens cored perpendicular to the bedding plane at depths of 479 m (specimen EST28518) and 482 m (EST44581). The initial characteristics of the samples are presented in Table 1. The water content was determined by measuring the initial and final weights of a rock piece before and after drying in the oven at 105 °C for 24 hours. The porosity and degree of saturation were calculated from carefully measuring the sample volume by hydrostatic weighing. The initial total suction was determined by using a dew point potentiometer (WP4, Decagon). As seen in Table 1 the sample EST28518 is not fully saturated at initial state with a degree of saturation of 77% corresponding to 34 MPa of suction for a porosity of 17.4%. Partial saturation resulted from the combined actions of coring, transport, storage and specimen preparation.

Table 1. Initial characteristics of the tested samples.

Specimen	EST28518
Depth (m)	479
Water content (%)	6.3
Dry density (Mg/m^3)	2.14
Specific gravity (Mg/m^3)	2.6
Void ratio	0.21
Porosity (%)	17.4
Degree of saturation (%)	77
Suction (MPa)	34

2.2. Sample preparation and setting

Once extracted from the borehole (perpendicular to bedding), cores were packed in specially designed cells (called T1 cells) that prevent desaturation and partially confine cores thanks to an expansive mortar cast around the core with also an axial stress of 0.6 time the in-situ stress applied by means of a calibrated spring. The diameter and length of cores in T1 cells are 100 and 300 mm, respectively. In the laboratory, the oedometer tests were performed in 38 mm diameter rings. COx specimens are difficult to trim in the laboratory because they often break along the bedding plane. To trim 38 mm diameter specimens, the 100 mm diameter core was first placed in special metal confining mould to ensure good confinement while trimming the internal 38 mm diameter cylinder by diamond coring in dry condition. The required height (around 10 mm) was afterwards obtained by cutting the 38 mm cylinder by using a small hand saw. Finally, the top and bottom surfaces were carefully polished by using a sand paper sheet

High pressure oedometer compression tests were carried out by means of a double lever arm oedometer (Marcial et al. 2002) able to apply a maximum axial stress of 113 MPa on a 38 mm diameter specimen. The sample was placed on a metal porous disc connected to two lateral valves to allow satisfactory saturation of the porous disc. Axial displacement was monitored by using an electronic transducer (Mitutoyo) connected to a data acquisition system. A preliminary calibration of the system was performed by running a load cycle along the total stress range (0 – 113 MPa) without sample so as to account for the effects of the elastic compressibility of the metallic porous disc, of the cell base and of the piston. The vertical calibrated elastic response obtained was subtracted to the total measured compression displacements obtained in all tests.

To avoid any further damage due to swelling during specimen resaturation, particular attention was devoted to the resaturation procedure that was conducted, following Mohajerani et al (2011), by infiltrating water with controlled volume change smaller than that corresponding to 2 µm swelling. To do so, the specimen was placed in the oedometer ring (that was previously coated with grease to reduce lateral friction) with initially dry porous disks. A low stress loading-unloading cycle (up to 0.44 MPa, corresponding to 1 kg load) was applied to ensure good contact between the specimen, the porous discs and the piston. During this cycle, the two lateral pore water valves connected to the bottom porous disk were closed to avoid any drying of the specimen. The saturation phase was started by infiltrating water from the bottom porous disk while following the vertical displacement gauge and imposing by progressive manual loading a maximum vertical displacement of 2 µm. The specimen response is illustrated in Figure 1 (specimen of Test T2) that shows that the maximum stress applied to neutralize swelling was 3.2 MPa. The relatively high displacement of 9 µm observed at the end of first day is due to imperfect control during night time. All specimens were saturated following the same procedure. The other specimens coming from core EST28518 were saturated at maximum stress between 2.8 and 3.5 MPa with initial degree of saturation of 77% and suction of 34 MPa.

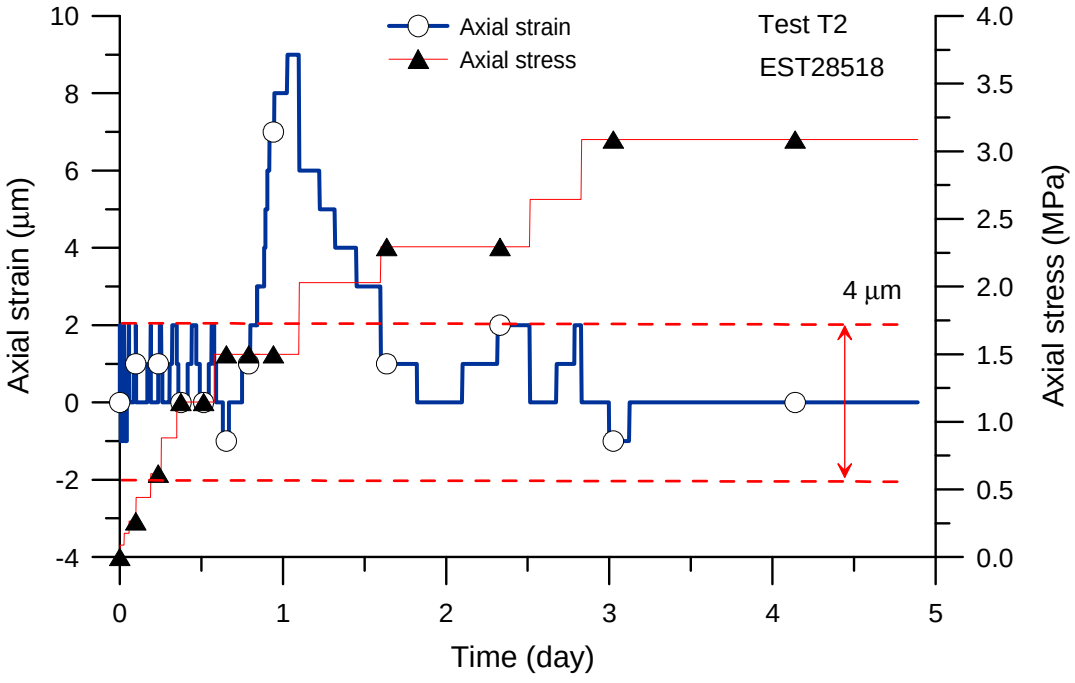

Figure 1. Resaturation process with limited volume change (< 2 µm), EST28518 specimen.

3. Experimental program

3.1. High pressure compression tests

Various mechanical loading paths were followed to investigate the compression-swelling behaviour of the COx claystone, as described in Table 2. Tests T1, T2, T3 and T4 were carried out along paths aimed at investigating the volume behaviour and microstructure changes at various level of compression. This series was conducted on specimens coming from the same core (EST28518) to avoid any dispersion due to differences in initial porosity or mineralogical composition. In tests T1 and T2, the specimens were loaded by steps up to 56 and 113 MPa respectively and afterwards quickly unloaded at constant water content. To do so, the porous stones were first desaturated by air flushing. The specimens were quickly step unloaded at constant water content under the same stresses as during the loading phase. The axial displacement was immediately noted before starting the next step, each step lasting around 1 minute. In tests T3 and T4, compressions (at 56 and 113 MPa respectively) were followed by standard unloading stages in which water was allowed to infiltrate the specimen and generate swelling.

Table 2. Test program.

Test	Specimen	Core	diameter (mm)	height (mm)	Procedure
T1	S1	EST28518	37.92	12.74	Resaturation at constant volume, High pressure compression up to 56 MPa, Unloading at constant water content.
T2	S2	EST28518	37.92	13.59	Resaturation at constant volume, High pressure compression up to 113 MPa, Unloading at constant water content.
T3	S3	EST28518	37.92	11.76	Resaturation at constant volume, High pressure compression up to 56 MPa, Unloading with hydration (swelling allow).
T4	S4	EST28518	37.92	11.65	Resaturation at constant volume, High pressure compression up to 113 MPa, Unloading with hydration (swelling allow)

3.2. Microstructural observations

MIP measurements and SEM observations were conducted at the end of each test in order to analyse the microstructure changes resulting from the loading path followed. To preserve the microstructure, dehydration was made by freeze-drying small pieces of claystone (1–3g in weight). These pieces were previously quickly frozen by immersion in slush nitrogen at – 210°C. Slush nitrogen was obtained by applying vacuum on liquid

nitrogen, bringing down its temperature from – 196°C (boiling temperature) to – 200°C (freezing temperature). Immersion in slush nitrogen is preferable because no boiling occurs around the specimen, resulting in faster freezing of water with no volume change. Ice was afterwards sublimated in a freeze-drier (see Tovey and Wong 1973, Gillott 1973, Delage and Pellerin 1984 and Delage et al. 2006 for more details). MIP tests were carried out in a Micromeritics-AutoPore IV 9500 porosimeter from a low initial pressure of 3.4 kPa up to 227.5 MPa, corresponding to entrance pore diameters of 363.6 µm and 5.5 nm respectively.

The intruded mercury porosity (n_{Hg}) was defined as the ratio of mercury intrusion volume V_{Hg} to specimen total volume V:

$$n_{Hg} = \frac{V_{Hg}}{V} \tag{1}$$

The pore entrance diameter (D) was determined from the intrusion pressure P_{Hg} by assuming a cylindrical pore shape:

$$D = \frac{4\sigma \cos\theta}{P_{Hg}} \tag{2}$$

where σ is the mercury-solid interfacial tension and θ is the mercury-solid contact angle (σ =0.484 N/m θ =141.3° according to Diamond 1970).

SEM observations were also conducted on freeze-dried specimens. To improve the quality of the surface observed, specimen were freeze-fractured. Freeze fracturing allows a better definition of the observation plane, given that fracture is not occurring, like when fracturing in the dry state, along any weakness plane with pulling out of some particles. The fracturing of a frozen specimen is governed by ice that also acts as an impregnation resin, avoiding any disturbance by maintaining all particles unmoved during fracturing. This is also a significant advantage compared to Environmental SEM in which fracture is made at wet state. Sticks were fractured along horizontal and vertical planes, with unfortunately no possibility of identifying the orientation of the bedding plane in vertical planes. SEM observations were conducted on horizontal and vertical planes.

4. High pressure compression oedometer tests

4.1. Tests T1 and T2

Samples S1 and S2 (EST28518) were loaded up to 56 and 113 MPa, respectively. Each loading step lasted up to 3-4 days so as to reach the stabilization of vertical displacement, as seen in Figure 2 in which the vertical stress and strain are plotted with respect to time. The compression curves in terms of porosity changes versus stress are presented in Figure 3a and b in linear scale and log scale of vertical stress, respectively. The shape of the compression curve is comparable with that obtained by Mohajerani et al. (2011) with, in linear scale, an initially upwards curved curve followed by a linear section above 15 MPa. Under 56 and 113 MPa, the compressive strains are 4.6 and 8.9 % respectively, values comparable to that obtained by Mohajerani et al. (2011, with 9.6 % compression strain under 113 MPa) and Heitz and Hicher (2002, with 8 % under 100 MPa). The initial phase of saturation is clearly observed in the semi-log plot (Figure 3b), showing that the resaturation with impeded swelling occurred until a vertical stress of the order of 2.6 – 3 MPa. The points of the quick unloading steps are also represented in the Figure.

Figure **3**b also shows that the instantaneous constant water unloading phases from 56 and 113 MPa occurred at constant water content during a short period of about 3 minutes with significant swelling (increases in porosity from 13.4 to 15.1% in test T1 - swelling of 42% - and from 9.3 to 12.2 % in T2 - swelling of 33%, Figure 3b).

The specimens were afterwards extracted from the oedometer cell allowing for (slight) radial and axial expansion as shown in Table 3 in which the other specimen characteristics are also given. Careful calliper measurements carried out 18 minutes after unloading provided porosities of 17.3 and 13.6 % for T1 and T2 respectively. Hydrostatic weighing carried out afterwards provided porosity values of 17.6 and 14 % respectively, quite close to that obtained by calliper measurements. As seen as in Table 3, the instantaneous unloading stage at constant water content provided swelling and desaturation in both specimens with a final degree of saturation S_r = 82% corresponding to a 21 MPa suction for T1 and S_r = 90% for T2 with a suction of 18 MPa. Actually, this rebound upon quick unloading at constant water content are not observed in soils that keep saturated with little rebound when unloaded (in a range of significantly smaller stresses in standard geotechnical testing). These rebounds are not in favour of easily investigating the effect of

compression on the microstructure, due to subsequent microstructure changes due to swelling (and desaturation) at constant water content. This point will be further discussed.

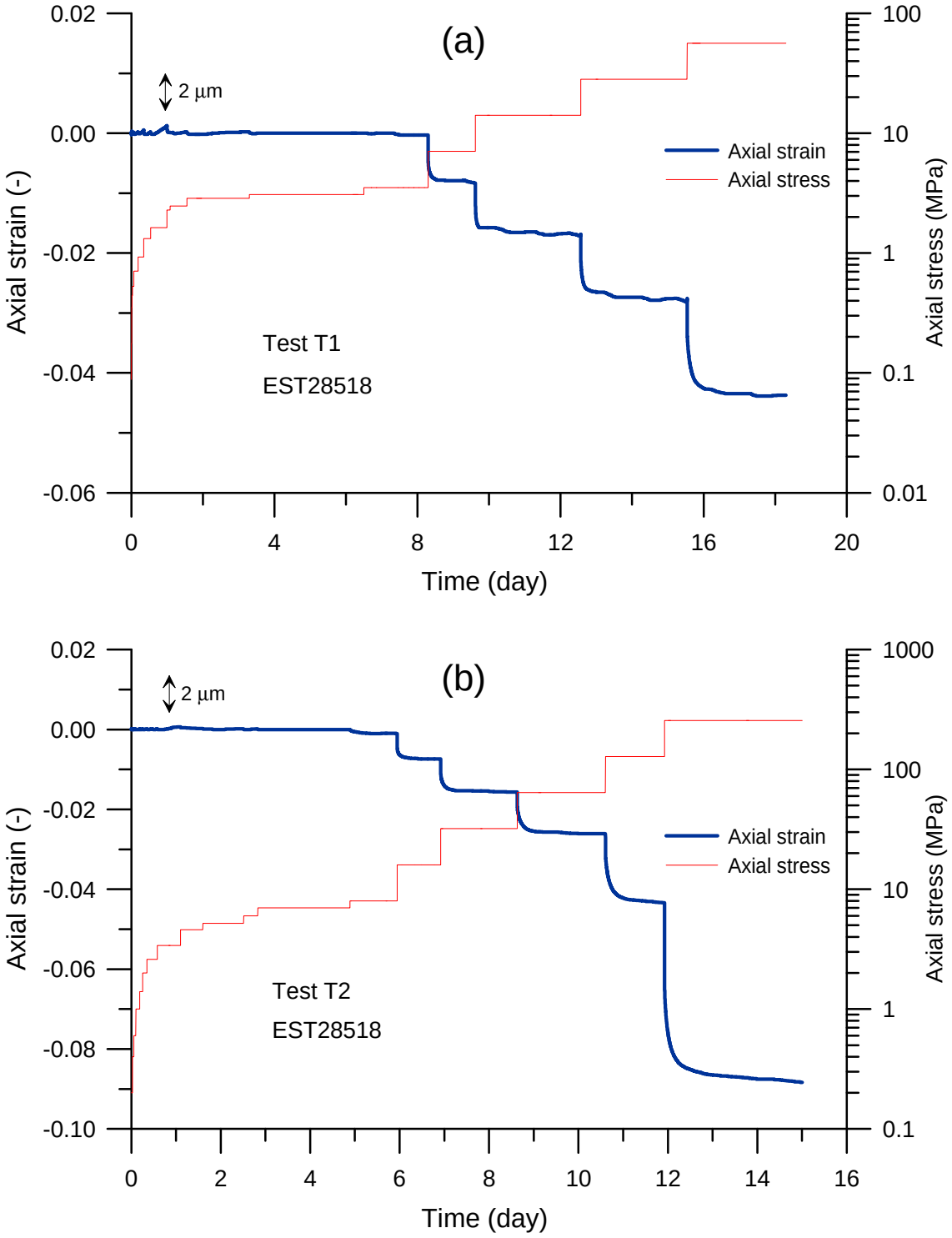

Figure 2. Axial compression and axial stress versus time, (a): Test T1, (b): Test T2.

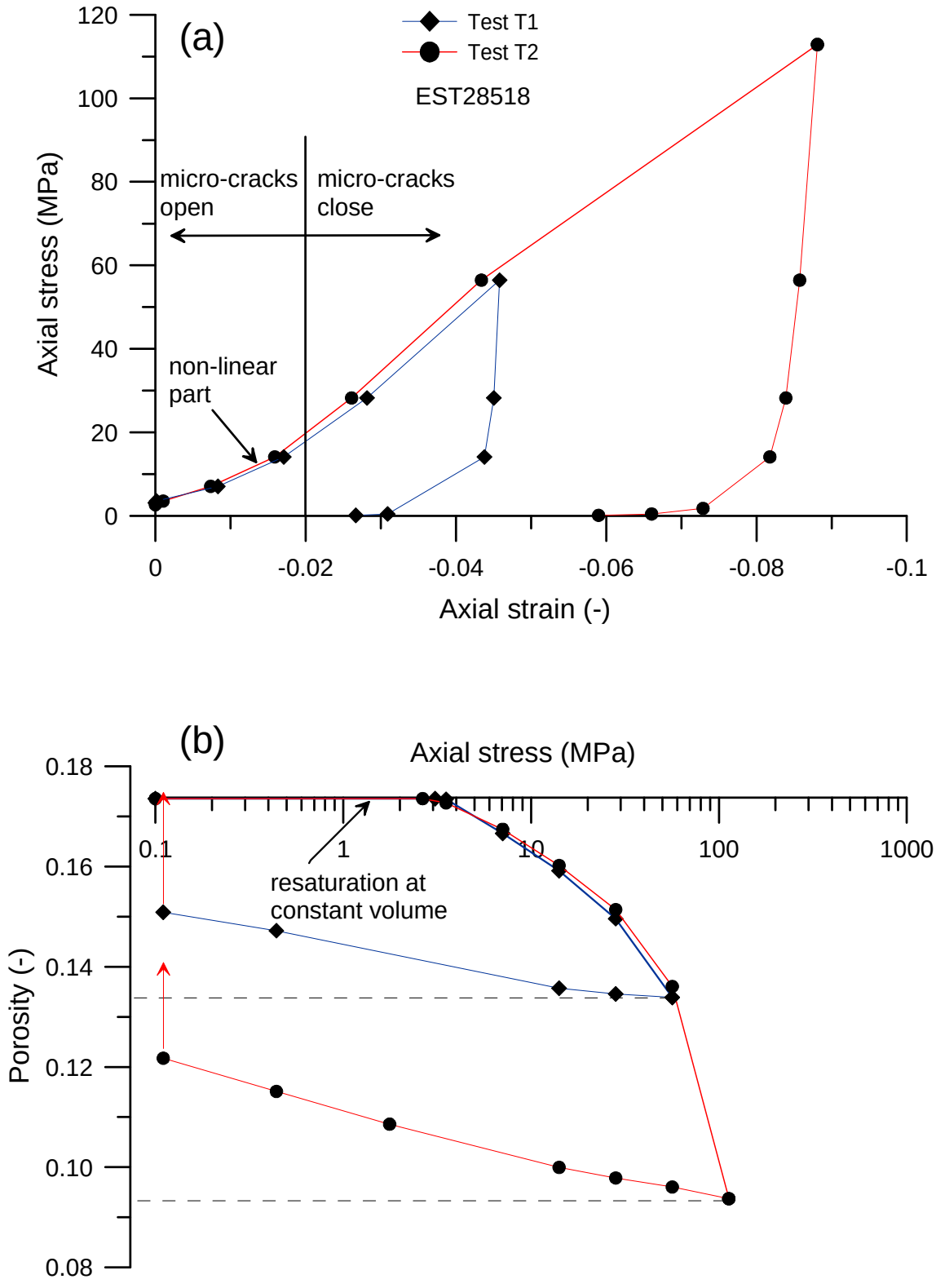

Figure 3. Oedometer compression curves (T1 and T2), (a): linear scale of stress; (b): log scale of stress.

Table 3. Characteristics of the specimens at the end of each test.

Specimen	Initial state	T1	T2	T3	T4
Water content (%)	6.3	6.7	5.7	9.4	10.1
Void ratio	0.21	0.21	0.16	0.25	0.29
Porosity (%)	17.4	17.5	14	20.1	22.2
Degree of saturation (%)	77	82	90	98	95
Suction (MPa)	34	21	18	1	6
Height (mm)	-	12.70	12.92	11.93	12.12
Diameter (mm)	-	38.05	38.05	38.04	38.04

4.2. Tests T3 and T4

Standard step loading-unloading tests were performed up to maximum axial stresses of 56 and 113 MPa on specimens S3 and S4, respectively. The changes in axial strain and stress versus time along both the loading and the unloading stages are presented in Figure 4. The compression curves are presented in linear scale of vertical stress in Figure 5a and in log scale in Figure 5b. The shape of the compression curve in linear scale is similar to that of test T1 and T2 , bringing some confidence in the quality of the data, with comparable values of maximum axial compression strains of 4.8 and 8.3% under 56 and 113 MPa, respectively.

Along the unloading phase, swelling curves comparable to that observed in swelling soils are observed upon unloading with significant swelling observed once stress is released (to 0.11 MPa). Under the same stress decrement, more swelling with larger slope is observed in the T4 specimen (loaded up to 113 MPa) compared to T3 (loaded to 56 MPa). As in soils, swelling curves are highly non-linear and end up at higher porosities than initial under the minimum stress of 0.11 MPa, with final porosities of both specimens (18.1 and 19.5 % for T3 and T4 respectively) larger than the initial one (17.4%). This trend is more clearly apparent in the semi log diagram of Figure 5b.

The specimens were afterward extracted from the oedometer cell and their characteristics determined (Table 3). Careful calliper measurements provided porosity values of 19.1 and 21.1 % for T3 and T4, respectively. The degrees of saturation of the swollen specimens were S_r = 98% with a 1 MPa suction for specimen T3 and S_r = 95% with a 6 MPa suction for specimen T4. This slight desaturation results from the release, a constant water content, of the 0.11 MPa stress.

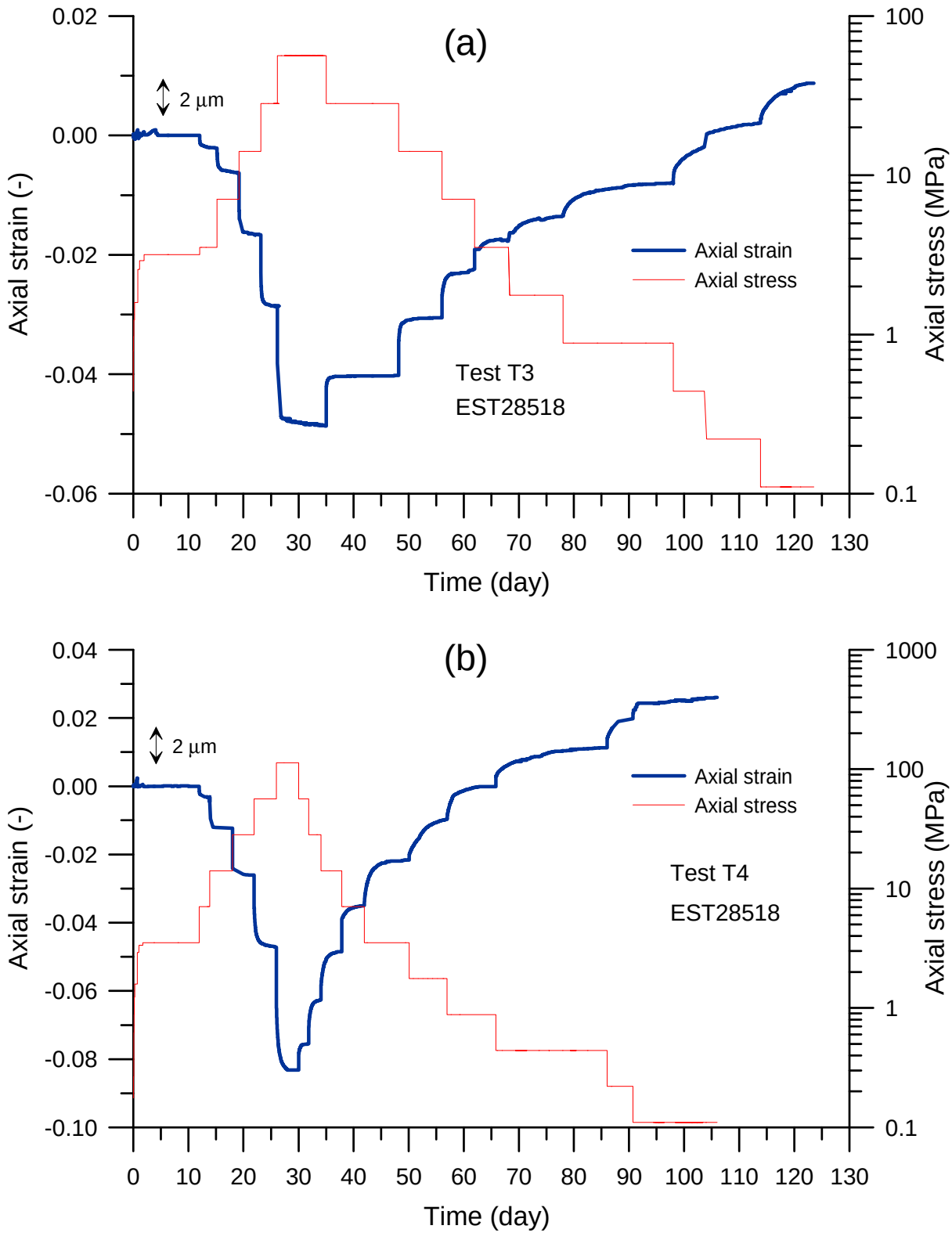

Figure 4. Axial compression and axial stress versus time, (a): Test T3, (b): Test T4.

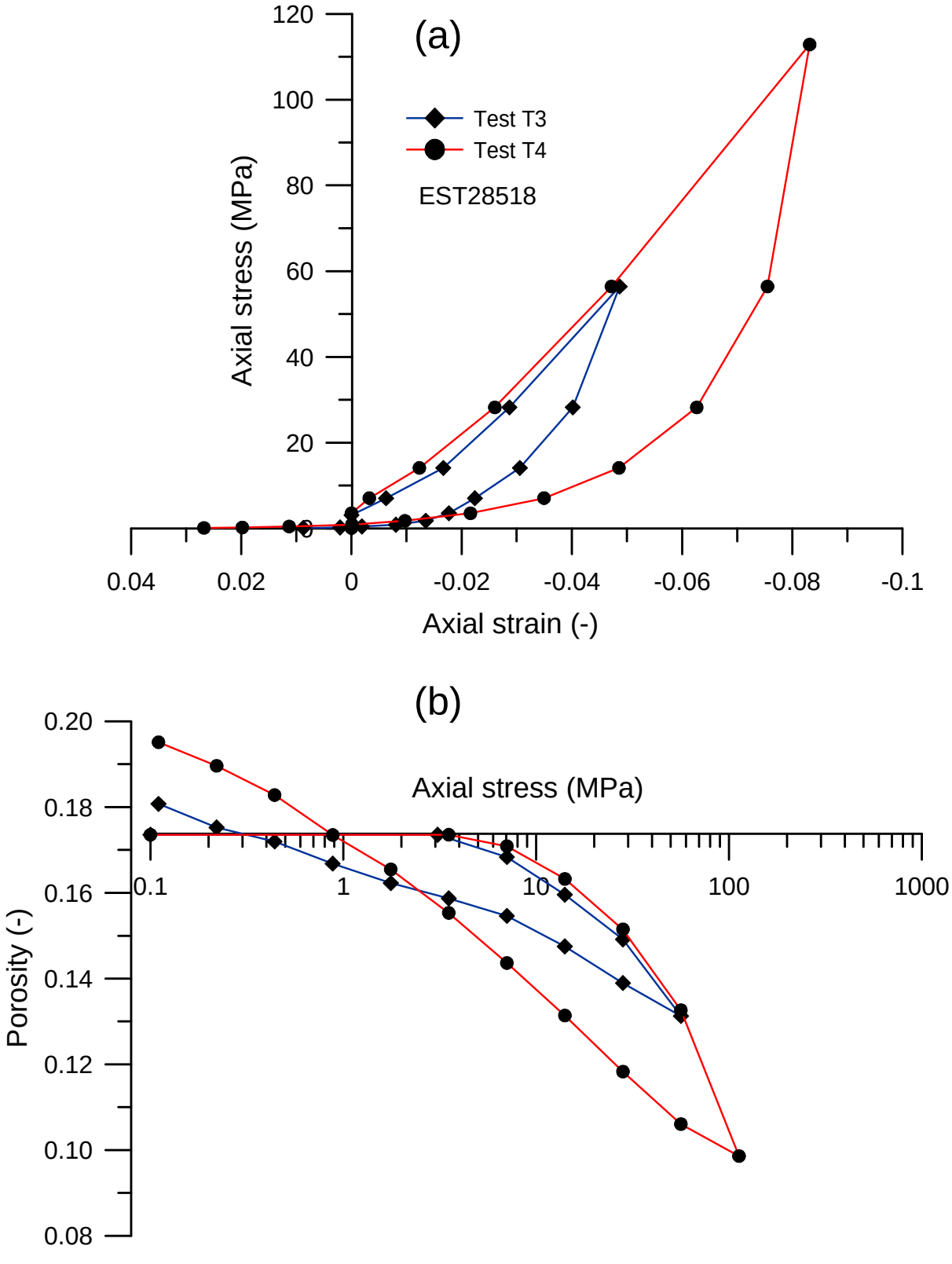

Figure 5. Oedometer compression curves (T3 and T4), (a): axial stress versus axial strain in linear scale; (b): porosity versus axial stress in semi-log scale.

5. Microstructure investigation

The microstructure change of the COx claystone specimen was investigated at various levels of compression by using both MIP measurements and SEM observations. The porosities of the specimens concerned by microstructure investigation are given in Table 4. Porosity values were first calculated at the end of the oedometer test, and afterwards measured by hydrostatic weighing. Values n_{Hg} obtained from the maximum volume of mercury intruded during MIP are also given.

Table 4. Porosity values obtained.

Specimen	State	n Oedometer curve	n_{Hg} (Intruded by mercury)	n (Total)	$n - n_{Hg}$
EST28518	initial	17.4	13.1	17.4	4.3
S1	T1	13,4	12.7	17.6	4.9
S2	T2	9,3	10.5	14.0	3.5
S3	T3	18.1	16.2	20.1	3.9
S4	T4	19.5	18.1	22.2	4.1

5.1. Pore size distribution curves

5.1.1. Initial state

The pore size distribution (PSD) curve obtained by using mercury intrusion porosimetry on sample EST28518 at initial state (S_r = 77%, n = 17.4%) is shown in Figure 6a in and Figure 6b in density function. A monomodal curve with quite a well defined pore population is identified, with an inflection point at 32 nm, in reasonable agreement with Yven et al. (2007) and Boulin et al. (2008) who however performed their MIP analysis on air dried specimens and obtained smaller average diameter of around 20 nm, probably because of some shrinkage due to oven drying (Wan et al. 2013 evidenced a global shrinkage of 1.4% on COx claystone specimens submitted to a suction of 150 MPa). As shown by these authors, this pore population is related to the average entrance pore diameter within the clay matrix. The comparison of the porosity intruded by mercury at the highest mercury pressure (n_{Hg} = 13.1% at P_{Hg} = 227.5 MPa corresponding to smallest diameter of 5.5 nm) is smaller than the total porosity from total volume measurement (n = 17.4%), confirming previous findings by Yven et al. (2007) about the existence of a pore volume of smaller size (corresponding here to a porosity of 4.3%). Indeed, Yven et al. (2007) estimated the porosity of small dimension (3 - 10 nm) at 33.5 % of the total porosity, in accordance with the 34% value with diameter

smaller than 10 nm found here. Boulin et al. (2008) also estimated that the porosity not intruded by mercury was equal to 25% of the total one.

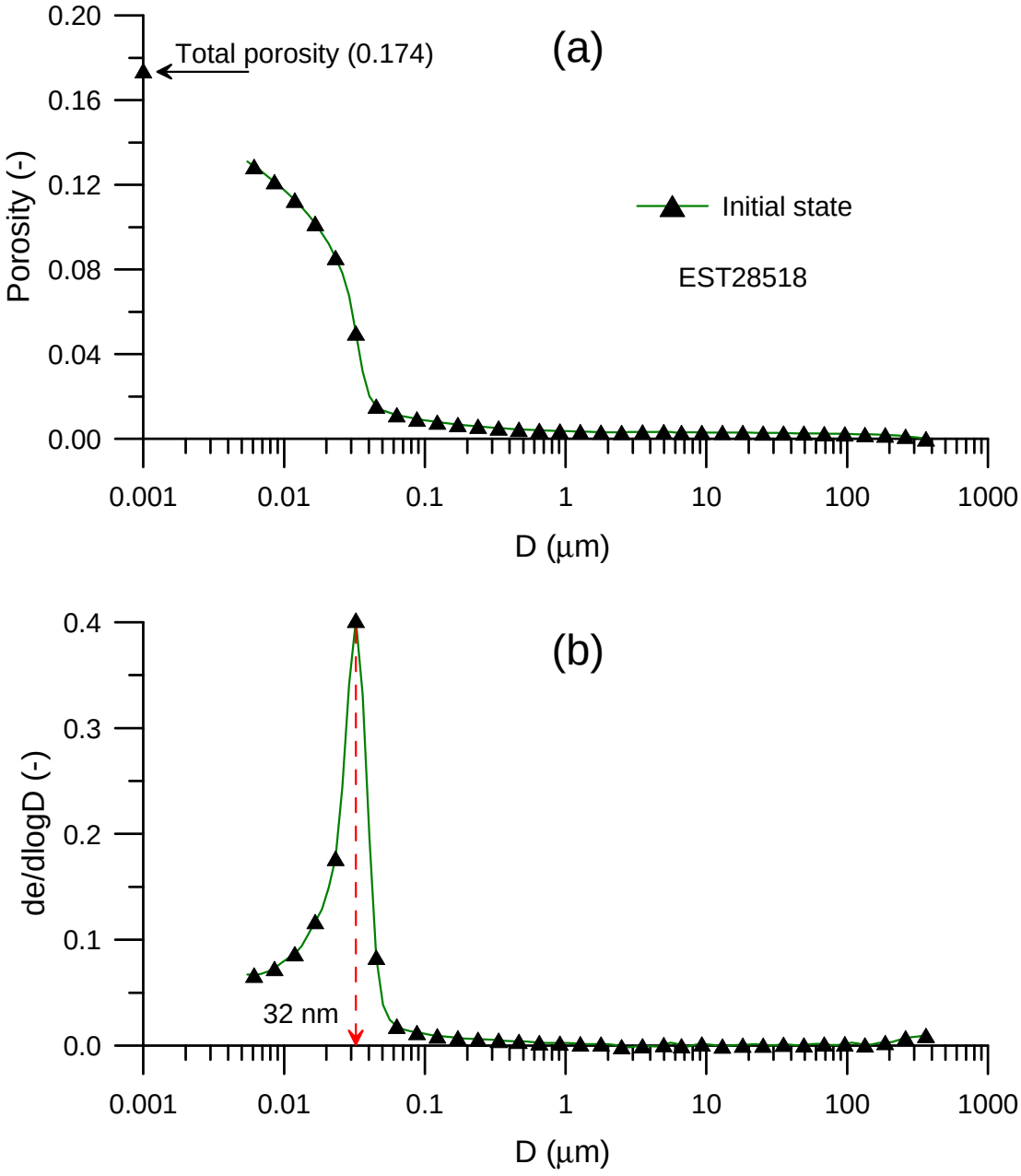

Figure 6. Pore size distribution of the sample EST28518 at initial state.

5.1.2. Compression at 56 and 113 MPa and instantaneous unloading

Figure 7 presents the PSD curves of specimens S1 and S2 (compressed to 56 and 113 MPa, respectively) and unloaded at constant water content, together with the PSD data of the sample at initial state of Figure 6. PSD results are presented in terms of both cumulative

curves (Figure 7a and b) and density function (Figure 7c). In Figure 7a, all curves are plotted starting from the same point at the maximum pore diameter (363.6 µm corresponding to initial pressure of 3.4 kPa). In this plot are also given the total porosities obtained from volume measurements by hydrostatic weighing. The data of Figure 7a confirm that the porosities intruded by mercury are lower than the total porosity of the specimens in all cases (see Table 4).

The total porosities of specimens compressed at 56 and 113 MPa obtained from the compression curves (equal to 13.4 and 9.3%, respectively) are also plotted in the graph. Indeed, the mercury intruded porosities after swelling at constant water content are larger than the total porosity before swelling, confirming the significant changes in microstructure during swelling. The curves of Figure 7a also show that there is an unexpected correspondence between the initial state (w = 6.3%, S_r = 77%) and that after compression at 56 MPa and subsequent swelling at constant water content (w = 6.7%, S_r = 82%). The comparable values of total porosities could be observed from

Figure **3**, but such a similarity in PSD was not necessarily expected. This evidences the difficulty of clearly identifying the effect of compression due to further changes in microstructure due to swelling upon unloading. However, an important conclusion drawn from comparing these curves is that there is no appearance of large pores after constant water content swelling, with no change observed at diameters larger than 500 nm. Swelling hence only mobilized the small porosity population. Further comment in this regard will be made in the discussion session.

When plotting curves with correspondence at the smallest pore detected (Figure 7b), one observes a pretty good superimposition of the cumulative curves for diameters smaller than 20 nm. Inspection of the density function curves of Figure 7c shows that there is a slight difference, with the characteristic pore defined at maximum slightly decreasing in diameter between the intact state and that compressed under 56 MPa. It seems however that there is little difference between the characteristic pores at 56 and 113 MPa, with a value decreasing from 27 to 26 nm, smaller than at initial state (32 nm).It seems that no difference in the PSD curves at 56 and 113 MPa is observed below a diameter of 20 nm.

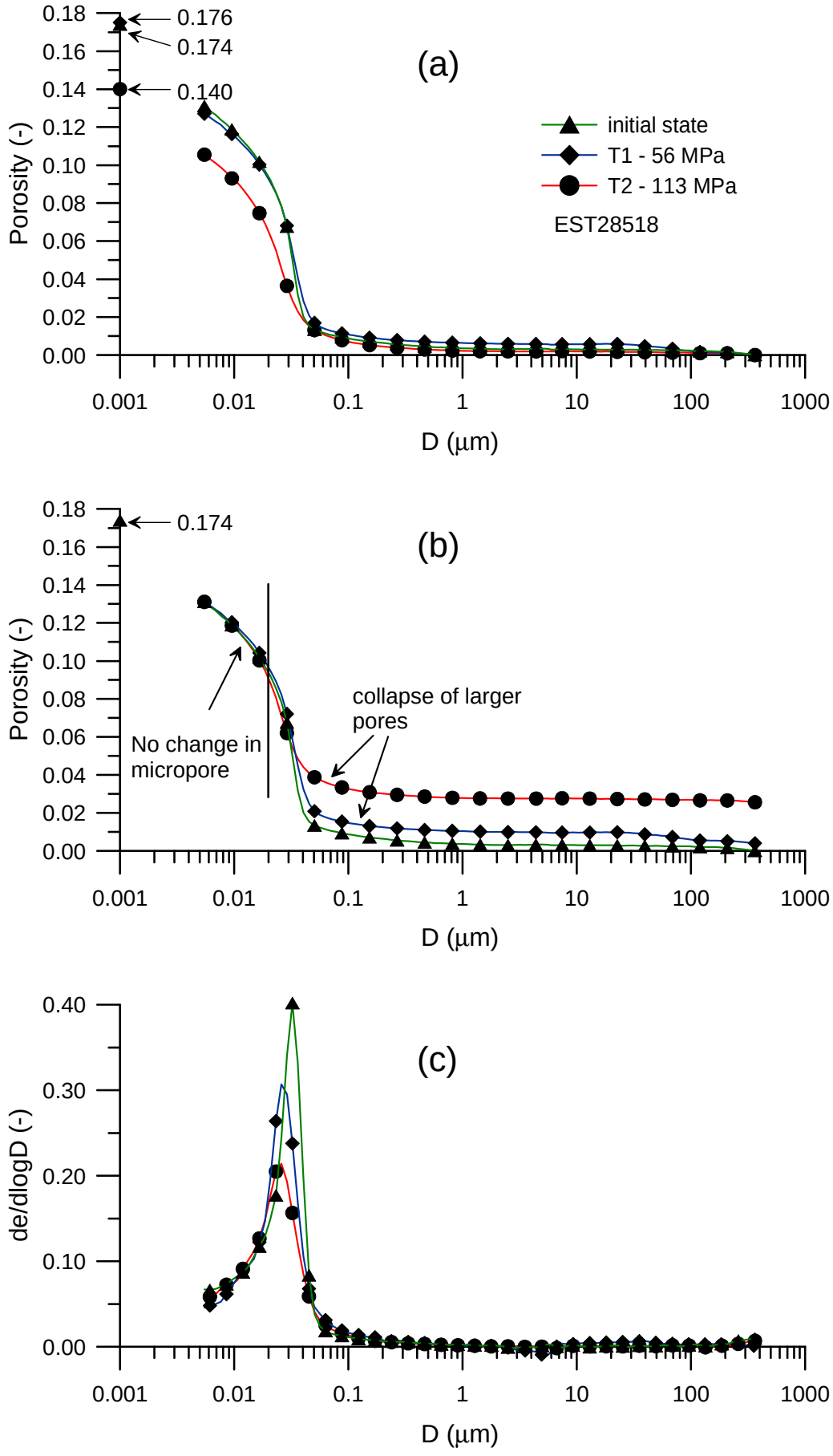

Figure 7. Results of MIP tests on COx claystone specimen of T1, T2 and initial state.

5.1.3. Compression/swelling tests at 56 and 113 MPa, tests T3 and T4

The cumulative PSD at initial state and after compression swelling tests T3 (56 MPa) and T4 (113 MPa) are presented in Figure 8a with correspondence of curves at largest pores, together with the total porosities values. Figure 8b shows the cumulative curves with correspondence at smallest pores and Figure 8c presents the density function curves (with an enlargement of the curves of large pores). The intruded mercury porosity n_{Hg} of T3 and T4 is equal to 16.2 and 18.1%, respectively, corresponding to total porosities of 20.1 and 22.2%, respectively. Data show that the unintruded porosity (diameters smaller than 5.5 nm) of tests T3 and T4 together with that at initial state (n_{Hg} = 13.1 %, n = 17.4%) does not change significantly with little effect of the compression/swelling stage, with values of 3.9% (T3), 4.1% (T4) and 4.3% (initial state).

Unlike specimens T1 and T2 that swelled at constant water content upon stress release (Figure 7), two populations of pores are clearly observed here both in cumulative and density function curves in the almost saturated specimens T3 and T4 after swelling due to water infiltration. The pore size density function (Figure 8) shows that large pore have entrance diameter between 5 and 100 µm for T3 (56 MPa) and up to more than 300 µm (the upper limit of MIP) for T4 (113 MPa). Simultaneously, the small pore population becomes slightly less well defined with a less sharp peak also showing a slight decrease in average radius from 32 nm (initial) to 29 nm (swelling after 56 MPa) and 26 nm (swelling after 113 MPa). This difference also appears in the cumulative curves plotted with correspondence at smallest pores (Figure 8b) with mercury intrusion starting in pores of 90 nm for T3 (56 MPa) and 200 nm for T4 (113 MPa). Little effect of swelling is detected below 20 nm with good superimposition of cumulative curves.

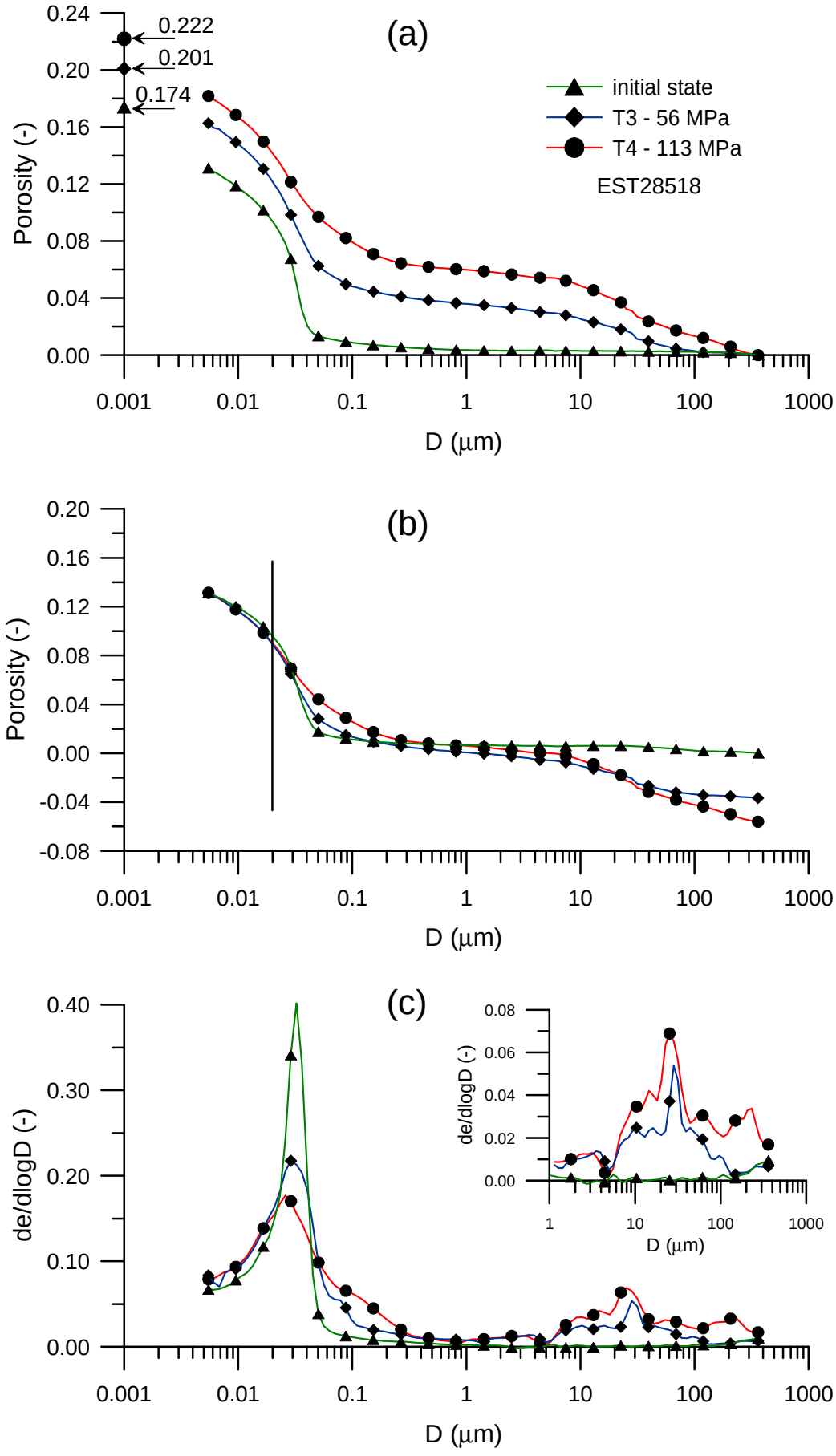

Figure 8. Results of MIP tests on COx claystone specimen of T3, T4 and initial state.

5.2. Scanning electron microscope observations

A series of SEM observations was conducted on freeze-fractured specimens. Figure 9a presents the SEM pictures at low magnitude (see bar scale of 200 µm) on a vertical plane of specimen T4 (113 MPa and swollen) with an enlargement of some area indicated in the Figure 9b and c. The orientation of the bedding plane is also indicated. The lowest magnitude photo (Figure 9a) evidences the presence of long cracks parallel to bedding within a dense clay matrix. Figure 9b provides more detail on a 20 µm wide crack. The clay matrix appears to be quite dense and some detritic inclusions can be observed, although strongly coated by the surrounding clay matrix. Figure 9c shows a zone in specimen T4 with various small cracks parallel to bedding.

An interesting feature of freeze-fracturing is its ability to pull out the grains that are located along the fracture plane and that let their prints in the clay matrix. This is particularly evident in Figure 9c where the prints left by pulled out rounded grains (probably quartz) are clearly evident. This feature evidences the coating of the clay matrix around the detritic grains, providing some doubt about the possibility of having pores at the interface between the clay matrix and the grains, as suggested by Yven et al. (2007). Some agglomerations of pyrite grains are also observed as indicated in the Figure.

The horizontal plane observed in Figure 10 shows that the fracture plane developed along a bedding plane, with clay particles mainly observed from their face. Detritic inclusions are not so apparent because of coating. A network of cracks (with inter-cracks distance between 100 and 200 µm) is also observed, corresponding to the intersection of the crack network with the fracture plane.

The distinction between the matrix and inclusions is somewhat easier in Figure 11 that shows large elongated inclusions on the right side (length between 50 and 100 µm) oriented parallel to stratification and smaller inclusions (left, from 20 to 40 µm) together with some prints left by grains pulled out during freeze-fracturing.

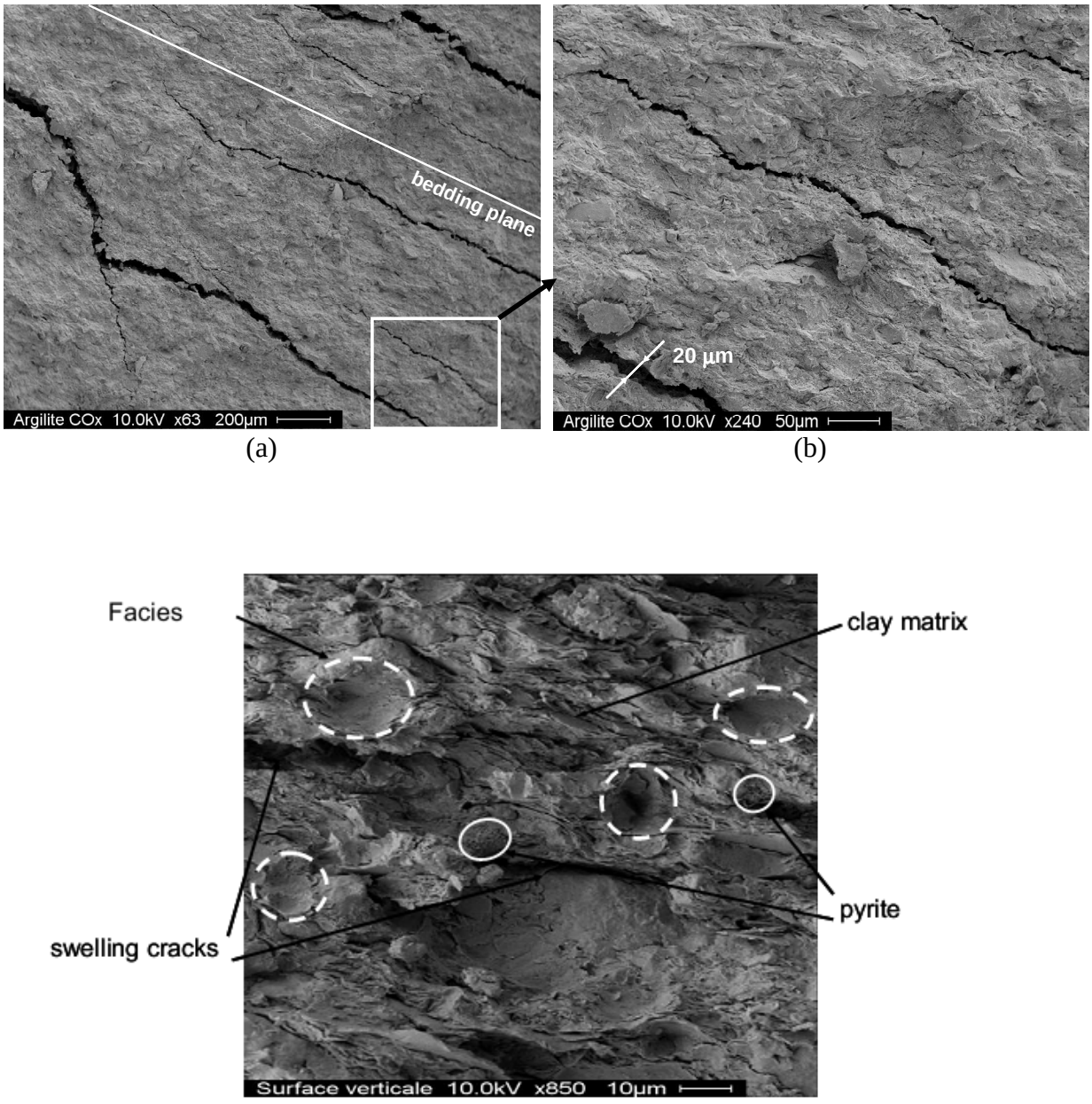

Figure 9. SEM pictures, vertical plane, specimen T4 (113 MPa and swollen)

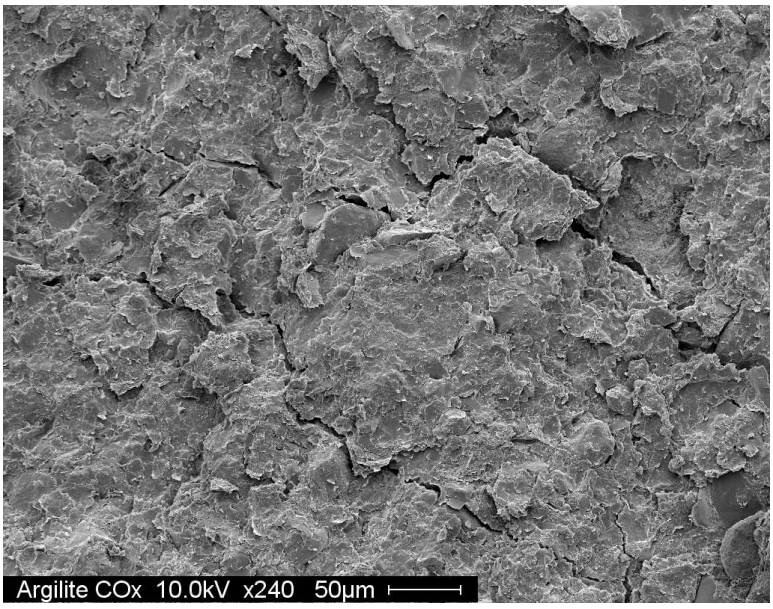

Figure 10. SEM picture of horizontal plane, T4 specimen.

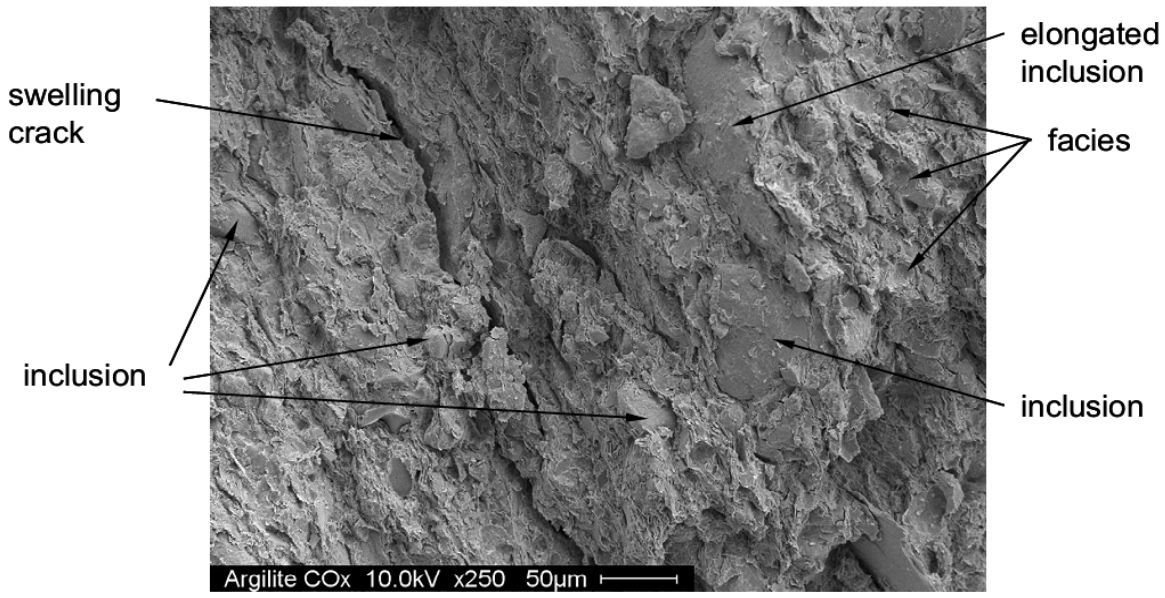

Figure 11. SEM picture of vertical plane, T4 specimen.

6. Discussion

6.1. Initial state

To interpret the microstructure changes due to compression, it was found useful to consider the conceptual model of the COx claystone microstructure proposed by Yven et al. (2007) based on the use various techniques (including scanning electron microscope, autoradiography, mercury intrusion porosimetry, oil, helium and nitrogen adsorption) and presented in Figure 12. The model shows how individual calcite or quartz detritic grains are embedded into a clay matrix (representing 45 – 50% of total constituents at the depth oh 490 m considered here) with interconnected porosity.

The interpretation of the well defined single pore population defined by an average value of 32 nm observed in the PSD curve of Figure 6 can be made by assimilating the clay matrix to an assembly of bricks made up of platelets of comparable thickness, as can be seen inin the scheme of Figure 12. The mean pore radius hence provides an estimate of the average platelets thickness. With an interlayer spacing of 0.96 nm (9.6 Å) typical of smectites and illites and with an average platelet thickness of 32 nm, an average number of around 32 layers by platelets can be roughly estimated, in accordance with data provided by Mitchell and Soga (2005). Of course, larger interlayer spacing could be considered in the case of hydrated smectites within the interstratified illite-smectite layers with one, two, three or more layers of water molecules adsorbed with corresponding thicknesses of 12.6, 15.6 and 18.6 Å (e.g. Mooney et al. 1952).

Fouché et al. (2004) obtained a pore population with a mean diameter of 50 nm on a freeze-dried COx claystone specimen with an initial water of 7.2% (slightly higher than that of the EST28518 specimen). Conversely, Sammartino et al. (2003), Yven et al. (2007) and Boulin et al. (2008) determined a mean diameter of 20 nm on oven dried specimens. It is suspected that the smaller mean diameter values determined on oven dried specimens are related to some shrinkage that does not occur when using freeze-drying, as done here.

Note that in the model of Figure 12, the interstratified illite-smectite swelling minerals are supposed to be located only in some platelets, with a clear distinction between swelling and non swelling platelets, a hypothesis not so easy to confirm. As commented above, the presence of pores at the interface between detritic inclusions and the clay matrix indicated in Figure 12 is not in agreement with the SEM observations carried out here (Figure 9 to Figure 11) in which close contact and coating was observed between the clay

matrix and the grains. This close contact is a mechanical consequence of sedimentation and further vertical stress increase due to burying at great depth.

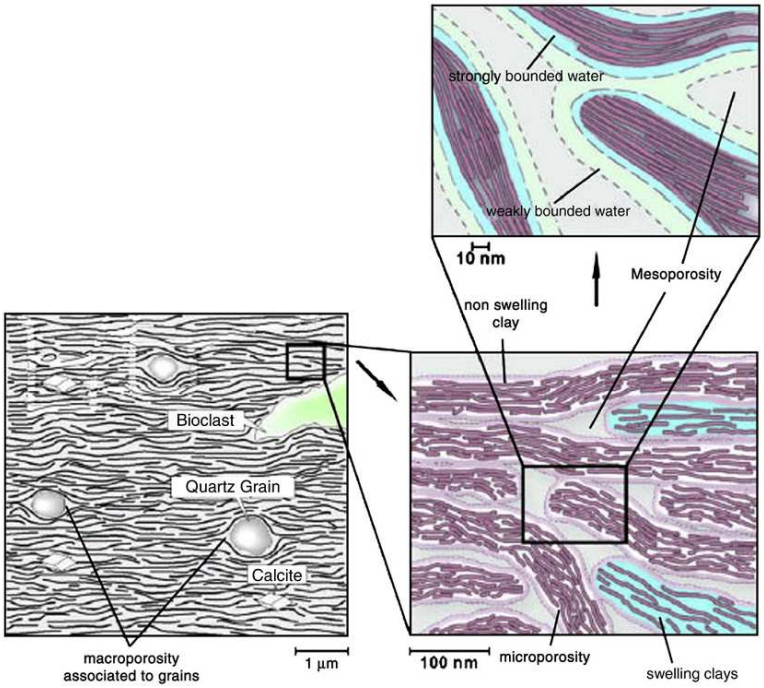

Figure 12. Conceptual model of COx clay microstructure (after Yven et al. 2007)

6.2. Compression behaviour

A significant difficulty in detecting the changes in PSD due to compression is due to the swelling and desaturation due to unloading. This desaturation, that does not occur in fine grained soils under smaller stresses (see for instance Delage et al. 2007 on the Boom clay), is compatible with the value of the final suction (21 MPa for T1), significantly larger than the air entry value of the COx claystone, found between 7 and 9 MPa by De la Vaissière and Talandier (2012) by means of gas penetration tests. To better analyse this desaturation, a specimen saturated at initial porosity with swelling impeded was afterwards unloaded at constant water content, like in tests T1 and T2. The result and interpretation of this test (Delage et al. 2014) showed that the sample also desaturated with swelling at constant water content (w = 8.4%) from a porosity of 17.4 to 21.2% (final degree of saturation of 81% and suction of 21 MPa) with very slight changes of the PSD curve. This showed that swelling at constant water content occurred with an internal water transfer from the initially saturated inter-platelet pores to smaller pores with diameter smaller than 5.5 nm, the lower limit detectable by MIP. Since swelling occurred, the water molecules transferred are likely to

have been attracted and fixed along the faces of the smectites minerals within the interstratified illite-smectite minerals of the clay matrix. The suction value of 20 MPa indicates a rather strong physico-chemical bond between the water molecules and the smectite minerals.

The same mechanism is suspected to also occur during the constant water content swelling observed when releasing stress on saturated specimens compressed at 56 and 113 MPa. Note that the suction measured in the specimen of test T1 after release is equal to 21 MPa and close to that obtained by Delage et al. (2014). This could explain why the PSD curve of specimen T2 (113 MPa) provides a mercury intruded porosity (n_{Hg} = 10.5%) larger than the total porosity that the specimen had under 113 MPa (n = 9.3%). In the same way, this internal water transfer could explain that the final porosity of specimen T1 compressed under 56 MPa (17.6%) is close to that of the initial one (17.4%, increased to 21.2% after unloading at a constant water content of 8.4% as shown by Delage et al. 2014). An interesting conclusion that can be drawn is that, given that all infra-porosities are comparable (see values of $n - n_{Hg}$ in Table 1), the infra-porosity (D < 5.5 nm) of the compressed specimens should be smaller under stress, showing that compression at high stress (56 and 113 MPa) affected some of the water adsorbed along the smectite minerals within the interstratified clay platelets by squeezing it into the interconnected network of inter-platelets pores, thus reducing the interlayer spacing in smectite minerals. In such case, the thickness of the "bricks" (i.e. the platelets) would reduce under compression, resulting in a reduction of the mean pore size characterized by the peak of the density function curve. This observation adds a new mechanism with respect to that described by Mohajerani et al. (2011) who only considered the ordered collapse of pores within a rigid clay matrix to explain the volume decrease during compression. In other words, the clay matrix appears to be somewhat compressible due to water expulsion from the intra-platelet porosity to the inter-platelet one. This reduction in thickness of the platelets would hence tend to reduce the average inter-platelets size, resulting in a shift towards smaller radius of the mean pore diameter observed in the PSD curves and a move leftwards of the peak of the density function curve.

To further analyse the validity of this assumption of collapse of inter-platelet pores according to their size with smaller pores remaining intact, another question arises as to whether the average diameter defined by the peak of the density function curve increased (from a value smaller than 26 nm) or kept constant (at 26 nm) during swelling at constant water content. In such case, the thickness of the "bricks" (i.e. the platelets) would reduce,

resulting in a reduction of the mean pore size identified by the peak of the density function curve.

Some relevant information can be obtained from the work of Wang et al. (2014). By submitting a COx specimen to changes in relative humidity, they observed by using Digital Image Correlation at microscopic level along a drying path a continuous shrinkage of the clay matrix in some areas with also the appearance of some cracks, showing that volume changes were the combination of both a continuous and a discontinuous process. This trend, also observed along wetting path during swelling, could be reasonably extrapolated here under stress changes. In some way, this would complete the first analysis of Mohajerani et al. (2011) about the collapse of pores and the resulting creation of cracks in collapsed zone during compression, by also considering, under such high stresses, a possible compression of the matrix with the mobilization of the water layers adsorbed along the smectite minerals. If this occurred, all interstratified platelets would be compressed with a reduction in thickness that would move the characteristic radius of the PSD at values smaller than the 26 nm detected after swelling. Under such a hypothesis, it seems likely that interstratified illite smectite minerals be scattered along the whole clay matrix and not localized in some specific platelets as illustrated in the conceptual model of Figure 12.

6.3. Swelling behaviour

Compared to the initial state characterized by a monomodal PSD defining a well classified entrance pore diameter representative of inter-particles pores, the swollen state of the specimens clearly exhibited two distinct pore populations, with a new population of very large pores in the range 5 – 300 μm. This pore population develops along a larger diameter range in the case of the specimen previously compressed to 113 MPa compared to that under 56 MPa. SEM observations indicated that these large pores corresponded to the cracks observed on swollen specimens, with thicknesses of the order of 20 μm.

There is also an effect of swelling on the initial pore population around the 32 nm average value, with the sharp peak characterizing the well classified inter-platelets pore population at initial state (with pore diameters between 50 and 5.5nm) becoming smoother and smoother with increased maximum compression stress. Pore diameters range between 90 and 5.5 nm for the 56 MPa specimen up to a larger range between 200 and 5.5 nm for the 113 MPa one. Considering again the bricks model, this indicates that some mutual movements between the bricks resulted in a less ordered arrangement. The appearance of a

wider range of inter-particles pores could also reflect some increase in brick thickness due to increase in the interlayer spacing due to the adsorption of water molecules along the smectites within the interstratified illite smectite minerals. However, changes in interlayer spacing would have involved changes in the infra-porosity smaller than 5.5 nm, which is not the case since the values of the unintruded porosity $n - n_{Hg}$ are almost constant and close to the initial one (Table 3). This is also confirmed by the fact observed in Figure 8b that no change is observed in the PSD curve below a diameter of 20 nm. Another conclusion that can hence be drawn is that the driving force of swelling is probably not resulting from adsorption of layers of water molecules at the interlayer level, but rather between clay platelets by the mobilisation of diffuse double layers in inter-platelet planar pores that are large enough to allow for their development.

6.4. Compression-swelling behaviour

The data obtained here allow to further detail the findings of Mohajerani et al. (2011) with respect to the coupling between damage and swelling, also found in other works on tectonised shales (Carter et al. 2010, Aversa et al. 1993). Indeed, more swelling is observed when more cracks are present. The mechanism of pore collapse proposed by Mohajerani et al. (2011) showed that more cracks are created when collapsing more pores under higher stress. The higher density of cracks at higher stress was identified here by means of MIP with a significantly larger volume of cracks obtained after compression at 113 MPa compared to 56 MPa. Further precision has also been gained about the probable mobilisation of the infra porosity during compression at high stress, and it was shown that swelling did not involve any change in pores of diameter smaller than 20 nm but rather involved diffuse double layer mechanisms within the inter-platelet porosity.

7. Conclusion

To further inspect some conclusions made by Mohajerani et al. (2011), a microstructure investigation on the effects of compression and swelling on the Callovo-Oxfordian claystone was carried out by means of the combined use of mercury intrusion porosimetry and scanning electron microscopy on freeze-dried specimens. To do so, COx specimens were compressed under high stresses (56 and 113 MPa) that were afterwards released in two ways: either at constant water content by avoiding any water exchange with

the specimen when releasing stress or by allowing swelling by water infiltration upon stress release.

The microstructure at initial (unsaturated) state was characterized by a monomodal pore size distribution curve with a mean pore diameter of 32 nm, larger than what was observed (around 20 nm) in previous published data (Sammartino et al. 2003, Boulin et al. 2008) on oven-dried specimens. Based on the standard brick model further elaborated by Yven et al. (2007), this difference was related to the shrinkage of the platelets during oven drying resulting from the expulsion of water molecules located along the smectite minerals within the intra-platelet porosity.

The swelling observed during stress release at constant water content, including on a sample only compressed to a (small) stress aimed at avoiding any swelling during hydration, was interpreted (Delage et al. 2014) by an internal transfer of water molecules from inter-platelet pores to much smaller intra-platelets pores along the smectite minerals, resulting in a crystalline swelling within the interstratified illite smectite minerals. The same phenomenon was observed after (high) stress release, making the analysis of the change in microstructure due to compression more difficult. The interpretation of the changes in pore size distribution evidenced that the compression volume changes could be due to the combined action of pore collapse (with creation of local micro-cracks) and of the expulsion of water molecules adsorbed along the smectite minerals in intra-platelets pores. This interpretation is compatible with Digital Image Correlation analysis at microscopic scale (Wang et al. 2014) that indeed indicated some local shrinkage in the clay matrix under increased suction.

The swelling due to water hydration during stress release appeared to be due to two phenomena. Firstly, the presence of large cracks as wide as 20 µm as observed in SEM and measured in MIP. Such cracks were suspected by Wan et al. (2013) in their study of free swelling when examining the water retention properties of the COx claystone. The PSD curves show that they correspond to 26% and 16% of the intruded mercury volume of the swollen specimen compressed up to 113 and 56 MPa respectively. Secondly, swelling is due to an enlargement of the inter-platelet porosity around the mean value of 32 nm determined at initial state. This pore population is much less well classified after swelling, showing a more disordered assembly of clay platelets within the clay matrix.

The tests carried out in this work have been made at very high stresses, much higher than what is supported by the COx claystone at the level of the Bure URL (490 m). These extreme conditions imposed were however interesting to evidence some micro-mechanisms occurring within the microstructure when submitting the claystone to stress changes, between

the two porosities of the clay matrix, i.e. the inter-platelets porosity (30 nm average diameter) and the intra-platelets pores where the water molecules are adsorbed along the smectites minerals within the inter-stratified illite-smectite platelets. These fundamentals mechanisms help better understand the macroscopic response of the COx claystone, and of other shales, under stress changes.

Acknowledgements

The authors are indebted to Andra, the French Agency for the management of radioactive waste, for funding this work and supporting the PhD work of the first author. Andra also provided the specimens studied.

References

[1] ANDRA (2005). Synthesis argile: evaluation of the feasibility of a geological repository in argillaceous formation. http://www.andra.fr/international/ download/andra-international-en/document/editions/266va.pdf

[2] Aversa S, Evangelista A, Leroueil S, Picarelli L (1993). Some aspects of the mechanical behaviour of structured soils and soft rocks. In: Anagnostopoulos, editor. Geotechnical engineering of hard soils–soft rocks. Rotterdam: Balkema

[3] Bornert M, Vales F, Gharbi H, Nguyen Minh D (2010). Multiscale full-field strain measurements for micromechanical investigations of the hydromechanical behaviour of clayey rocks Strain 46(1): 33–46

[4] Boulin PF, Angulo-Jaramillo R, Daian JF, Talandier J, Berne P (2008). Pore gas connectivity analysis in Callovo–Oxfordian argillite. Applied Clay Science 42: (1–2) 276–283

[5] Carter TG, Castro SO, Carvalho JL, Hattersley D, Wood K, Barone FS, et al (2010). Tunnelling issues with Chilean tertiary volcaniclastic rocks. Mir conference; Problemi di stabilit a nelle opere geotecniche. Capitolo 11, Torino

[6] Davy CA, Skoczylas F, Barnichon JD, Lebon P (2007). Permeability of macro-cracked argillite under confinement: gas and water testing. Physics and Chemistry of the Earth 32(8–14): 667-80

[7] De La Vaissière R, Talandier J (2012). Gas injection tests in the Meuse/Haute Marne underground research laboratory. Proceedings of the Transfert 2012

Conference, Ecole Centrale de Lille Eds, 360–368

[8] Delage P, Pellerin FM (1984). Influence de la lyophilisation sur la structure d'une argile sensible du Quebec. Clay Minerals 19(2): 151–160

[9] Delage P, Lefebvre G (1984). Study of the structure of a sensitive Champlain clay and of its evolution during consolidation. Canadian Geotechnical Journal 21 (1): 21–35

[10] Delage P, Audiguier M, Cui YJ, Howat MD (1996). Microstructure of a compacted silt. Canadien Geotechnical Journal 33(1): 150–158

[11] Delage P, Marcial D, Cui YJ, Ruiz X (2006). Ageing effects in a compacted bentonite: a microstructure approach. Géotechnique 56 (5): 291–304

[12] Delage P, Le TT, Tang AM, Cui YJ, Li XL (2007). Suction effects in deep Boom clay block samples. Géotechnique 57 (1): 239–244

[13] Delage P (2010). A microstructure approach of the sensitivity and compressibility of some Eastern Canada sensitive clays. *Géotechnique* 60 (5), 353-368.

[14] Delage P (2009). Compaction behaviour of clay: discussion. Géotechnique 59 (1), 75-76

[15] Delage P, Menaceur H, Tang AM, Talandier J (2014). Suction effects in deep Callovo-Oxfordian claystone specimen. Géotechnique Letters 3(2), 84-88

[16] Delage P (2014). The oedometer compression curve is a pore size distribution curve in loose structured clays. Proc. TC105 International Symposium on Geomechanics from micro to macro (2), 1251 – 1254, K. Soga et al. eds, CRC Press. Cambridge, UK

[17] Diamond S (1970). Pore size distribution in clays. Clays Clay Miner. 18, 7–23

[18] Escoffier S, Homand F, Giraud A, Hoteit N, Su K (2005). Under stress permeability determination of the Meuse/Haute-Marne mudstone. Engineering Geology 81(3):329–40

[19] Fouché O, Wright H, Le Cléach JM, Pellenard P (2004). Fabric control on strain and rupture of heterogeneous shale samples by using a non-conventional mechanical test. Applied Clay Science 26 (1–4): 367–387

[20] Gaucher G, Robelin C, Matray JM, Négrel G, Gros Y, Heitz JF, Vinsot A, Rebours H, Cassagnabère, Bouchet A (2004). ANDRA underground research laboratory: interpretation of the mineralogical and geochemical data acquired in the Callovian-Oxfordian formation by investigative drilling. Physics and Chemistry of the Earth 29: 55-77

[21] Gillott JE (1973). Methods of sample preparation for microstructural analysis of soil. Proc. 4th Int. Working Meeting on Soil Micromorphology, ed GK Rutherford, Kingston, 143–164

[22] Heitz JF, Hicher PY (2002). The mechanical behaviour of argillaceous rocks – some questions from laboratory experiments. Proc Int Symp Hydromech Thermo-hydromech Behav Deep Argillaceous Rock: 99–108

[23] Lebon P, Mouroux B (1999). Knowledge of the three French underground laboratory sites. Engineering Geology 52: 251–256

[24] Marcial D, Delage P, Cui YJ (2002). On the high stress compression of bentonites. Canadian Geotechnical Journal 39 (4): 812–820

[25] Mitchell JK, Soga K (2005). Fundamentals of soil behaviour. John Wiley New-York

[26] Mohajerani M, Delage P, Monfared M, Tang AM, Sulem J, Gatmiri B (2011). Oedometer compression and swelling behaviour of the Callovo-Oxfordian argillite. International Journal of Rock Mechanics and Mining Sciences 48(4): 606-615

[27] Monfared M, Sulem J, Delage P, Mohajerani M (2012). On the THM behaviour of a sheared Boom clay sample: Application to the behaviour and sealing properties of the EDZ. Engineering Geology 124:47-58

[28] Mooney RW, Keenan AC, Wood LA (1952). Adsorption of water vapor by montmorillonite. II. Effect of exchangeable ions and lattice swelling as measured from X-ray diffraction. J. Am. Chem. Soc. 74: 1371–1374

[29] Pham QT, Vales F, Malinsky L, Nguyen Minh D, Gharbi H (2007). Effects of desaturation-resaturation on mudstone. Physics and Chemistry of the Earth 32: 646–655

[30] Sammartino S, Bouchet A, Prêt D, Parneix JC, Tevissen E (2003). Spatial distribution of porosity and minerals in clay rocks from the Callovo–Oxfordian formation (Meuse/Haute-Marne, Eastern France)—implications on ionics species diffusion and rock sorption capability. Applied Clay Science 23 (1–4): 157–166

[31] Tang CS, Tang AM, Cui YJ, Delage P, Schroeder C, Shi B (2011). A study of the hydro-mechanical behaviour of compacted crushed argillite. Engineering Geology 118: 93–103

[32] Tovey NK, Wong KY (1973). The preparation of soils and other geological materials for the scanning electron microscope. Proceedings of the International Symposium on Soil Structure, Gothenburg, Sweden, 176-183

[33] Tsang CF, Bernier F, Davies C (2005). Geohydromechanical processes in the excavation damaged zone in crystalline rock, rock salt, and indurated and plastic clays in the context of radioactive waste disposal. International Journal of Rock Mechanics and Mining Sciences 42: 109–25

[34] Valès F (2008). Modes de déformation et d'endommagement de roches argileuses profondes sous sollicitations hydro-mécaniques. PhD thesis Ecole Polytechnique : Paris

[35] Valès F, Nguyen Minh D, Gharbi H, Rejeb A (2004). Experimental study of the influence of the degree of saturation on physical and mechanical properties in Tournemire shale (France) Applied Clay Science 26:197–207

[36] Wan M, Delage P, Tang AM, Talandier J (2013). Water retention properties of the Callovo-Oxfordian claystone. International Journal of Rock Mechanics and Mining Sciences 64: 96–104

[37] Wang LL, Bornert M, Héripré E, Yang DS, Chanchole S (2014). Irreversible deformation and damage in argillaceous rocks induced by wetting/drying. Journal of Applied Geophysics 107: 108-118

[38] Wileveau Y, Cornet FH, Desroches J, Blumling P (2007). Complete in situ stress determination in an argillite sedimentary formation. Phys Chem Earth A/B/C; 32(8–14):866–78

[39] Yven B, Sammartino S, Geroud Y, Homand F, Villieras F (2007). Mineralogy texture and porosity of Callovo-Oxfordian claystones of the Meuse/Haute-Marne region (eastern Paris Basin), Mémoires de la Société géologique de France, ISSN 0249-7549, 178: 73-90

[40] Zhang CL, Rothfuchs T (2008). Damage and sealing of clay rocks detected by measurements of gas permeability. Physics and Chemistry of the Earth A/B/C 33 (Suppl. 1):S363–73

[41] Zhang CL (2013). Sealing of fractures in claystone. Journal of Rock Mechanics and Geotechnical Engineering 5:214–220

Further insight into the compression-swelling behaviour of the Callovo-Oxfordian claystone

Hamza MENACEUR, Pierre DELAGE and Jean-Michel PEREIRA

Ecole des Ponts ParisTech, Navier/CERMES, France

1. Introduction

Thanks to their low permeability, high radionuclide retention capability, swelling behaviour and self sealing properties, claystones are considered as possible geological barriers for the storage of high activity radioactive wastes at great depth. In this context, a better physical and theoretical understanding of their swelling behaviour is important. In recent years, the compression-swelling behaviour of claystones has been investigated by several authors (Aversa et al. 1993, Davy et al. 2007, Carter et al. 2010, Zhang and Rothfuchs 2008, Zhang 2013).

Although not so common in rock mechanics, one-dimension oedometer compression appeared to be a simple method to investigate the compression behaviour of claystones. This was done for example by Heitz and Hicher (2002) on a series of claystones that they compressed up to a maximum stress of 100 MPa. More recently, Mohajerani et al. (2011) performed a series of oedometer tests on specimens of the Callovo-Oxfordian (COx) claystone to further investigate their compression-swelling behaviour in relation with microstructure features. They proposed a conceptual model of the change in claystone microstructure during compression based on earlier findings obtained on structured fine-grained soils by Delage and Lefebvre (1984) who found from mercury intrusion porosimetry data that compression occurred by the orderly collapse of the pores of a fragile porous matrix, starting by the largest ones and progressively affecting smaller and smaller ones. In the COx claystone, that also exhibits a well classified pore population with a mean pore diameter between 20 and 30 nm typical of a clay matrix that represents around 50% in mass of the total constituents (Gaucher et al. 2004, Yven et al. 2007, Boulin et al. 2008), collapse is suspected to occur in inter-platelets pores within the clay matrix (Mohajerani et al. 2011).

As observed in structured fine grained soils, the collapse of pores in the COx claystone was then suspected to result in local micro-cracks that afterwards enhanced swelling.

The detailed observation of swelling during stress release after compression at two different maximum stresses (28 and 113 MPa) made by Mohajerani et al. (2011) showed that, under the same stress decrement, larger swelling occurred in the specimen compressed at higher stress. Given that it has been shown (e.g. Davy et al. 2007) that the swelling properties of the COx claystone are generated by the mobilization of smectites minerals within cracks (the reason also of the good self-sealing properties of the claystone, see for instance Zhang and Rothfuchs 2008), the model interpretation is that compression at higher stress results in a denser network of induced micro-cracks that, in turn, result in stronger swelling.

Various evidences of the coupling between damage and swelling in claystones and shales exist. Aversa et al. (1993) performed oedometer compression tests on Italian tectonised shales and observed that samples compressed under higher stresses had greater swelling index, a feature that they related to the presence of discontinuities. Davy et al. (2007) measured a 3 MPa swelling pressure between to half-cylinders obtained by previously submitting a triaxial specimen to a Brasilian tensile test. The relation between swelling and damage has also been evidenced by Carter et al. (2010) from tunnelling in swelling ground. From field observations and laboratory tests, Carter et al. (2010) observed that swelling was highly enhanced in sheared zones. They showed that either natural mechanical disturbance (fault, shear band) or man induced disturbance (excavating-trimming) could break down the bonds that, in normal rock mass, confine the swelling clays from freely expanding. The swelling properties due to discontinuities were also investigated in the extreme case of crushed COx argillite by Tang et al. (2011). Based on oedometer tests, these authors obtained swelling pressures between 1 to 5 MPa, comparable to the data of Davy et al. (2007).

Other evidence of the sensitivity of claystones to changes in stress and water content that may result in damage has been provided by Valès (2008), Bornert et al. (2010) and Wang et al. (2014). By using Digital Image Correlation (DIC) at microscopic scale, they evidenced the appearance of cracks resulting from hydration and swelling under zero stress conditions. The occurrence of swelling and cracks resulting from hydric damage has been also demonstrated by Wan et al. (2013) in a detailed investigation of the water retention properties of the COx claystone. Note also that scanning electron microscope observation

showed that the swelling of the Romainville clay (a stiff clay from the Paris area, France) was clearly due to the development of micro-cracks (Geremew et al. 2009).

In this paper, the methodology used by Mohajerani et al. (2011) is used in an attempt to further understand the compression swelling behaviour of the COx claystone. Various swelling compression tests were carried out with an investigation of the microstructure of the swollen specimens by means of mercury intrusion porosimetry and scanning electron microscope on freeze-dried specimens. Also, careful attention was devoted to the distinction between the elastic and the physico-chemical components of the swelling strain.

2. Materials and methods

2.1. The Callovo-Oxfordian claystone

The COx claystone is a sedimentary rock from the Jurassic period, deposited 155 millions years ago on top of a layer of Dogger limestone that was afterwards covered by an Oxfordian limestone layer. The thickness of the COx layer is about equal to 150 m. The COx claystone is composed of a clay matrix containing detritic grains of quartz and calcite with a mineralogical composition depending on depth, with significant changes in carbonate and clay contents. At the URL depth (490 m), the COx contains 45–50% clay minerals that constitute a matrix in which other detritic components (20–30% carbonates and 20–30% quartz and feldspar) are embedded (Gaucher et al. 2004).

In this study, an oedometer compression test was carried out on a specimen cored perpendicular to the bedding plane at depth of 482 m (specimen EST44581). The initial characteristics of the tested specimen are presented in Table 1 in which other initial characteristics obtained on the specimen core EST28518 are also given. The water content was determined by measuring the initial and final weights of a rock piece before and after drying in the oven at 105°C for 24 hours. The porosity and degree of saturation were calculated from carefully measuring the sample volume by hydrostatic weighing. The initial total suction was determined by using a dew point potentiometer (WP4, Decagon). As seen in Table 1, specimen EST44581 is not fully saturated at initial state with a degree of saturation of 91% corresponding to 15 MPa of suction for a porosity of 16.2%. The degree of saturation of specimen EST28518 is smaller (77%) corresponding to a higher 34 MPa suction. Partial saturation resulted from the combined actions of coring, transport, storage and specimen

preparation. Values of degree of saturation of 77 and 91% are relatively high and indicate satisfactory conservation of the specimens with reasonably low drying.

Table 1. Initial characteristics

Specimen	EST44581	EST28518
Depth (m)	482	479
Water content (%)	6.7	6.3
Dry density (Mg/m^3)	2.18	2.14
Specific gravity (Mg/m^3)	2.6	2.6
Void ratio	0.19	0.21
Porosity (%)	16.2	17.4
Degree of saturation (%)	91	77
Suction (MPa)	15	34

2.2. Experimental techniques

The oedometer tests were carried out on high stress double level arm oedometer able to apply a maximum stress of 113 MPa on oedometer specimens of 38 mm diameter (Marcial et al. 2002). The sample was placed on a metal porous disc connected to two lateral valves to allow satisfactory saturation of the porous disc. Axial displacement was monitored by using an electronic transducer (Mitutoyo) connected to a data acquisition system. A preliminary calibration of the system was performed by running a load cycle along the total stress range (0 – 113 MPa) without any sample so as to account for the effects of the elastic compressibility of the metallic porous disc, of the cell base and of the piston. The vertical calibrated elastic response obtained was subtracted to the total measured compression displacements obtained in all tests.

Particular attention was devoted to the resaturation phase to avoid any further damage due to swelling. Following Mohajerani et al. (2011), the resaturation was conducted by carefully limiting volume changes during water infiltration. To do so, the vertical displacement gauge was manually followed and the specimen was progressively loaded to compensate any swelling with a tolerance fixed at 2 µm. The specimen response is illustrated in Figure 1 that shows that the maximum stress applied to neutralize swelling was 0.97 MPa for EST44581 specimen with an initial degree of saturation of 91% and a suction of 15 MPa. The specimens coming from core EST28518 were saturated following the same procedure. They were saturated at maximum stress between 3.2 and 3.5 MPa with initial degree of saturation of 77% and suction of 34 MPa. This shows that the swelling properties at initial state depends on the initial degree of saturation, the drier the specimen, the larger the suction and the maximum applied stress.

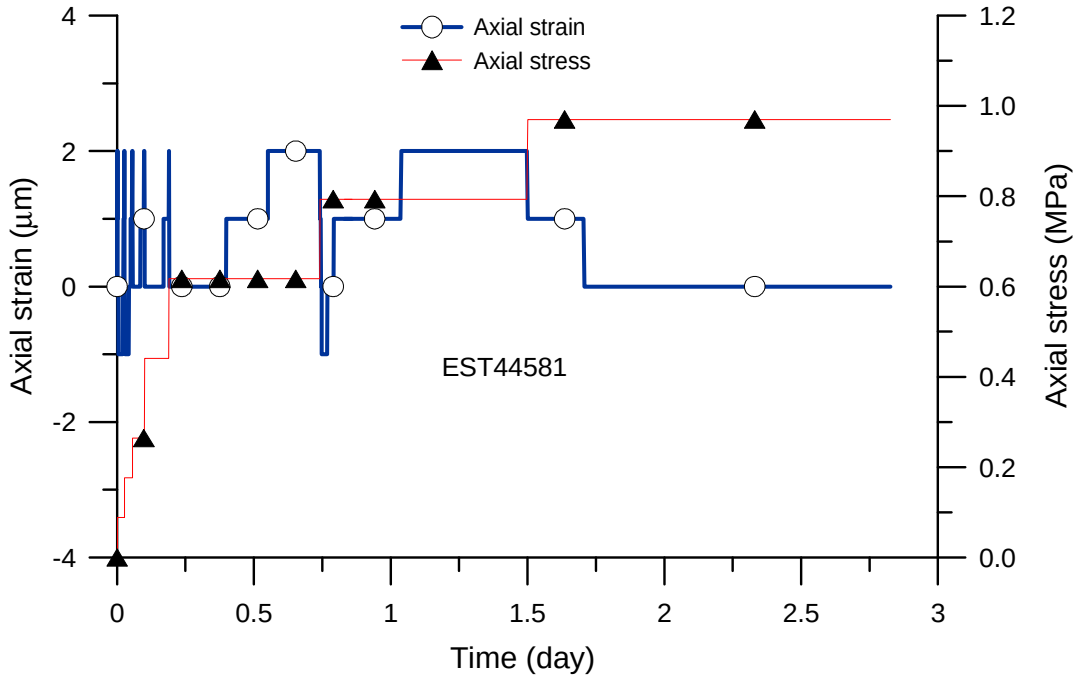

Figure 1. Resaturation process with limited volume change (vertical displacement < 2 µm), EST44581 specimen.

3. The compression-swelling behaviour of the COx claystone

3.1. Compression swelling curves

The results of two compression-swelling tests up to maximum vertical stresses of 56 MPa (test T3) and 113 MPa (test T4) are presented in Figure 2 in terms of axial stress versus axial compression strain either in linear scale (Figure 2a) or semi-log scale of vertical stress as done in standard soil mechanics (Figure 2b). The changes in axial stress and strain with respect to time of test T3 (56 MPa) and T4 (113 MPa) are presented in Figure 3. They provide the details of the step loading and unloading processes and indicate that the duration of loading/unloading steps was around 6 days so as to achieve axial displacement stability (supposed to be satisfactory with a displacement rate of 1 µm/day).

The stress-strain data of Figure 2 are comparable to that of similar oedometer compression tests carried out by Mohajerani et al. (2011) on EST28522 COx specimen of 22% porosity. The compression curve exhibits slight upward curvature along the loading path, whereas the swelling curves are typical of swelling clays, with swelling strain significantly increasing at smaller stresses. The specimen volume, once the stress completely released, becomes larger than the initial one. As commented above, one can observe that for

a given stress decrement (from 60 to 30 MPa or from 30 to 15 MPa), the specimen compressed at 113 MPa exhibits larger swelling strain than that compressed at 56 MPa.

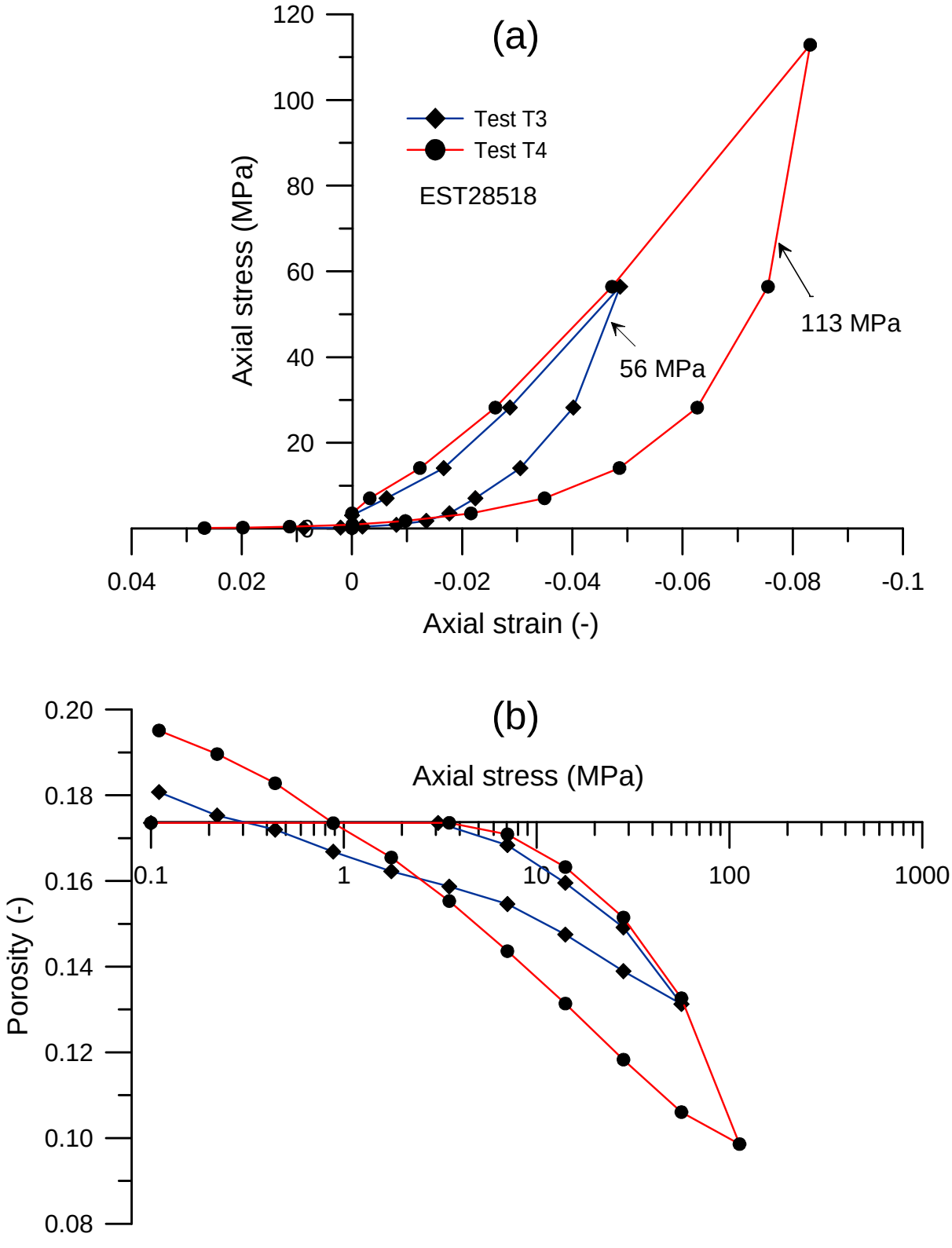

Figure 2. Compression-swelling test on the COx EST28518 specimen.

The detailed observation of the release curves with respect to time of Figure 3 shows that the first release from 113 MPa to 56 MPa stabilizes after a smaller period of time (17 hours) compared to stress releases at smaller stresses that are longer, up to 12 days. This is linked to the fact that very little physico-chemical swelling due to water adsorption along the smectite minerals seems to occur during this first release phase, with strain mainly due elastic rebound. The longer equilibration time observed when releasing stresses in the lower stress range is linked to the mobilisation of physico-chemical swelling, with the adsorption of water molecules along the faces of the smectite minerals. This process is probably governed by the transfer of water from large pores to the swelling sites.

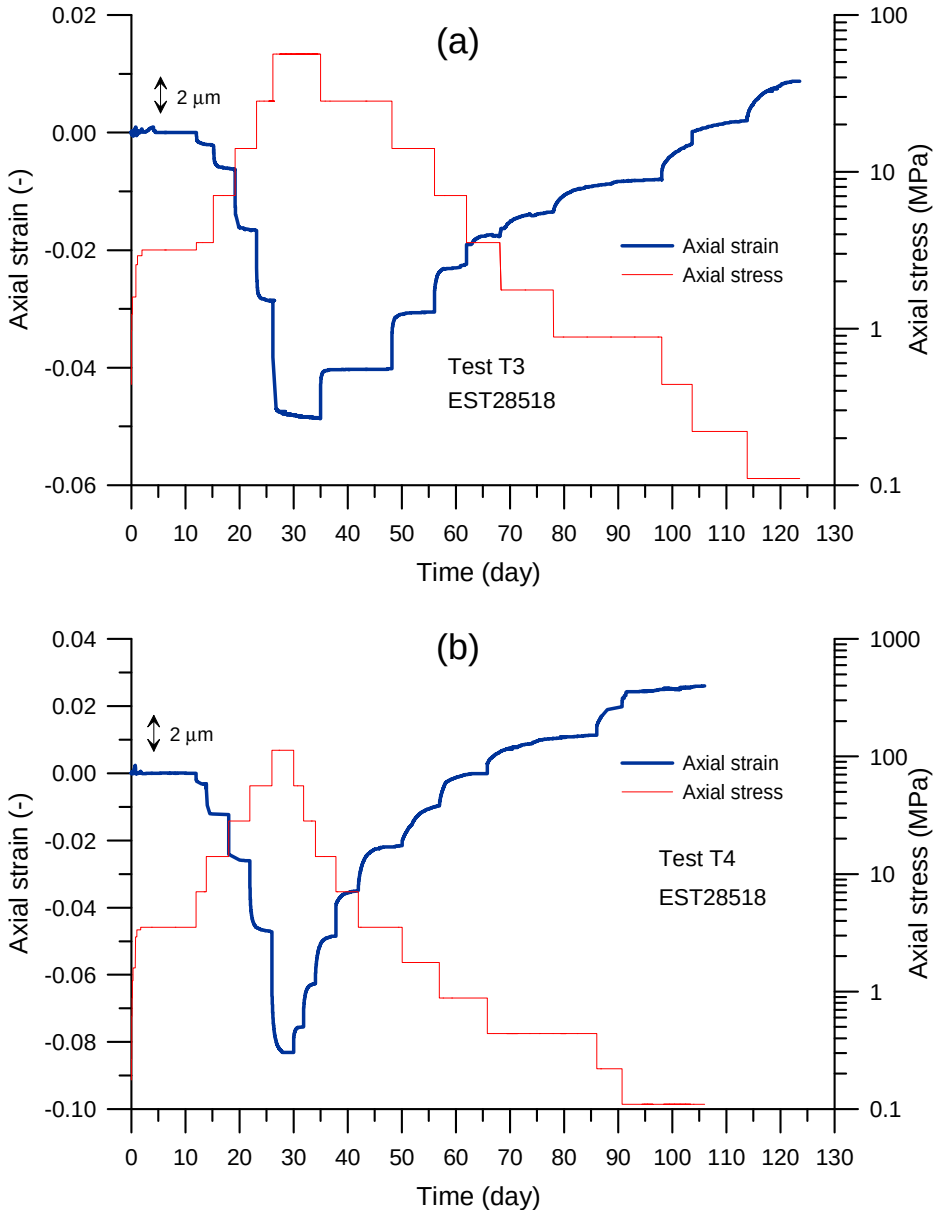

Figure 3. Changes in axial stress and strain with time.

A compression test with various unloading-reloading cycles from stresses of 3.5, 7, 14 and 28 MPa (minimum stress during unloading 0.88 MPa) was carried out on specimen EST44581 (ϕ = 16.2%) and the changes in axial stress and strain with respect to time are plotted in Figure 4. The stress/strain curves are presented in Figure 5a) and b) in linear and semi-log plots, respectively. The upwards curvature of the curve is somewhat more marked than in Figure 2. The cycle from 14 MPa was repeated twice with good repeatability.

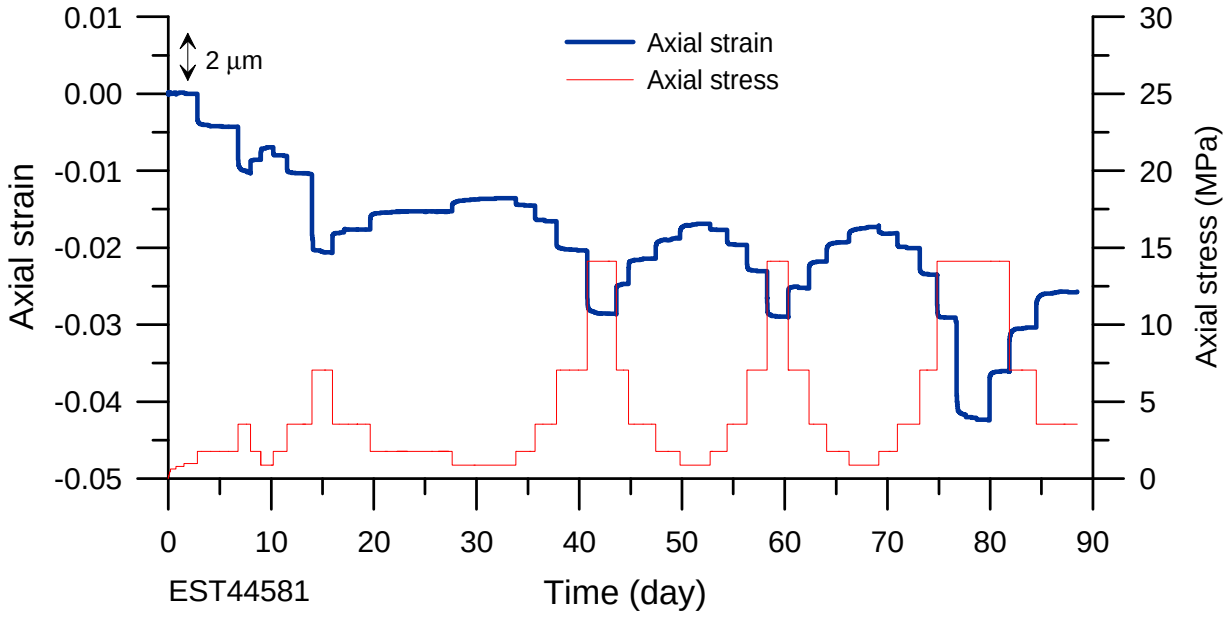

Figure 4. Axial strain and axial stress versus time.

3.2. Microstructure changes due to swelling

The pore size distribution (PSD) curve of the specimen at initial state (porosity 17.4%, suction 34 MPa and degree of saturation 77%) is presented in Figure 6 together with that obtained after compression and swelling at maximum stresses of 56 and 113 MPa. PSD data are presented in terms of both cumulative and density function curves (Figure 6a and b, respectively).

The initial state is defined by a well defined single pore population with an average value of 32 nm, comparable in shape to that observed by Sammartino et al. (2003) and Boulin et al. (2008). Comparison of the mercury intruded porosity (ϕ_{Hg} = 13.1%) with the total one (ϕ = 17.4%) shows that there exist what we call an infra-porosity ($\phi_{infra} = \phi - \phi_{Hg}$)

with entrance diameter smaller than 5.5 nm, the smallest intruded pores when mercury pressure is at maximum value of 227.5 MPa.

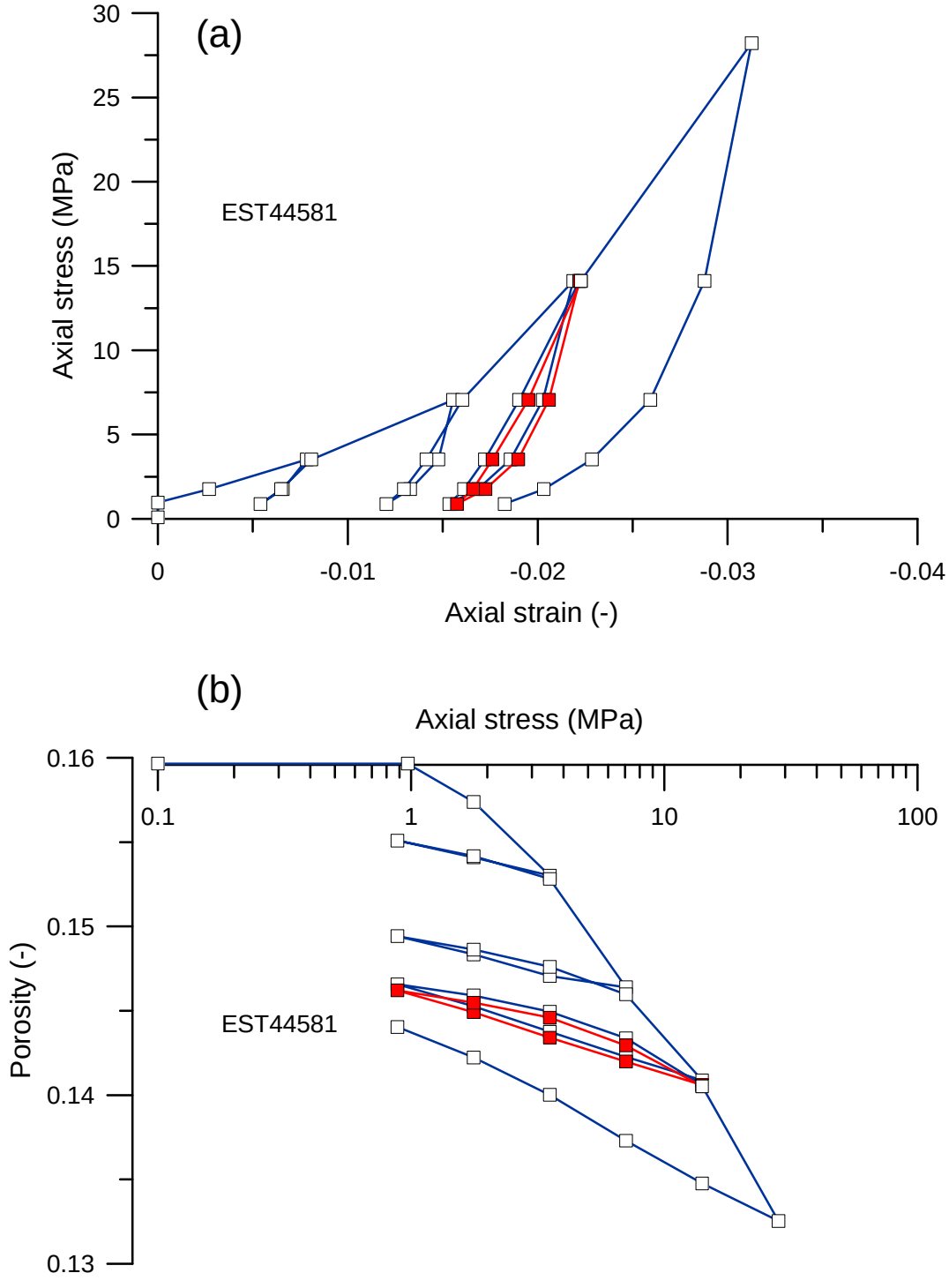

Figure 5. Compression test with stress cycles, EST44581.

Based on a model of the COx microstructure proposed by Yven et al. (2007) in which isolated detritic grains of quartz or calcite are embedded in a clay matrix, the interpretation of the well classified PSD curve of Figure 6 can be made by assimilating the clay matrix to an assembly of bricks made up of platelets of comparable thickness. The mean pore radius hence provides an estimate of the average platelet thickness. With an interlayer spacing of 0.96 nm (9.6 Å) typical of dry smectites and illites and with an average platelet thickness of 32 nm, an average maximum number of around 32 layers by platelet can be roughly estimated, in accordance with data provided by Mitchell and Soga (2005). This number is smaller in hydrated cases given that the interlayer spacing of hydrated smectites then increases.

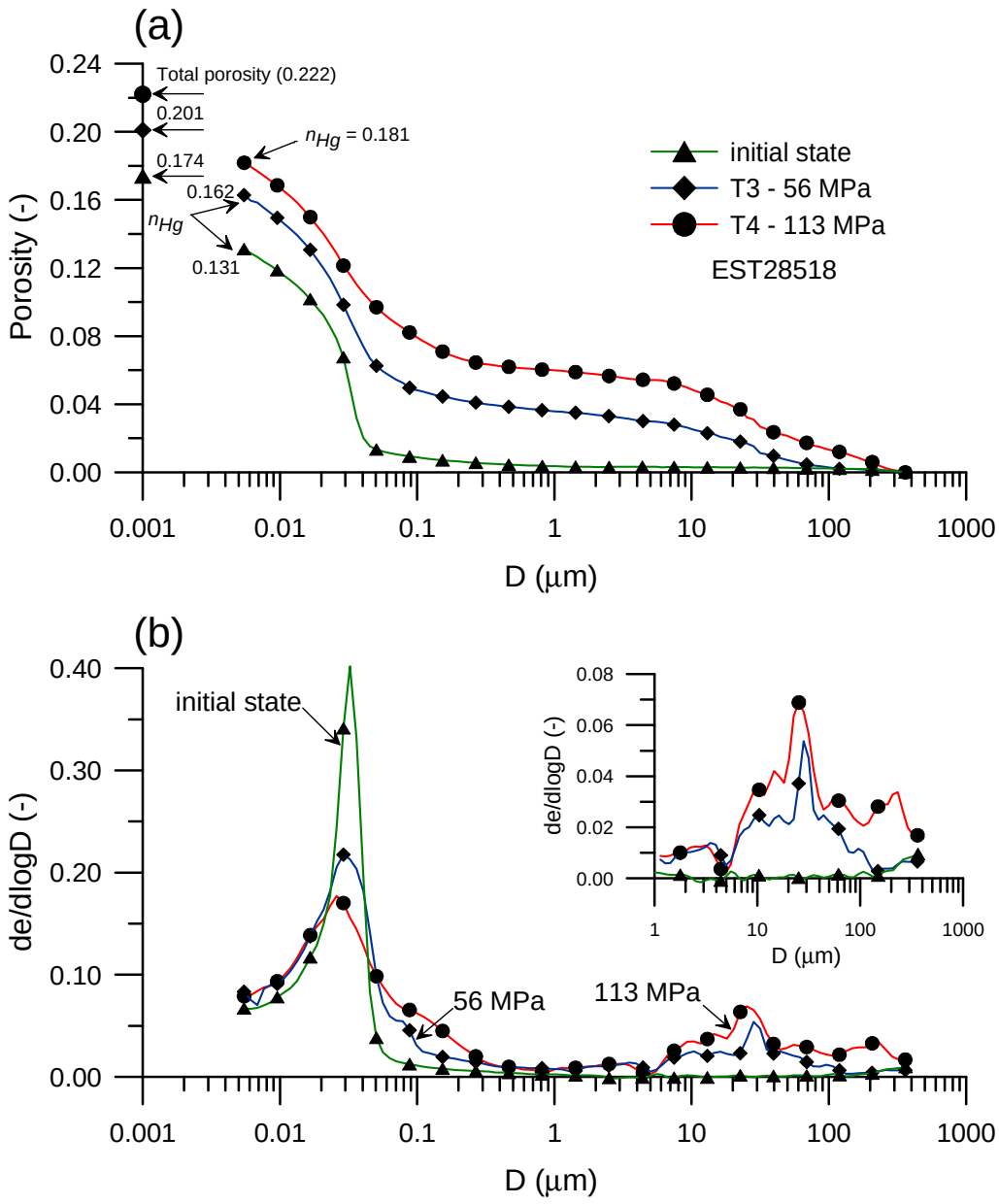

Figure 6. PSD curves, EST28518 : a) cumulative porosity; b) pore size density function

The swollen states (ϕ = 20.1% after compression at 56 MPa and 22.2% after compression at 113 MPa) are characterised by a bimodal pore distribution. There is little changes in small pores with diameter smaller than 20 nm with comparable values of infra-porosity (ϕ_{infra} = 3.9 and 4.1% for 56 and 113 MPa, respectively). The small pores population with mean diameter of 32 nm is less well classified and enlarged with largest diameters of 110 nm at 56 MPa and 290 nm at 113 MPa. More importantly, a new population of large pores appears in the range 45-130 µm at 56 MPa and 45-360 µm at 113 MPa.

As clearly seen in the SEM photo of Figure 7 these large pores correspond to long and continuous cracks that develop along the bedding planes. The PSD curves of Figure 6 indicate that this crack network has larger pore volume in the case of swelling after compression under 113 MPa.

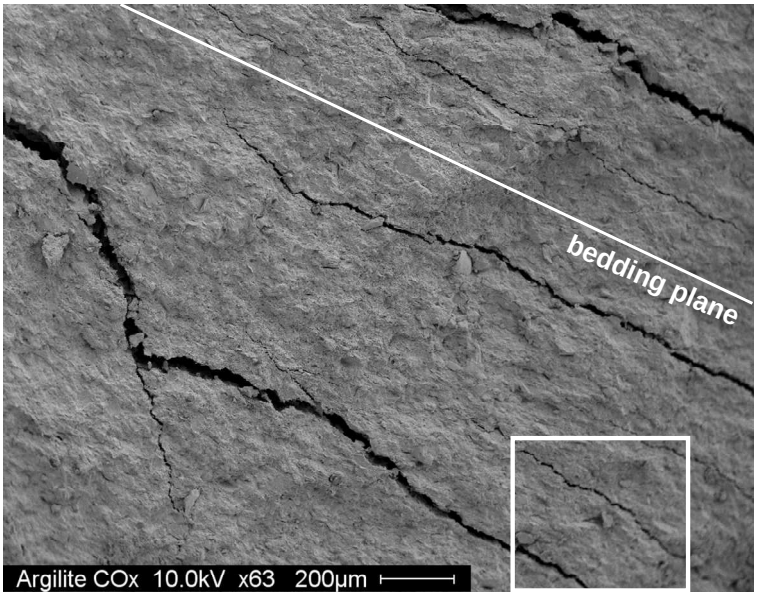

Figure 7. SEM picture of vertical plane, EST28518.

4. Phenomenological expression of the physico-chemical swelling

Previous experimental observations showed that the hydration of micro-cracks plays a role in the swelling of a COx specimen previously compressed, the higher the maximum compression stress, the higher the swelling. A more detailed identification of swelling was made previously with a distinction between elastic rebound and physico-chemical swelling based on both the stress strain curves of the compression tests and the change in strain with respect to time during unloading phases. Figure 8 further illustrates the distinction proposed

between the linear elastic swelling strain increment ε^e determined at the first unloading phase from the highest applied stress, and the physico-chemical swelling strain increment ε^{pc} with the total swelling strain ε given by the relation:

$$\varepsilon = \varepsilon^e + \varepsilon^{pc} \quad (1)$$

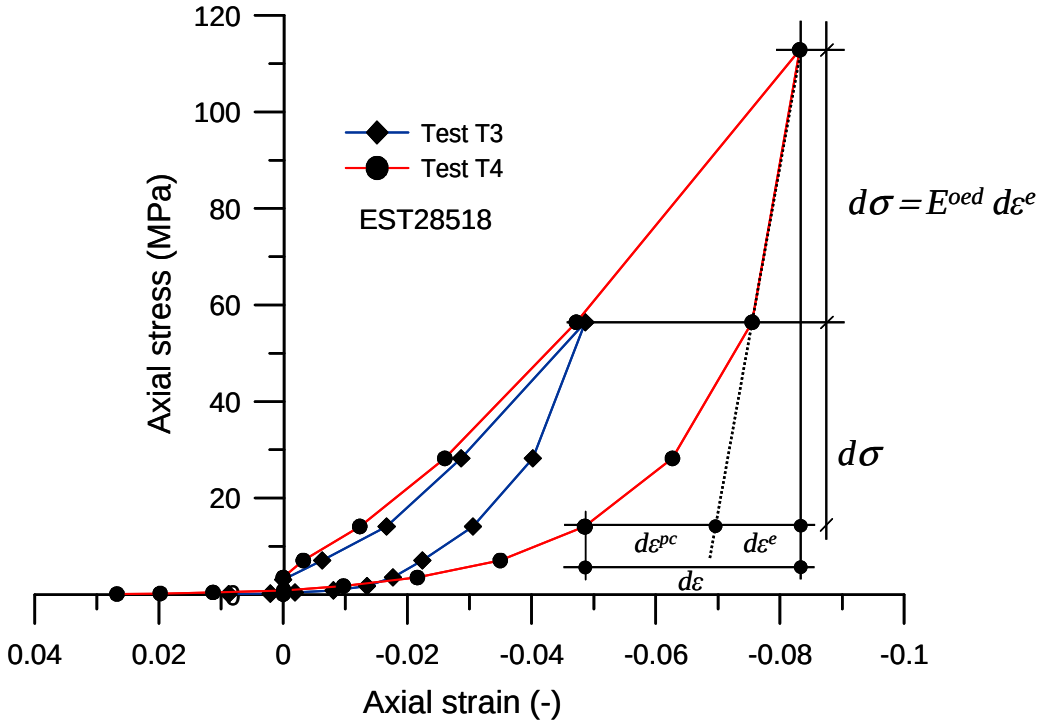

Figure 8. Elastic and physico-chemical swelling strain increment.

The changes in physico-chemical swelling ε^{pc} with stress from the compression tests of Figure 2 and Figure 5 are plotted together in Figure 9 with comparable data taken from compression test on specimen EST28522 with maximum stress of 113 MPa carried out by Mohajerani et al. (2011). There is good agreement between the two tests carried out at 113 MPa, and a regular arrangement of the curves with respect to the maximum stress applied, the smaller the maximum stress, the smaller the physico-chemical swelling. The smaller physico-chemical swelling values at lower stress obtained on specimen EST28522 compared to specimen EST28518 should be related to the difference in the criterion adopted to end a swelling step. In test EST28522, four days were waited for at each unloading step, a shorter period of time criterion that did not allow total mobilisation of the physico-chemical swelling. The larger swelling observed in the two first points could be related to the

difference in porosity between both specimens (22% for EST28522 compared to 17% for EST28518). A more porous specimen has larger clay content, the driving force of swelling.

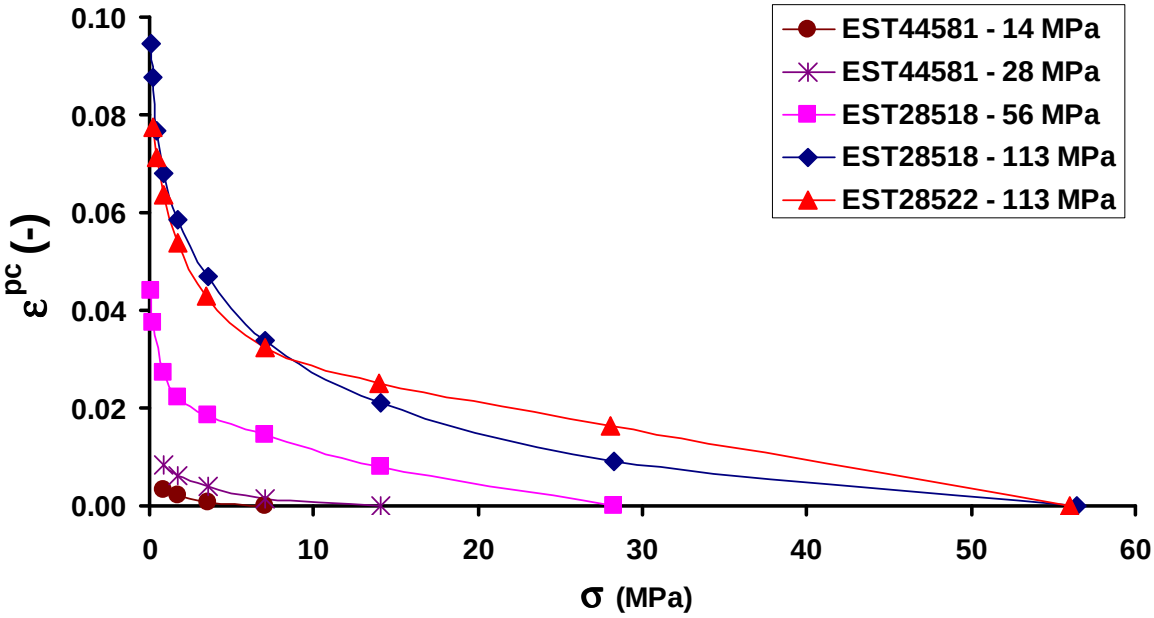

Figure 9. Physico-chemical swelling strain versus axial strain during unloading phase.

The effect of stress on the magnitude of swell can be accounted for by normalising the compression swelling curve with respect to the maximum supported stress σ_{max} as done in Figure 10 in which the data of Figure 2 and Figure 5 are plotted together with that of comparable test carried out with σ_{max} = 113 MPa on specimen from core EST28522 (initial porosity ϕ = 22%) by Mohajerani et al. (2011). The set of normalised curves obtained shows reasonable correspondence along the loading paths for maximum compression stresses of 56 and 113 MPa, with some difference observed on the specimen compressed to 28 MPa. There is also good correspondence between the tests along the unloading paths except for the test at maximum stress of 56 MPa. An average value of the slope α = 4.5 can however be taken for the first unloading path from the maximum stress that defines the elastic rebound ε^e providing the following expression for the elastic rebound:

$$\frac{\sigma}{\sigma_{\max}} = \alpha \frac{\varepsilon^e}{\varepsilon_{\max}} + \beta \qquad (2)$$

with β = -3.5

providing the following stress-strain expression:

$$\sigma = \alpha \frac{\sigma_{\max}}{\varepsilon_{\max}} \varepsilon^{e} + \beta \sigma_{\max} \tag{3}$$

giving the following expression of the oedometer elastic modulus with respect to the maximum stress from which unloading was carried out:

$$E_{oed} = \alpha \frac{\sigma_{\max}}{\varepsilon_{\max}} \tag{4}$$

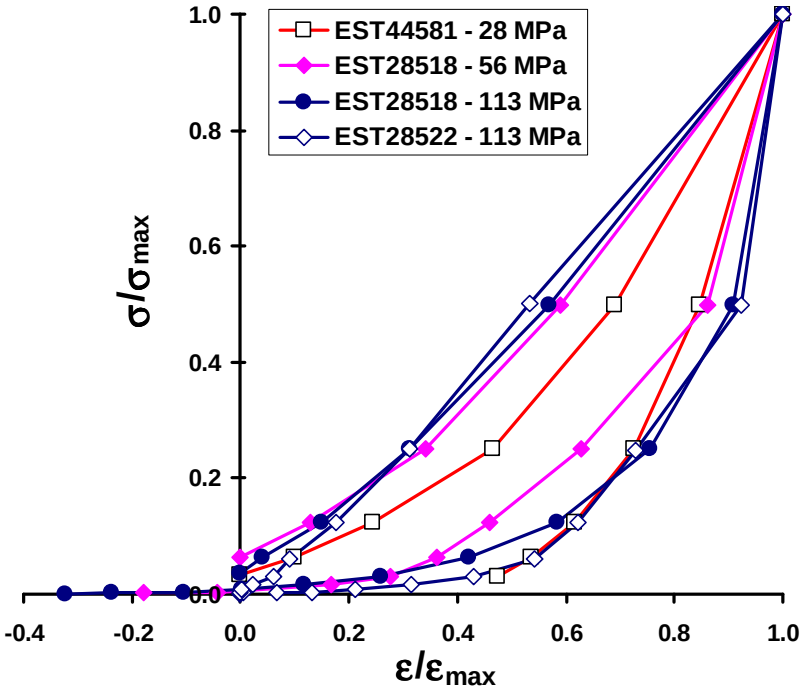

Figure 10. $\varepsilon/\varepsilon_{max}$ versus σ/σ_{max} curves.

The changes in physico-chemical swelling ε^{pc} with respect to stress normalized by the maximum supported stress σ_{max} are presented in Figure 11 in a semi-log diagram. The set of normalised curves show a regular arrangement of the curves with respect to the maximum stress applied, the smaller the maximum stress, the smaller the physico-chemical swelling. As a consequence, the following relation characterising the physico-chemical swelling can be written:

$$\varepsilon^{pc} = C_{spc}(\sigma_{\max}) \log \frac{\sigma}{\sigma_{\max}} \tag{5}$$

where $C_{spc}(\sigma_{max})$ is a coefficient characterizing the slope of the change in physico-chemical swelling with respect to the normalized stress. All the $C_{spc}(\sigma_{max})$ values obtained from Figure 11 are plotted together in Figure 12 with respect to the maximum stress supported. The Figure shows that there is a linear relationship between C_{spc} coefficient and the maximum stress supported: ($C_{spc} = a\sigma_{max} + b$) with $a = 1.44 \times 10^{-4}$ (MPa)$^{-1}$ and $b = -6.37 \times 10^{-4}$, providing the following swelling expression for the physico-chemical swelling strain:

$$\varepsilon^{pc} = (a\sigma_{\max} + b)\log\frac{\sigma}{\sigma_{\max}} \tag{6}$$

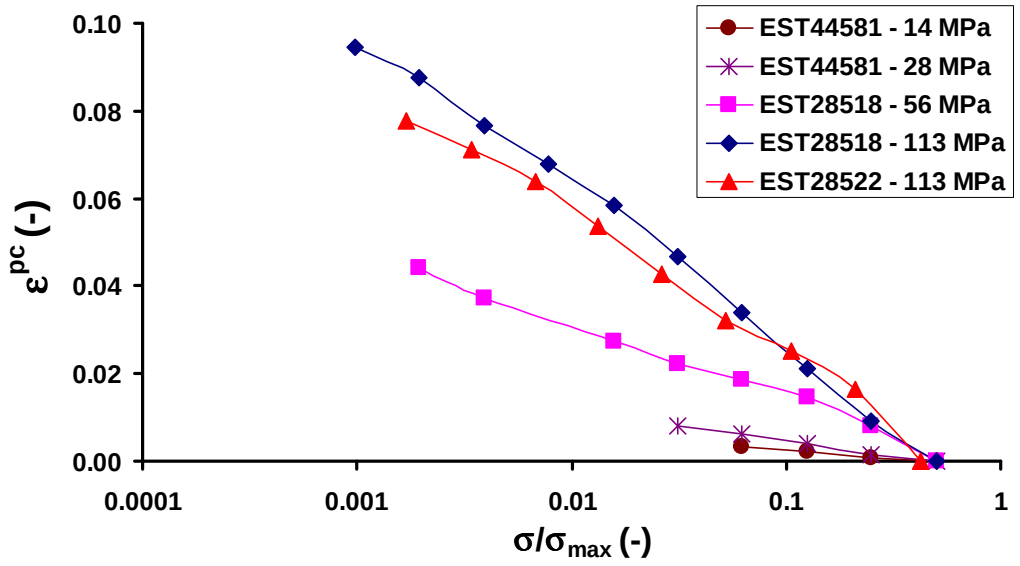

Figure 11. Changes in physico-chemical swelling versus normalized stress.

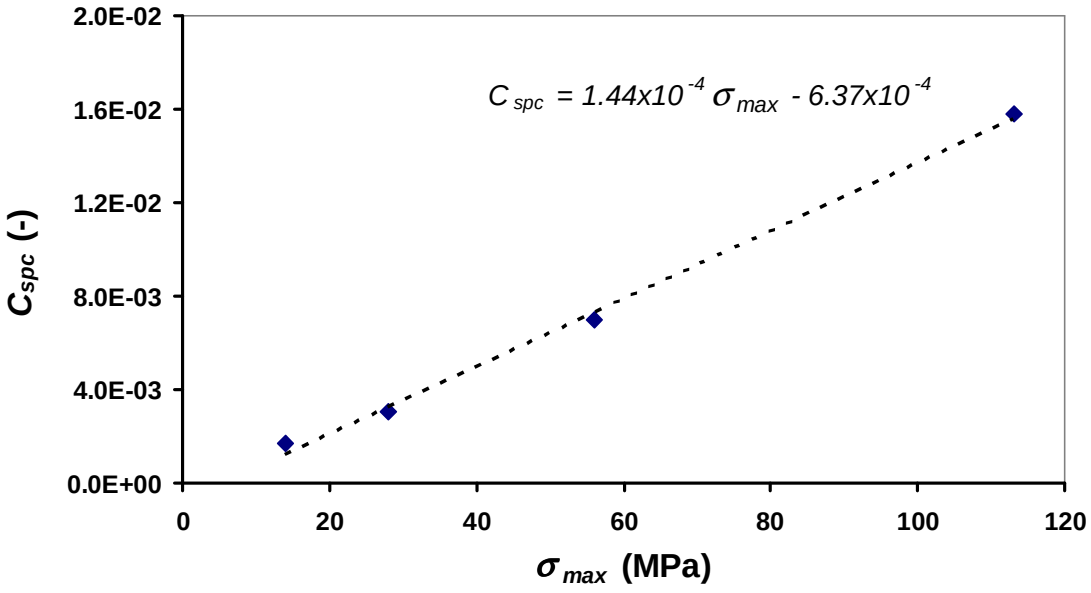

Figure 12. C_{spc} versus the maximum stress supported.

5. Discussion

To better understand the compression swelling behaviour of the COx claystone following Mohajerani et al. (2011), some oedometer compression tests were carried out and complemented by a microstructure investigation by using mercury intrusion porosimetry tests carried out on specimens at initial and swollen states after compression at 56 and 113 MPa. A more detailed analysis of the physico-chemical part of the swelling strain was also made.

The compression-swelling data obtained here were compatible with that of Mohajerani et al. (2011) with comparable shapes of the compression swelling curves and more swelling obtained after compression at higher stress. The MIP and SEM investigations demonstrated that well defined cracks were observed on swollen specimens, with higher swelling corresponding to a larger pore volume of the cracks. At the same time, the well classified pore size distribution around the typical 32 nm pore diameter of the initial state was altered with the development, on the swollen specimens, of larger pores up to various hundreds of nanometers. Note however that it was not possible to directly check here the validity of Mohajerani et al. (2011) concept of progressive and ordered collapse of pores during compression, given the changes in microstructure occurring during stress release and swelling. However, it was interesting to note that two consecutive stress cycles carried out from a maximum stress of 14 MPa were very similar. This indicates that, given that the maximum applied stress of 14 MPa has not been over-passed during the second loading stage, there has not been more damage induced by pore collapse, resulting in a subsequent swelling under unloading similar to the first one.

An idea of the intensity of damage obtained during compression can however be obtained by considering the pore volume corresponding to the cracks in the PSD curves of the swollen specimens (Figure 6). Given that the PSD of pores with diameter smaller than 20 nm does not significantly change, one can conclude that the main effect of swelling is due to the cracks that are more significant after compression under 113 MPa, with a larger pore volume than after compression at 56 MPa. An idea here could be to consider that a larger volume of swollen cracks would result from a larger number of cracks formed by pore collapse.

A detailed examination of the unloading curves made it possible to propose a distinction between the elastic and the physico-chemical components of the swelling strain. The normalisation of the compression swelling curves provided, for all the tests carried out, an expression of the elastic rebound strain with respect to the maximum stress applied. A

simple phenomenological expression of the physico-chemical swelling strain developed with respect to the maximum applied stress was also obtained.

Finally, the question of the physico-chemical nature of the driving force of swelling arises. In cracks, in which the main swelling phenomenon seems to occur, there is a possibility of having the development of diffuse double layer repulsion, given that the inter-platelets distance is large enough. Further investigation accounting for the cations nature and concentration in the pore water and the resulting repulsive actions could help for better understanding the swelling driving force.

6. Conclusion

In this chapter, the swelling behaviour of the COx claystone has been investigated by performing oedometric compression tests, complemented by MIP and SEM analyses to study the evolution of its microstructure. It has been shown that the specimen swell more during unloading if the were previously subjected to a higher stress, the final porosity after unloading being larger than the initial one.

The microstructure investigations allow concluding that the material is damaged during compression. This damage increases with the applied stress and is characterised by the occurrence of cracks that are significantly larger than the characteristic size of natural pores. Upon unloading, the presence of these cracks is certainly responsible for the activation of the swelling of the clay matrix. The more damaged the material initially is, the more it swells.

A simple phenomenological model has been proposed to model the swelling behaviour of the COx claystone. This model distinguishes two components of strains. The first one is a linear elastic strain. The second one accounts for physico-chemical swelling. This second strain component introduces a swelling index that depends on the maximum stress achieved during compression. This modelling approach is a first satisfactory step in the modelling of damage-enhanced swelling of the COx claystone.

Acknowledgements

The authors are grateful for ANDRA (French Agency for Nuclear Waste Management) for funding this research.

References

[1] Aversa S, Evangelista A, Leroueil S, Picarelli L (1993). Some aspects of the mechanical behaviour of structured soils and soft rocks. In: Anagnostopoulos, editor. Geotechnical engineering of hard soils–soft rocks. Rotterdam: Balkema

[2] Bornert M, Vales F, Gharbi H, Nguyen Minh D (2010). Multiscale full-field strain measurements for micromechanical investigations of the hydromechanical behaviour of clayey rocks Strain 46(1): 33–46

[3] Boulin PF, Angulo-Jaramillo R, Daian JF, Talandier J, Berne P (2008). Pore gas connectivity analysis in Callovo–Oxfordian argillite. Applied Clay Science 42: (1–2) 276–283

[4] Carter TG, Castro SO, Carvalho JL, Hattersley D, Wood K, Barone FS, et al (2010). Tunnelling issues with Chilean tertiary volcaniclastic rocks. Mir conference; Problemi di stabilit a nelle opere geotecniche. Capitolo 11, Torino

[5] Davy CA, Skoczylas F, Barnichon JD, Lebon P (2007). Permeability of macro-cracked argillite under confinement: gas and water testing. Physics and Chemistry of the Earth 32(8–14): 667-80

[6] Delage P, Lefebvre G (1984). Study of the structure of a sensitive Champlain clay and of its evolution during consolidation. Canadian Geotechnical Journal 21 (1): 21–35

[7] Delage P (2010). A microstructure approach of the sensitivity and compressibility of some Eastern Canada sensitive clays. *Géotechnique* 60 (5), 353-368.

[8] Delage P (2014). The oedometer compression curve is a pore size distribution curve in loose structured clays. Proc. TC105 International Symposium on Geomechanics from micro to macro (2), 1251 – 1254, K. Soga et al. eds, CRC Press. Cambridge, UK

[9] Gaucher G, Robelin C, Matray JM, Négrel G, Gros Y, Heitz JF, Vinsot A, Rebours H, Cassagnabère, Bouchet A (2004). ANDRA underground research laboratory: interpretation of the mineralogical and geochemical data acquired in the Callovian-Oxfordian formation by investigative drilling. Physics and Chemistry of the Earth 29: 55-77

[10] Geremew Z, Audiguier M, Cojean R (2009). Analysis of the behaviour of a natural expansive soil under cyclic drying and wetting. Bulletin of Engineering Geology and the Environment (68) 3: 421-436

[11] Heitz JF, Hicher PY (2002). The mechanical behaviour of argillaceous rocks – some questions from laboratory experiments. Proc Int Symp Hydromech Thermo-hydromech Behav Deep Argillaceous Rock: 99–108

[12] Marcial D, Delage P, Cui YJ (2002). On the high stress compression of bentonites. Canadian Geotechnical Journal 39 (4): 812–820

[13] Menaceur H, Delage P, Tang AM, Talandier J (2014). A microstructure investigation of the compression-swelling behaviour of shales: the case of the Callovo-Oxfordian claystone. Engineering Geology. (submitted)

[14] Mitchell JK, Soga K (2005). Fundamentals of soil behaviour. John Wiley New-York

[15] Mohajerani M, Delage P, Monfared M, Tang AM, Sulem J, Gatmiri B (2011). Oedometer compression and swelling behaviour of the Callovo-Oxfordian argillite. International Journal of Rock Mechanics and Mining Sciences 48(4): 606-615

[16] Tang CS, Tang AM, Cui YJ, Delage P, Schroeder C, Shi B (2011). A study of the hydro-mechanical behaviour of compacted crushed argillite. Engineering Geology 118: 93–103

[17] Valès F, Nguyen Minh D, Gharbi H, Rejeb A (2004). Experimental study of the influence of the degree of saturation on physical and mechanical properties in Tournemire shale (France) Applied Clay Science 26:197–207

[18] Valès F (2008). Modes de déformation et d'endommagement de roches argileuses profondes sous sollicitations hydro-mécaniques. PhD thesis Ecole Polytechnique : Paris

[19] Wan M, Delage P, Tang AM, Talandier J (2013). Water retention properties of the Callovo-Oxfordian claystone. International Journal of Rock Mechanics and Mining Sciences 64: 96–104

[20] Wang LL, Bornert M, Héripré E, Yang DS, Chanchole S (2014). Irreversible deformation and damage in argillaceous rocks induced by wetting/drying. Journal of Applied Geophysics 107: 108-118

[21] Yven B, Sammartino S, Geroud Y, Homand F, Villieras F (2007). Mineralogy texture and porosity of Callovo-Oxfordian claystones of the Meuse/Haute-Marne region (eastern Paris Basin), Mémoires de la Société géologique de France, ISSN 0249-7549, 178: 73-90

[22] Zhang CL, Rothfuchs T (2008). Damage and sealing of clay rocks detected by measurements of gas permeability. Physics and Chemistry of the Earth A/B/C 33

(Suppl. 1):S363–73

[23] Zhang CL (2013). Sealing of fractures in claystone. Journal of Rock Mechanics and Geotechnical Engineering 5:214–220

Chapitre 3 : Comportement thermo-mécanique de l'argilite du Callovo-Oxfordien

Introduction

L'argilite du Callovo-Oxfordien (COx) sera soumise à des sollicitations couplées: variation de contrainte lors de l'excavation des galeries et variation de température due à la nature exothermique des déchets, ce qui rend nécessaire l'étude de son comportement thermo-mécanique couplé pour une meilleure compréhension de la réponse du champ proche au voisinage des galeries et des alvéoles de stockage.

Les données sur la réponse thermique des argilites sont rares dans la bibliographie. Des investigations sur le comportement déviatorique de l'argilite du COx à l'aide d'essais triaxiaux ont été réalisées par différent auteurs. Actuellement, les données publiées concernant les propriétés mécaniques apparaissent dispersées à cause d'une part de la variabilité naturelle des propriétés de l'argilite du COx avec en particulier la variation de la composition minéralogique avec la profondeur. D'autre part, les différences entre les méthodes expérimentales adoptées et plus précisément entre certains paramètres caractéristiques des essais, notamment la taille d'éprouvette, les conditions de drainage, le degré de saturation et la vitesse de cisaillement, ont aussi des effets sur la variabilité des résultats.

Dans ce chapitre, on présente les résultats d'une série d'essais drainés réalisés au triaxial à cylindre creux (Monfared et al. 2011) à deux températures différentes (25 et 80°C) sur des échantillons saturés avec soin sous contrainte in-situ. L'éprouvette cylindrique creuse a un diamètre intérieur de 60 mm, extérieur de 100 mm, une hauteur de 70-80 mm et un chemin de drainage court correspondant à la demie épaisseur du cylindre, soit 10 mm. Le programme expérimental réalisé est destiné à étudier l'effet de la température sur la résistance au cisaillement et sur les changements de volume en conditions saturées et drainées dans l'argilite du COx. Des essais de perméabilité radiale ont été également effectués à 25 et 80°C afin d'avoir une meilleure compréhension de l'effet de la température sur la perméabilité.

Ce travail a été soumis dans la revue «*International Journal of Rock Mechanics and Mining Science*», on reproduit dans ce chapitre l'article dans sa version en anglais.

On the thermo-mechanical behaviour of the Callovo-Oxfordian claystone

Hamza MENACEUR[1], Pierre DELAGE[1], Anh-Minh TANG[1], Nathalie CONIL[2]

[1] *Ecole des Ponts ParisTech, Navier/CERMES, France*

[2] *Andra, Bure, France*

Abstract

The Callovo-Oxfordian (COx) claystone is considered as a potential host rock in the French concept of high level radioactive waste disposal at great depth. To better understand and to complement existing published data on the thermo-hydro-mechanical behaviour of the COx claystone, an experimental program was carried out by using a hollow cylinder triaxial device specially developed for low permeability materials. Special care was devoted to the saturation of the specimens that was made under stress conditions close to in-situ, and to conditions ensuring full drainage thanks to a reduced drainage length and low shear rate. Tests were carried out under in-situ, half to in-situ and twice the Terzaghi mean effective in-situ stress at 25°C and 80°C to investigate the effects in the close field of the temperature elevation due to the exothermic nature of the waste. Some radial permeability tests were conducted at various temperatures. The data obtained showed that there is little effect of temperature on the elastic parameters determined, whereas a tendency to a decrease in shear strength was noted, compatible with the few published data. Temperature also appeared to have little effect on the intrinsic permeability, with higher flows mainly due to the decrease in water viscosity.

Keywords

Claystone · Permeability · Excavation damaged zone · Shear band · Undrained heating · Self sealing.

1. Introduction

In many countries (including Belgium, France and Switzerland), deep argillaceous formations are considered as potential host rock for the disposal of high activity radioactive waste at great depth. Because of low permeability, good self sealing properties and ability to retain radionuclides, the Callovo-Oxfordian (COx) claystone has been selected in France as potential host rock by Andra, the French agency for the management of radioactive waste. Andra developed an Underground Research Laboratory [1] in the COx layer at a depth of 490 m near the village of Bure (East of France) to perform in-situ investigations devoted to various aspects of radioactive waste disposal, including the thermo-hydro-mechanical response of the host rock in the close field, in configurations close to that prevailing during the operational phase of the waste disposal [1].

In the French concept, the canisters containing the radioactive waste are to be placed in disposal cells that consist in horizontal cased microtunnels of 70 cm in diameter and at least 80 m in length. Due to the exothermic nature of radioactive wastes, the rock in the close field and the excavation damaged zone (EDZ) around disposal cells and galleries will be submitted to a temperature elevation. A maximum temperature of 90°C at the cells wall is considered in the French concept, a condition that has obvious economic consequences in terms of both the density of the network of gallery and disposal cells and the number of canisters that can be placed along a given length of excavated disposal cell.

Various investigations have been carried out on the thermal behaviour of clays but that of claystones is much less documented. In clays, the importance of the overconsolidation ratio has clearly been emphasized, with significant effects in volume change and shear strength response [1, 2, 3, 4, 5, 6].

Various investigations have been carried out about the hydro-mechanical behaviour of the COx claystone based on triaxial tests [7, 8, 9, 10, 11]. Actually, published data on the shear strength properties of the COx claystone appear to be somewhat dispersed partly due to the natural variability of the properties of the claystone. The mineralogical composition of the COx claystone changes with depth, in particular in terms of clay and calcite content. The depth of 490 m at which the Bure URL has been excavated corresponds to a maximum clay content of around 50%, selected to ensure the best isolating properties in terms of low permeability, self-sealing and radionuclides retaining ability.

Another possible reason of the observed dispersion of the published mechanical characteristics of the COx is related to the various testing methodologies adopted. A first

important parameter is the specimen size that obviously controls the easiness and the period of time necessary to fully saturate specimens. Claystone specimens can be significantly desaturated due to the consecutive effects of coring, core isolation from evaporation, core transportation and storage and, finally, machining in the laboratory. Claystones are very sensitive to changes in water content and triaxial tests carried out at various degrees of saturation evidenced a significant increase of the mechanical strength with lower degree of saturation [8, 9, 12, 13, 14].

Another parameter largely dependent on the specimen size is the quality of the drainage ensured during triaxial testing. Due to the very low permeability of claystones (around 10^{-20} m^2 for the COx claystone), fully drained tests that are necessary for a sound determination of their intrinsic mechanical characteristics are difficult to achieve [15]. Good drainage can be ensured either by adopting slow enough shearing rate or by adopting testing devices with small drainage length. This can be made either by testing small specimens or by adopting specimen shapes with reduced drainage length [15, 16, 11]. These aspects will be commented in more details later.

In this paper, fully saturated and fully drained triaxial thermal tests were carried out on COx specimens by using a hollow cylinder thermal triaxial device with short drainage length specially developed for low permeability geomaterials [16]. This thermal device has already successfully been used to test the Boom clay from Belgium [17], the Opalinus clay from Switzerland [18] and the COx claystone from France [19]. The experimental program carried out here was aimed at further investigate the effects of temperature on the shear strength response of the COx claystone by comparing tests carried out at 80°C with tests run at 25°C, following the work of Mohajerani et al. [19] on thermal volume changes. Triaxial tests were complemented by constant head radial permeability tests run at both temperatures to investigate the effects of temperature on permeability.

2. The Callovo-Oxfordian claystone

2.1. Mineralogical composition

The COx claystone is a sedimentary rock deposited 155 millions years ago on top of a layer of Dogger limestone that was afterwards covered by an Oxfordian limestone layer. The thickness of the COx layer is about equal to 150 m. The COx claystone is composed of a clay matrix containing some grains quartz and calcite with a mineralogical composition

depending on depth with significant changes in carbonate and clay contents. At the depth of the Bure URL (490 m), the average mineralogical composition of COx claystone is as follows [20]: 45-50% clay fraction composed of 10-24% interstratified illite/smectite layers, 17-21% illite, 3-5% kaolinite, 2-3% chlorite. The claystone also contains 28% carbonate, 23% quartz and 4% other minerals (feldspars, pyrite, dolomite, siderite and phosphate minerals). The total porosity varies in the COx layer between 14% in carbonated levels and 19.5% in the more argillaceous levels [21].

The characteristics of the specimens tested are presented in Table 1. Specimens come from various cores named EST45414 (specimen S1, depth 498 m), EST30734 (S2, depth 612 m) and EST285nn (S3-S4, depth 479 m) and EST45407 (S5, depth 499 m). These cores have been extracted at distinct locations. They were selected because they are located approximately at the same level in the claystone layer. Specimen S1 and S5 have a porosity between 13 and 13.5% and a water content around 2.2% corresponding to degrees of saturation between 38 and 39%. A suction of 109 MPa was measured in specimen S1 by using a WP4 dew-point tensiometer. Specimens S2, S3 and S4 have larger porosity between 16.5 and 17.8%, higher water content of around 6% corresponding to degrees of saturation between 80 and 85%. The suctions of specimens S2 and S4 are equal to 31 and 34 MPa, respectively.

Table 1. Initial characteristics of the tested specimens.

Specimen	Ref. Core	Depth (m)	Height (mm)	Water content (%)	Dry unit mass (Mg/m^3)	Porosity (%)	Degree of saturation (%)	Suction (MPa)
S1	EST45414	498	73.13	2.11	2.35	13.0	38	109
S2	EST30734	612	73.95	5.88	2.26	16.5	80	31
S3	EST28514	477	75.00	6.76	2.21	17.6	85	-
S4	EST28518	479	71.02	6.10	2.20	17.8	80	34
S5	EST45407	499	72.60	2.27	2.34	13.5	39	-

2.2. Shear strength and thermal effects in the COx claystone

Published data about the shear properties of the COx claystone determined by running triaxial tests are variable. This is due to the natural variability observed in the COx claystone layer. The specimens tested do not necessarily come from the same borehole location or from the same depth whereas the mineralogical composition of the claystone is dependent upon the depth at which the specimen has been cored. For instance, specimens with higher calcite content and smaller clay content extracted from layers deeper than that of the Bure URL (that

is located at the level of maximum clay content) are stiffer and stronger, as recently confirmed in terms of Young modulus by means of micro-indentation and mini compression tests (UCS) run by Hu et al. [22] on COx unsaturated specimens extracted from depths of 490, 503 and 522 m. By testing COx specimens from various depths, Chiarelli [7] showed that the Young modulus increased with larger calcite content (between 6 and 15 GPa for calcite content between 20 and 52%) and decreased with larger clay fraction (between 15 and 6.5 GPa for clay fraction between 28 and 50%).

Beside natural variability, the testing procedure adopted is another important parameter to consider when comparing the data from various laboratories on COx specimens. Tests have been run in both saturated and unsaturated conditions with drainage conditions not always described in enough detail. By running a series of unconfined compression tests on COx specimens equilibrated at various suctions between 2.7 and 155.2 MPa (by using saturated saline solutions), Pham et al. [13] confirmed the sensitivity of the COx claystone to changes in water content already quoted by Chiarelli et al. [8], Zhang and Rothfuchs [9] and more recently by Zhang et al. [23]. They obtained trends comparable to that evidenced by Valès et al. [12] on the Tournemire shale, with significant increase in strength in drier states. The unconfined compression strengths that Pham et al. [13] obtained at failure varied between 27 MPa in a state close to saturated under a 98% relative humidity (suction 2.7 MPa, water content 5.24%, degree of saturation not given) and 58 MPa in a much drier state under a 32% relative humidity (suction 155.2 MPa, water content 1.65%, degree of saturation not given).

Prior to inspect further experimental data, it was found useful to present the technical procedures used and published in the literature including the depth at which specimens were extracted, the size of the specimen, their porosity, water content, degree of saturation, testing rate and drainage length (an important parameter with respect of drainage conditions). The data obtained in the works of Chiarelli [7] and Chiarelli et al. [8], Zhang and Rothfuchs [9], Pham et al. [13] and Hu et al. [11] are presented in Table 2. One can see that various sizes of triaxial specimens have been used, the smallest being the 20 × 20 mm cylindrical specimen used by Hu et al. [11], the longest one being the 100 mm high and 35 mm diameter used by Chiarelli [7] and Chiarelli et al. [8]. Pham et al. [13] used a specimen of 72 mm in height and 36 mm in diameter whereas Zhang and Rothfuchs [9] used a slightly larger specimen (40 mm in diameter and 80 mm in length). Both sizes are close to standard triaxial specimens of 38 mm in diameter and 76 mm in height.

Whenever carried out, the saturation procedure has not always been described in details by the authors. Some values of degree of saturation are given, that correspond to the initial one as obtained when receiving the specimen in the laboratory (i.e. between 73 and 100 % for Chiarelli [7] and Chiarelli et al. [8] who tested their specimens at their initial degree of saturation). The smallest degree of saturation was obtained after drying to investigate the effects of change in water content on the shear strength (1.65% by Pham et al. [13] and 2.8% by Zhang and Rothfuchs [9]). Although they did not comment about their saturation procedure, Zhang and Rothfuchs [9] obtained almost fully saturated specimens at S_r = 99%. On their small specimen, Hu et al. [11] achieved complete saturation by imposing a 1.5 MPa back-pressure on the bottom of the specimen until monitoring the same value on the top. The change with time of the pore pressure measured at the top of the specimen indicated that full saturation occurred after 70 hours in the 20 mm high specimen.

The drainage conditions imposed during the tests are not always described in detail. It seems that most often drainage was ensured by porous discs on top and bottom of the specimens. The other important parameter is the strain rate imposed, that varies between the largest value of 6.5×10^{-6} s^{-1} (Zhang and Rothfuchs [9]) in undrained tests down to 10^{-7} s^{-1} in Hu et al [11] in drained tests with a drainage length of 10 mm. The corresponding speeds are also given in Table 2 in µm/mn, knowing that drained tests in clayey soils (permeability of 10^{-17}m^2) are typically conducted at a speed of 1 µm/mn with a 19 mm drainage length equal to the specimen radius, thanks to lateral drainage allowed by filter papers placed all around the sample. In this regard, given the claystone average permeability of 10^{-20} m^2, it seems that drainage was not ensured in the tests of the Table run with speeds larger than 3µm/mn and drainage lengths larger than 40 mm. Conversely, the strain rate of 10^{-7} s^{-1} (speed of 0.12 µm/mn) adopted by Hu et al. [11] with a drainage length of 10 mm should ensure satisfactory drainage.

Note that, in fully saturated clayey soil specimens, imperfect drainage leads to over-estimate the shear strength. When specimens are not fully saturated, things are different because water is under a suction state and generally keeps retained by the specimen with only air exchanges. The shear strength properties can then be over-estimated by partial saturation.

Table 2. Characteristics published tests about the shear properties of the COx claystone.

Authors	N° Specimen	Depth (m)	Spec. height (mm)	Spec. diameter (mm)	Porosity (%)	Water content (%)	Degree of saturation (%)	Type of test	Testing rate (s^{-1}) µm/mn Drainage length *H*
Chiarelli (2000), Chiarelli et al. (2003)	EST 02172	451-467	100	35	11.5* *Est. 15.3*	4 – 5.7	73 – 93	Triaxial	6×10^{-6} 3.6µm/mn *H* = 50 mm
Chiarelli (2000), Chiarelli et al. (2003)	EST 02277	469	100	35	11 – 13.5* *Est. 14.6 – 18*	4 – 7	85 – 100	Triaxial	6×10^{-6} 3.6µm/mn *H* = 50 mm
Chiarelli (2000), Chiarelli et al. (2003)	EST 02354	482	100	35	11.8 – 13.8* *Est. 15.7 – 18.4*	4 – 7	90 – 100	Triaxial	6×10^{-6} 3.6µm/mn *H* = 50 mm
Zhang & Rothfuchs (2004)	EST 05677-02	487	80	40	16.1	7.1	99	UCS	6.5×10^{-6} 3.1µm/mn *H* = 40 mm
Zhang & Rothfuchs (2004)	EST 05677-04	487	80	40	16.1	2.8	39	UCS	6.5×10^{-6} 3.1µm/mn *H* =40 mm
Zhang & Rothfuchs (2004)	EST 05677-01	487	98	50	16.1	7.1	99	Undrained triaxial multistage	6.5×10^{-6} 3.8µm/mn *H* =49 mm
Pham et al. (2007)	EST 205D	451	72	36	10 – 14	1.65 – 5.24	Various S_r	UCS	Not given
(2014a)	EST 30446	521.5	20	20	11.8	6.2	100	Triaxial	10^{-7} s^{-1} 0.12µm/mn *H* = 10 mm

* porosity value obtained by Chiarelli et al. (2003) from mercury intrusion porosimetry tests. Estimated total porosity values are given in italics based on our observation that 25% of the total porosity was not intruded at 200 MPa in the tests that we performed on COx specimens at 490 m.

Fig. 1 presents a synthesis of the shear strength data from tests of Table 2 from the authors mentioned above, plotted in a diagram giving the shear stress at failure with respect to the constant confining Terzaghi effective stress applied during the test. One observes that the data of Chiarelli [7] at various depths with varying degree of saturation exhibit more dispersion and are located clearly above other data, probably because of partial saturation. The most coherent set of data is provided by Hu et al. [11] on specimens EST30446 from vertical borehole in the URL at a depth of around 521.5 m, with good correspondence between drained and undrained saturated tests. The data of Zhang and Rothfuchs [9] come from both UCS tests and two multistage undrained tests on apparently saturated specimens (saturation procedure not described in the paper). In perfectly saturated clayey soils, undrained triaxial tests carried out at various confining stresses would provide a horizontal

failure criterion providing only one value of undrained shear strength. It is not the case here with a slope comparable to that obtained in drained conditions. Imperfect saturation could be a reason why the criterion is not horizontal. The data of Hu et al. [11] provide, adopting a Mohr Coulomb criterion, a friction angle around 21° close to what could be obtained from that of Zhang and Rothfuchs [9]. The data of Chiarelli [7], [8], more dispersed, would provide higher friction angles.

The cohesion that would be obtained from Zhang and Rothfuchs [9]'s data (9 MPa, Fig. 1) is higher than that from Hu et al. [11], possibly due to partial saturation as well. This is compatible with data on the shear strength properties of unsaturated soils [24] that evidenced little effect of suction on the friction angle but significant effect on the cohesion, the higher the suction, the higher the cohesion.

There is little published data on the thermal behaviour of claystones. In terms of volume changes in clays, the important influence of overconsolidation, initially evidenced by Hueckel and Baldi [2] on Boom clay and Pontida clay, was confirmed by others (see for instance [4] on Boom clay and [5] on compacted clay). It is well established that normally consolidated clays (that never supported any overburden higher than what they supported when extracted) contract when heated under constant load whereas overconsolidated clays (that supported during their geologic history an overburden higher that what they were supporting when extracted, due for instance to erosion of upper layers) tend to exhibit elastic thermal expansion. A combined dilating-contracting behaviour can be observed on slightly overconsolidated clays, like for instance Boom clay.

The volume changes of the COx claystone submitted to temperature elevation under constant isotropic stress close to in-situ conditions was recently investigated in fully saturated and fully drained conditions by Mohajerani et al. [19] by using the hollow cylinder triaxial apparatus. They observed a thermal contraction, evidencing behaviour comparable to that of normally consolidated clays. On the Opalinus clay, Monfared et al. [18] observed a dilating-contracting behaviour with expansion up to a temperature of 65° close to the maximum estimated temperature supported during its geological history (65-70°C). Expansion was followed by contraction at higher temperature (up to 80°C). Interestingly, a subsequent temperature cycle up to 80°C exhibited thermal expansion, evidencing a thermal hardening phenomenon.

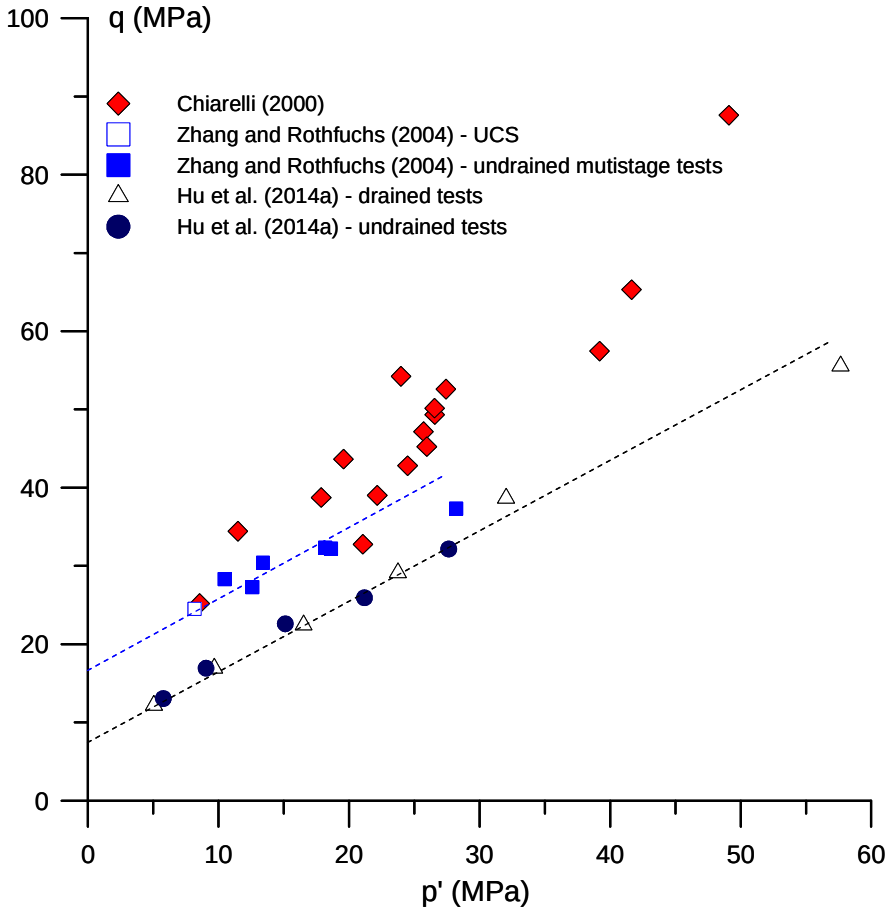

Fig. 1. Published shear strength data of the COx claystone.

Zhang et al. [25] run at various temperatures (from 20 to 115°C) undrained triaxial shearing tests (strain rate 10-7 s-1) under constant 3 MPa confining stress on Opalinus clay specimens with bedding planes inclined of 30-40°. The specimens had an initial degree of saturation of 88%. Zhang et al. [25] observed in such conditions a more ductile behaviour at elevated temperature with clear decrease in strength due to temperature elevation (maximum shear strength of 20 MPa at 20°C and of 5 MPa at 115°C). More recently, Zhang et al. [26] conducted triaxial micro-compression tests on unsaturated standard triaxial specimens submitted to a relative humidity of around 74%. They observed little sensitivity with respect to temperature in the stress strain curves obtained between 20 and 95°C under a confining stress of 15 MPa (around twice the in-situ effective stress), whereas a decrease in peak stress (with small sensitivity in the elastic regime) was observed under a confining stress of 5 MPa (smaller than the in-situ stress). Masri et al. [27] conducted a series of what they called "pseudo-drained" triaxial shear tests at temperatures between 20 and 250°C under three confining pressures (5, 10 and 20 MPa) at an axial strain rate of 10^{-6} s^{-1} on specimens not fully saturated (degree of saturation not provided). Specimens of 37 mm in diameter and

74 mm in height were bored with air pressure from cubic blocks extracted in the Tournemire URL (France). Their observations are comparable to that made by Zhang et al. [25] on Opalinus clay, with significantly more ductile behaviour observed at elevated temperature and peak stress decreasing from 90 MPa at 20°C down to 40 MPa at 250°C (tests run with bedding perpendicular to specimen axis).

The two previous works indicate that there is a suspicion of having an increase in ductility and a decrease in shear strength in claystones with elevated temperature. However, due to obvious experimental difficulties, these results are based on tests that have not been conducted under fully saturated and drained conditions. The necessity and interest of exploring this issue with well adapted devices and procedures, as proposed in this work, are hence confirmed.

3. Experimental device

3.1. Description

A global overview of the hollow cylinder triaxial cell specially designed to investigate the thermo-hydro-mechanical behaviour of low permeability clays and claystones [16] is presented in Fig. 2a that schematically shows the triaxial cell containing the hollow cylinder specimen (external diameter D_{ext} = 100 mm, internal diameter D_{int} = 60 mm, height H = 70-80 mm). Note that the same confining pressure is applied along both the external and internal lateral faces of the specimen thanks to a connection between these two volumes. As shown in Fig. 2a-b, a major advantage of this device is provided by the two lateral drainages in the inner and outer walls of the hollow cylinder specimen. These drainages are made up of two geotextiles bands placed along the specimen, with no contact between the bands and the upper and lower drainages. These lateral drainages reduce the specimen drainage length down to half the thickness of the hollow cylinder, i.e. 10 mm. Satisfactory drainage conditions are achieved during mechanical and thermal loading provided the strain rate and temperature elevation rate is small enough. Numerical calculations carried out by Monfared et al. [18] showed that a stress rate of 0.5 kPa/mn ensured satisfactory drainage in hollow cylinder specimens with permeability as low as 10^{-20} m^2.

The axial force is applied by using an integrated piston specially developed (Fig. 2a). The displacements of the piston are controlled by a pressure-volume controller (maximum pressure of 60 MPa) connected to the upper chamber of the piston. The applied axial force is

directly measured by a local immersed force sensor fixed at the bottom end of the piston. It can also be estimated from the pressure exerted and measured by the PVC.

Fig. 2b shows a schematic view of the hydraulic connections between the specimen, the pressure-volume controllers (PVC) and the pressure transducers (PT). PVC1 is used to apply the confining pressure whereas the other three PVCs are used to apply and control the pore fluid pressure. The device also comprises a system used to monitor local strains composed of two axial and four radial local displacement transducers (LVDTs, precision ± 1μm, Fig. 2c).

The heating system consists of a heating electric belt placed around the cell with a temperature regulator with a precision of ±0.1°C. Temperature is measured inside the cell close to the specimen by a thermocouple. The cell is covered by insulating layer in order to limit heat exchanges with the environment.

(a)

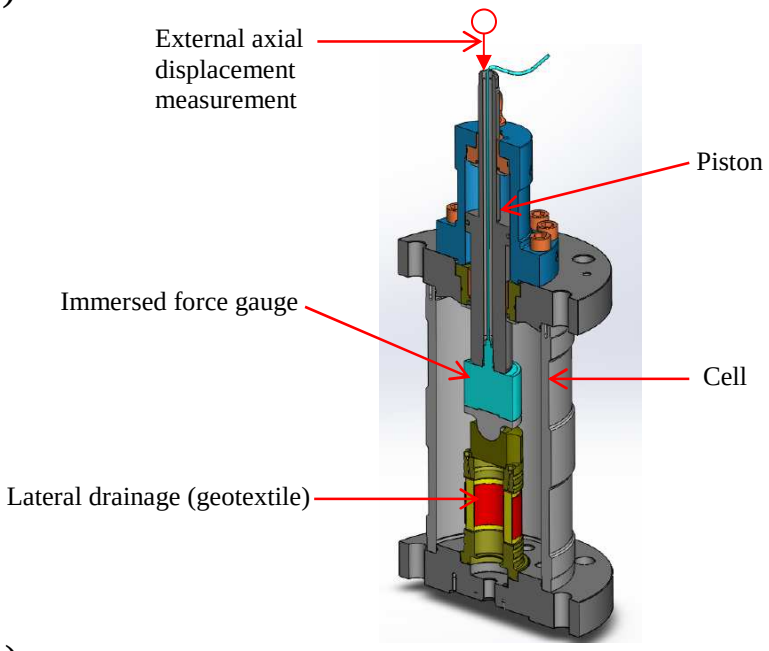

(b)

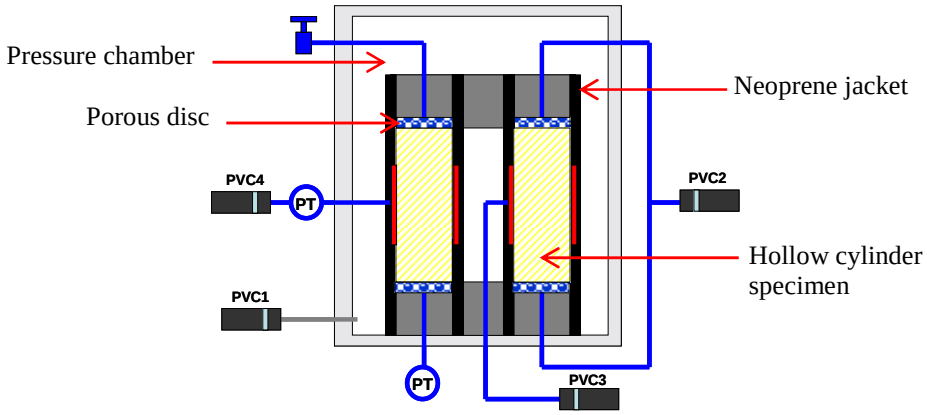

(c)

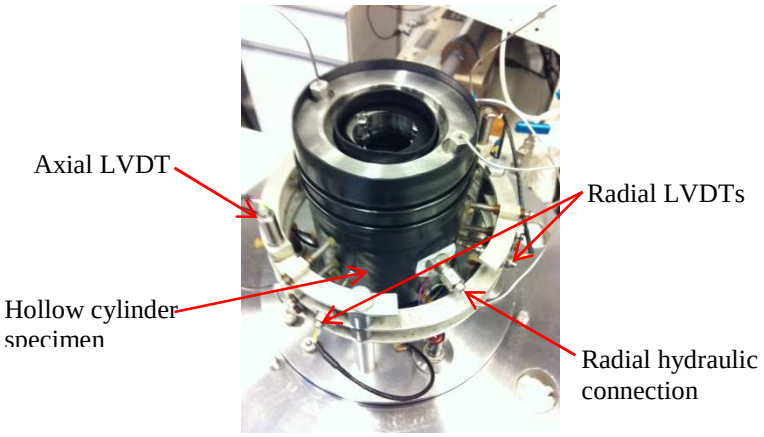

Fig. 2. (a): Hollow cylinder triaxial cell, (b): Scheme of the hydraulic connections, (c): Local strain measurement system.

3.2. Preliminary resaturation procedure

As shown by Monfared et al. [16], an interesting feature of the hollow cylinder triaxial cell is its ability to ensure good initial saturation of specimens of very low permeability (around 10^{-20} m^2 in the case of the COx claystone) within a reasonable period of time thanks to a drainage path equal to half the thickness of the hollow cylinder. Proper preliminary resaturation of specimens that have been desaturated during coring, conservation, transport and machining in the laboratory is essential. The initial degree of saturation of the specimens appears to be an important parameter with respect to specimen quality.

As recalled by Delage et al. [28] on the Boom clay, Monfared et al. [18] on the Opalinus clay and Mohajerani et al. [29] on the COx claystone, it is important to resaturate specimens of swelling clays under stress conditions close to in-situ ones in order to avoid further perturbation due to swelling during hydration. The in-situ state of stress at the level of the Bure URL has been investigated in detail by Wileveau et al. [30] who provided the following values: vertical total stress σ_v = 12.7 MPa, minor horizontal total stress σ_h = 12.4 MPa and major horizontal total stress σ_H = 16.2 MPa, situ pore pressure u = 4.7 MPa. Mohajerani et al. [29] used a confining stress of 12 MPa and a pore pressure of 4 MPa, resulting in a Terzaghi effective stress of 8 MPa. So as to reduce the risk of leaks due to possible perforation of the neoprene jacket under high stresses, it was preferred here to adopt the same Terzaghi 8 MPa effective stress value with lower values, i.e. a 9 MPa confining pressure and a 1 MPa pore pressure.

Fig. 3 shows the volume changes calculated from the water injected from the back pressure PVCs compared to that monitored by local LVDT measurements during the saturation phase of tests T3 (specimen EST28514, porosity ϕ = 17.6%, initial degree of saturation S_{ri} = 85%) and T6 (specimen EST45407, ϕ = 13.5%, S_{ri} = 39%). The curves show that the stabilization of the water injected and of the volume changes derived from the local LVDTs occurred after two days in both cases. The higher volume change obtained from the water injected from the PVC is due to the effect of the water volume needed to saturate the porous elements in contact with the specimen, i.e. the lateral geotextiles and the upper and lower porous discs. One can also observe that the water injected from PVCs in test T6 (7.4%, S_{ri} = 39%, Fig. 3b) is significantly larger than that injected in test T3 (2.3%, S_{ri} = 85%, Fig. 3a) because of the significantly smaller initial degree of saturation in T6. A slightly larger swelling is monitored by the LVDTs in test T3 (1.18% compared to 1.04% for T6),

perhaps linked to the difference in clay fraction between both specimens, with a larger clay fraction in the more porous T3 specimen (porosity 17.6%).

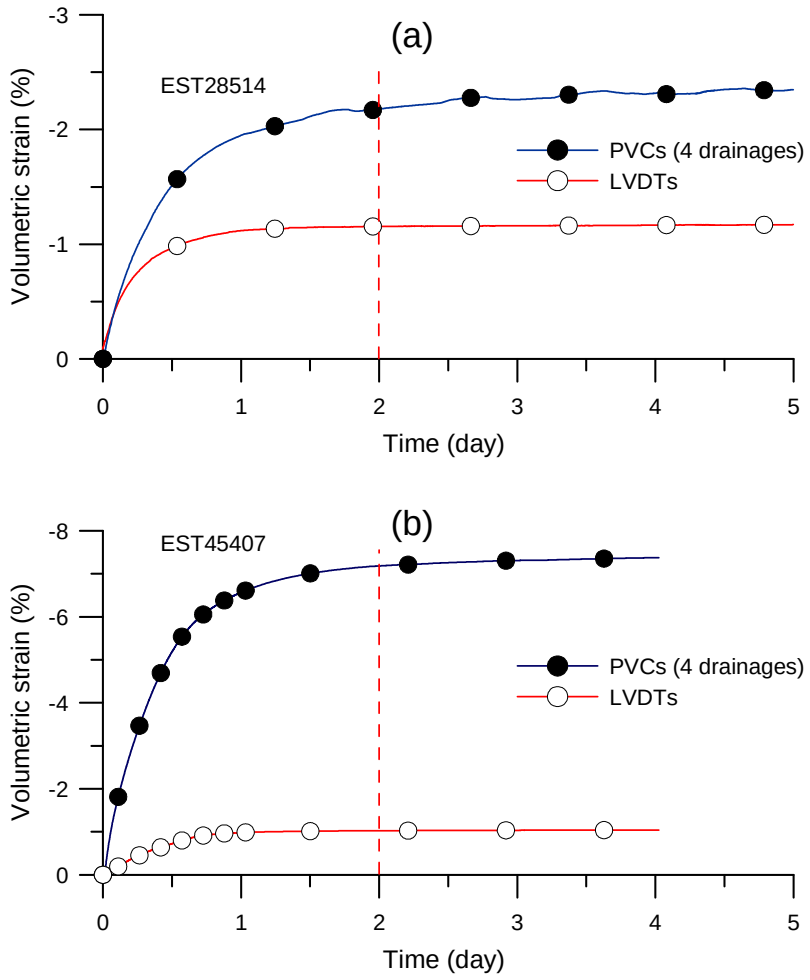

Fig. 3. Volume changes and water exchanges during resaturation phase; (a) test T3, (b) test T6.

3.3. Radial permeability tests

Steady state permeability measurements were carried out by applying a radial pressure gradient across the specimen and by measuring inflow and outflow fluxes by using the PVCs. Permeability tests were carried out on specimens with an initial backpressure of 1 MPa by closing the valves connected to the top and bottom of the specimen and by applying a pressure excess of 0.5 MPa through the external geotextile while maintaining the internal pressure equal to 1 MPa.

The radial intrinsic permeability k_r (m^2) was calculated using the flow rates as follows:

$$k_r = \frac{Q\mu_w \ln(R_{ext} / R_{\text{int}})}{2\pi h \Delta u} \quad (1)$$

where Q is the water flow; μ_w the water viscosity (equal to 8.90 x 10^{-4} Pa.s at 25°C and 3.55 x 10^{-4} Pa.s at 80°C), R_{ext} and R_{int} the external and internal specimen radius, respectively (R_{ext} = 50 mm; R_{int} = 30 mm); h the flow height (h =50 mm); and Δu the pressure difference between the inner and outer walls of the specimen (Δu = 0.5 MPa).

3.4. Comments on the hollow cylinder device

As commented previously, the advantages of the hollow cylinder device in term of both resaturation duration and drainage conditions are provided by the short drainage length equal to half the thickness of the cylinder (10 mm), thanks to the external and internal lateral drainages. Compared to small triaxial specimens that also have short drainage paths, the hollow cylinder configuration also allows the monitoring of axial and radial local strains thanks to the larger specimen size. Also, this specific configuration allows perform radial permeability tests in sheared specimens by forcing the water flux in the network of shear bands. This ability has proven being quite useful in the investigation of the self-sealing properties of the Boom clay [17] and of the Opalinus clay [31]. However, based on the experience gained in the previous studies during the TIMODAZ European project (see Li et al. [32]) and also gained in previous investigations carried out on the COx clay [19], some difficulties have been met in link with the difficulty of machining 100 mm diameter hollow cylinder specimens (see Monfared et al. [17] for more details). This firstly requires large cores of 100 mm in diameter, which is expensive and not so common. Most cores presently extracted from the Bure URL by Andra have a diameter of 80 mm. In this study, good quality hollow cylinder specimens were obtained on a lathe specially devoted to trimming claystone specimen at CEA, the French research institute in nuclear energy.

For this reason of availability of large diameter cores, the tests of this program had to be carried out on available specimens from different origins and initial characteristics, as shown in Table 1.

3.5. Experimental program

Five different loading paths were performed on six hollow cylinder specimens that were machined with the axis perpendicular to bedding to investigate some aspects of the thermo-hydro-mechanical behaviour of the COx claystone, as described in Table 3 and in Fig. 4. The same stress path was followed for tests T2 and T3. All specimens were previously saturated as described in section 3.2. Tests T1, T2, T3 and T4 were carried out along paths aimed at investigating the shear response at 25°C, as shown in Fig. 4. To do so, constant confining pressure tests were carried out at 25°C close to in-situ condition (σ_3 = 9 MPa, u = 1 MPa), around half the in-situ condition (σ_3 = 5 MPa, u = 1 MPa) and twice the in-situ condition (σ_3 = 17 MPa, u = 1 MPa).

The same program was planned at 80°C but the test planned under twice the in-situ stress condition failed due to leakage and no more hollow cylinder specimen was available to do it again. The tests under constant confining stress finally performed at 80°C were test T5 on specimen EST45414 (like T1) under stress conditions close to in-situ (σ_3 = 9 MPa, u = 1 MPa) and test T5 on specimen EST 45407 under half the in-situ condition (σ_3 = 5 MPa, u = 1 MPa).

Table 3. Experimental programme.

Test	Specimen	Ref. Core	Programme	Permeability test
T1	S1	EST45414	Shear under σ' = 8MPa at 25°C [B-C]	-
T2	S2	EST30734	Isotropic unloading to σ' = 4MPa (swelling) [B-C], shear at 25°C [C-D]	-
T3	S3	EST28514	Isotropic unloading to σ' = 4MPa (swelling) [B-C], shear at 25°C [C-D]	-
T4	S4	EST28518	Drained isotropic compression up to σ' = 16MPa [B-C], shear at 25°C [C-D]	-
T5	S1	EST45414	Drained heating up to 80°C [B-C], shear under σ' = 8MPa at 80°C [C-D]	-
T6	S5	EST45407	Isotropic unloading to σ' = 4MPa [B-C], drained heating up to 80°C [B-C], shear at 80°C [C-D]	[B], [C], [D]

The tests carried out under half the in-situ condition are expected to swell during the stress release from the initial in-situ condition under which they have been resaturated (see Mohajerani et al. [33]). Particular care was put in following this swelling phase to make sure that the specimen reached equilibrium in water content. It seemed that this stress path was preferable to get a relevant response, compared to the standard stress path in which the

specimen would have been directly submitted to the desired stress state prior to perform the resaturation procedure.

Steady state permeability tests were also planned in some tests. Their interest is to provide further insight on the effects of temperature, compression and swelling on the permeability. Successful radial steady state permeability tests were performed in test T6 at points B (after resaturation), C (after swelling) and D (after heating the swelled specimen up to 80°C).

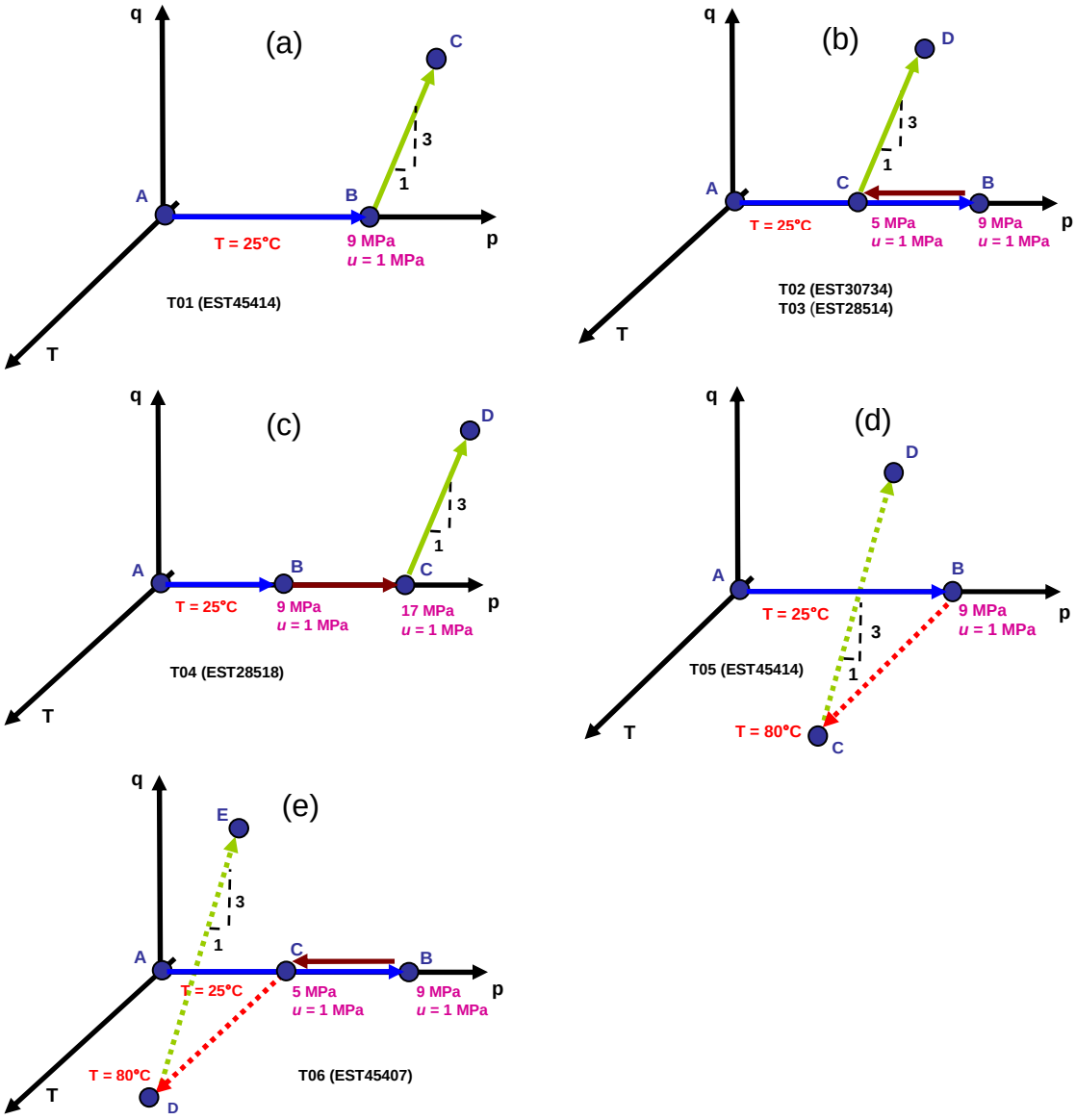

Fig. 4. Thermo-hydro-mechanical paths followed during the tests carried out.

4. Experimental results

4.1. Test at 25℃

Test T1, a drained shear test at constant confining stress close to the in-situ effective stress, was carried out with a constant axial displacement rate of 0.4 µm/mn while measuring the strength by using both the immersed force gauge and the pressure measurement provided by the PVC applying the axial force. One observes in Fig. 5 the changes in axial, radial and volumetric strains with respect to the shear stress ($q = \sigma_1 - \sigma_3$). The curves show that the maximum value of the shear stress at peak is 23 MPa. A good correspondence was observed between the force measured by the immersed force gauge and that obtained from by the external measurement provided by the CPV pressure applied on the piston chamber (not given here). The peak is reached at 0.62% of local axial strain and 0.24% of local radial strain. Note that the two axial LVDTs transducers have not moved at the beginning of the test, up to 4 MPa of shear stress.

Fig. 5 also shows that the axial strain at peak found by external LVDT is of the order of 1.45%, significantly higher than the 0.62% strain monitored by the local axial LVDT. This difference is due to the non-negligible effects of the compressibility of the whole system of axial stress application. It shows that Young's modulus obtained from external axial measurements might be significantly underestimated.

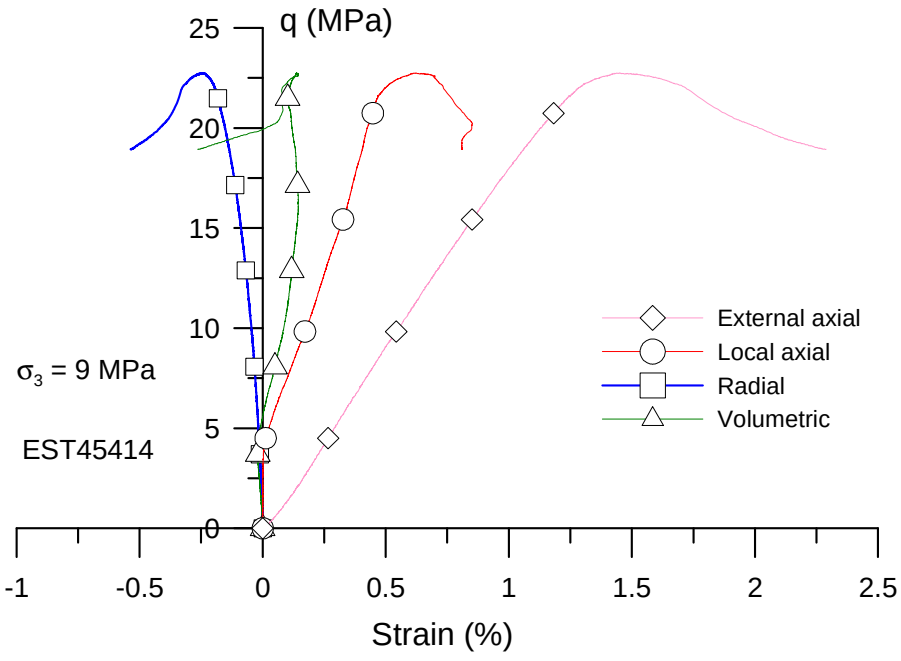

Fig. 5. Drained shear test under in-situ effective stresses at 25°C, test T1.

A contracting dilating behaviour is observed before reaching the peak with a transition observed at 16.5 MPa. The post-peak response is controlled by strain localisation and the response of the resulting discontinuity observed after failure. Indeed, one observes on the photographs of the specimen at the end of the test (Fig. 6) a network of shear bands with an inclination of 66° with respect to horizontal. One also notes the darker colour of the specimen due to full saturation, compared to the initial clearer grey colour of COx specimens.

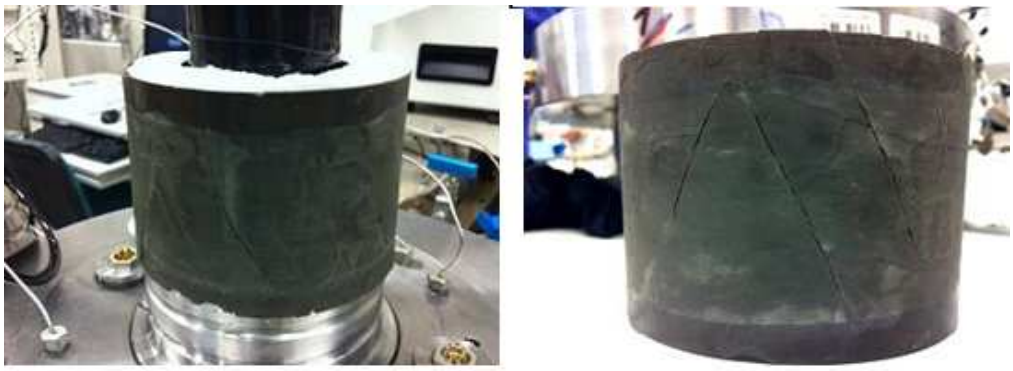

Fig. 6. COx claystone at the end of the test T1.

Once resaturated under in-situ stress condition, the specimens of tests T2, T3 and T6 were unloaded to a stress state close to half the in-situ one ($\sigma_3 - u = 4$ MPa) in drained condition with the four drainages connected to a PCV imposing a backpressure $u = 1$ MPa. To do so, the confining pressure was decreased from 9 to 5 MPa at a slow rate of 1 kPa/mn. During this phase, the specimen volume monitored by LVDTs transducers increased by 1.21%, 1.12% and 0.63% after 12 days for tests T2, T3 and T6 respectively. In a standard fashion, more swelling was observed in the direction perpendicular to bedding as seen in Fig. 7. The larger swelling observed in the specimens of tests T2 and T3 of larger porosity (16.5 and 17.6% respectively) confirm the effect of a larger clay fraction, as previously mentioned in Section 3.2 when describing the resaturation phase.

Specimens were afterwards maintained under a confining pressure of 5 MPa for a few days in order to see possible swelling under a constant mean effective stress lower than the in-situ one (~8 MPa). A volumetric swelling ratio of 0.013%/day, 0.022%/day and 0.010%/day were measured by LVDTs for T2, T3 and T6 respectively.

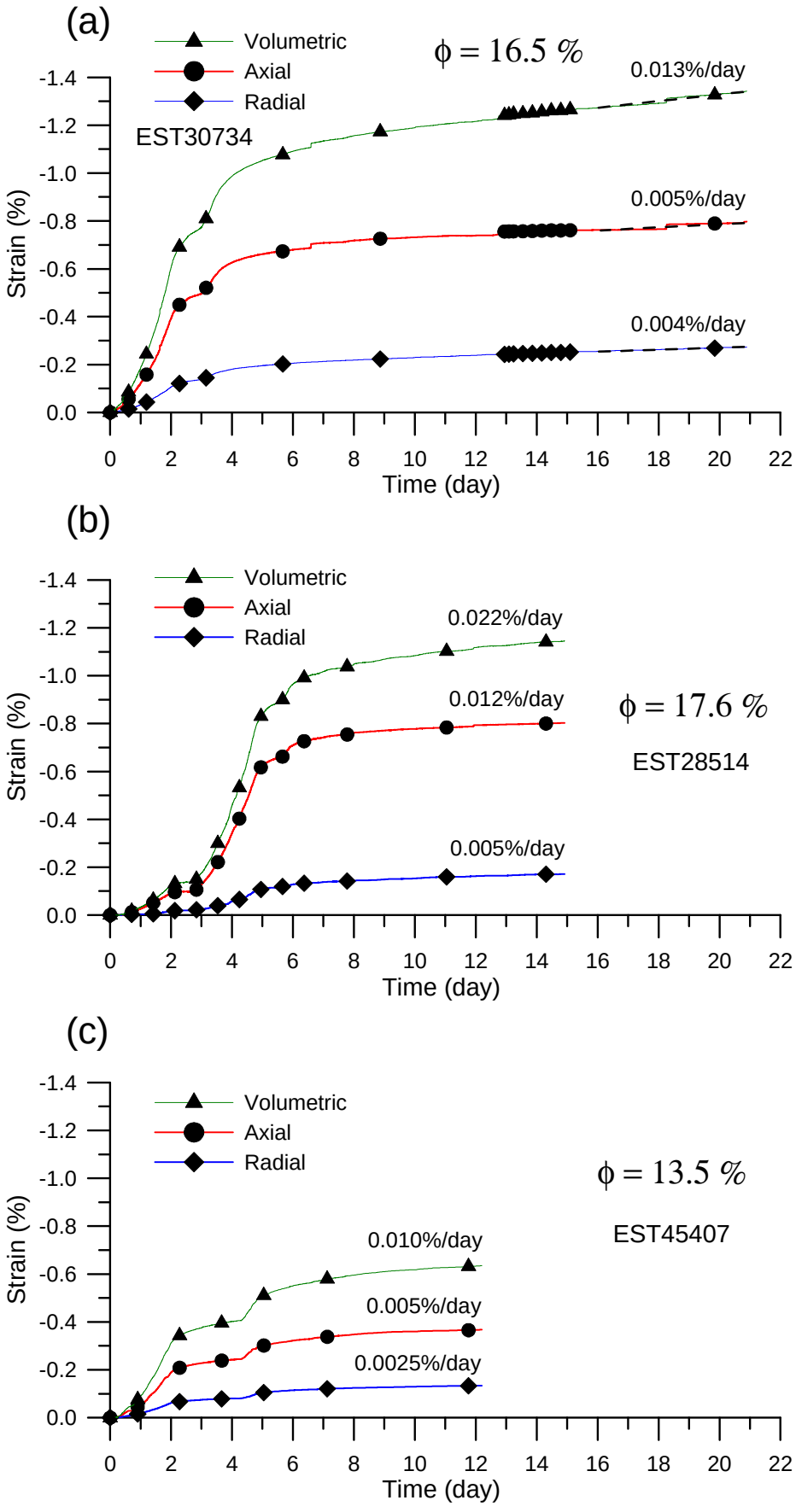

Fig. 7. Drained isotropic unloading phase, (a): T2, (b): T3, (c): T6.

The specimens of tests T2 (ϕ = 16.5%) and T3 (ϕ = 17.6%) were then sheared under a constant confining stress equal to half the in-situ effective stress (4MPa) in drained conditions with axial displacement rates of 0.5µm/mn and 0.4µm/mn respectively. Fig. 8 shows the axial, radial and volumetric strains changes with respect to shear stress for both specimens. A peak strength value of 10.5 MPa at axial and radial strains of 1.06% and 0.24% respectively is observed for T2. A peak strength value of 10.3 MPa at axial and radial strains of 1.01% and 0.33% respectively was obtained for T3, showing good repeatability in the response of those two specimens of comparable porosity.

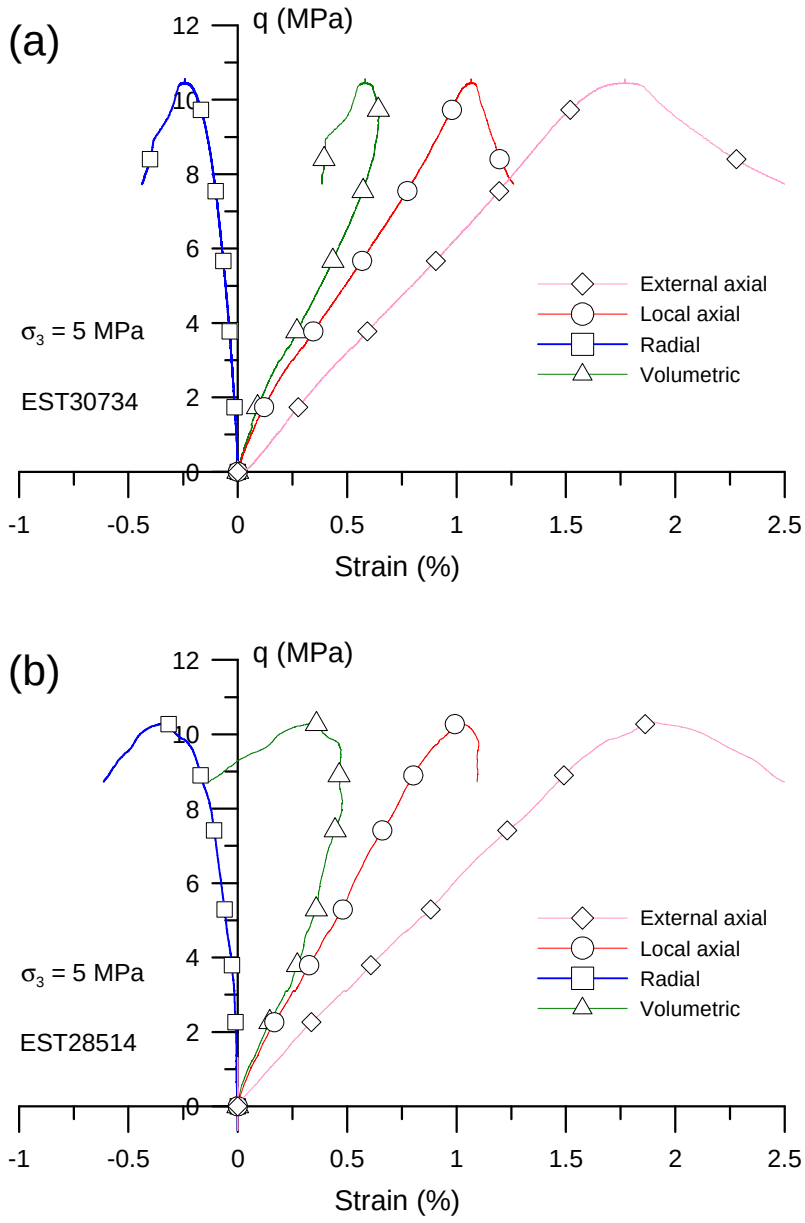

Fig. 8. Drained shear test under half in-situ effective stresses at 25°C, (a): test T2, (b): test T3.

Fig. 9 presents the axial, radial and volumetric strain with respect to the shear stress for specimen of test T4 under a constant value of confining stress close to twice the in-situ one (8 MPa) with a peak strength at 25.5 MPa at axial and radial strains of 1.15% and 0.60% respectively.

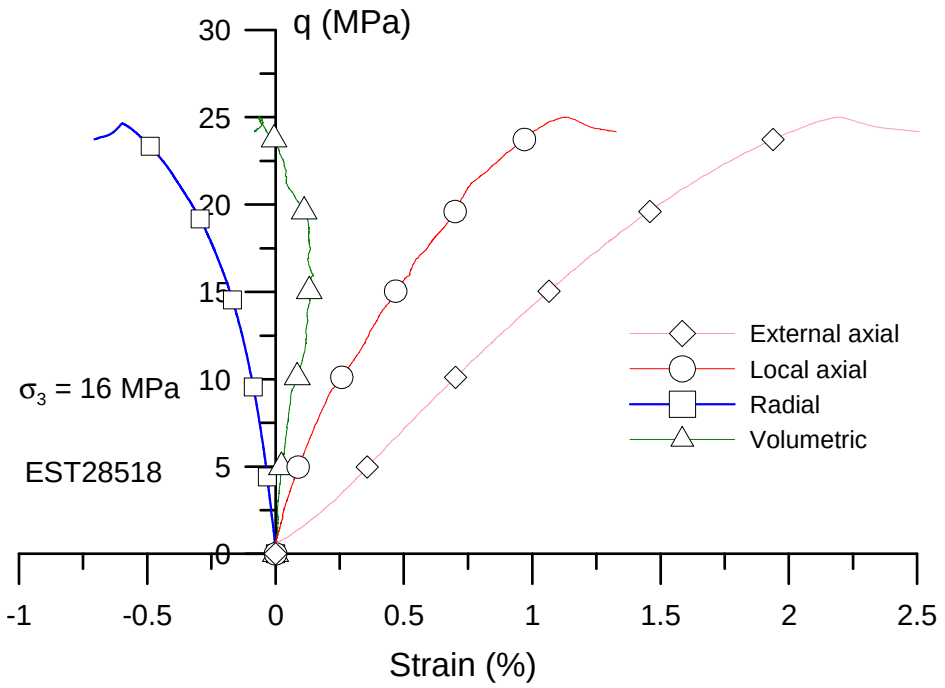

Fig. 9. Drained shear test under twice in-situ effective stresses at 25°C, test T4.

4.2. Drained heating test

Once resaturated under an effective confining stress close to in-situ (cell pressure σ_3 = 9 MPa, back pressure u = 1 MPa), a drained heating test (T5) was carried out under the same constant effective stress on specimen EST45414 (ϕ = 13%). A comparable test (T6) was carried out under half the in-situ effective stresses (σ_3 = 5 MPa, u = 1 MPa) on specimen EST45407 (ϕ = 13.5%). To do so, the cell was slowly heated up to 80°C with a slow heating rate of 0.5°C/h [4, 18], keeping the four drainage open (top, bottom, lateral inner and outer).

Fig. 10 presents the thermal local axial, radial and volumetric strains obtained from LVDT measurements during the drained heating test. As already observed by Mohajerani et al. [19], they show that the drained thermal volumetric response of the COx claystone under constant in-situ stress is characterized by a contraction occurring from the beginning of the test, with axial strains slightly larger than radial strains, showing slight degree of anisotropy in the thermal response. This anisotropy shows that the direction perpendicular to bedding

(axial strains) is somewhat more sensitive than that parallel to bedding (radial strains). At 80°C, the axial strain is equal to 0.06% (characterised by a slope $C_{T\perp}$ = 1.14 × 10^{-5} °C^{-1}), compared to 0.06% for the radial strain (characterised by a slope $C_{T\perp}$ = 1.06 × 10^{-5} °C^{-1}), resulting in a slope of 3.16 × 10^{-5} °C^{-1} for the volume changes.

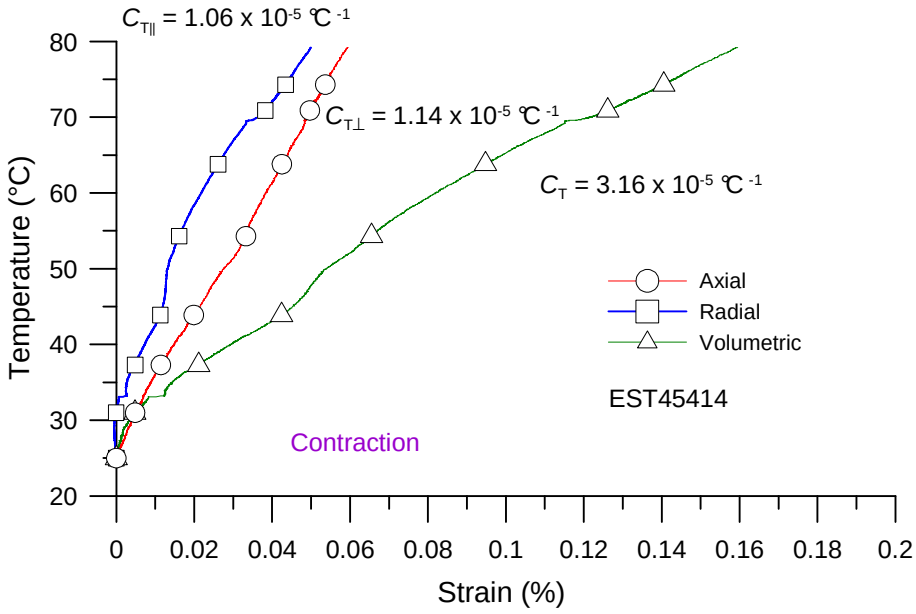

Fig. 10. Axial, radial and volumetric strains measured during a drained heating test (0.5°C/h) under in-situ effective stresses, test T5.

Fig. 11 shows the thermal response obtained during the drained heating test carried out under half the in-situ effective stresses (test T6). The changes in axial strain also indicate a continuous and almost linear contraction with a slope (perpendicular to bedding) $C_{T\perp}$ = 0.96 × 10^{-5} °C^{-1}. In this test, no more change was observed in radial strain above 37°C, due to some friction effect in the radial LVDT. However, the changes in axial strain observed up to 37°C are comparable to the radial ones, with a slope (parallel to bedding) $C_{T\parallel}$ = 0.77 × 10^{-5} °C^{-1}. Based on this value, a volumetric thermal contraction coefficient of 2.49 × 10^{-5} °C^{-1} is obtained. Thermal contraction appears to be slightly smaller under half in-situ stress conditions than under in-situ ones.

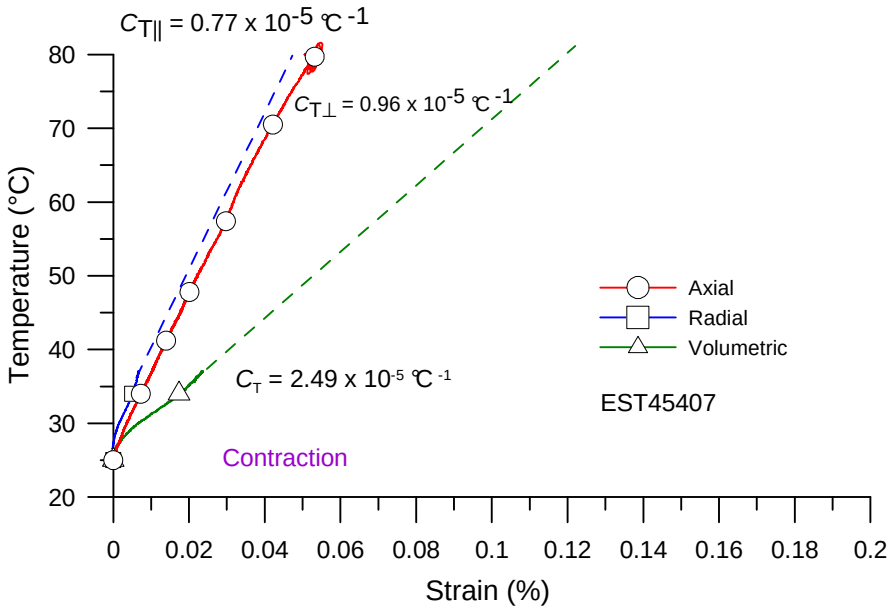

Fig. 11. Axial, radial and volumetric strains measured during a drained heating under half in-situ effective stresses, test T6.

4.3. Shear tests at 80℃

Once the drained heating phase completed, specimens of tests T5 and T6 were submitted to drained shearing with a constant axial displacement rate of 0.3µm/min and 0.4µm/min respectively. Fig. 12a shows that the shear stress at 80°C under in-situ stress condition reached a peak value of 20 MPa at 0.75% of axial strain and 0.31% of radial strain in test T5. The volume change is characterized by a contracting behaviour, at the beginning (up to a 14.6 MPa), followed by a dilation phase up to the peak. As previously, Fig. 12a shows that the axial strain found by an external measurement at peak is about 1.2%, significantly higher than that given by the local measurement.

The shear test at 80°C carried out under half the in-situ effective stresses (4MPa) is presented in Fig. 12b. This curves shows that the shear stress reaches its maximum value of 16 MPa at 1.25% and 0.35% of axial and radial strain respectively.

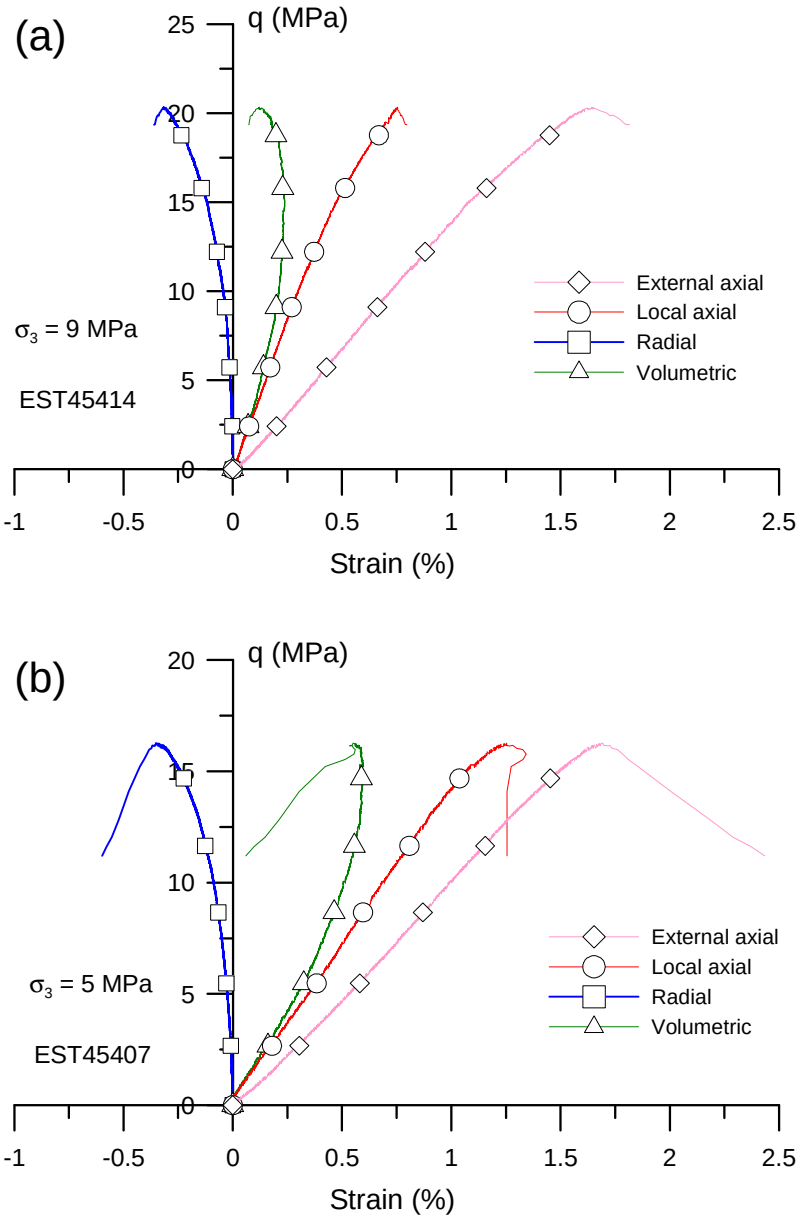

Fig. 12. Drained shear test at 80°C, (a): test T5, (b): test T6.

4.4. Failure criterion

All the peak values (q_{max}) obtained in the previous tests are brought together in Fig. 13 together with the data of Hu et al. [11] that also concern fully saturated and drained tests. The tests run at 25°C on three specimens with a porosity of 16-17% are located along a line parallel to that obtained at 80°C on specimens with porosity around 13%. There is unfortunately only one point at 25°C for a specimen with porosity around 13%. The failure points at 80°C obtained under in-situ effective stress from a specimen with porosity close to

13% is located slightly below that at 25°C. This set of data will be further commented in the Discussion section.

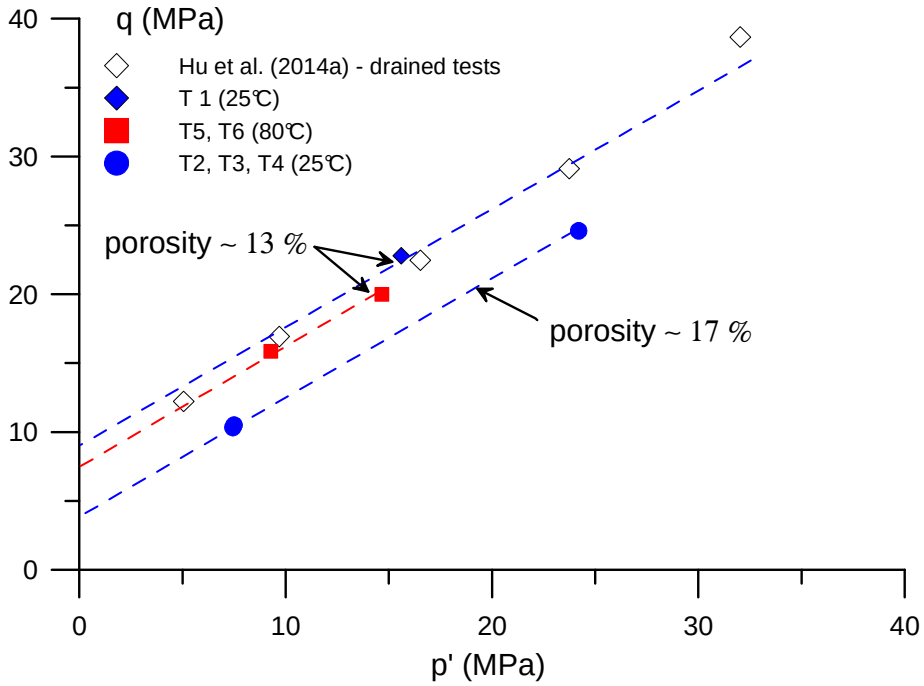

Fig. 13. Shear strength of all tests carried out in the plan q-p'.

4.5. Radial permeability tests

Radial permeability tests were carried out in some cases to investigate the effects of volume changes and of temperature on water transport. Given that specimens were machined with axis perpendicular to bedding, the flow of water during radial permeability tests is governed by the permeability parallel to bedding. As described in Section 3.3, tests were carried out by applying a 1.5 MPa pore pressure on the external lateral face of the hollow cylinder while maintaining the pressure on the internal face equal to the initial back pressure of 1 MPa. The confining pressure was kept equal to 9 MPa.

The inflow and outflow curves monitored by the upstream and downstream PVCs for the test after resaturation under in-situ stress conditions of the specimen of test T6 (porosity 13.6%) are presented in Fig. 14 (in which the *Q* final inflow and outflow are indicated). Actually, a tiny leak was observed on the upstream PVC when bringing back the pressure from 1.5 to 1 MPa at the end of the test. This leak (estimated by 23% of the monitored inflow at point B) was accounted for and inflow curves corrected accordingly (note however that the correction was made under 1 MPa whereas tests were carried out under 1.5 MPa). Less

confidence is hence given to inflow curves compared to outflow curve that were not affected by any leak.

Fig. 14 shows that, once the upstream injection starts, it was necessary to wait for 30 minutes before monitoring any outflow with the downstream PVC. This period of time was necessary to install steady state conditions and to reach the new effective stress state resulting from the 1.5 MPa pore pressure exerted along the external face of the specimen. By applying Darcy's law on the outflow observed at the end of test (Q = 3.35 × 10^{-12} m^3/s), a radial permeability of 0.9 × 10^{-20} m^2 is obtained. That obtained from the inflow value (Q = 3.88 × 10^{-12} m^3/s) is close, although slightly larger (k = 1.1 × 10^{-20} m^2), confirming the good quality of the measurement (with satisfactory correction of the upstream leak).

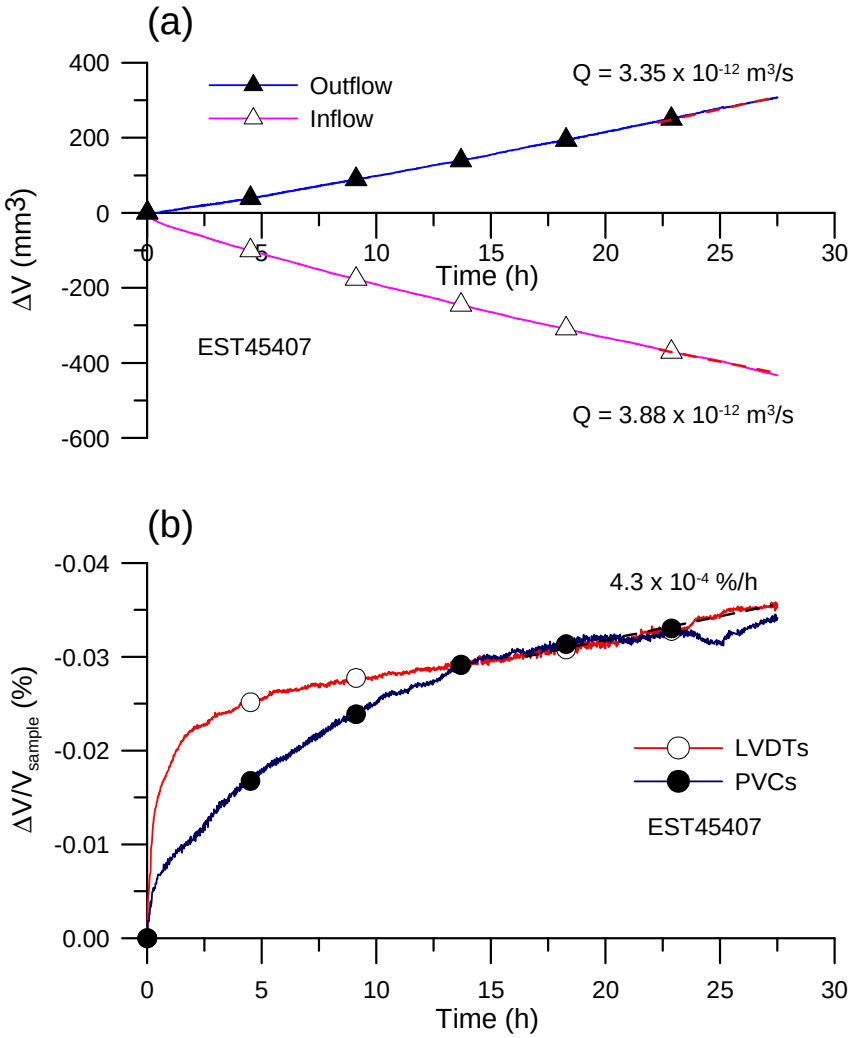

Fig. 14. Radial permeability test at point B, after resaturation T6, (a): inflow and outflow, (b): volume change.

Fig. 14b shows the changes in volume obtained from water exchanges (calculated from the upstream and downstream PVCs data) and from local LVDTs measurements. For some reason, the two curves are not in good correspondence during the first 14 hours with LVDTs indicating fast swelling during the first two hours. Both curves afterwards correspond and indicate that the specimen slightly swells (0.034% after 27 hours with a final swelling rate of 4.3×10^{-4} h^{-1}). The amount of water adsorbed during the test explains the slight difference between the inflow and outflow data, and between the two calculated permeabilities.

Another radial permeability test was carried out in test T6 after releasing the confining stress to half the in-situ value to investigate the effect of the resulting 0.63% swelling (Point C, Fig. 4). Inflow and outflow data (Fig. 15a) are comparable to that observed above with no outflow during the first hour, providing at the end of test radial permeability values of 1.2×10^{-20} m^2 and 1.6×10^{-20} m^2, respectively. These values are slightly higher than before stress release and are related to the 0.63% swelling. The PVC volume change curve (Fig. 15b) provides a slightly larger volume change value than LVDTs at end of test. The final swelling rate is 5.9×10^{-4} h^{-1}.

The data of the permeability test finally carried out after drained heating (Point D, Fig. 4, test T6, thermal contraction 0.106%, see Fig. 11) are presented in Fig. 16 a and b. This test had to be stopped after only 7 hours with a final swelling rate of 3.7×10^{-3} h^{-1}. Even after a shorter period of time, swelling is close to 0.07%, i.e. almost twice that observed in the two previous tests at 25°C, indicating possible enhancing of swelling with elevated temperature. Compared to previous tests at 25°C, larger fluxes are obtained ($Q_{inflow} = 2.52 \times 10^{-11}$ m^3/s and $Q_{outflow} = 1.58 \times 10^{-11}$ m^3/s). Here, the difference between inflow and outflow is larger than previously. Given that the upstream leak correction done at 25°C could not be valid here, only the outflow curve is considered to provide an (intrinsic) permeability value equal to 1.8×10^{-20} m^2. As further commented in the Discussion session, larger fluxes are related to the decrease in water viscosity. A larger permeability is observed at 80°C in spite of a slight porosity reduction.

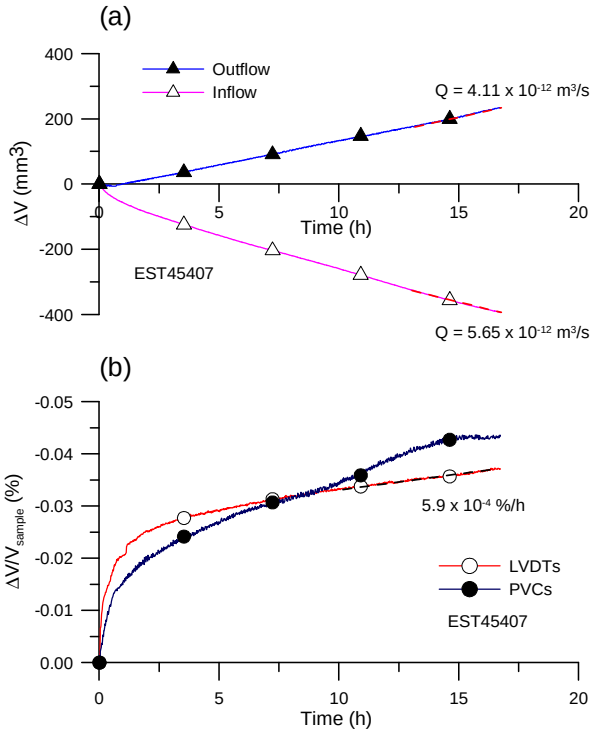

Fig. 15. Radial permeability test at point C, after swelling T6, (a): inflow and outflow, (b): volume change.

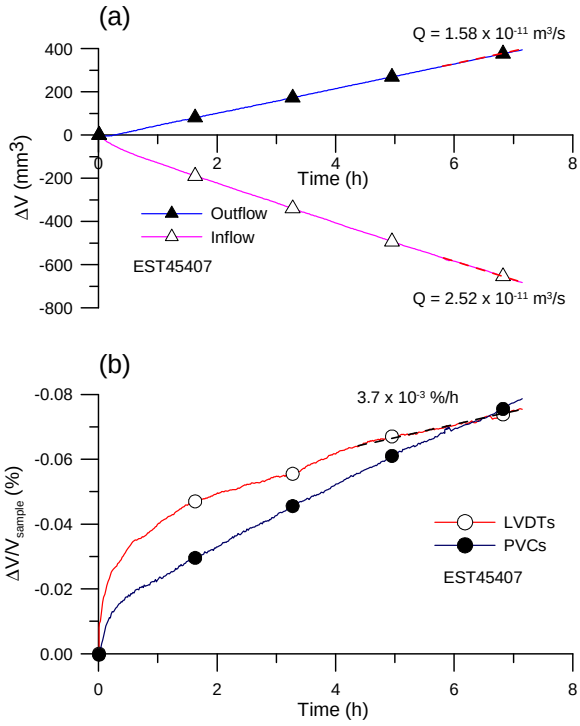

Fig. 16. Radial permeability test at point D, after heating T6, (a): inflow and outflow, (b): volume change.

5. Discussion

5.1. Elastic response

A series of triaxial tests have been conducted on COx claystone specimens along various thermo-hydro-mechanical paths (Fig. 4) in fully saturated and drained conditions by using the hollow cylinder device. Although all of the tests initially planned were not successful because of the technical difficulty of getting hollow cylinder specimens and of running hollow cylinder triaxial tests, some conclusions can be drawn from the data obtained. The various shear stress/axial strain curves obtained on specimens trimmed with axis perpendicular to bedding allow the determination of some elastic constants that partly describe the transverse isotropic elastic behaviour of the COx claystone. As described by Cheng et al. [34], the stress-strain elastic relationship for a transverse isotropic material is as follows:

$$\begin{pmatrix} d\varepsilon_1 \\ d\varepsilon_2 \\ d\varepsilon_3 \end{pmatrix} = \begin{pmatrix} \frac{1}{E_1} & -\frac{\nu_{21}}{E_2} & -\frac{\nu_{21}}{E_2} \\ -\frac{\nu_{12}}{E_1} & \frac{1}{E_2} & -\frac{\nu_{23}}{E_2} \\ -\frac{\nu_{12}}{E_1} & -\frac{\nu_{23}}{E_2} & \frac{1}{E_2} \end{pmatrix} \begin{pmatrix} d\sigma_1 \\ d\sigma_2 = 0 \\ d\sigma_3 = 0 \end{pmatrix} \quad (2)$$

with $d\sigma_2 = d\sigma_3 = 0$ under "triaxial" conditions and where ν_{23} and E_2 are the Poisson ratios and Young modulus in the plane of isotropy (2-3), and ν_{12}, ν_{21} and E_1 are the Poisson ratio and Young modulus in the plane perpendicular to the plane of isotropy. The Young modulus and Poisson ratio perpendicular to bedding can be calculated by using the data of the drained triaxial test using Eq. (3) and Eq. (4).

$$\frac{d\varepsilon_1}{d\sigma_1} = \frac{1}{E_1} \quad (3)$$

$$\frac{d\varepsilon_2}{d\sigma_1} = -\frac{\nu_{12}}{E_1} \quad (4)$$

From the data of Fig. 5 under a confining stress close to in-situ (8 MPa Terzaghi effective stress), a value E_1 = 3.2 GPa is obtained from the shear stress-axial strain curve for a mobilisation of 0.1% of axial strain, with ν_{12} = 0.30 (Table 4). When the confining stress has been released close to half the in-situ one, values E_1 = 1.5 GPa and 1.3 GPa are deduced from tests T2 and T3 respectively with Poisson's ratio ν_{12} = 0.10 in both cases (Fig. 8). Conversely, when the confining stress is increased to twice the in-situ stress (test T4, Fig. 9), values of Young modulus and Poisson's ratio of 5.5 GPa and 0.34, respectively, are obtained.

Table 4. Evolution of the elastic parameters.

Test	Ref. Core	Porosity (%)	σ' (MPa)	Temperature (°C)	q_{max} (MPa)	E_1 (GPa)	ν_{12}
T1	EST45414	13.0	8	25	23.1	3.2	0.30
T2	EST30734	16.5	4	25	10.5	1.5	0.10
T3	EST28514	17.6	4	25	10.3	1.3	0.10
T4	EST28518	17.8	16	25	24.6	5.5	0.34
T5	EST45414	13.0	8	80	20.0	3.4	0.26
T6	EST45407	13.5	4	80	16.1	1.4	0.10

At 80°C, the estimated values of the E_1 Young's modulus and the ν_{12} Poisson ratio are E_1 = 3.4 GPa and ν_{12} = 0.26, respectively, under a confining stress close to in-situ. Values E_1 = 1.4 GPa and ν_{12} = 0.10, respectively, were obtained under a confinement of half the in-situ stress.

All the values obtained at 25 and 80°C are plotted together in Fig. 17 that clearly shows that there is no effect of temperature on the elastic properties determined here (Young's modulus E_1 and Poisson coefficient ν_{12}). Similar comparison has been drawn by Mohajerani et al. [19] from isotropic compression tests, showing no effect of temperature (80°C) on the elastic compression parameters. The Young's modulus also regularly increases with the effective confining stress. It is important to recall that all the points tested here started from previous saturation under in-situ stress, with the smaller confining stress at half in-situ stress (4 MPa) obtained by subsequent stress release (and mobilisation of swelling). The Poisson ratio ν_{12}, equal to 0.30 at initial state under in-situ stress (8 MPa) decreases to 0.10 when the confining effective stress is released at 4 MPa, both at 25 and 80°C, confirming the independency of the elastic parameters with respect to temperature. Conversely, ν_{12} only slightly changes from 0.30 to 0.34 when the confining effective stress is increased at 16 MPa. This could indicate that the decrease observed when releasing the effective confining stress could be related to the slight swelling mobilized, an hypothesis to further confirm.

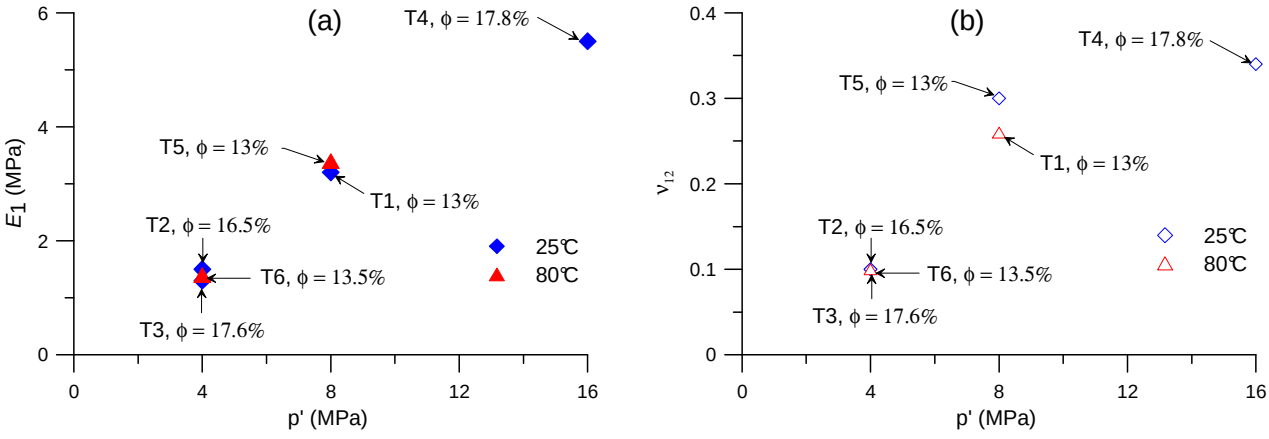

Fig. 17. Elastic parameters, (a): Young's modulus, (b): Poisson coefficient.

It seems difficult to compare the data obtained here with published data that appear to have generally been obtained based on other experimental procedure like for instance, for the Young modulus, from unconfined compression tests under not fully saturated conditions [13, 26]. Data on the Poisson ratio are less available.

5.2. Thermal volume changes

Two drained heating tests were performed to investigate the thermal volumetric response of the COx claystone under stress conditions close to in-situ (mean Terzaghi effective stress of 8 MPa) and to half the in-situ stress (mean Terzaghi effective stress of 4 MPa). They confirmed the contracting behaviour already evidenced by Mohajerani et al. [19], but with smaller contraction coefficient, as indicated in Table 5. Whereas Mohajerani et al. [19] observed a significantly anisotropic thermal response with thermal contraction coefficients of 3.15 and 6.50 × 10^{-5}°C^{-1} parallel and perpendicular to bedding, respectively, the contraction observed here is less marked and less anisotropic with $C_{T\perp}$ = 1.15 × 10^{-5}°C^{-1} perpendicular to bedding and $C_{T//}$ = 1.06 × 10^{-5} °C^{-1} parallel to bedding under in-situ stress. These values slightly decreased to $C_{T\perp}$ = 0.96 × 10^{-5}°C^{-1} and $C_{T//}$ = 0.77 × 10^{-5}°C^{-1} under half in-situ stress. This smaller contraction under smaller stress is not surprising. A possible reason of the significantly smaller contraction observed here could come from the differences in origin and in porosity between the specimens, with Mohajerani et al.'s [19] specimen significantly more porous (17.9% compared to around 13% here). More porous samples have larger clay content and clay content is the driving force of thermal contraction, given that the grains of quartz and calcite contained in the clay matrix simultaneously expand, probably resulting in some thermal damage at the interface between the grains and the clay matrix.

Table 5. Thermal contraction coefficients.

Specimen	Ref. Core	σ' (MPa)	Depth (m)	Porosity (%)	$C_{T//}$ (x 10^{-5} °C^{-1})	$C_{T\perp}$ (x 10^{-5} °C^{-1})
S5	EST45414	8	491	13.0	1.06	1.15
S6	EST45407	4	491	13.5	0.77	0.96
Mohajerani et al. (2014)	EST25820	8	480	17.9	3.15	6.50

The COx claystone is known to have supported a maximum temperature of 50°C during its geological history [35]. Unlike what was observed in the Opalinus clay by Monfared et al. [18], one does not observe here an initial thermal expansion up to 50°C. For some reason, the thermal hardening phenomenon observed on the Opalinus clay is not observed here.

5.3. Shear strength and temperature effects

Fig. 13 shows the values of peak strength (q_{max}) as a function of effective mean stress *p'* for all of the tests carried out here, together with the data obtained by Hu et al. [11] at 25°C under fully saturated conditions. The porosity of the specimens is also mentioned, given that the specimens tested by Hu et al. [11] have a porosity of around 13%. The Figure shows that the failure shear stress at 25°C are reasonably well organised with respect to their porosity, with good correspondence between tests T1 (EST45414) under in-situ confining stress (T = 25°C, p' = 8 MPa, ϕ = 13%, $q_{failure}$ = 23 MPa) and the data obtained by Hu et al. [11] at a comparable value of porosity and same temperature. The failure data obtained at 25°C with the specimens of 17% porosity are located below that at 13%, exhibiting smaller shear strength for more porous specimens, in a standard fashion. All tests at 25°C (including Hu et al. [11] data) are aligned along parallel lines that define a friction angle of 21° equal to that proposed by Hu et al. [11]. There is a decrease in cohesion that makes the more porous specimen weaker with a cohesion of 1.94 MPa at 17% compared to 4.2 MPa at 13%. Note however that the shear strength data obtained here appear to be somewhat small with respect to the data of undrained compression tests carried out for Andra by various laboratories that provided undrained compression strengths (UCS) around 20 MPa (Conil, personal communication). Indeed, Pham et al. [13] reported a UCS of 28 MPa on a specimen not fully saturated tested under a 98% relative humidity. A possibility of underestimating the shear strength by the size and shape of the specimens tested (hollow cylinder here and small cylinder for Hu et al. [11]) might be considered.

The two points obtained at a porosity of 13% at a temperature of 80°C are located slightly below the points at the same porosity and 25°C, indicating a slight reduction in shear strength due to temperature. The slight difference observed is actually in the range of the dispersion observed when testing COx specimens, and this preliminary observation is of course to be confirmed by further fully saturated and drained tests. This trend is however in agreement with previous suggestions taken from the works of Zhang et al. [25] on the Opalinus clay and of Masri et al. [27] on the Tournemire shale.

5.4. Permeability tests

Steady state radial permeability tests were performed by imposing a pore pressure increase (Δu = 0.5 MPa) on the outer face while maintaining the pore pressure equal to 1 MPa on the inner face of the hollow specimen. Water exchanges were monitored by using the PVCs and LVDTs were used to monitor local volume changes. In spite of some differences observed in the transient phase during the set up of the new effective stress conditions resulting from the application of the 1.5 MPa external pore pressure, the comparison of volume change data from LVDT measurements and from the water exchanges monitored by the PVCs was reasonably satisfactory (in spite of a tiny leak), providing some confidence in the permeability values obtained.

The radial permeability values (parallel to bedding) obtained at various stages of test T6 (points B, C and D in Fig. 4) are presented in Table 6. The values of permeability adopted and discussed below are that obtained from the outflow curves. A reference permeability value of 0.9×10^{-20} m^2 was obtained under in-situ stress conditions, a value in the range of magnitude of published data (more often measured along the axial direction) for the COx claystone, between 10^{-20} and 10^{-22} m^2 m^2 [33, 36, 37, 38].

Table 6. Effect of swelling and temperature on the COx claystone permeability (T6, porosity 13.5 %).

State	Test	Ref. Core	$k_{r\ inflow}$ (m^2)	$k_{r\ outflow}$ (m^2)
After resaturation, 25°C, [B]	T6	EST45407	1.1×10^{-20}	0.9×10^{-20}
After swelling, 25°C, [C]	T6	EST45407	1.6×10^{-20}	1.4×10^{-20}
After heating, 80°C, [D]	T6	EST45407	2.9×10^{-20}	1.8×10^{-20}

A slight change from 0.9×10^{-20} m^2 to 1.2×10^{-20} m^2 was obtained after the 0.63% swelling due to stress release from in-situ to half the in-situ stress. After drained heating at 80°C (with a thermal contraction of 0.12% followed by a swelling of 0.07%), larger inflow and outflow were observed due to the increase in water viscosity (from 8.90×10^{-4} Pa.s at 25°C to 3.55×10^{-4} Pa.s at 80°C). The permeability at 80°C appeared to be slightly larger and equal to 1.8×10^{-20} m^2. Although these first results should be confirmed, they show that the permeability is not totally independent of temperature, unlike what was previously observed on the Boom clay [39], with a slight increase with temperature. Note that this tests also showed an enhancement of swelling with temperature, with around twice more swelling at 80°C compared to 25°C under same stress conditions.

6. Conclusion

Published data on the shear strength properties of the Callovo-Oxfordian claystone exhibit some variability due to the natural variability of the deposit, to the changes of the claystone characteristics with depth and also to the testing procedures adopted. An inspection of published data indeed showed that the specimens tested came from various boreholes and from various depths and that the testing procedures were variable in terms of specimen saturation and drainage conditions. It is well known that partial saturation and drainage overestimate the shear strength properties of the COx claystone, and this seems to be somewhat linked to the variability observed in the published data.

Few data are available about the thermal response of the COx claystone. The tests carried out here were performed after careful saturation under in-situ stress conditions and in fully drained conditions thanks to the use of a hollow cylinder triaxial apparatus with reduced drainage length specially designed for testing low permeability rocks. Triaxial tests were carried out at 25 and 80°C to get some preliminary insights on the effects of temperature on the shear strength properties of the claystone. Also, some steady state radial permeability tests were carried out at 25 and 80°C to investigate the effect of temperature on the claystone permeability.

Although somewhat small with respect to the previous UCS data gathered by Andra, the shear strength data obtained here are in good agreement with that of tests also carried out in fully saturated and drained conditions by Hu et al. [11] on specimens of the same porosity (13%). Some effects of the porosity have also been evidenced, with smaller shear strength values obtained on specimens with higher porosity (17%). The thermal contraction of the COx claystone upon heating under constant in-situ stress evidenced by Mohajerani et al. [19] was confirmed. Subsequent shear tests at 80°C showed little changes of the elastic parameters with temperature, confirming the findings of Mohajerani et al. [19]. The preliminary results obtained in this work evidenced a more ductile response and slightly smaller shear strengths of the COx claystone at elevated temperature, in agreement with the few available published data on shales and claystones. Finally, radial permeability tests performed parallel to bedding demonstrated that the intrinsic permeability did not change significantly with elevated temperature, the larger flow observed at 80°C during the test being mainly due to the decrease in viscosity of water.

The preliminary data obtained here on temperature effects on the shear strength behaviour of the COx claystone need to be further confirmed by complementary tests, they

however confirm some trends already observed on the COx claystone and on other clay rocks. A better understanding of the thermo-hydro-mechanical response of claystone will allow a better understanding and modelling of the coupled THM actions that prevail in the close field once the exothermic wastes have been placed.

Acknowledgements

The authors are grateful to Andra who founded this work that is part of the PhD work of the first author. Andra also provided the COx specimens tested in this work.

References

[1] ANDRA (2005). Synthesis argile: evaluation of the feasibility of a geological repository in argillaceous formation. http://www.andra.fr/international/ download/andra-international-en/document/editions/266va.pdf

[2] Hueckel T, Baldi G. Thermoplasticity of saturated clays: experimental constitutive study. Journal of Geotechnical Engineering 1990; 116(12):1768–1796.

[3] Hueckel T, Pellegrini R. Thermoplastic modeling of undrained failure of saturated clay due to heating. Soils Found 1991; 31(3):1-16.

[4] Sultan N, Delage P, Cui YJ. Temperature effects on the volume change behaviour of Boom clay. Engineering Geology 2002; 64(2-3):135-145.

[5] Cekerevac C, Laloui L. Experimental study of thermal effects on the mechanical behaviour of a clay. International Journal for Numerical and Analytical Methods in Geomechanics 2004; 28:209–228.

[6] Hueckel T, François B, Laloui L. Explaining thermal failure in saturated clays. Géotechnique 2009; 59 (3):197-212.

[7] Chiarelli AS. Étude expérimentale et modélisation du comportement mécanique de l'argilite de l'est. PhD thesis, Université Lille I ; 2000.

[8] Chiarelli AS, Shao JF, Hoteit N. Modeling of elastoplastic damage behavior of a claystone. International Journal of Plasticity 2003; 19:23-45.

[9] Zhang CL, Rothfuchs T. Experimental study of the hydro-mechanical behaviour of the Callovo-Oxfordian argillite. Applied Clay Science 2004; 26(1-4): 325-336.

[10] Hoxha D, Giraud A, Homand F, Auvray C. Saturated and unsaturated behaviour modelling of Meuse-Haute/Marne argillite. International Journal of Plasticity 2007;

23:733–766.

[11] Hu DW, Zhang F, Shao JF. Experimental study of poromechanical behavior of saturated claystone under triaxial compression. Acta Geotechnica 2014a; 9:207-214.

[12] Valès F, Nguyen Minh D, Gharbi H, Rejeb A. Experimental study of the influence of the degree of saturation on physical and mechanical properties in Tournemire shale (France). Applied Clay Science 2004; 26:197–207.

[13] Pham QT, Vales F, Malinsky L, Nguyen Minh D, Gharbi H. Effects of desaturation-resaturation on mudstone. Physics and Chemistry of the Earth 2007; 32:646–655.

[14] Yang D, Chanchole S, Valli P, Chen L. Study of the Anisotropic Properties of Argillite Under Moisture and Mechanical Loads. Rock Mechanics and Rock Engineering 2012; 46(2):247–257.

[15] Wu B, Tan CP, Aoki T. Specially designed techniques for conducting consolidated undrained triaxial tests on low permeability shales. International Journal of Rock Mechanics and Mining Sciences 1997; 34:3-4), paper No. 336.

[16] Monfared M, Delage P, Sulem J, Mohajerani M, Tang AM, De Laure E. A new hollow cylinder triaxial cell to study the behaviour of geomaterials with low permeability. International Journal of Rock Mechanics and Mining Sciences 2011; 48 (4):637-649.

[17] Monfared M, Sulem J, Delage P, Mohajerani M. On the THM behaviour of a sheared Boom clay sample: Application to the behaviour and sealing properties of the EDZ. Engineering Geology 2012; 124:47-58.

[18] Monfared M, Sulem J, Delage P, Mohajerani M. A laboratory investigation on thermal properties of the Opalinus claystone. International Journal of Rock Mechanics and Rock Engineering 2011b; 44(6):735-747.

[19] Mohajerani M, Delage P, Sulem J, Monfared M, Tang A.M, Gatmiri B. The thermal volume change of the Callovo-Oxfordian claystone. International Journal of Rock Mechanics and Rock Engineering 2014; 47:131-142.

[20] Gaucher G, Robelin C, Matray JM, Négrel G, Gros Y, Heitz JF, Vinsot A, Rebours H, Cassagnabère, Bouchet A. ANDRA underground research laboratory: interpretation of the mineralogical and geochemical data acquired in the Callovian-Oxfordian formation by investigative drilling. Physics and Chemistry of the Earth 2004; 29:55-77.

[21] Yven B, Sammartino S, Geroud Y, Homand F, Villieras F. Mineralogy, texture and porosity of Callovo-Oxfordian claystones of the Meuse/Haute-Marne region (eastern Paris Basin). Mémoires de la Société géologique de France, ISSN 0249-7549 2007; 178: 73-90.

[22] Hu DW, Zhang F, Shao JF, Gatmiri B. Influences of Mineralogy and Water Content on the Mechanical Properties of Argillite. Rock Mechanics and Rock Engineering 2014b; 47:157-166.

[23] Zhang F, Xie SY, Hu DW, Shao JF, Gatmiri B. Effect of water content and structural anisotropy on mechanical property of claystone. Applied Clay Science 2012; 69:79–86.

[24] Fredlund DG, Rahardjo H, Fredlund MD. Unsaturated soil mechanics in engineering practice. 2012; Wiley, New-York.

[25] Zhang CL, Rothfuchs T, Su K, Hoteit N. Experimental study of the thermo-hydro-mechanical behaviour of indurated clays. Phys Chem Earth Parts A/B/C 2007; 32(8–14):957–965.

[26] Zhang F, Hu DW, Xie SY, Shao JF. Influences of temperature and water content on mechanical property of argillite. European Journal of Environmental and Civil Engineering 2014; 18(2):173–189.

[27] Masri M, Sibai M, Shao JF, Mainguy M. Experimental investigation of the effect of temperature on the mechanical behavior of Tournemire shale. International Journal of Rock Mechanics and Mining Sciences 2014; 70:185–191.

[28] Delage P, Le TT, Tang AM, Cui YJ, Li XL. Suction effects in deep Boom clay block specimens. Géotechnique 2007; 57(1):239–244.

[29] Mohajerani M, Delage P, Monfared M, Tang A.M, Sulem J, Gatmiri B. A laboratory investigation of thermally induced pore pressures in the Callovo-Oxfordian claystone. International Journal of Rock Mechanics and Mining Sciences 2012; 52:112-121.

[30] Wileveau Y, Cornet FH, Desroches J, Blumling P. Complete in situ stressdetermination in an argillite sedimentary formation. Phys Chem Earth A/B/C 2007; 32(8–14):866–78.

[31] Monfared M, Sulem J, Delage P, Mohajerani M. Temperature and Damage Impact on the Permeability of Opalinus Clay. International Journal of Rock Mechanics and Rock Engineering 2014; 47:101–110.

[32] Li Y, Weetjens E, Sillen X, Vietor T, Li X, Delage P, Labiouse V, Charlier R. Consequences of the thermal transient on the evolution of the damaged zone around a repository for heat-emitting high-level radioactive waste in a clay formation: a performance assessment perspective. Rock Mechanics and Rock Engineering 2014; 47:3-19.

[33] Mohajerani M, Delage P, Monfared M, Tang A.M, Sulem J, Gatmiri B. Oedometric compression and swelling behaviour of the Callovo-Oxfordian argillite. International Journal of Rock Mechanics and Mining Sciences 2011; 48(4):606-615.

[34] Cheng A HD. Material coefficients of anisotropic poroelasticity. International Journal of Rock Mechanics and Mining Sciences 1997; 34(2):199-205.

[35] Blaise T, Barbarand J, Kars M, Ploquin F et al. Reconstruction of low temperature (<100 _C) burial in sedimentary basins: A comparison of geothermometer in the intracontinental Paris Basin. Marine and Petroleum Geology 2013; **http://dx.doi.org/10.1016/j.marpetgeo.2013.08.019**.

[36] Escoffier S. Caractérisation expériementale du comportement hydro-mécanique des argillites de Meuse/ Haute Marne. PhD thesis, INPL Nancy ; 2002.

[37] Escoffier S, Homand F, Giraud A, Hoteit N, Su K. Under stress permeability determination of the Meuse/Haute-Marne mudstone. Engineering Geology 2005; 81:329–340.

[38] Delay J, Trouiller A, Lavanchy JM. Propriétés hydrodynamiques du Callovo-Oxfordien dans l'Est du bassin de Paris : comparaison des résultats obtenus selon différentes approches 2006 ; C.R. Geoscience 338.

[39] Delage P, Sultan N, Cui YJ. On the thermal consolidation of Boom clay. Canadian Geotechnical Journal 2000; 37(2):343-354.

Chapitre 4 : Propriétés d'auto-colmatage de l'argilite du Callovo-Oxfordien

Introduction

Dans le contexte du stockage dans les couches géologiques profondes, l'excavation des galeries engendre une perturbation majeure et conduit à la création de la zone endommagée par l'excavation (EDZ, Tsang et al. 2005). En raison de la redistribution des contraintes et la convergence des parois des galeries lors de l'excavation, un réseau de plans de cisaillement se développe dans l'EDZ, illustré dans la Figure 1 (Armand et al. 2013)

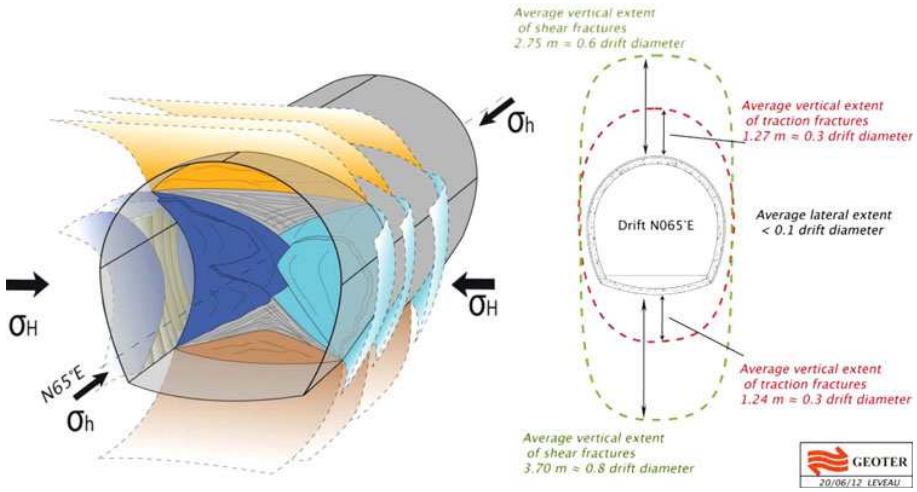

Figure 1. Modèle conceptuel d'un réseau de fractures induites autour d'une galerie parallèle à la contrainte horizontale majeure.

Les déchets de haute activité et à vie longue sont exothermiques et la température peut augmenter jusqu'à 90°C à proximité des parois des galeries dans la conception française (ANDRA, 2005). Cette augmentation de température conduit à une augmentation de pression interstitielle et une diminution de la contrainte moyenne effective dans l'EDZ due au phénomène de pressurisation thermique (e.g. Mohajerani et al. 2012). Cela pourrait entraîner une rupture thermo-mécanique (Hueckel and Pellegrini 1991, Hueckel et al. 2009) ou une réactivation thermique d'une bande de cisaillement préexistante (Monfared et al. 2012).

Les propriétés d'auto-colmatage des fractures dans les argilites envisagées pour le stockage souterrain profond ont été étudiées sur l'argile à Opalinus par Monfared et al. (2014) et Zhang et Rothfuchs (2008) et sur l'argilite du COx par Davy et al. (2007) et Zhang (2013). Les résultats obtenus ont montré que l'effet de la bande de cisaillement sur la perméabilité n'est pas significatif, ce qui confirme les bonnes propriétés d'auto-colmatage de l'argilite. Dans ce cadre et en raison de l'existence limitée des données sur l'argilite du COx, d'autres investigations doivent être effectuées afin d'améliorer la compréhension et la prévision des processus d'auto-colmatage.

Dans ce chapitre on présente les résultats d'un essai spécifique concernant la réponse thermo-hydro-mécanique d'une discontinuité de cisaillement, sous la forme d'un article soumis à la revue internationale «*Rock Mechanics and Rock Engineering*».

On the Thermo-Hydro-Mechanical behaviour of a sheared Callovo-Oxfordian claystone sample with respect to the EDZ behaviour

Hamza MENACEUR[1], Pierre DELAGE[1], Anh Minh TANG[1], Nathalie CONIL[2]

[1] *Ecole des Ponts ParisTech, Navier/CERMES, France*

[2] *ANDRA, Chatenay-Malabry, France*

Abstract

To better understand the impact of temperature elevation on the response of the excavation damaged zone around repository cells and galleries for radioactive waste disposal, the combined effects of shear and temperature elevation were investigated in the laboratory on the Callovo-Oxfordian claystone. To do so, a hollow cylinder thermal triaxial cell with short drainage path specifically developed for low permeability rocks was used. Once properly saturated under stress conditions close to in-situ, the specimen was sheared along a constant effective mean stress path mimicking the stress path followed during gallery excavation. The shear stress was afterwards released and an undrained heating test was performed on the sheared specimen. It was observed that the temperature increase under undrained conditions led to a thermal increase in pore water pressure resulting in a decrease in mean effective stress that brought back the sheared specimen to failure, evidencing a thermally induced failure. Steady state radial permeability tests performed at various stages of the test demonstrated that the overall permeability of the sheared specimen was comparable to that before shearing, confirming the excellent self-sealing properties of the Callovo-Oxfordian claystone. This shows that, in spite of being possibly remobilized by temperature elevation, the EDZ will keep an overall permeability constant equal to that of the massive rock, keeping the same isolation properties.

Keywords

Claystone · Permeability · Excavation damaged zone · Shear band · Undrained heating · Self sealing.

1. Introduction

The Callovo-Oxfordian (COx) claystone has been selected as a potential host rock for deep geological repository of high-level radioactive waste in France because of its low permeability, good self sealing properties and good radionuclide adsorption capacity. The host rock around the repository cells containing the exothermic waste canisters will be submitted to various coupled mechanical, hydraulic and thermal phenomena including the development of an excavation damaged zone (EDZ) that might affect the overall rock permeability in the close field (Armand et al. 2014). The heat emitted by the high-level radioactive waste will increase temperature in the host rock, with a maximum admitted temperature of 90°C around the waste canisters in the French concept (ANDRA 2012). This temperature elevation might have some effects on the crack network of the EDZ. This problem was investigated in the framework of the TIMODAZ European research project devoted to the "Thermal Impact on the Damaged Zone around a radioactive waste disposal in clay host rocks" (Li et al. 2014). The temperature elevation might also lead to an increase in pore pressure and a decrease in effective stress in the EDZ due to thermal pressurization (Mohajerani et al. 2012), resulting in possible thermo-mechanical failure (Hueckel and Pellegrini 1991; Hueckel et al. 2009). In this context, Monfared et al. (2012) investigated the thermal reactivation of a pre-existing shear band in undrained conditions in the Boom clay.

The effects of cracks on water transfers have been investigated by various authors in various clays and claystones. The experimental investigation of Zhang (2011) on fractured COx and Opalinus clay specimens showed that the permeability of fractured specimens decreased significantly by several orders of magnitude upon hydration of the cracks, thanks to the hydration of the smectite minerals in the clay matrix that resulted in clogging the fractures. Davy et al. (2007) also observed that the permeability of a confined cylindrical COx specimen containing an artificial crack made by previously carrying out a Brazilian tensile test was comparable to that of the intact claystone. Comparable conclusions were drawn by Zhang (2011) on the Opalinus clay and the COx claystone and by Monfared et al. (2012) on the Boom clay, confirming their good self sealing capacity.

The effects of heating on the permeability of intact clays have been investigated by Morin and Silva (1984); Delage et al. (2000); Zhang (2013), among others. Data showed that the change in water transfer with temperature was only due to the changes in water viscosity, resulting in a constant intrinsic permeability with respect to temperature changes. Note however that available literature data on the effects of temperature on the permeability of

damaged clays and claystones materials are scarce. Recently, Monfared et al. (2014) showed that the intrinsic permeability of a sheared Opalinus clay specimen remained almost equal to that of intact specimens at both 25 and 80°C, confirming the good self-sealing properties of the Opalinus clay at elevated temperature.

The presents work aims at investigating the effect of temperature elevation on a COx claystone specimen previously damaged by a shear test that resulted in the development of a network of shear planes, following the approach followed by Monfared et al. (2012) on the Boom clay. Once sheared, the shear stress was released prior to reactivate the shear bands by temperature elevation. Permeability tests run at various stages of the test allowed to monitor possible changes in permeability due to damage and temperature elevation. To do so, a thermal hollow cylinder triaxial cell recently developed for this purpose (Monfared et al. 2011a) was used. The two main characteristics of this device are, on the one hand, a short drainage path (half the thickness of the cylinder) allowing for good saturation and drainage conditions and, on the other hand, the possibility of running radial permeability tests at various temperatures by establishing a water flow between the inner and outer faces of the hollow cylinder through the shear plane network.

2. Material and methods

2.1. The Callovo-Oxfordian claystone

The Callovo-Oxfordian claystone is a marine sediment from the Jurassic period, deposited 155 millions years ago between the Callovian and the Oxfordian ages in the western area of the Parisian basin. It has been since that time submitted to various significant tectonic effects including some horizontal stresses resulting from the Alpine orogenese.

The mineralogical composition of the COx claystone varies with depth with significant changes in carbonate and clay contents. The COx total connected porosity varies between 14% in carbonated levels and 19.5% in more argillaceous levels (Yven et al. 2007). At the Underground Research Laboratory (URL) at Bure, Eastern France, the formation (at 490m depth) is relatively homogenous and made up of a clay matrix containing carbonates, quartz and accessory minerals. The clay fraction (45-50%) is made up of mixed layers of interstratified illite/smectite (20 – 24%) and illite (17-21%) with also small amounts of kaolinite and chlorite. It also contains 20% calcite, 23% quartz and 4% of various other minerals such as feldspars, pyrite, dolomite, siderite and phosphate (Gaucher et al. 2004).

The smectite percentage in the clay fraction is responsible for the swelling and self-sealing behaviour of the COx claystone (Davy et al. 2007; Zhang and Rothfuchs 2008; Mohajerani et al. 2011).

In the present work, an experiment was performed on a hollow cylinder specimen taken from a core (EST30734) perpendicular to the bedding, extracted at the same level as that of the URL. The specimen was carefully trimmed from 100 mm diameter core on a lathe. The initial characteristics of the sample are presented in Table 1. The initial gravimetric water content of the sample was 7.4 %. The porosity and degree of saturation were calculated by measuring the sample volume by hydrostatic weighing. The initial total suction was determined by using a dew point potentiometer (WP4, Decagon). As seen in the Table 1, the sample is not saturated at initial state with a degree of saturation of 94% corresponding to a suction of 6.1 MPa with a porosity of 17.5%. The partial saturation of the specimen resulted from the combined actions of coring, transport, storage and trimming.

Table 1. Initial characteristics of the tested sample.

	Height (mm)	Water content (%)	Degree of saturation (%)	Porosity (%)	Dry unit mass (Mg/m^3)	Suction (MPa)
EST30734	73.37	7.4	94	17.5	2.23	6.1

2.2. Experimental device

The hollow cylinder triaxial cell specially designed (Monfared et al. 2011a) to investigate the thermo-hydro-mechanical behaviour of low permeability clays and claystones was used. A global overview of the cell is presented in Fig. 1a, that schematically shows the hollow cylinder specimen (external diameter φ_{ext} = 100 mm, internal diameter φ_{int} = 60 mm, height h = 70-80 mm) inside the triaxial cell. The same confining pressure is applied along both the external and internal lateral faces of the sample. As shown in Fig. 1a-b, a major advantage of this device is the presence of two lateral drainages in the inner and the outer walls of the hollow cylinder sample made up of two geotextiles bands placed along the sample with no connection with the upper and lower drainages. These lateral drainages reduce the specimen drainage length down to half of the thickness of the hollow cylinder (10 mm). They also allow carrying out radial permeability tests so as to capture the effects of shear bands on the soil's permeability. Compared to standard full cylinder triaxial samples with drainage at top and bottom ends, the short drainage path allows reducing the time

needed to fully resaturate an initially unsaturated claystone sample by a factor of seven (Monfared et al. 2011a). Also, satisfactory drainage conditions are achieved during mechanical and thermal loading provided the strain rate and temperature elevation rate are small enough.

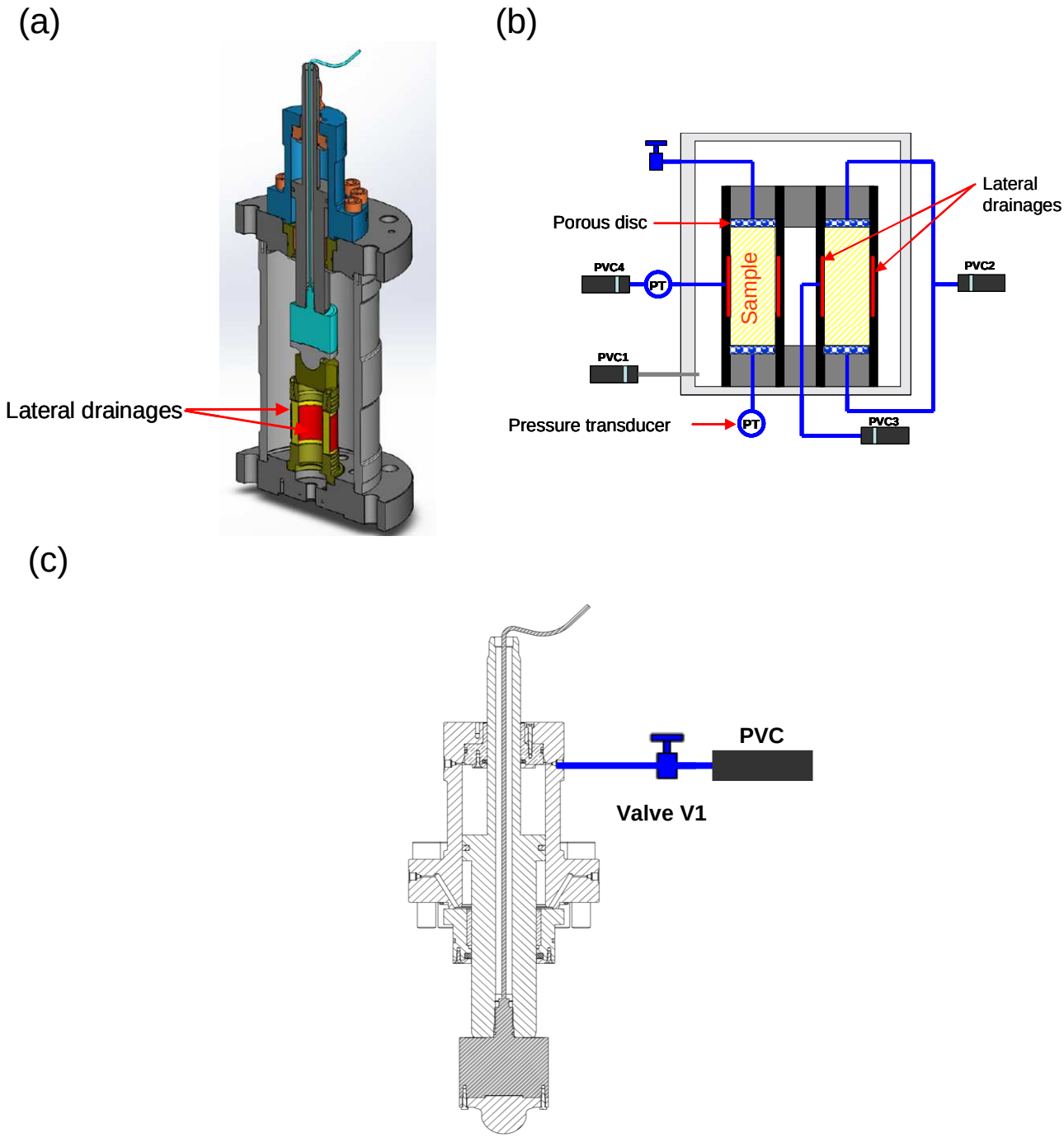

Fig. 1. (a) Hollow cylinder triaxial cell, (b) general setting of the connections with the pressure volume controllers (PVC), (c) System for applying deviatoric stress.

Fig. 1b also shows a schematic view of the hydraulic connections between the sample, the pressure-volume controllers (PVC) and the pressure transducers (PT). PVC1 is used to apply the confining pressure whereas the other three PVCs are used to apply and control the pore fluid pressure. The device is also equipped with two axial and four radial local displacement transducers (LVDTs, accuracy ± 1μm) to monitor local strains. The heating system consists of a heating electric belt placed around the cell with a temperature regulator with an accuracy of ± 0.1°C. Temperature is measured inside the cell close to the sample by a thermocouple. An insulating layer covers the cell in order to limit heat exchanges with the surrounding environment.

The shear stress is applied by using an integrated piston specially developed and manufactured (Fig. 1c). This piston is hydraulically activated by a pressure-volume controller (maximum pressure of 60 MPa). As shown in Fig. 1c, the piston is connected to the PVC, which controls the movement of the piston and thus applies the shear stress. The applied force is directly measured by a local immersed force sensor installed at the end of the piston.

2.3. Sample resaturation

As shown by Monfared et al. (2011a), an interesting feature of the hollow cylinder triaxial cell is to ensure good initial saturation of samples of very low permeability (around 10^{-20} m^2 in the case of the COx claystone) within a reasonable period of time, thanks to a reduced drainage path. As recalled by Delage et al. (2007) on the Boom Clay, Monfared et al. (2011b) on the Opalinus clay and Mohajerani et al. (2011) on the COx claystone, it is important to resaturate specimens of swelling clays under stress conditions close to the in-situ ones in order to avoid further perturbation due to swelling during hydration.

The in-situ state of stress in the Bure URL has been investigated in details by Wileveau et al. (2007) who provided the following values:

- vertical total stress σ_v = 12.7 MPa
- minor horizontal total stress σ_h = 12.4 MPa
- major horizontal total stress σ_H = 12.7–14.8 MPa
- pore pressure u = 4.9 MPa.

Mohajerani et al. (2014) used a confining stress of 12 MPa and a pore pressure of 4 MPa, resulting in a Terzaghi effective stress of 8 MPa when performing experiments using the hollow cylinder triaxial cell. Perforation of the neoprene jacket has been observed during some experiments under such high pressures. To avoid this problem, the confining pressure

applied in this study was equal to 9 MPa and the pore pressure to 1 MPa, so as to apply the same Terzaghi mean effective stress of 8 MPa. Once applied the confining stress, specimen saturation was carried out by injecting water from the back-pressure PVC.

Fig. 2 shows the volume changes calculated from the water injected from the PVC compared to that monitored by local LVDT measurements during the saturation phase. The two curves show a stabilisation after 2 days. A swelling rate of 0.02%/day is afterwards obtained from both the LVDT measurements and the volume of water injected. The higher total volume obtained from the injected water is related the saturation of the soil specimen and of the porous elements of the drainage system (upper and lower porous discs, lateral geotextiles).

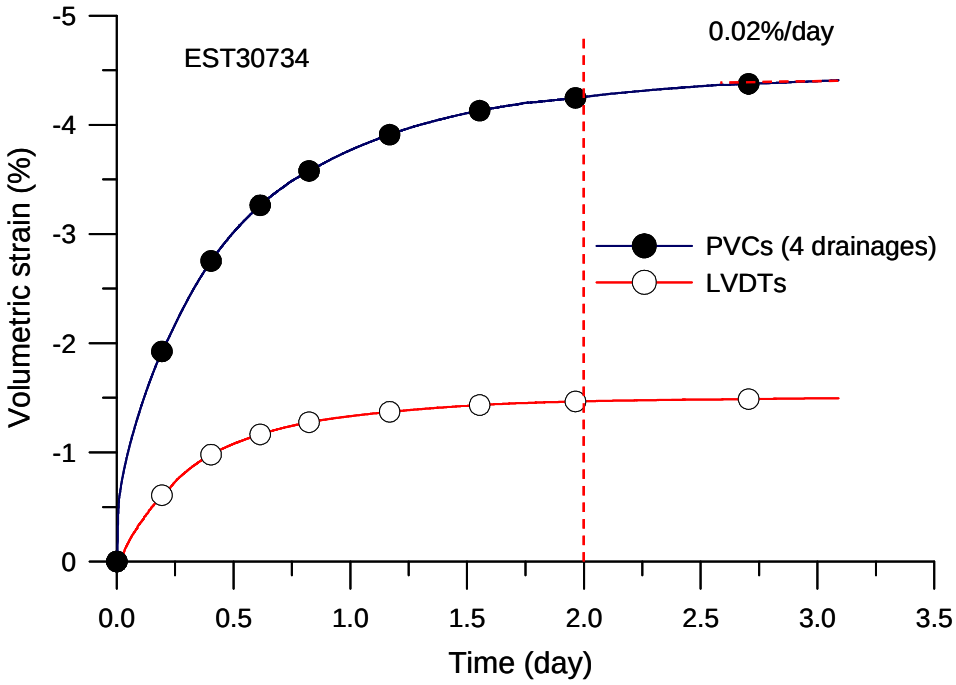

Fig. 2. Volume changes and water exchanges during saturation.

2.4. Radial permeability tests

Steady state radial permeability tests were carried out by applying a pressure difference between the outer and the inner lateral faces of the hollow cylinder specimen and by measuring the inflow and outflow water fluxes by using the PVCs. This procedure is particularly adapted to investigate the effects of shear bands on the permeability of sheared hollow cylinder specimens. Permeability tests were carried out on a specimen submitted to an initial back pressure of 1.0 MPa by closing the valves connected to the top and bottom of the

sample and by applying a pressure of 1.5 MPa through the external geotextile while maintaining the pressure in the internal geotextile equal to 1.0 MPa.

In a standard fashion, the radial intrinsic permeability k_r (m^2) was calculated using the flow rates as follows:

$$k_r = \frac{Q\mu_w \ln(R_{ext} / R_{\text{int}})}{2\pi h \Delta u} \quad (1)$$

where Q is the water flow; μ_w the water viscosity (equal to 8.90 x 10^{-4} Pa.s at 25°C and 3.55 x 10^{-4} Pa.s at 80°C), R_{ext} and R_{int} the external and internal sample radius, respectively (R_{ext} = 50 mm; R_{int} = 30 mm); h the flow height (h =50 mm); and Δu the pressure difference between the inner and outer walls of the sample (Δu = 0.5 MPa).

2.5. Experimental program

The sample was tested along a thermo-hydro-mechanical path aimed at reproducing the stress state in the close field of the excavated gallery. The path followed is shown in Fig. 3. The test was aimed at investigating the possibility of reactivating a shear band by thermal pressurisation and at capturing the effect of the shear band formation on the radial permeability.

Once resaturated close to the in-situ stress state [point B in Figure 3], the sample was sheared at 25°C [B-C] in drained conditions along a constant mean effective stress *p'* path. The axial deformation was afterwards kept constant, resulting in a release in shear stress *q* [C-D] during the radial permeability test at point C. Then, the sheared sample was heated at 80°C in undrained conditions [D-E]. Finally, the cell temperature was reduced to 25°C and the stress state was set at isotropic condition (point F: p = 6.6 MPa) prior to running a drained heating test. Radial steady state permeability tests were carried out after initial resaturation (point [B]), right after shearing [C], after shear stress release [D], after heating the sheared sample up to 80°C [E] and after cooling the sheared sample down to 25°C [F].

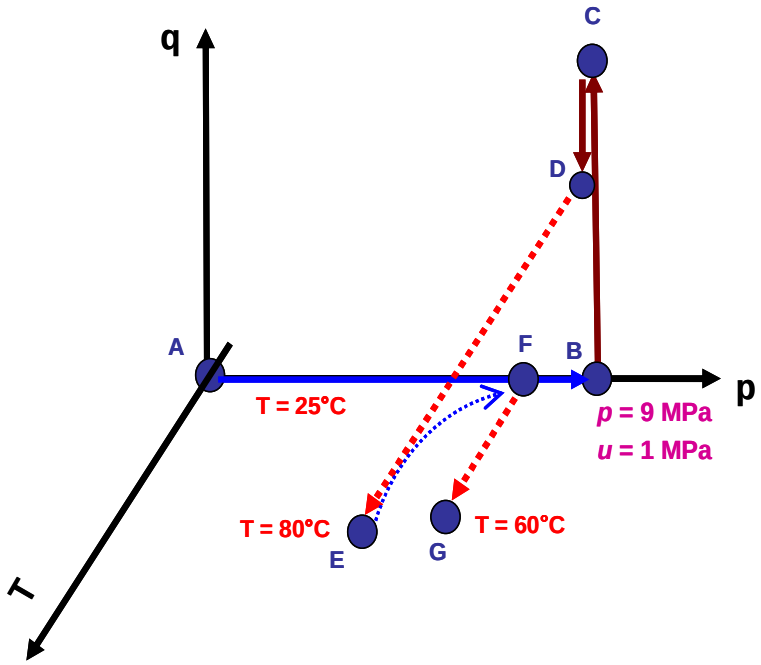

Fig. 3. Schematic view of the THM loading paths followed.

3. Experimental results

3.1. Initial radial permeability (point B)

Two permeability tests were performed at point B to check the repeatability of the procedure. The water exchanges monitored by the upstream and downstream PVCs during the first test are presented in Fig. 4a. The axial and radial strains obtained from the local LVDT measurements are plotted in Fig. 4b-c, with an almost similar response observed for measurements in the same direction. Fig. 4d shows the changes in specimen volume during the test, calculated from both the water exchanges monitored by the upstream and downstream PVCs and the local LVDT measurements. Good correspondence is observed between these two independent measurements, bringing confidence in their quality and in the water tightness of the system. The volume changes curves from LVDTs also show that after a transient infiltration phase during the first 10 hours, a constant infiltration rate of 1.2×10^{-21} % h^{-1} is afterwards observed. This trend is typical of swelling clays and claystones and has already been observed by, Monfared et al. (2011b) on the Opalinus clay and Mohajerani et al. (2011) on the COx claystone and, on the Boom clay, Cui et al. (2009); Monfared et al. (2012) and Bésuelle et al. (2014).

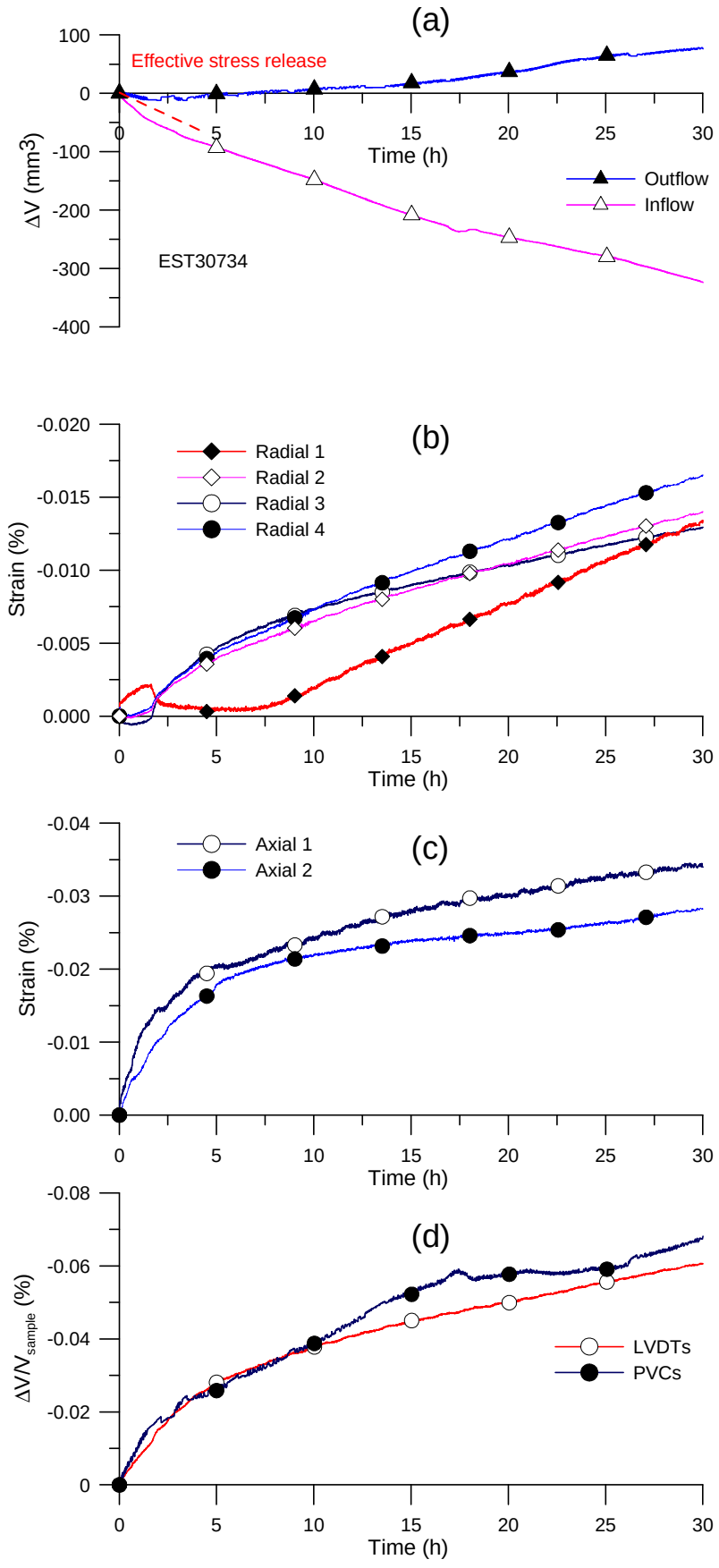

Fig. 4. Radial steady state permeability test at point B (first test), (a): inflow and outflow, (b): radial strains, (c): axial strains, (d): volume change.

The flow curves of Fig. 4a show that the upstream PVC injects water (at 1.5 MPa) into the sample (initial back pressure 1 MPa) from the beginning of the test, as expected. However, one observes that it is necessary to wait for 3.5 hours before monitoring any outflow with the downstream PVC. Also, the downstream PVC indicates the occurrence of water infiltration into the sample during the 3 first hours through the internal phase submitted to the smallest 1 MPa pressure. Combined observation of Fig. 4a and Fig. 4d shows that this infiltration through the downstream face corresponds to the transient phase of the swelling process observed in Fig. 4d. This transient swelling phase is due to the release of the effective stress profile along the radial path followed by the water flow due to the application of the 1.5 MPa pressure along the outer face of the sample. Once this transient phase completed, a steady phase occurs with some injected water kept within the sample, explaining the difference between the outflow and inflow after 25 hours in Fig. 4a.

By applying Darcy's law during the last 5 hours of the test on the outflow data, a value of radial permeability of 7.3×10^{-21} m^2. Note that an apparent smaller value of 2.2×10^{-21} m^2 (including the water absorbed by swelling) is derived from the inflow curve.

For the second test run in same conditions, Fig. 5a shows comparable response in terms of inflow and outflow curves with respect to stress release during the transient initial phase. However, as seen in Fig. 5b, volume change stabilisation was observed in this second test after 10 hours with no steady state swelling as observed previously. As a consequence, comparable permeability values (4.8×10^{-21} m^2 and 5.0×10^{-21} m^2) were obtained in the final steady state phase from outflow and inflow data, respectively.

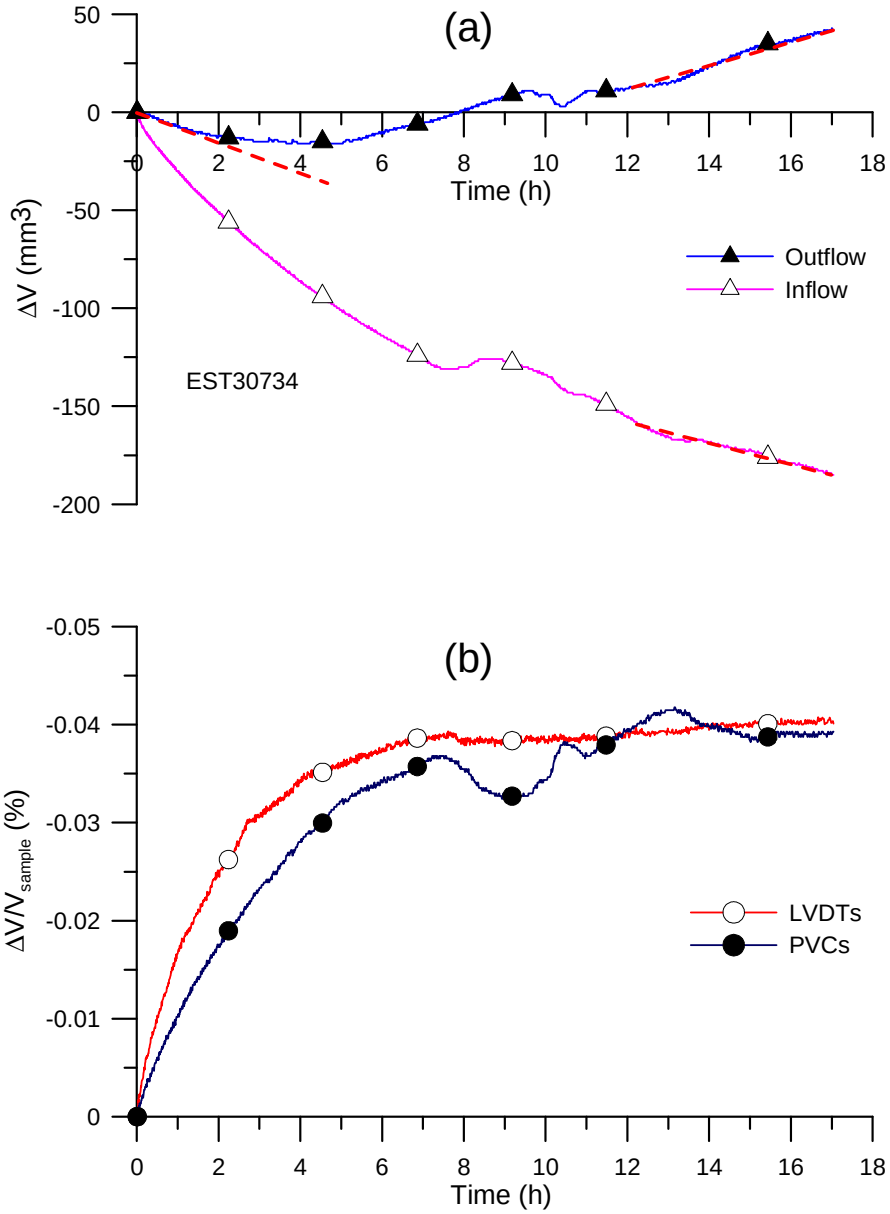

Fig. 5. Radial permeability at point B (second test), (a): inflow and outflow, (b): volume change.

3.2. Shearing under constant effective mean stress at drained conditions (path B-C)

Once resaturated under in situ stress state at 25°C, the sample was loaded with a constant axial displacement rate of 0.35µm/min (chosen low enough to ensure drained conditions, see Monfared et al. 2011a) while maintaining the mean stress constant. This was achieved by controlling the change in confining pressure ($\Delta\sigma_3$) following the relation $\Delta\sigma_3 = -\frac{dq}{3}$ (where q is the shear stress $\sigma_1 - \sigma_3$). The changes in axial, radial and volumetric strains with respect to shear stress are presented in Fig. 6. One observes that the shear stress

reaches a maximum value of 11 MPa at 0.52% of axial strain and -0.25% of radial strain. A contracting-dilating behaviour is observed before peak with a transition at q = 8.2 MPa. Note that the post-peak response is governed by strain localisation and the mobilisation of shear planes.

The photographs of the sample at the end of the test are presented in Fig. 7. One observes a more apparent shear band with an inclination of 67° with respect to horizontal, among a network of other shear bands.

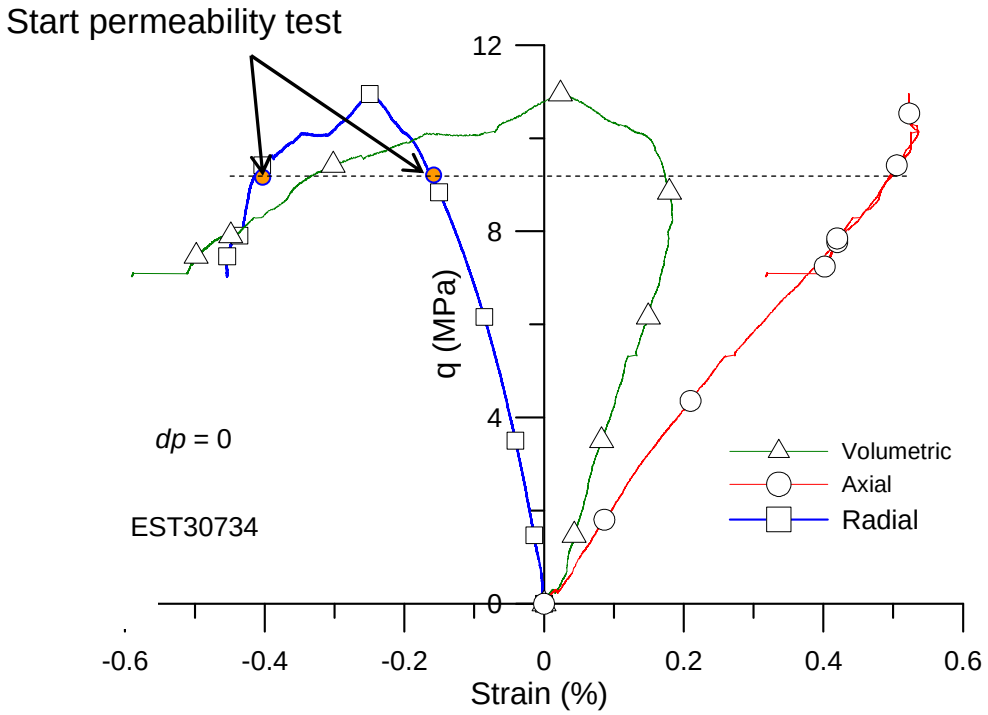

Fig. 6. Stress-strain for the shear test under constant effective mean stress at drained conditions (path B-C).

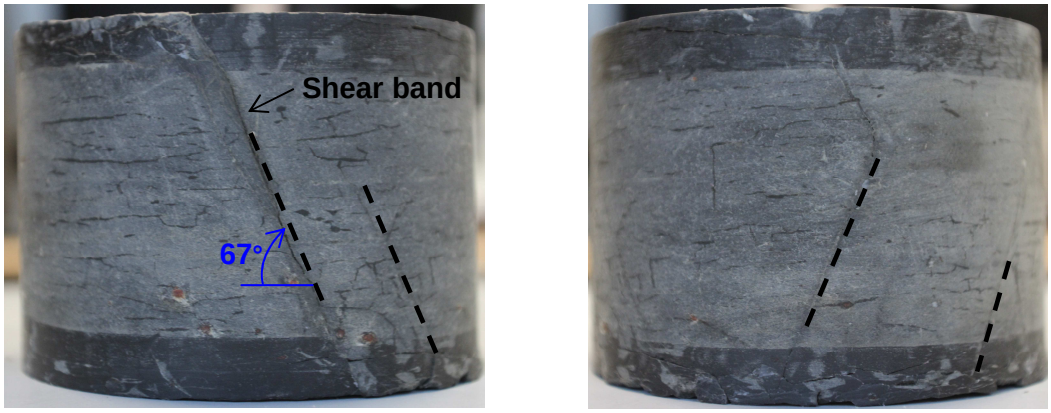

Fig. 7. COx specimen at the end of the test.

The effect of the shear bands on the overall specimen permeability was investigated by carrying out radial permeability tests after shearing at point C, as indicated in Table 2. Once the sample sheared (Point C), a permeability test was carried out. As shown in Fig. 6, a decrease in shear stress took place once the permeability test started. This decrease can be related to the reactivation of shear bands due to the application of 0.5 MPa of excess pressure. Fig. 8a, which presents both the inflow and outflow curves with respect to time, shows no effect of the stress release phase, with water expelled in the downstream PVC since the beginning of the test. Fig. 8bshows the sample volume change during the permeability test. One observes that the volume change calculated from LVDT measurements is larger than that calculated from water exchanges because LVDT measurements incorporate both the swelling of the sample and the possible sliding of blocks along some shear bands. Unlike in other permeability tests, no satisfactory correspondence was observed between the responses of axial and radial LVDTs (Fig. 8c-d), with in particular opposite responses of the axial LVDTs. This confirms the mobilisation of shear planes and the relative movement of blocks during the permeability test.

Inspection of Fig. 8a shows that the outflow rate, maximal at the beginning of the test, afterwards decreases to finally reach a final slope (after 16 h) that corresponds to a permeability of 4.1×10^{-21} m^2, a value comparable to that obtained from Fig. 5 (the permeability that would be calculated from the outflow rate at the beginning of the test is equal to 1.7×10^{-20} m^2).

Table 2. Effect of the shear loading and heating on COx claystone permeability (EST30734).

	$k_{r\ inflow}$ (m^2)	$k_{r\ outflow}$ (m^2)	$k_{r\ mean}$ (m^2)
Before shearing, (B)	5.0×10^{-21}	4.8×10^{-21}	4.9×10^{-21}
After shearing, (C)	1.8×10^{-20}	4.1×10^{-21}	1.1×10^{-20}
After deviatoric stress release, (D)	5.6×10^{-21}	3.2×10^{-21}	4.4×10^{-21}
At 80°C, (E)	4.1×10^{-21}	2.0×10^{-21}	3.0×10^{-21}
After cooling, 25°C, (F)	6.1×10^{-21}	1.7×10^{-21}	3.9×10^{-21}

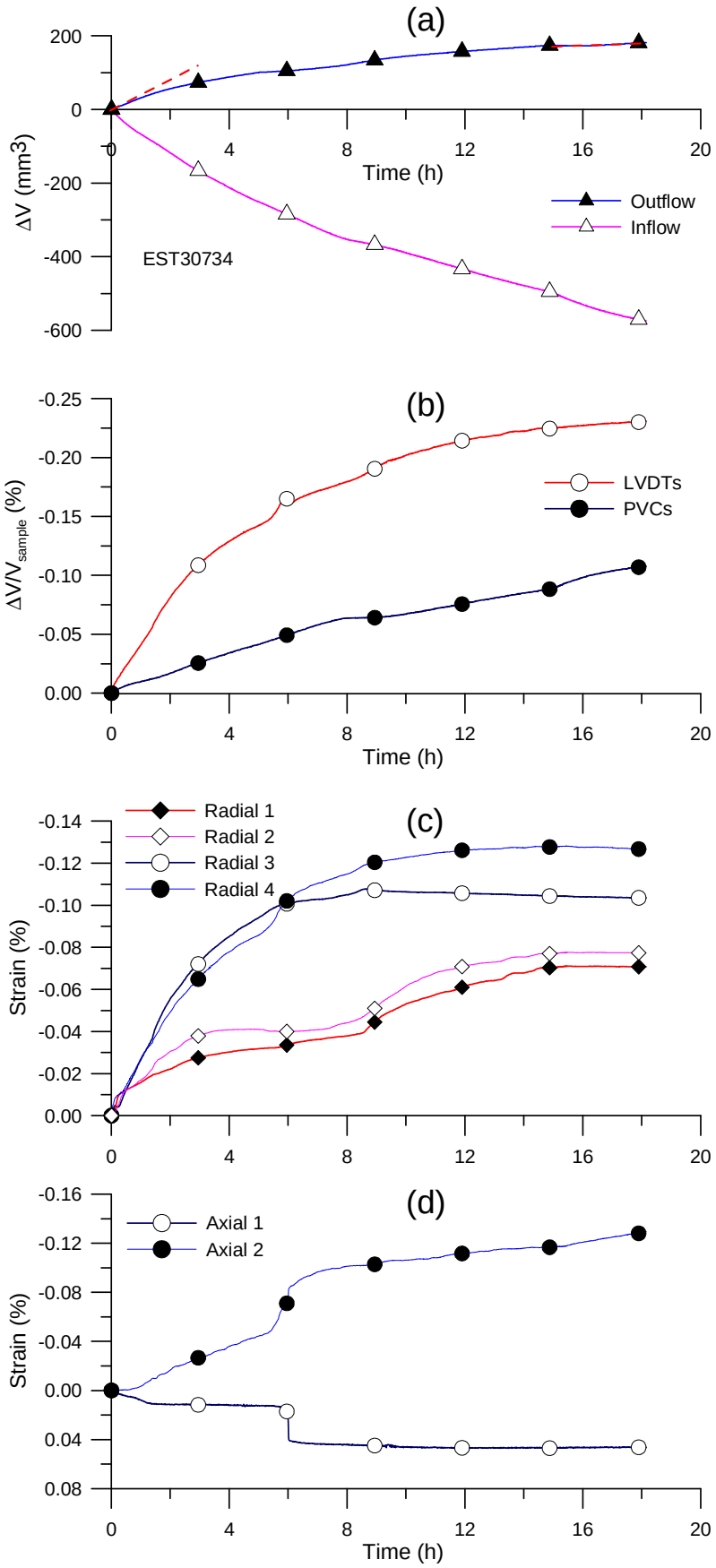

Fig. 8. Radial permeability test at point C, (a): inflow and outflow, (b): volume change, (c): radial strains, (d): axial strains.

Fig. 9 shows the results of a permeability test that was carried out after the two days (Point D). The response in terms of inflow and outflow is comparable to that observed at initial state with some effect of effective stress release at the beginning. The calculated values of radial permeability are equal to 5.6×10^{-21} m^2 and 3.2×10^{-21} m^2 from inflow and outflow, respectively. These values are close to that of the sample before shearing. The specimen volume changes monitored by the water exchanges and LVDT measurements (Fig. 9b) are in good agreement and comparable to those obtained during the permeability test before shearing.

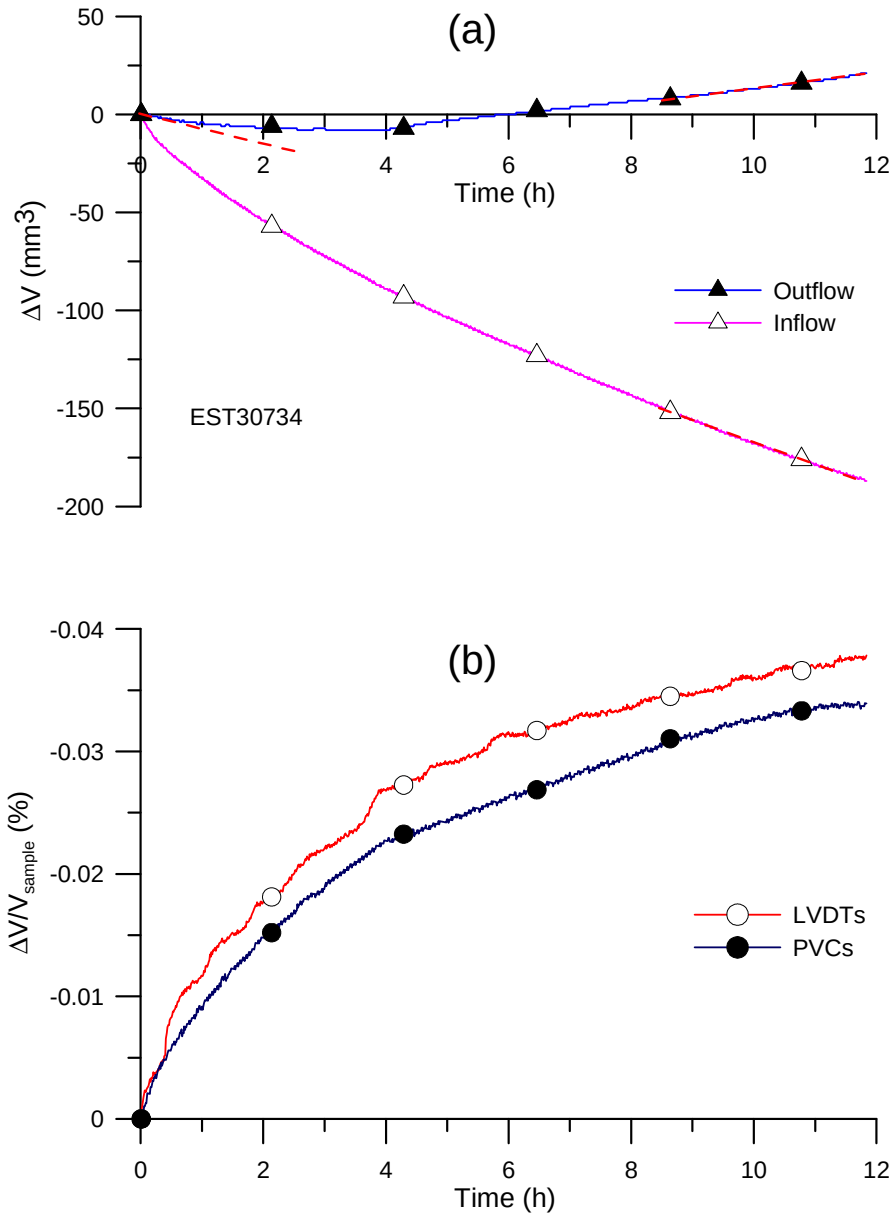

Fig. 9. Radial permeability test at point D, (a): inflow and outflow, (b): volume change.

3.3. Heating under undrained conditions (path D-E)

At the end of the shear test (path C-D) at 25°C, the shear stress q equals 7.3 MPa, the confining pressure equals 6.6 MPa and the back pressure equals 1.0 MPa. From this state, the vertical displacement of the piston was blocked by closing valve V1 (Fig. 1c). The confining pressure was kept constant at 6.6 MPa and the specimen was heated at a rate of 1°C/h under undrained conditions. Fig. 10a shows the change in shear stress with respect to temperature. The shear stress first decreased from 7.3 MPa to 7.1 MPa at 25.6 °C and afterwards increased up to a peak (7.8 MPa) at 28.5 °C, followed by a progressive quasi-linear decrease to 5.3 MPa at 80°C.

The changes in pore pressure during this path are presented in Fig. 10b (up to 60°C because a leak then occurred in the pressure transducers). One can observe that the pore pressure quickly increased from 1.0 to 1.5 MPa when the temperature increased from 25.0 to 28.5 °C, with a mean rate of 0.14 MPa/°C. At temperature higher than 28.5°C, the rate of pore pressure increase versus temperature increase became lower (0.005 MPa/°C).

The changes in axial and radial strains with respect to temperature are presented in Fig. 10c. Below 28.5°C, strains were negligible. Above 28.5°C, the axial strain increased while the radial strain decreases. Axial strain data above 38°C were unfortunately not monitored (no further change due to friction effects in the LVDT).

Examination of the inflow and outflow curves at 80°C (Point E, Fig. 11a) evidences larger fluxes compared to previous tests. However, the intrinsic permeability values obtained from inflow and outflow curves are equal to 4.1×10^{-21} m^2 and 2×10^{-21} m^2, respectively. They are comparable to the values obtained previously before and after shearing. This confirms that the larger fluxes observed are due to the decrease in water viscosity μ_w with temperature (from 8.90×10^{-4} Pa.s at 25°C to 3.55×10^{-4} Pa.s at 80°C).

Fig. 11b shows the changes in sample volume during the test with good correspondence between water exchanges and LVDT measurements. A swelling of 0.087% is observed at the end of the test.

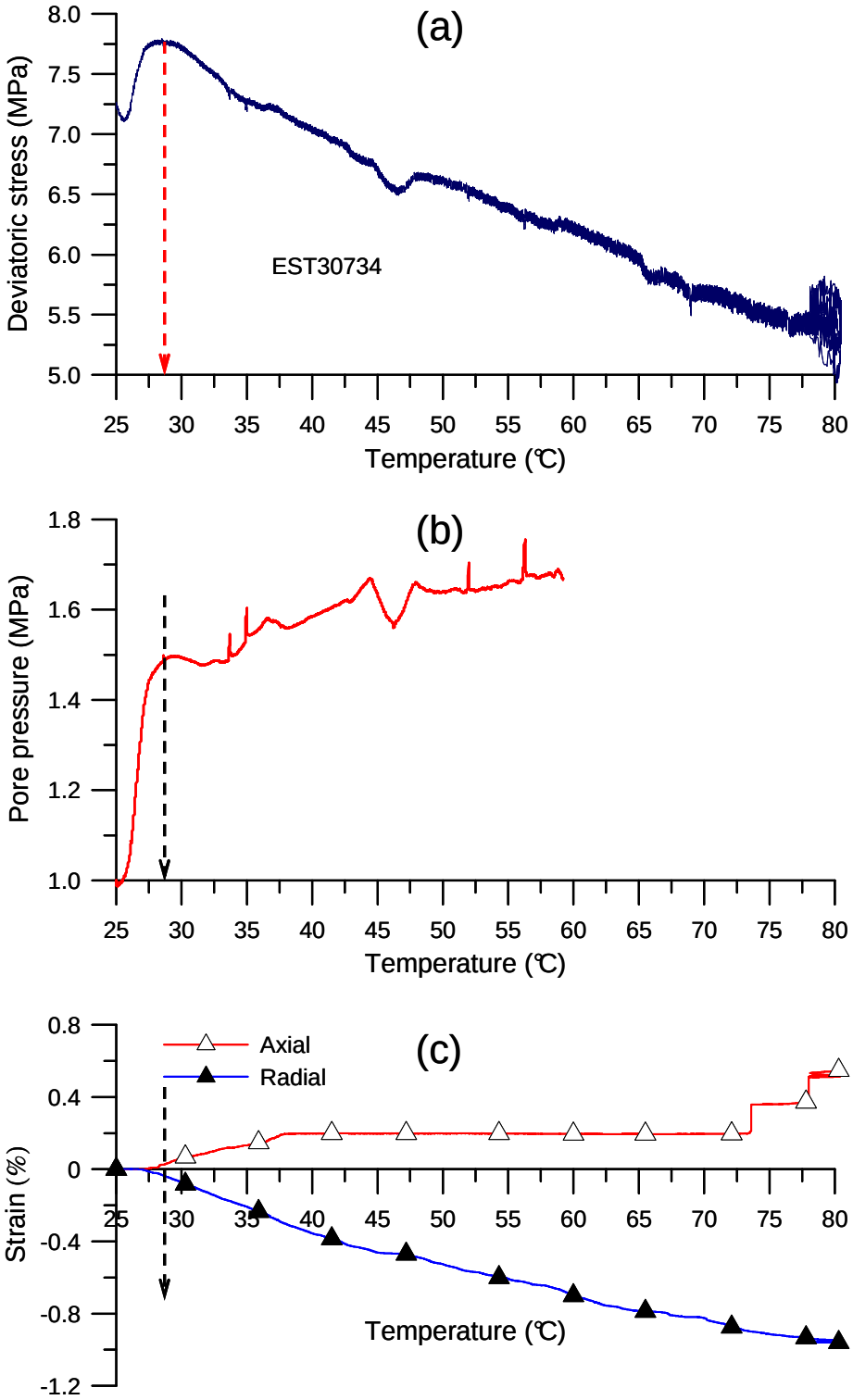

Fig. 10. Undrained heating test, (a): Shear stress change, (b): Pore pressure change, (c): Axial and Radial strains captured by LVDTs.

The subsequent cooling phase (path E-F) was performed at constant confining pressure (σ_3 = 6.6 MPa). During this phase, a leak in the application system of the shear stress led to a decrease in shear stress down to 0 MPa. The sample was then submitted to the combined

effect of temperature decrease followed by shear stress release and it appeared difficult to analyse the resulting response to this poorly controlled thermo-mechanical stage.

The permeability test carried out at point F (25°C) provides inflow and outflow permeability values of 6.1 × 10^{-21} m^2 and 1.7 × 10^{-21} m^2, respectively (Fig. 12a). As in previous tests, a swelling of 0.05% occurred (Fig. 12b).

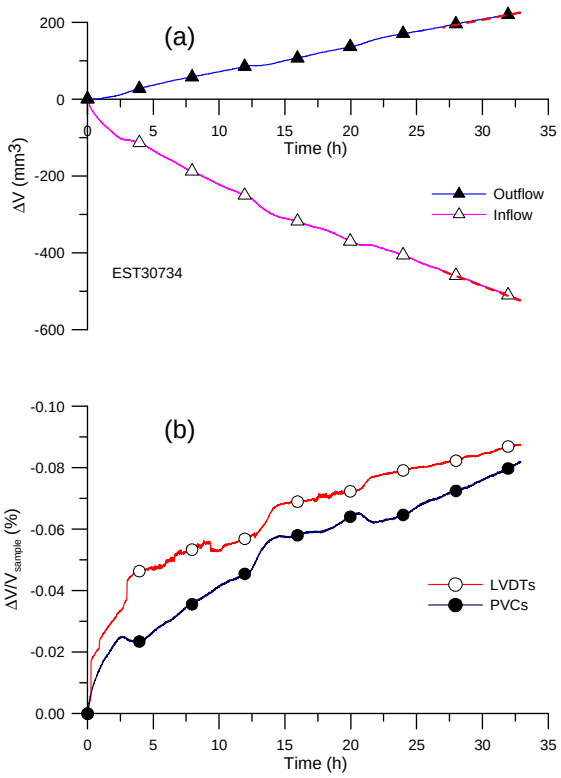

Fig. 11. Radial permeability test at point E,
(a): inflow and outflow, (b): volume change.

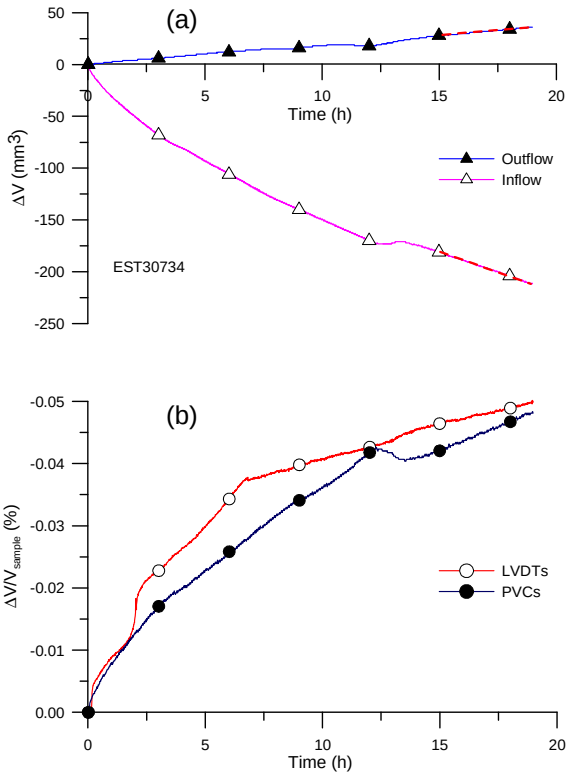

Fig. 12. Radial permeability test at point F,
(a): inflow and outflow, (b): volume change.

3.4. Isotropic drained heating of the sheared sample (F-G)

From point F, the specimen was slowly heated up to 48°C with a heating rate of 0.5°C/h, low enough to ensure drained conditions (Sultan et al. 2002; Monfared et al. 2011b). The local axial, radial and volumetric strains obtained from the LVDTs are presented in Fig. 13. Contraction of the sheared sample occurred from the beginning of the test, with radial strains larger than axial strains, showing some anisotropy in the thermal response. At 48°C, the axial strain is equal to 0.007% (characterised by a slope $C_{T\perp}$=0.28 x 10^{-5} °C^{-1}) compared to 0.027% ($C_{T||}$= 1.26 x 10^{-5} °C^{-1}) for the radial strain.

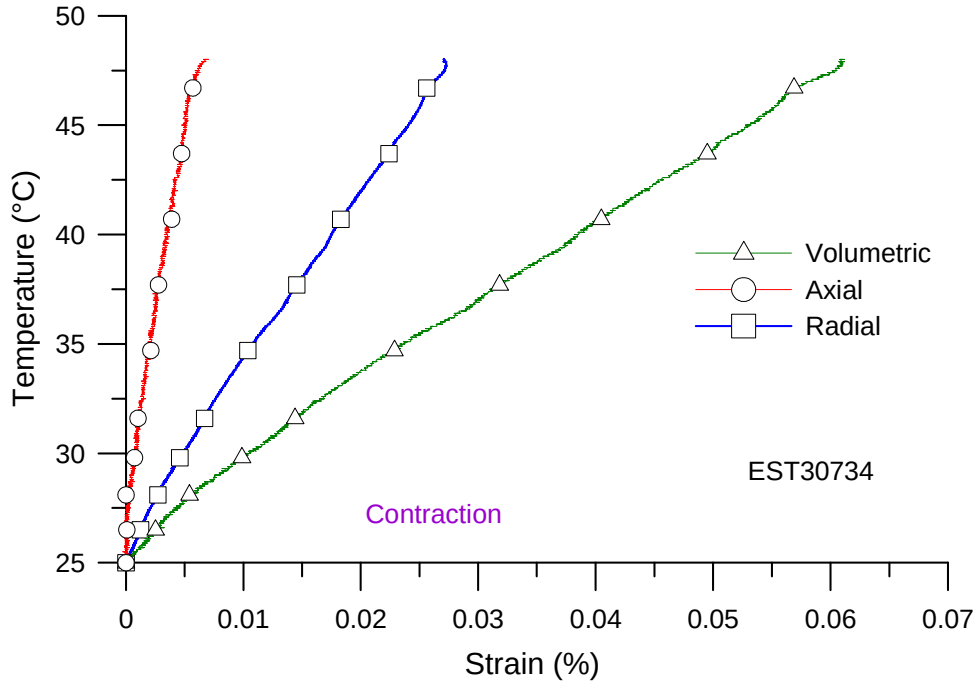

Fig. 13. Isotropic drained heating test.

4. Discussion

The test carried out in this work was aimed at further investigating some thermomechanical issues related to the behaviour of the excavation damaged zone that develops around galleries and repository cells excavated at great depth into a claystone. To do so, the first stage of the test was aimed at mimicking the stress path followed during excavation, by running a shear test at constant mean effective stress up to failure. This first stage carried out in drained conditions provided some insight into the shear strength and failure properties of the Callovo-Oxfordian claystone. As seen in Fig. 6 (path B-C-D), the curves obtained are comparable to other data obtained on the COx claystone, with axial strains (perpendicular to bedding) larger than radial ones (e.g. Chiarelli et al. 2003; Homand et al. 2003; Zhang and Rothfuchs 2004; Hu et al. 2014).

The corresponding stress path plotted in a $q - p'$ diagram presented in Fig. 14 exhibits some small perturbations at the beginning of the test at low shear stress due to some technical problems with the PVC controlling the confining pressure, for p' values smaller than 1.0 MPa. The mean effective stress p' afterwards stabilizes at 7.9 MPa. The Figure shows that failure is reached at a peak shear stress of 11 MPa (point C). This is a rather small value compared to that obtained under comparable conditions by Zhang and Rothfuchs (2004) and Hu et al. (2014). This confirms the variability already observed in the failure criteria of the

COx clay, that depends on the specimen origin and of the layer in which it has been excavated, together with other technical parameters like the experimental procedures followed (including the specimen size and shape, the resaturation procedure followed and the drainage conditions imposed). Visual observation made at the end of the test on the sheared specimen (Fig. 7) evidenced a shear network that obviously affected the post-peak response that was characterised by the mobilisation of the shear planes and the mutual sliding of blocks.

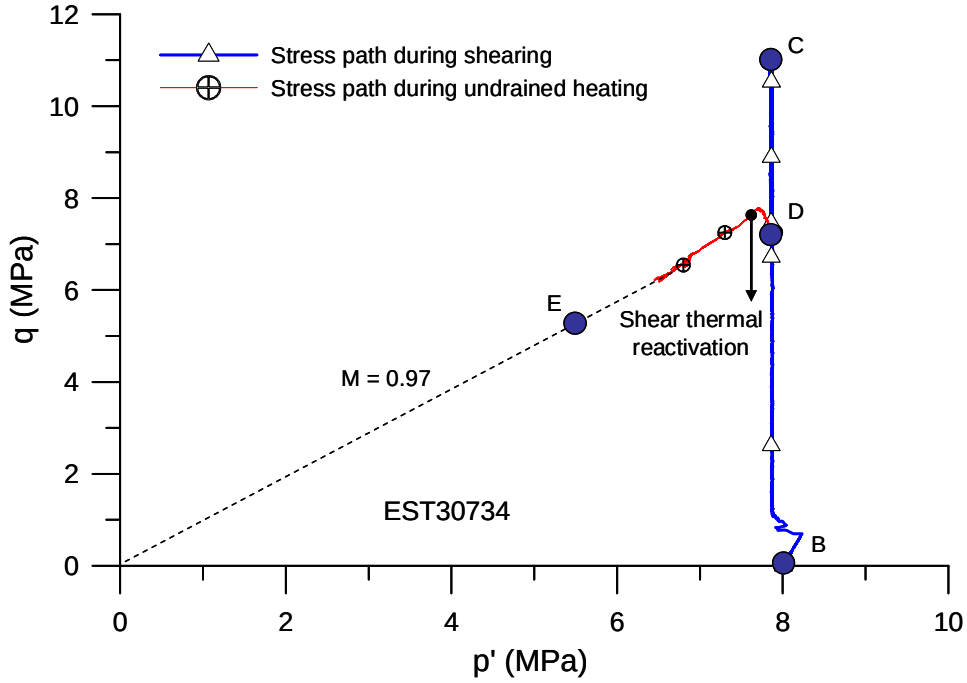

Fig. 14. Stress path in q-p' plane.

Particular attention was devoted to the changes in permeability along the various stages of the test to capture possible effects of strain localisation and temperature elevation on the overall response of the specimen. Permeability tests were carried out by running constant head steady state radial permeability tests in the hollow cylinder specimen, by imposing a pore pressure increase (Δu = 0.5 MPa) on the outer face of the cylinder while monitoring water exchanges by using the pressure volume controllers. Unlike in standard triaxial testing on full cylinders that only involves an axial flow of water through the sample that may or may not be affected by a shear plane, the hollow cylinder configuration does impose a radial flow through the network of shear bands created at failure, in a direction parallel to bedding. It is hence particularly adapted to capture the effects of shear bands on the permeability. In this regard, this device usefully completes previous procedures carried

out on sample in which tensile cracks were created (Davy et al. 2007). Both procedures then cover the water transfer properties of both the tensile and shear cracks that characterise the EDZ (Armand et al. (2014), allowing better investigation of the self-sealing properties of the claystone.

During permeability tests, the volume changes of the specimen were monitored by both the amount of water exchanges monitored by the PVC and the local strain measurements provided by the LVDTs. Quite a good correspondence was observed between these data in most tests, providing good confidence in the permeability values obtained. The combined effects of the effective stress release (progressively induced when applying the pore pressure increment of 0.5 MPa on the outer face), the specimen hydration and the swelling induced, and the final stabilization of water flows could clearly be identified in the curves of water exchanges provided by the PVC.

At the beginning of the test, a reference permeability value just after resaturation under conditions close to in-situ stress (p = 9 MPa and u = 1 MPa, point B) of 4.9 x 10^{-21} m^2 was obtained. This value is in the range of magnitude of intrinsic permeability of the COx claystone, estimated between 10^{-20} and 10^{-22} m^2, (Escoffier et al. 2005; Delay et al. 2006; Mohajerani et al. 2011). Further changes due to shearing and temperature elevation could then be monitored by running similar tests at each stage of the test.

The 0.5 MPa excess pore pressure applied on the external face of the sheared sample induced a decrease in shear stress down to 7.3 MPa (path C-D) related to the reactivation of shear bands. The important conclusion drawn from the permeability test after this stage was that, in spite of the clear appearance of shear bands observed all around the sample, they were no decrease in permeability at ambient temperature, confirming the good self-sealing properties of the COx claystone.

After the shear stress release phase, the undrained heating of the sheared sample exhibited a first stage up to a temperature of 28.5°C during which an increase in shear stress up to a peak at 7.75 MPa was coupled to a fast increase in pore pressure up to a maximal value of 1.49 MPa (Fig. 10a and Fig. 10b) with no change detected in the LVDT measurements (Fig. 10c). During this stage in which the specimen was stable with no mobilisation of the shear planes, an estimation of the thermal pressurisation coefficient can be made.

The total pore pressure change during undrained heating is given from the water mass change equation ($dM_w = 0$) as follows:

$$du = Bdp + \Lambda dT \quad (2)$$

where B is the Skempton coefficient (Skempton 1954) and Λ is the thermal pressurisation coefficient. Eq. (2) indicates that the total pore pressure change is due to a part related to the total stress change ($Bdp = B\frac{dq}{3}$) and a part related to temperature change (du_T):

$$du_T = \Lambda dT = du - B\frac{dq}{3} \quad (3)$$

The Skempton coefficient of saturated COx claystone was found equal to 0.87 (Mohajerani et al. 2014) for a saturated sample of the same porosity (17.7%). The pore pressure induced by the temperature increase can be calculated by using Eq. (3), providing a thermal pressurisation coefficient equal to 0.156 MPa/°C between 25 and 28.5°C. This value is in agreement with the results of Mohajerani et al. (2012) who observed that the thermal pressurisation coefficient slightly decreased with increased temperature, with a value of 0.145 MPa/°C at 32°C.

Once the peak reached, the shear stress started decreasing linearly while the increase in pore pressure became smaller and less regular. During this stage, the LVDT measurements evidenced a decrease in specimen length combined to an increase in radius, capturing the displacements resulting from the thermal reactivation of the shear bands and the mutual sliding of the blocks, in agreement with data obtained by Monfared et al. (2012) on the Boom clay. This reactivation resulted in a somewhat irregular response in pore pressure.

Due to thermal pore fluid pressurisation in the sheared sample and to the resulting decrease in effective stress during the undrained heating phase (D-F), the stress path moved towards the left. A continuous decrease in q and p' was afterwards observed in the plane q – p' (Fig. 14) with a constant ratio q/p' equal to $M = 0.97$, that corresponded to a friction angle $\varphi' = \arcsin(\frac{3M}{6+M}) = 24.7°$. This value, that is typical of a residual state in which a pre-sheared plane is reactivated, is in good agreement with the results of Zhang and Rothfuchs

(2004) at ambient temperature on the COx claystone. It would tend to indicate that the residual friction angle is not temperature dependent.

The sheared sample submitted to drained heating between 25 to 48°C (path F-G, Fig. 13) exhibited a thermal contraction. Contraction is larger in the direction parallel to bedding than perpendicular to bedding, with an anisotropy ratio of 4.5. This trend is not in agreement with recent data of Monfared et al. (2011b, on the Opalinus clay) and of Mohajerani et al. (2014, on the COx claystone) showing larger thermal contraction perpendicular to bedding. It is suspected here that the radial thermal contraction could be enhanced by the subvertical cracks (with an angle of 67°C with respect to horizontal, see the photo of the sheared specimen in Fig. 7) along which the smectite phase is mobilised. Note also that some mobilisation of the shear band could also intervene.

The permeability test run at 80°C on the sheared sample showed that the intrinsic permeability of COx claystone was not dependent on temperature, with the larger fluxes observed only related to the decrease in water viscosity with temperature, in agreement with previous results on intact Boom clay sample (Delage et al. 2000). As already observed in the Boom clay and the Opalinus clay, the good self-sealing properties of the COx claystone are confirmed at elevated temperature.

5. Conclusion

An experimental program was carried out in a new hollow cylinder triaxial cell with a short drainage path specially designed for low permeability rocks to investigate some thermo-hydro-mechanical issues in the EDZ around galleries excavated in claystones. The sample was first resaturated under a stress state close to in-situ stress conditions in order to minimize swelling and damage during resaturation.

To complete the understanding of the response of the EDZ around a gallery submitted to temperature elevation like that induced by exothermic radioactive waste, a COx specimen was submitted in the hollow cylinder triaxial apparatus to a stress path close to that supported in the close field during excavation, i.e. to shear at constant total mean stress. Once the sample sheared and the post-peak regime with shear bands reached, the shear stress was released. Subsequent undrained thermal pressurization led to a decrease in mean effective stress that brought back the sheared sample to failure.

The results of radial permeability tests on COx claystone specimens showed that the damage induced by shearing that resulted in the development of a network of shear bands

around the sample did not affect the sample permeability, confirming the excellent self-sealing properties of the COx claystone. Like in the case of other clays and claystones, self-sealing properties are made possible thanks to the smectite fraction of the clay matrix that is mobilized along shear bands. The results of radial permeability test on heated samples already sheared evidenced the mobilisation of larger fluxes that were only due to the decrease in water viscosity with temperature, with no significant change in the intrinsic permeability. The results obtained here confirm the good self-sealing properties the COx claystone and extend them to elevated temperature.

Indeed, the presence of smectite minerals in the clays and claystones presently considered in Europe for the deep disposal of radioactive waste (the Boom clay in Belgium, the Opalinus clay in Switzerland and the Callovo-Oxfordian claystone in France) provide efficient self-sealing properties that result in the fact that the overall permeability of the EDZ is comparable to that of the intact rock. This point already evidenced in tensile cracks is now confirmed in shear cracks thanks to the special device used here.

Acknowledgements

The authors are indebted to ANDRA, the French agency for the management of radioactive waste disposal, for funding this research.

References

[1] ANDRA (2012) Référentiel du comportement THM des formations sur le site de Meuse/ Haute-Marne. D.RP.AMFS.1 2.0024

[2] Armand G, Leveau F, Nussbaum C, De La Vaissière R, Noiret A, Jaeggi D et al (2014) Geometry and properties of the excavation-induced fractures at the Meuse/Haute-Marne URL drifts. Rock Mechanics and Rock Engineering 47:21-41

[3] Bésuelle P, Viggiani G, Desrues J, Coll C, Charrier P (2014) A Laboratory Experimental Study of the Hydromechanical Behavior of Boom Clay. International Journal of Rock Mechanics and Rock Engineering 47:143–155.

[4] Chiarelli AS, Shao JF, Hoteit N (2003) Modeling of elastoplastic damage behavior of a claystone. International Journal of Plasticity 19: 23-45

[5] Cui YJ, Le TT, Tang A.M, Delage P and Li XL (2009) Investigating the time dependent behaviour of Boom clay under thermo-mechanical loading. Géotechnique 59(4): 319-329

[6] Davy CA, Skoczylas F, Barnichon JD, Lebon P (2007) Permeability of macro-cracked argillite under confinement: gas and water testing. Physics and Chemistry of the Earth 32(8–14):667–80

[7] Delage P, Sultan N, Cui YJ (2000) On the thermal consolidation of Boom clay. Canadian Geotechnical Journal 37(2): 343-354

[8] Delage P, Le TT, Tang AM, Cui YJ, Li XL (2007) Suction effects in deep Boom clay block samples. Géotechnique 57(1): 239–244

[9] Delay J, Trouiller A, Lavanchy JM (2006) Propriétés hydrodynamiques du Callovo-Oxfordien dans l'Est du bassin de Paris : comparaison des résultats obtenus selon différentes approches. C.R. Geoscience 338

[10] Escoffier S, Homand F, Giraud A, Hoteit N, Su K (2005) Under stress permeability determination of the Meuse/Haute-Marne mudstone. Engineering Geology 81(3):329–40

[11] Gaucher G, Robelin C, Matray JM, Négrel G, Gros Y, Heitz JF, Vinsot A, Rebours H, Cassagnabère, Bouchet A (2004) ANDRA underground research laboratory: interpretation of the mineralogical and geochemical data acquired in the Callovian-Oxfordian formation by investigative drilling. Physics and Chemistry of the Earth 29:55-77

[12] Homand F, Chiarelli AS, Hoxha D (2003) Caractéristiques physiques et mécaniques du granite de la Vienne et de l'argilite de l'Est. Revue Française de Génie Civil 6(1):11-20

[13] Hu DW, Zhang F, Shao JF (2014) Experimental study of poromechanical behavior of saturated claystone under triaxial compression. Acta Geotechnica 9:207–214

[14] Hueckel T, Pellegrini R (1991) Thermoplastic modeling of undrained failure of saturated clay due to heating. Soils Found 31(3):1-16

[15] Hueckel T, François B, Laloui L (2009) Explaining thermal failure in saturated clays. Géotechnique 59 (3):197-212

[16] Li Y, Weetjens E, Sillen X, Vietor T, Li X, Delage P, Labiouse V, Charlier R (2014) Consequences of the thermal transient on the evolution of the damaged zone around a repository for heat-emitting high-level radioactive waste in a clay formation: a performance assessment perspective. *Rock Mechanics and Rock Engineering* 47:3-19

[17] Mohajerani M, Delage P, Monfared M, Tang A.M, Sulem J, Gatmiri B (2011) Oedometric compression and swelling behaviour of the Callovo-Oxfordian argillite. International Journal of Rock Mechanics and Mining Sciences 48(4):606-615

[18] Mohajerani M, Delage P, Monfared M, Tang A.M, Sulem J, Gatmiri B (2012) A laboratory investigation of thermally induced pore pressures in the Callovo-Oxfordian claystone. International Journal of Rock Mechanics and Mining Sciences 52:112-121

[19] Mohajerani M, Delage P, Sulem J, Monfared M, Tang A.M, Gatmiri B (2014) The thermal volume change of the Callovo-Oxfordian claystone. International Journal of Rock Mechanics and Rock Engineering 47:131-142

[20] Monfared M, Delage P, Sulem J, Mohajerani M, Tang AM, De Laure E (2011a) A new hollow cylinder triaxial cell to study the behaviour of geomaterials with low permeability. International Journal of Rock Mechanics and Mining Sciences 48 (4):637-649

[21] Monfared M, Sulem J, Delage P, Mohajerani M (2011b) A laboratory investigation on thermal properties of the Opalinus claystone. International Journal of Rock Mechanics and Rock Engineering 44(6):735-747

[22] Monfared M, Sulem J, Delage P, Mohajerani M (2012) On the THM behaviour of a sheared Boom clay sample: Application to the behaviour and sealing properties

of the EDZ. Engineering Geology 124:47-58

[23] Monfared M, Sulem J, Delage P, Mohajerani M (2014) Temperature and Damage Impact on the Permeability of Opalinus Clay. International Journal of Rock Mechanics and Rock Engineering 47:101–110

[24] Morin R, Silva AJ (1984) The effects of high pressure and high temperature on some physical properties of ocean sediments. Journal of Geophysical Research 89(B1):511–526

[25] Skempton AW (1954) The pore pressure coefficients A and B. Géotechnique 4:143–147

[26] Sultan N, Delage P, Cui YJ (2002) Temperature effects on the volume change behaviour of Boom clay. Engineering Geology 64(2-3):135-145

[27] Wileveau Y, Cornet FH, Desroches J, Blumling P (2007) Complete in situ stress determination in an argillite sedimentary formation. Phys Chem Earth A/B/C; 32(8–14):866–78

[28] Yven B, Sammartino S, Geroud Y, Homand F, Villieras F (2007) Mineralogy, texture and porosity of Callovo-Oxfordian claystones of the Meuse/Haute-Marne region (eastern Paris Basin). Mémoires de la Société géologique de France, ISSN 0249-7549, 178: 73-90

[29] Zhang CL and Rothfuchs T (2004) Experimental study of the hydro-mechanical behaviour of the Callovo-Oxfordian argillite. Applied Clay Science 26(1-4):325-336

[30] Zhang CL, Rothfuchs T (2008) Damage and sealing of clay rocks detected by measurements of gas permeability. Physics and Chemistry of the Earth A/B/C 33 (Suppl. 1):S363–73

[31] Zhang CL (2011) Experimental evidence for the self-sealing of fractures in claystone. Physics and Chemistry of the Earth 36: 1972–1980

[32] Zhang CL (2013) Sealing of fractures in claystone. Journal of Rock Mechanics and Geotechnical Engineering 5:214–220

Conclusions générales et perspectives

Le stockage des déchets radioactifs à vie longue et forte activité dans les couches géologiques profondes peu perméables comme les argilites nécessite l'étude de divers aspects du comportement THM de l'argilite du Callovo-Oxfordien et les thèmes abordés dans ce travail s'y rattachent.

Propriétés de rétention d'eau

Afin de mieux comprendre les changements de teneur en eau à proximité des parois sous l'effet de l'évaporation engendrée par la ventilation des galeries et du remouillage qui interviendra une fois les galeries fermées, du fait de l'infiltration d'eau depuis la roche saturée, une étude microstructurale des propriétés de rétention d'eau a été réalisée à l'aide de la porosimétrie au mercure sur des échantillons lyophilisés préalablement soumis à différentes valeur de succions. Le long de chemin de séchage, la microstructure de l'état initial désaturé est caractérisée par une seule population de pores bien classée autour d'un diamètre caractéristique de 32 nm qui correspond à l'épaisseur moyenne des plaquettes d'argile. Le passage à 150 et 331 MPa de succion est traduit par une légère modification au niveau des courbes porosimétriques. La courbe porosimétrique garde la même allure avec un diamètre caractéristique légèrement déplacé vers des valeurs plus petites (28-27 nm). Le séchage a également un effet sur l'infra-porosité non détectée par l'intrusion de mercure (diamètre <5.5 nm), qui est de l'ordre de 4% à l'état initial (34 MPa de succion) et passe à 3% à 150 et 331 MPa de succion. Le séchage à l'étuve produit un effet plus fort d'une part sur la taille des pores qui passent à un diamètre caractéristique de 20 nm et d'autre part sur l'infra-porosité qui passe à 1%.

L'humidification à 9 MPa de succion conduit à la saturation de l'argilite du COx sans changement dans la microstructure, alors que l'humidification à succion nulle donne lieu à l'apparition d'une nouvelle population de pores traduisant la formation des fissures de quelques micromètres. Les concepts décrivant l'hydratation progressive des smectites par la mise en place successive de molécules d'eau en fonction de la succion appliquée est apparue utile pour comprendre les propriétés de rétention d'eau dans l'argilite du COx.

Couplage compression-gonflement

L'étude du couplage compression-gonflement de l'argilite du COx a été menée par la réalisation d'une série d'essais oedométriques complétée par des observations microstructurales par l'utilisation conjointe de la porosimétrie au mercure et le microscope électronique à balayage. Des échantillons ont été comprimés jusqu'à des contraintes maximales de 56 et 113 MPa avant d'être déchargés dans deux conditions: i) à teneur en eau constante et ii) en permettant l'infiltration de l'eau, comme dans les essais de gonflement standard. Les résultats obtenus sur les échantillon déchargés à teneur en eau constante ont permis d'interpréter la compression comme une action combinée de l'écrasement des pores (entraînant des fissures locales) au niveau inter-plaquettes dans la matrice argileuse, et de la compression des plaquettes elles-mêmes par l'expulsion de certaines molécules d'eau adsorbées dans les feuillets de smectite dans les plaquettes interstratifiées illite-smectite. Le gonflement du à l'infiltration de l'eau pendant le déchargement a entraîné des modifications des pores à deux niveaux: par la création des fissures de quelques dizaines de micromètres, et par un désordre induit au niveau de la porosité inter-plaquettes qui est devenue moins bien organisée, avec une plus grande gamme de diamètre de pores par rapport à l'état initial.

Comportement thermo-mécanique

Une importance particulière a été accordée au comportement thermo-mécanique de l'argilite du COx saturée, vu les rares données existantes du fait de la difficulté de réalisation des essais au laboratoire. Une cellule triaxiale cylindre creux à faible chemin de drainage (égal à la demie épaisseur du cylindre creux, 10mm) développée spécialement pour les matériaux peu perméable (Monfared et al. 2011a) a été utilisée. Toutes les éprouvettes testées ont été préalablement resaturées sous un état de contrainte proche à celle en place afin de limiter les perturbations liées au gonflement. Les principaux résultats obtenus sont les suivants :

- Les données de résistance au cisaillement obtenues sont en bon accord avec celles obtenues à partir d'essais également réalisés dans des conditions complètement saturées par Hu et al. (2014a) sur des éprouvettes de porosité similaire ;
- Des valeurs de résistances au cisaillement plus faibles sont obtenues sur des éprouvettes de plus forte porosité ;
- Les essais de chauffage isotrope drainé sous des conditions de contrainte proche à celle in-situ et ½ in-situ ont confirmé le comportement plastique contractant de

l'argilite du COx lors, déjà identifié par Mohajerani et al. (2014), avec une contraction moins importante pour des éprouvettes de plus faible porosité ;

- Les essais de cisaillement à une température élevée à 80°C n'ont pas montré de changement significatif des paramètres élastiques ;
- Les résultats préliminaires obtenus montrent un comportement plus ductile et une résistance au cisaillement moins importante à une température plus élevée, en accord avec les rares données publiées sur les argilites ;
- Les essais de perméabilité radiale réalisés à 25 et 80°C montrent que la perméabilité intrinsèque de l'argilite du COx ne change pas significativement avec l'augmentation de la température, le débit plus important observé pendant l'essai à 80°C étant essentiellement lié à la diminution de la viscosité de l'eau avec l'augmentation de la température ;

Propriétés d'auto-colmatage

Pour étudier les propriétés d'auto-colmatage et les effets combinés de l'augmentation de la température et d'une discontinuité de cisaillement sur la perméabilité, un programme expérimental spécifique a été réalisé à l'aide la cellule triaxiale cylindre creux afin de reproduire la situation de l'argilite du COx dans la zone endommagée par l'excavation. L'augmentation de la température autour des galeries de stockage engendre une surpression interstitielle par le phénomène de pressurisation thermique dans la zone endommagée et cette surpression peut créer de nouvelles fissures et/ou réactiver des fissures préexistantes, comme l'ont déjà montré Monfared et al. (2012) dans le cas de l'argile de Boom. Les résultats obtenus sur l'argilite du Callovo-Oxfordien ont montré que le chauffage non drainé d'une éprouvette préalablement portée à la rupture conduit à la réactivation d'un plan de cisaillement par la pressurisation thermique du fluide interstitiel. L'effet de l'endommagement induit par le cisaillement sur la perméabilité a été également étudié en réalisant des essais de perméabilité avant et après cisaillement à 25 et 80°C. Les résultats obtenus n'ont montré aucun effet de l'endommagement sur la perméabilité, confirmant les bonnes propriétés d'auto-colmatage de l'argilite du COx à différentes températures.

Perspectives

L'argilite du Callovo-Oxfordien est un matériau anisotrope à cause de l'existence de plans de stratification. Tous les essais réalisés dans ce travail ont été menés sur des éprouvettes provenant de carottes perpendiculaire au plan du litage. Une étude plus complète de l'anisotropie des propriétés mécaniques, hydriques et thermiques de l'argilite paraît nécessaire pour compléter la base des données caractérisant son comportement.

Cette étude a mis en évidence les bonnes capacités d'auto-colmatage de l'argilite, confirmant que les fractures n'avaient pas d'influence significative sur la perméabilité à l'eau de l'argilite saturée. Néanmoins l'étude du couplage endommagement-perméabilité en condition non saturée est également un point important à explorer. Cela permettra de mieux comprendre les changements de perméabilité pendant la phase de ventilation des galeries, durant laquelle l'argilite se trouve à l'état non saturé, ainsi que la phase post-fermeture de production de gaz par la corrosion des colis des déchets.

Références bibliographiques

[1] Ahmed S, Lovell CW, Diamonds S (1974). Pore sizes and strength of compacted clay. ASCE J. Geotech. Engng 100, No 4: 407–425

[2] ANDRA (2005). Synthesis argile: evaluation of the feasibility of a geological repository in argillaceous formation. http://www.andra.fr/international/ download/andra-international-en/document/editions/266va.pdf

[3] ANDRA (2012). Référentiel du comportement THM des formations sur le site de Meuse/ Haute-Marne. D.RP.AMFS.1 2.0024

[4] Armand G, Leveau F, Nussbaum C, De La Vaissière R, Noiret A, Jaeggi D et al (2014). Geometry and properties of the excavation-induced fractures at the Meuse/Haute-Marne URL drifts. Rock Mechanics and Rock Engineering 47:21-41

[5] Aversa S, Evangelista A, Leroueil S, Picarelli L (1993). Some aspects of the mechanical behaviour of structured soils and soft rocks. In: Anagnostopoulos, editor. Geotechnical engineering of hard soils–soft rocks. Rotterdam: Balkema

[6] Ben Rhaiem H, Pons CH, Tessier D (1985). Factors affecting the microstructure of smectites: role of cations and history of applied stresses, In: Schultz et al. (eds) Proc Int Clay Conf, Denver, The Clay Mineralogical Soc, pp 292–297

[7] Bérend I, Cases JM, François M, Uriot JP, Michot LJ, Masion A, Thomas F (1995). Mechanism of adsorption and desorption of water vapour by homoionic montmorillonites: 2. The Li+, Na+, K+, Rb+ and Cs+ exchanged forms. Clays and Clay Minerals 43: 324−336

[8] Bésuelle P, Viggiani G, Desrues J, Coll C, Charrier P (2014). A Laboratory Experimental Study of the Hydromechanical Behavior of Boom Clay. International Journal of Rock Mechanics and Rock Engineering 47: 143–155

[9] Bishop AW, Kumapley NK, El Ruwayih A (1974). The influence of pore water tension on the strength of a clay. Proc. Royal Soc. London vol. 1286: 511-554.

[10] Blaise T, Barbarand J, Kars M, Ploquin F et al. (2013). Reconstruction of low temperature (<100 _C) burial in sedimentary basins: A comparison of geothermometer in the intracontinental Paris Basin. Marine and Petroleum Geology **http://dx.doi.org/10.1016/j.marpetgeo.2013.08.019**

[11] Bornert M, Vales F, Gharbi H, Nguyen Minh D (2010). Multiscale full-field strain measurements for micromechanical investigations of the hydromechanical behaviour of clayey rocks Strain 46(1): 33–46

[12] Boulin PF, Angulo-Jaramillo R, Daian JF, Talandier J, Berne P (2008). Pore gas connectivity analysis in Callovo–Oxfordian argillite. Applied Clay Science 42: (1–2) 276–283

[13] Carter TG, Castro SO, Carvalho JL, Hattersley D, Wood K, Barone FS, et al (2010). Tunnelling issues with Chilean tertiary volcaniclastic rocks. Mir conference; Problemi di stabilit a nelle opere geotecniche. Capitolo 11, Torino

[14] Cases JM, Bérend I, François M, Uriot JP, Michot LJ, Thomas F (1997). Mechanism of adsorption and desorption of water vapour by homoionic montmorillonite: 3. The Mg2+, Ca2+, Sr2+ and Ba2+ exchanged forms. Clays and Clay Minerals 45: 8−22

[15] Cekerevac C, Laloui L (2004). Experimental study of thermal effects on the mechanical behaviour of a clay. International Journal for Numerical and Analytical Methods in Geomechanics 28: 209–228

[16] Cheng A HD. Material coefficients of anisotropic poroelasticity (1997). International Journal of Rock Mechanics and Mining Sciences 34(2): 199-205

[17] Chiarelli AS (200). Étude expérimentale et modélisation du comportement mécanique de l'argilite de l'est. PhD thesis, Université Lille I

[18] Chiarelli AS, Shao JF, Hoteit N (2003). Modeling of elastoplastic damage behavior of a claystone. International Journal of Plasticity 19: 23-45

[19] Cui YJ, Le TT, Tang A.M, Delage P and Li XL (2009). Investigating the time dependent behaviour of Boom clay under thermo-mechanical loading. Géotechnique 59(4): 319-329

[20] Davy CA, Skoczylas F, Barnichon JD, Lebon P (2007). Permeability of macro-cracked argillite under confinement: gas and water testing. Physics and Chemistry of the Earth 32(8–14): 667-80

[21] De La Vaissière R, Talandier J (2012). Gas injection tests in the Meuse/Haute Marne underground research laboratory. Proceedings of the Transfert 2012 Conference, Ecole Centrale de Lille Eds, 360–368

[22] Delage P, Pellerin FM (1984). Influence de la lyophilisation sur la structure d'une argile sensible du Quebec. Clay Minerals 19(2): 151–160

[23] Delage P, Lefebvre G (1984). Study of the structure of a sensitive Champlain clay and of its evolution during consolidation. Canadian Geotechnical Journal 21 (1): 21–35

[24] Delage P, Audiguier M, Cui YJ, Howat MD (1996). Microstructure of a compacted silt. Canadien Geotechnical Journal 33(1): 150–158

[25] Delage P, Sultan N, Cui YJ (2000). On the thermal consolidation of Boom clay. Canadian Geotechnical Journal 37(2): 343-354

[26] Delage P, Marcial D, Cui YJ, Ruiz X (2006). Ageing effects in a compacted bentonite: a microstructure approach. Géotechnique 56 (5): 291–304

[27] Delage P, Le TT, Tang AM, Cui YJ, Li XL (2007). Suction effects in deep Boom clay block samples. Géotechnique 57 (1): 239–244

[28] Delage P (2009). Compaction behaviour of clay: discussion. Géotechnique 59 (1), 75-76

[29] Delage P (2010). A microstructure approach of the sensitivity and compressibility of some Eastern Canada sensitive clays. *Géotechnique* 60 (5): 353-368

[30] Delage P (2014). The oedometer compression curve is a pore size distribution curve in loose structured clays. Proc. TC105 International Symposium on Geomechanics from micro to macro (2), 1251 – 1254, K. Soga et al. eds, CRC Press. Cambridge, UK

[31] Delage P, Menaceur H, Tang AM, Talandier J (2014). Suction effects in deep Callovo-Oxfordian claystone specimen. Géotechnique Letters 3(2): 84-88

[32] Delay J, Trouiller A, Lavanchy JM (2006). Propriétés hydrodynamiques du Callovo-Oxfordien dans l'Est du bassin de Paris : comparaison des résultats obtenus selon différentes approches. C.R. Geoscience 338

[33] Diamond, S. (1970). Pore size distribution in clays. Clays Clay Miner 18 :7–23

[34] Doran IG, Sivakumar V, Graham J, Johnson A (2000), Estimation of in-situ stresses using anisotropic elasticity and suction measurements. Géotechnique 50(2): 189-196

[35] Escoffier S (2002). Caractérisation expériementale du comportement hydro-mécanique des argillites de Meuse/ Haute Marne. PhD thesis, INPL Nancy

[36] Escoffier S, Homand F, Giraud A, Hoteit N, Su K (2005) Under stress permeability determination of the Meuse/Haute-Marne mudstone. Engineering Geology 81(3): 329–40

[37] Ferrage E, Lanson B, Sakharov BA, Drits VA (2005). Investigation of smectite hydration properties by modeling experimental X-ray diffraction patterns: Part I. Montmorillonite hydration properties. Am. Mineral 90: 1358–1374

[38] Fouché O, Wright H, Le Cléach JM, Pellenard P (2004). Fabric control on strain and rupture of heterogeneous shale samples by using a non-conventional mechanical test. Applied Clay Science 26 (1–4): 367–387

[39] Fredlund DG, Rahardjo H, Fredlund MD (2012). Unsaturated soil mechanics in engineering practice: Wiley, New-York.

[40] Gaucher G, Robelin C, Matray JM, Négrel G, Gros Y, Heitz JF, Vinsot A, Rebours H, Cassagnabère, Bouchet A (2004). ANDRA underground research laboratory: interpretation of the mineralogical and geochemical data acquired in the Callovian-Oxfordian formation by investigative drilling. Physics and Chemistry of the Earth 29: 55-77

[41] Gens A (2011). On the hydromechanical behaviour of argillaceous hard soils-weak rocks. In: Proc. 15th European conference on Soil Mechanics & Geotechnical Engineering, Athens

[42] Gillott JE (1973). Methods of sample preparation for microstructural analysis of soil. Proc. 4th Int. Working Meeting on Soil Micromorphology, ed GK Rutherford, Kingston, 143–164

[43] Heitz JF, Hicher PY (2002). The mechanical behaviour of argillaceous rocks – some questions from laboratory experiments. Proc Int Symp Hydromech Thermo-hydromech Behav Deep Argillaceous Rock: 99–108

[44] Homand F, Chiarelli AS, Hoxha D (2003). Caractéristiques physiques et mécaniques du granite de la Vienne et de l'argilite de l'Est. Revue Française de Génie Civil 6(1): 11-20

[45] Hoxha D, Giraud A, Homand F, Auvray C (2007). Saturated and unsaturated behaviour modelling of Meuse-Haute/Marne argillite. International Journal of Plasticity 23: 733–766

[46] Hu DW, Zhang F, Shao JF (2014a). Experimental study of poromechanical behavior of saturated claystone under triaxial compression. Acta Geotechnica 9: 207–214

[47] Hu DW, Zhang F, Shao JF, Gatmiri B (2014b). Influences of Mineralogy and Water Content on the Mechanical Properties of Argillite. Rock Mechanics and Rock Engineering 47: 157-166

[48] Hueckel T, Baldi G (1990). Thermoplasticity of saturated clays: experimental constitutive study. Journal of Geotechnical Engineering 116(12): 1768–1796

[49] Hueckel T, Pellegrini R (1991). Thermoplastic modeling of undrained failure of saturated clay due to heating. Soils Found 31(3): 1-16

[50] Hueckel T, François B, Laloui L (2009). Explaining thermal failure in saturated clays. Géotechnique 59 (3): 197-212

[51] Jougnot D, A Revil, Lu N, Wayllace A (2010). Transport properties of the Calloxo-Oxfordian clay-rock under partially saturated conditions, Water Resources Research, 46, W08514, doi:10.1029/2009WR008552

[52] Lebon P, Mouroux B (1999). Knowledge of the three French underground laboratory sites. Engineering Geology 52: 251–256

[53] Li Y, Weetjens E, Sillen X, Vietor T, Li X, Delage P, Labiouse V, Charlier R (2014). Consequences of the thermal transient on the evolution of the damaged zone around a repository for heat-emitting high-level radioactive waste in a clay formation: a performance assessment perspective. Rock Mechanics and Rock Engineering 47: 3-19

[54] Marcial D, Delage P, Cui YJ (2002). On the high stress compression of bentonites. Canadian Geotechnical Journal 39 (4): 812–820

[55] Masri M, Sibai M, Shao JF, Mainguy M (2014). Experimental investigation of the effect of temperature on the mechanical behavior of Tournemire shale. International Journal of Rock Mechanics and Mining Sciences 70: 185–191

[56] Méring J, Glaeser R (1954). Sur le rôle de la valence des cations échangeables dans la montmorillonite. Bulletin de la Société Francaise de Minéralogie et Cristallographie 77: 519−530

[57] Mitchell JK, Soga K (2005). Fundamentals of soil behaviour. John Wiley New-York

[58] Mohajerani M, Delage P, Monfared M, Tang AM, Sulem J, Gatmiri B (2011). Oedometer compression and swelling behaviour of the Callovo-Oxfordian argillite. International Journal of Rock Mechanics and Mining Sciences 48(4): 606-615

[59] Mohajerani M, Delage P, Monfared M, Tang A.M, Sulem J, Gatmiri B (2012). A laboratory investigation of thermally induced pore pressures in the Callovo-Oxfordian claystone. International Journal of Rock Mechanics and Mining Sciences 52: 112-121

[60] Mohajerani M, Delage P, Sulem J, Monfared M, Tang A.M, Gatmiri B (2014). The thermal volume change of the Callovo-Oxfordian claystone. International Journal of Rock Mechanics and Rock Engineering 47: 131-142

[61] Monfared M, Delage P, Sulem J, Mohajerani M, Tang AM, De Laure E (2011a). A new hollow cylinder triaxial cell to study the behaviour of geomaterials with low permeability. International Journal of Rock Mechanics and Mining Sciences 48 (4): 637-649

[62] Monfared M, Sulem J, Delage P, Mohajerani M (2011b). A laboratory investigation on thermal properties of the Opalinus claystone. International Journal of Rock Mechanics and Rock Engineering 44(6): 735-747

[63] Monfared M, Sulem J, Delage P, Mohajerani M (2012). On the THM behaviour of a sheared Boom clay sample: Application to the behaviour and sealing properties of the EDZ. Engineering Geology 124: 47-58

[64] Monfared M, Sulem J, Delage P, Mohajerani M (2014). Temperature and Damage Impact on the Permeability of Opalinus Clay. International Journal of Rock Mechanics and Rock Engineering 47: 101–110

[65] Mooney RW, Keenan AC, Wood LA (1952). Adsorption of water vapor by montmorillonite. II. Effect of exchangeable ions and lattice swelling as measured from X-ray diffraction. J. Am. Chem. Soc. 74: 1371–1374

[66] Morin R, Silva AJ (1984). The effects of high pressure and high temperature on some physical properties of ocean sediments. Journal of Geophysical Research 89(B1): 511–526

[67] Norrish K (1954). The swelling of montmorillonite. Discussions of the Faraday society 18: 120−133

[68] Pham QT, Vales F, Malinsky L, Nguyen Minh D, Gharbi H (2007). Effects of desaturation-resaturation on mudstone. Physics and Chemistry of the Earth 32: 646–655

[69] Revil A, Lu N (2013). Unified water sorption and desorption isotherms for clayey porous materials, Water Resources Research 49(9): 5685-5699

[70] Saiyouri N, Tessier D, Hicher PY (2004). Experimental study of swelling in unsaturated compacted clays. Clay Minerals 39: 469–479

[71] Sammartino S, Bouchet A, Prêt D, Parneix JC, Tevissen E (2003). Spatial distribution of porosity and minerals in clay rocks from the Callovo–Oxfordian formation (Meuse/Haute-Marne, Eastern France)—implications on ionics species diffusion and rock sorption capability. Applied Clay Science 23 (1–4): 157–166

[72] Skempton AW (1954). The pore pressure coefficients A and B. Géotechnique 4: 143-147

[73] Skempton AW (1961). Horizontal stresses in an overconsolidated Eocene clay. Proceedings of the 5th International Conference on Soils Mechanic and Foundation Engineering, Paris pp: 351-357

[74] Skempton AW, Sowa VA (1963). The behaviour of saturated clays during sampling and testing. Géotechnique 13(4): 269-290

[75] Sridharan A, Altschaeffl AG, Diamond S (1971). Pore size distribution studies. J. Soil Mech. Found. Div. ASCE 97, No. 5 : 771–787

[76] Sultan N, Delage P, Cui YJ (2002). Temperature effects on the volume change behaviour of Boom clay. Engineering Geology 64(2-3): 135-145

[77] Tang CS, Tang AM, Cui YJ, Delage P, Schroeder C, Shi B (2011). A study of the hydro-mechanical behaviour of compacted crushed argillite. Engineering Geology 118: 93–103

[78] Tovey NK, Wong KY (1973). The preparation of soils and other geological materials for the scanning electron microscope. Proceedings of the International Symposium on Soil Structure, Gothenburg, Sweden, 176-183

[79] Tsang CF, Bernier F, Davies C (2005). Geohydromechanical processes in the excavation damaged zone in crystalline rock, rock salt, and indurated and plastic clays in the context of radioactive waste disposal. International Journal of Rock Mechanics and Mining Sciences 42: 109–25

[80] Valès F (2008). Modes de déformation et d'endommagement de roches argileuses profondes sous sollicitations hydro-mécaniques. PhD thesis Ecole Polytechnique : Paris

[81] Valès F, Nguyen Minh D, Gharbi H, Rejeb A (2004). Experimental study of the influence of the degree of saturation on physical and mechanical properties in Tournemire shale (France) Applied Clay Science 26:197–207

[82] Wan M, Delage P, Tang AM, Talandier J (2013). Water retention properties of the Callovo-Oxfordian claystone. International Journal of Rock Mechanics and Mining Sciences 64: 96–104

[83] Wang LL (2012). Micromechanical experimental investigation and modelling of strain and damage of argillites under combined hydric and mechanical loads. PhD thesis, Ecole Polytechnique, France

[84] Wang LL, Bornert M, Héripré E, Yang DS, Chanchole S (2014). Irreversible deformation and damage in argillaceous rocks induced by wetting/drying. Journal of Applied Geophysics 107: 108-118

[85] Wileveau Y, Cornet FH, Desroches J, Blumling P (2007). Complete in situ stress determination in an argillite sedimentary formation. Phys Chem Earth A/B/C 32(8–14): 866–78

[86] Wu B, Tan CP, Aoki T (1997). Specially designed techniques for conducting consolidated undrained triaxial tests on low permeability shales. International Journal of Rock Mechanics and Mining Sciences 34: 3-4, paper No. 336

[87] Yang D, Chanchole S, Valli P, Chen L (2012). Study of the Anisotropic Properties of Argillite Under Moisture and Mechanical Loads. Rock Mechanics and Rock Engineering 46(2): 247–257

[88] Yven B, Sammartino S, Geroud Y, Homand F, Villieras F (2007). Mineralogy texture and porosity of Callovo-Oxfordian claystones of the Meuse/Haute-Marne region (eastern Paris Basin), Mémoires de la Société géologique de France, ISSN 0249-7549, 178: 73-90

[89] Zhang CL and Rothfuchs T (2004). Experimental study of the hydro-mechanical behaviour of the Callovo-Oxfordian argillite. Applied Clay Science 26(1-4): 325-336

[90] Zhang CL, Rothfuchs T, Su K, Hoteit N (2007). Experimental study of the thermo-hydro-mechanical behaviour of indurated clays. Phys Chem Earth Parts A/B/C 32(8–14): 957–965

[91] Zhang CL, Rothfuchs T (2008). Damage and sealing of clay rocks detected by measurements of gas permeability. Physics and Chemistry of the Earth A/B/C 33 (Suppl. 1): S363–73

[92] Zhang CL (2011). Experimental evidence for the self-sealing of fractures in claystone. Physics and Chemistry of the Earth 36: 1972–1980

[93] Zhang CL (2013). Sealing of fractures in claystone. Journal of Rock Mechanics and Geotechnical Engineering 5: 214–220

[94] Zhang F, Xie SY, Hu DW, Shao JF, Gatmiri B(2012). Effect of water content and structural anisotropy on mechanical property of claystone. Applied Clay Science 69: 79–86

[95] Zhang F, Hu DW, Xie SY, Shao JF (2014). Influences of temperature and water content on mechanical property of argillite. European Journal of Environmental and Civil Engineering 18(2): 173–189